Degradation and Lifetime Prediction of High-Temperature Pressure Seals for Usage in Solar Thermochemical Reactors

Degradierung und Lebensdauerprognose von Hochtemperatur-Druckdichtungen für den Einsatz in solarthermischen Reaktoren

Von der Fakultät für Maschinenwesen der Rheinisch-Westfälischen Technischen Hochschule Aachen zur Erlangung des akademischen Grades einer Doktorin der Ingenieurwissenschaften genehmigte Dissertation

vorgelegt von

Estefanía Vega Puga

Berichter: Univ.-Prof. Dr. rer. nat. Christian Sattler
Prof. Dr.-Ing. Sven Wießner

Tag der mündlichen Prüfung: 02. Dezember 2025

Abstract

Green hydrogen production via solar thermochemical water splitting presents a promising pathway towards the decarbonisation of energy systems. Among the emerging technologies, the R2Mx solar thermochemical reactor, introduces a novel configuration with separated reduction and oxidation zones and movable redox material assemblies (RMAs). This separation enables greater process flexibility and scalability potential but also imposes demanding requirements on sealing components operating under high-temperature and vacuum conditions. Ensuring the functional integrity of these seals is critical, yet the degradation behaviour and service lifetime of polymer-based sealing materials in such environments remain poorly characterised. This work investigates the high-temperature degradation mechanisms, failure modes, and performance of fluoroelastomer (FKM) and perfluoroelastomer (FFKM) O-rings, as well as polytetrafluoroethylene (PTFE) rod seals, at temperatures between 200 °C and 300 °C. Despite their commercial availability, limited experimental data exists on these materials under prolonged use at high temperatures.

This research addresses this gap through a multidisciplinary approach combining several analyses. First, finite element thermal simulations of the R2Mx prototype were used to estimate realistic operational conditions for the seals. Subsequently, both sealing materials (O-rings and rod seals) were subjected to long-term thermal ageing in air and tested in custom-built test rigs that replicate the R2Mx's operational conditions. For O-rings, degradation was assessed through multiple chemical and mechanical degradation indicators. The thermo-oxidative degradation of FKM arises from thermally induced dehydrofluorination while FFKM's degradation is driven by chain scission. A 75% compression set was identified as the end-of-life criterion, correlating well with leakage beyond a threshold value, enabling service lifetime predictions via time-temperature superposition. Failure of FKM and FFKM O-rings was found to occur abruptly and is predicted to arise after 220 and 400 operational days, respectively, at 200 °C under an 8-h daily operation scenario. On the other hand, PTFE lip seals were tested using different rods' surface finishes and concluded that wear is the primary degradation factor across all conditions. Furthermore, the wear mechanism transitioned from abrasive to adhesive and finally thermally driven failure between 250 °C and 300 °C. A 1% wear was defined as end-of-life criterion, with corresponding lifetime estimates of 220 and 140 operational days at 250 °C and 275 °C, respectively. Unlike O-rings, rod seals exhibited progressive failure, marked by a steady increase in leakage over time. Finally, a numerical model was developed to assess the impact of leakage on the reactor's solar-to-fuel efficiency. While efficiency losses remained minor (< 4%) under conservative leakage scenarios, high leakage rates could result in up to 17% efficiency reduction. This work establishes a scientific and practical foundation for understanding the degradation mechanisms of the studied polymers and predicting service lives of high-temperature sealing systems, supporting reliable and efficient operation of advanced solar thermochemical reactors.

Zusammenfassung

Die Erzeugung von grünem Wasserstoff durch solarthermochemische Wasserspaltung ist ein vielversprechender Weg zur Dekarbonisierung. Der solarthermochemische Reaktor R2Mx stellt eine innovative Konfiguration mit getrennten Reduktions- und Oxidationszonen und zyklisch betriebenen Redox-Materialstrukturen dar. Diese Trennung erhöht Flexibilität und Skalierbarkeit, stellt aber auch hohe Anforderungen an Dichtungen, die bei Hochtemperatur- und Vakuumbedingungen verwendet werden. Die Integrität dieser Dichtungen ist entscheidender, doch Degradationsverhalten und Lebensdauer polymerbasierten Dichtungsmaterialen in solchen Umgebungen sind noch wenig charakterisiert. In dieser Arbeit werden die Hochtemperatur-Degradationsmechanismen, Versagensmodi und die Leistung von O-Ringen aus Fluorkautschuk (FKM) und Perfluorkautschuk (FFKM) sowie von Polytetrafluorethylen (PTFE)-Wellendichtungen bei Temperaturen zwischen 200 °C und 300 °C untersucht. Trotz ihrer kommerziellen Verfügbarkeit gibt es nur wenige experimentelle Daten über diese Werkstoffe im Langzeiteinsatz bei hohen Temperaturen.

Diese Forschungsarbeit schließt jene Lücke durch einen multidisziplinären Ansatz mit mehreren Analysen. Zunächst wurden thermische Simulationen des R2Mx-Prototyps realisiert, um realistische Dichtungsbetriebsbedingungen zu ermitteln. Anschließend wurden beide Dichtungen (O-Ringe und Wellendichtungen) einer längeren thermischen Alterung in Luft unterzogen und in speziell entwickelten Prüfständen getestet, die die Betriebsbedingungen des R2Mx simulieren. Bei den O-Ringen wurde die Degradation anhand chemischer und mechanischer Indikatoren bewertet. Die thermo-oxidative Degradation von FKM erfolgt durch Dehydrofluorierung, und die von FFKM durch Kettenspaltung. Als Kriterium für das Lebensdauerende wurde ein Druckverformungsrest von 75% festgelegt, der mit Leckagen über einem Schwellenwert korreliert und so eine Vorhersage der Lebensdauer per Zeit-Temperatur-Verschiebung ermöglicht. Das Versagen der FKM- und FFKM-O-Ringe trat abrupt auf und wurde bei 200 °C und 8 h/Tag nach 200 bzw. 400 Betriebstagen erwartet. Im Gegensatz dazu wurden PTFE-Lippendichtungen mit unterschiedlichen Wellenoberflächen getestet, wobei der Verschleiß als primärer Degradationfaktor ermittelt wurde. Zwischen 250 °C und 300 °C änderte sich der Verschleißmechanismus von abrasiv über adhäsiv zu thermisch. Als Kriterium für das Lebensdauerende wurde ein Verschleiß von 1% definiert, was einer geschätzten Lebensdauer von 223 bzw. 140 Betriebstagen bei 250 °C bzw. 275 °C entspricht. Im Gegensatz zu den O-Ringen erfolgte das Versagen progressiv mit stetig steigender Leckage. Schließlich wurde ein numerisches Modell entwickelt, um den Einfluss von Leckagen auf den Wirkungsgrad des Reaktors zu bewerten. Während die Wirkungsgradverluste unter konservativen Leckageszenarien gering blieben (< 4%), konnten hohe Leckraten zu Verlusten von bis zu 17% führen. Damit schaffen die Ergebnisse dieser Arbeit eine wissenschaftliche und praktische Grundlage für das Verständnis der Degradationsmechanismen der untersuchten Polymere und für die Vorhersage der Lebensdauer von Hochtemperatur-Dichtungssystemen und unterstützt damit den zuverlässigen und effizienten Betrieb fortschrittlicher solarthermischer Reaktoren.

Acknowledgements

First and foremost, I want to thank Prof. Dr. Christian Sattler, for granting me the opportunity to conduct my doctoral research under his supervision at the Institute of Future Fuels, German Aerospace Centre (DLR), in Cologne. His guidance and continued support throughout this journey were invaluable and deeply appreciated.

I am also grateful to Prof. Dr. Sven Wießner for kindly serving as co-examiner of this thesis. His insightful comments and expertise greatly contributed to improving various aspects of this work.

A special mention goes to Dr. Stefan Brendelberger, my direct supervisor, whose scientific mentorship, critical feedback, and advise shaped every stage of this research. Thank you for the freedom to explore ideas and countless hours of discussion.

I am thankful to Dr. Anja Kömmling, Dr. Volker Wachtendorf, and Dr. Matthias Jaunich, from the Bundesanstalt für Materialforschung und -prüfung (BAM) in Berlin. Their expertise in polymer science, thoughtful discussions, and consistent readiness to provide feedback were crucial to the success of this work. I also thank them for performing the long-term compressive stress relaxation tests and IR measurements of O-ring samples.

Furthermore, I wish to thank the Materials Research Institute at DLR**,** particularly Janine Wischek, for granting me access to their experimental facilities and for the warm and welcoming atmosphere. I am especially grateful to Prof. Dr. Marion Bartsch for her insightful discussions and for reviewing both publications and sections of this thesis.

My thanks extend to Dr. Martin Roeb, head of our department, for supporting my work and fostering a productive research environment. I also thank Prof. Dr. Robert Pitz-Paal and Prof. Dr. Bernhard Hoffschmidt for their valuable input during our doctoral progress meetings.

Furthermore, I would like to thank Etienne Perin, Leonhard Kölz, and Elif Kocacinar, students I had the pleasure to work with and supervise, and whose work contributed to this thesis in various aspects.

To the entire team at the Institute of Future Fuels, thank you for the motivating and friendly office environment, which made my long commutes more than worthwhile. I am grateful to the Solar Furnace team in Cologne, especially Fabio Pierno and Carsten Speke, for their invaluable help with the experiment setup and their support when technical issues arose. Particular thanks to my dear fellow doctoral students, specially Enric and Yasuki, who were always there, and happy to share their similar experiences with a cup of coffee in hand.

Most importantly, I want to express my heartfelt appreciation to my parents and friends for their continuous support during these demanding times. Your encouragement and belief in me made all the difference. To Jonas, who saw every step of this journey, lifted me up when I needed it the most, and never shied away from providing professional feedback on my figures. Thank you for being my rock, I could not have done this without you.

Contents

Nomenclature

Latin characters

A	area
C	sealing clearance
$c_{p,(.)}$	specific heat capacity
d	diameter
E_a	apparent activation energy
F_{ij}	view factor from surface i to surface j
G	absolute Gibbs energy
h_{conv}	convection coefficient
h	height
H	absolute enthalpy
$k_{(.)}$	thermal conductivity
K	rate constant
L	length
M	molar mass
m	mass
$n_{(.)}$	amount of substance
$\dot{N}$	molar flux
$p_{(.)}$	pressure
P	Power
q	leakage rate
Q	heat
R	universal gas constant
R^2	coefficient of determination

R_a	average roughness
R_z	mean roughness depth
S	absolute entropy
S	pumping speed
T	temperature
t	time
v	velocity
V	volume
w	weight
W	wear

Greek symbols

β	extinction coefficient
δ	non-stoichiometry
ε	emissivity
κ	wear rate
η_{StF}	solar-to-fuel efficiency
ϕ_{dual}	dual-scale porosity
φ_{O_2}	oxygen consumption rate
ρ	density
$\sigma_{(.)}$	contact stress
σ	Stefan-Boltzmann constant
τ	retardation time
μ	dynamic viscosity
ν	stochiometric factor

Reoccurring subscripts and superscripts

amb	ambient
aux	auxiliary processes
conv	convection

f	final
i	initial
ins	insulation
l	leakage
L	limit
ox	oxidation
rad	radiation
red	reduction
ss	stainless steel
sur	surface

Abbreviations

ATR	attenuated total reflectance
CAD	computer-aided design
CFD	computational fluid dynamics
CS	compression set
CSR	compression stress relaxation
DLO	diffusion-limited oxidation
EPDM	ethylene propylene diene monomer
FEA	finite element analysis
FFKM	perfluoroelastomer
FKM	fluoroelastomer
HF	hydrofluoric acid
HFP	hexafluoropropylene
HHV	higher heating value
IR	infrared
MCT	mercury cadmium telluride
MRU	mobile redox units
PDMS	polydimethylsiloxane
PFAAs	polymeric perfluoroalkyl acids

PFAS	per- and polyfluoroalkyl substances
PFOA	perfluorooctanoic acid
PFOS	perfluorooctane sulfonate
PMVE	perfluoromethyl vinyl ether
PTFE	polytetrafluoroethylene
R2Mx	receiver-reactor cavity system with multiple mobile redox units
RMA	redox material assembly
RPC	reticulated porous ceramic
SD	squeeze degree
StF	solar-to-fuel
TAIC	triallyl isocyanurate
TFE	tetrafluoroethylene
TGA	thermogravimetric analysis
TTS	time-temperature superposition
UHV	ultra-high vacuum
VDF	vinylidene fluoride

List of Figures

List of Tables

1. Introduction

In the pursuit of climate change mitigation and the achievement of carbon neutrality, a substantial increase in the global renewable energy supply portfolio is not only imperative, but also expected. For instance, according to the European climate law the EU is legally obliged to achieve climate neutrality by 2050 [1]. A goal that will only be achieved by significantly increasing the proportion of renewable energy sources in electricity generation, heating systems, and fuel consumption. Current EU targets include 42.5% renewable energy overall consumption, as well as, 5.5% share of advanced biofuels and renewable fuels of non-biological origin in the transport sector [1,2]. The two fastest growing renewable energy sources in the EU are solar and wind [3]; however their intermittency, an inherent technological drawback, calls for an effective diversification of the employed renewable energy technologies and the integration of renewable energy carriers, such as hydrogen and synthetic renewable fuels, to provide successful energy storage solutions. Renewable synthetic fuels have the potential to decarbonise several hard-to-electrify sectors such as long-haul road transport, shipping, aviation, and heavy industries, as well as to serve as energy storage for intermittent renewable electricity sources [4]. However, realising their full potential depends on the development of sustainable production pathways. At present, the production of key precursors, such as hydrogen, predominantly relies on carbon-intensive processes such as steam methane reforming of natural gas and coal gasification [5].

Solar thermal processes present a viable alternative to sustainably produce hydrogen and carbon monoxide, key building blocks for the synthesis of renewable fuels. Synthesis gas (syngas), a mixture of H_2 and CO, can be further processed into base chemicals and liquid hydrocarbons through stablished methods such as Fischer-Tropsch synthesis. While both components are essential for renewable fuel production, this work focuses on sustainable hydrogen generation as a representative case study, given its central role in many decarbonisation strategies and the extensive research attention it has received. Thermally driven solar technologies have a high theoretical efficiency potential, which arises from utilising the entire solar spectrum and the direct use of solar heat, bypassing the need for intermediate electricity generation. Solar thermal water splitting is driven by high temperatures achieved utilising concentrated solar irradiation. Sunlight is concentrated using mirrors that can be arranged in a variety of ways such as in solar towers or parabolic dishes [6,7]. Water decomposition in a single step is known as direct thermolysis and,

while it offers a straight forward process, it is technically challenging to accomplish, due to its extremely high operating temperature requirement (4500 K for complete dissociation) and high-temperature separation of products to avoid the formation of an explosive mixture [8,9]. To circumvent these technical challenges, two-step thermochemical cycles rely on a metal oxide active material and alternating reduction-oxidation (redox) reactions to facilitate the splitting of water [10–12]. In the first step of the redox cycle (Eq. (1.1)), the metal oxide is reduced at high temperatures in an endothermic reaction, thereby releasing oxygen. This step is typically performed at low oxygen partial pressures (1 mbar), corresponding to medium vacuum levels. In the second step (Eq. (1.2)), water is split as the metal oxide is re-oxidised by absorbing oxygen from steam. This second step takes place at 1 bar and generally at lower temperatures than the previous step. The redox material can be once again thermally reduced (step 1), with the overall process transforming high-temperature thermal energy into chemical energy as hydrogen.

$$\mathrm{MO_{ox}} \rightarrow \mathrm{MO_{red}} + \frac{\nu}{2}\,\mathrm{O_2} \tag{1.1}$$

$$\mathrm{MO_{red}} + \nu\,\mathrm{H_2O} \rightarrow \mathrm{MO_{ox}} + \nu\,\mathrm{H_2} \tag{1.2}$$

$\mathrm{MO_{ox}}$ and $\mathrm{MO_{red}}$ represent the metal oxide in its oxidised and reduced states, respectively, while ν is the stoichiometric factor, which depends on the redox material used and its oxidation and reduction states. In addition to H_2O splitting, two-step thermochemical cycles are capable of splitting CO_2 and co-splitting H_2O and CO_2.

At the core of the solar thermochemical water splitting process is the solar reactor, where the redox cycle is performed. Many diverse reactor technology approaches and concepts may be identified, with either direct [13–16] or indirect [17,18] heating of the active redox material and the use of different redox material morphologies such as particles [14,18,19] or structures [6,7,20–26]. A detailed overview of the solar reactor types developed for two-step thermochemical cycles is provided in Chap. 2.2. A key metric for evaluating the solar reactor's performance is the solar-to-fuel (StF) efficiency (Eq. (1.3)), which compares the calorific value of the amount of fuel produced (n_{fuel}) to the total energy input, which is a sum of the solar radiative energy input and the additional parasitic consumption of auxiliary processes [27].

$$\eta_{\mathrm{StF}} = \frac{\mathrm{HHV_{fuel}} \int_0^{t_{\mathrm{cycle}}} \dot{n}_{\mathrm{fuel}}(t)\,dt}{\int_0^{t_{\mathrm{cycle}}} \dot{Q}_{\mathrm{sun}}(t) + \dot{Q}_{\mathrm{aux}}(t)\,dt} \tag{1.3}$$

The higher the StF efficiency, the more competitive is the production of solar hydrogen utilising a determined reactor type. Current reactor efficiencies, even for the state-of-the-art technology [6],

remain on the single digits and are considerably below the theoretical potential, prompting the need for further development in this area.

In this context, the receiver-reactor cavity system with multiple mobile redox units (R2Mx) concept has been proposed and is currently under development at the German Aerospace Centre (DLR) Cologne site, in coordination with other DLR locations [22,23,26]. The R2Mx system features separate reduction and oxidation reactors, where the redox reactions can occur simultaneously and be decoupled from each other in terms of duration and operational conditions such as pressure and temperature. The active redox material is arranged into several redox material assemblies (RMA), which are operated independently and moved cyclically between the reaction zones. This innovative approach exhibits a high predicted StF efficiency (> 14%) even for non-optimised designs and has advantages in part-load flexibility and scalability potential [22]. However, one of the main technical challenges of the R2Mx concept lies in reliably maintaining atmospheric separation between the reaction zones, particularly under high-temperature and vacuum conditions. Continuous cyclic pressure sealing in thermochemical reactors remains a relatively underexplored topic, since conventional cavity receiver-reactor designs [6,16,20] perform the redox reactions sequentially within a single chamber and therefore do not require dynamic seals. Failure of the pressure sealing system in the R2Mx reactor, could render the system inoperable, making the understanding of seal degradation, failure mode, and durability under extreme operating conditions essential to ensure the reactor's performance and reliability.

On this basis, the aim of this thesis is to evaluate the high-temperature degradation behaviour and service lifetime of polymer-based sealing materials used in solar thermochemical reactors, with particular focus on their functional performance and impact on system efficiency. This work presents a comprehensive and multidisciplinary investigation into the thermal, mechanical, and operational behaviour of fluoroelastomer (FKM) and perfluoroelastomer (FFKM) O-rings, as well as polytetrafluoroethylene (PTFE) rod seals, under high-temperature conditions between 200 °C and 300 °C. Although these are commercially available polymers, experimental data concerning their degradation and performance under such extreme thermal conditions remains scarce. This thesis addresses that gap by providing both fundamental knowledge and a practical foundation for understanding the high-temperature ageing of these sealing materials. A key outcome of the work is the development of a methodology for estimating service lifetime based on material degradation, along with the definition of end-of-life criteria tailored to each seal type; contributions that hold broader relevance for high-temperature sealing applications across several industries.

In this work a multi-step approach was followed. First, to establish a foundation for this research, the initial chapters focus on providing a comprehensive review of the current state of knowledge related to two-step solar thermochemical hydrogen production (Chap. 2), fluid sealing

technology and fluoropolymers used in pressure sealing applications (Chap. 3). Next, a prototype of the examined R2Mx reactor is introduced and a finite element simulation is performed to derive approximate operating parameters, such as temperatures, for the investigated pressure sealing system, which comprises two types of seals; O-rings and rod seals (Chap. 4). An experimental campaign with the aim of assessing the degradation mechanisms of the O-rings used in the gate and predicting its service lifetime is performed and reported in Chap. 5. Here, an accelerated ageing programme complemented by several tests including infrared (IR) microscopy, optical microscopy, mechanical properties analyses, and leakage rate measurements was employed. A second experimental investigation focusing on the rod seal is outlined (Chap. 6). Its degradation and lifetime prediction are investigated utilising accelerated wear tests with a rough rod and a dedicated test stand. Based on the results from the aforementioned experimental studies, a numerical model on the effect of leakage on the StF efficiency of a generic R2Mx system is presented in Chap. 7. Finally, Chap. 8 summarises the conclusions of the study, provides a reflective evaluation of the presented work, and an outlook for further research.

2. Solar thermochemistry

This chapter presents the context for studying high-temperature pressure sealing by examining the investigated solar reactor technology and the current state of research in the field. The chapter begins with an introduction to two-step thermochemical redox cycles relevant for fuel production, followed by a discussion of the ceria-based cycle, including key thermodynamic and kinetic principles. Subsequently, an overview of the existing solar reactor concepts and recent technological developments is presented. Next, a detailed description of the R2Mx reactor concept, which is part of the core focus of this work, is provided. Finally, general pressure sealing systems' configurations for reactors of type R2Mx are introduced.

2.1. Two-step solar thermochemical cycles

Thermochemical cycles offer a promising pathway for sustainable fuel production by splitting water using a metal oxide and high-temperature heat, ideally from renewable sources such as concentrated solar radiation. However, early research in the 1960s and 1970s explored nuclear heat usage for low-temperature cycles with several (more than three) reaction steps [28–31]. Modern two-step thermochemical cycles use metal oxides as reactive intermediates, undergoing alternating reduction-oxidation (redox) reactions to enable the dissociation of water into hydrogen and oxygen (Eqs. (1.1) and (1.2)) [10–12]. Given their high temperature requirement, these cycles use concentrated solar energy as heat source. Their appeal lies in their high-efficiency potential and the elimination of electricity dependence (for water splitting), positioning them as a compelling technology for future green fuel production. Harnessing solar energy for thermochemical cycles is of particular interest due to the vast abundance of solar energy, as the total Earth's solar irradiation potential is about 8000 times larger than the world's primary energy demand of 2023 [32,33].

A range of materials have been explored as redox candidates for two-step thermochemical cycles, including zinc oxide [34–38], ferrites [39–41], iron oxides [42–45], perovskites [46–48], and both doped [49–51] and undoped [6,7,20,52–54] cerium oxide CeO_2 (ceria). These materials are broadly classified into volatile and non-volatile systems based on whether the redox material remains in the solid state during the high-temperature reduction step (Eq. (1.1)) [55]. Volatile redox cycles, such as the ZnO/Zn cycle, typically exhibit high theoretical solar-to-fuel efficiencies, due

to their greater oxygen exchange capacities, which yield higher fuel output per unit mass of redox material. Schunk et al. [56] developed a heat transfer model for analysing the solar-driven dissociation of ZnO and predicted an efficiency of over 55% for a 1 MW reactor when operating at temperatures above 2000 K. However, ZnO/Zn cycle practical implementation remains highly challenging, as during the reduction step, zinc oxide thermally dissociates into gaseous zinc and oxygen at around 2200 °C. To avoid recombination of the products, either high-temperature gas separation or ultra-fast quenching to ambient temperature is required; both of which pose significant technical challenges and efficiency losses. For instance, a 100-kW solar reactor developed by Koepf et al. [57] achieved only 0.17% solar-to-fuel efficiency, primarily due to low zinc yields caused by the difficulty of effectively quenching the product gases.

In contrast, non-volatile redox materials retain their solid phase during redox cycling and can be subdivided into those undergoing stoichiometric reduction and those forming nonstoichiometric phases by releasing only a fraction of their lattice oxygen. A stoichiometric system exhibiting some promise is the Fe_3O_4/FeO cycle. Because the thermal decomposition of Fe_3O_4 requires temperatures up to 2700 °C, doping with transition metals such as Co, Ni, Zn, or Mn is often employed to lower the reduction temperature. The Hydrosol-plant project at DLR focused on developing a 750 kW system comprising three solar reactors with directly irradiated nickel-ferrite structures [58]. While nickel-ferrite showed initial promise, its susceptibility to sintering and side reactions accelerate degradation and reduce long-term stability [43]. Lorentzou et al. [59] compared nickel-ferrite and ceria within the same project framework, identifying ceria as the superior redox material under all evaluated conditions. Consequently, more recent experiments inspired by the Hydrosol reactor concept utilised ceria coated ZrO_2 foams in a 250 kW reactor tested in a solar simulator [16].

Nonstoichiometric materials such as perovskites and ceria (in both doped and undoped forms) have gained increased attention in recent times. Perovskites, with the general formula ABO_3 (where A and B are metal cations), offer a highly tuneable structure, enabling a wide compositional design space [45]. Although certain perovskite formulations [47,60–62] show excellent redox characteristics, their cycling stability has not yet matched that of ceria. Research efforts are ongoing to identify optimal perovskite compositions, with methods such as density functional theory (DFT) [63–65] and machine learning [66,67] increasingly employed to efficiently navigate the immense chemical space of perovskite materials. Nevertheless, today ceria is still widely regarded as the benchmark material for solar thermochemical H_2O and CO_2 splitting. Accordingly, the following section focuses specifically on the ceria-based thermochemical redox cycle.

2.1.1. The ceria redox cycle

Cerium oxide (CeO_2), commonly referred to as ceria, has emerged as an attractive redox material due to its unique combination of favourable properties. Among non-volatile, non-stoichiometric

metal oxides, ceria stands out for its comparatively high oxygen exchange capacity [68–70], its fast redox kinetics [71,72], and its ability to maintain its fluorite crystal structure across a broad range of temperatures and non-stoichiometry values [73]. Furthermore, cerium is the most abundant of the rare earth elements in the Earth's crust [74], which supports its scalability for large-scale fuel production applications. The ceria-based thermochemical cycle relies on reversible non-stoichiometric redox reactions. In the first, high-temperature step, ceria is reduced in an endothermic reaction, thereby releasing oxygen from its lattice (Eq. (2.1)). The reduction reaction is favoured at high temperatures and low O_2 partial pressures [68], and therefore the typical temperature of the reduction step is approximately 1500 °C [20,52,53]. The necessary high-temperature heat is supplied by concentrated solar irradiation. In the second lower-temperature step, the reduced ceria is re-oxidised by H_2O to produce H_2 (Eq. (2.2)). The oxidation of ceria is exothermic [75] and typically takes place at temperatures of about 600–1000 °C [53,75,76]. Ceria is not consumed in the process and therefore can be cycled repeatedly between the reaction steps, effectively producing hydrogen from water and sunlight. These two redox steps are summarised by the following reactions and standard enthalpy changes:

$$\mathrm{CeO_{2-\delta_{ox}}} \rightarrow \mathrm{CeO_{2-\delta_{red}}} + \frac{\Delta\delta}{2}\mathrm{O_2} \qquad \Delta H^o \approx 475\ \mathrm{kJ\ per\ 1/2\ mole\ O_2} \tag{2.1}$$

$$\mathrm{CeO_{2-\delta_{red}}} + \Delta\delta\ \mathrm{H_2O} \rightarrow \mathrm{CeO_{2-\delta_{ox}}} + \Delta\delta\ \mathrm{H_2} \qquad \Delta H^o \approx -234\ \mathrm{kJ/mol\ H_2} \tag{2.2}$$

where δ_{ox} and δ_{red} are the oxygen non-stoichiometry after oxidation and reduction, respectively, and $\Delta\delta = \delta_{red} - \delta_{ox}$. As mentioned in Chap. 1, ceria based thermochemical redox cycles are also capable of dissociating CO_2 into CO; either within the same reactor used for water-splitting or in a separate one. The resulting mixture of H_2 and CO, syngas, servers as a versatile feedstock for the production of a range of chemical commodities and liquid hydrocarbons via catalytic processes such as Fischer-Tropsch synthesis.

Thermodynamics

Ceria crystallises in a cubic fluorite structure, where cerium exists predominantly in the Ce^{4+} oxidation state. Upon reduction, a fraction of Ce^{4+} ions are reduced to Ce^{3+}, accompanied by the release of lattice oxygen to the gas phase. This process results in the formation of oxygen vacancies within the fluorite lattice to preserve overall charge neutrality. The fluorite structure of ceria is notably tolerant to non-stoichiometry, capable of sustaining significant oxygen vacancy concentrations (up to $\delta \approx 0.35$) without undergoing a phase transition to the Ce_2O_3 structure [68,77]. On the macroscopic level, oxidised ceria has a yellow/orange colour and upon reduction it has been reported to change colour to blue or almost black [70]. Figure 2.1 illustrates the equilibrium oxygen non-stoichiometry (δ) of ceria as a function of temperature and oxygen partial pressure, p_{O_2},

utilising the thermodynamic model developed by Bulfin et al. [54]. At high temperatures and low p_{O_2}, ceria undergoes significant reduction, leading to high δ values. Conversely, under oxidising conditions, characterised by lower temperatures, δ approaches zero as the material reverts to a more stoichiometric state.

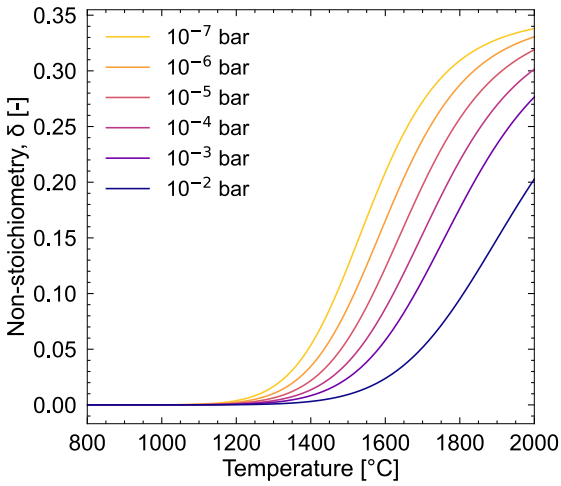

Figure 2.1: Non-stoichiometry of ceria at equilibrium as a function of temperature and oxygen partial pressure calculated using the model developed by Bulfin et al. [54].

Thermochemical fuel production with ceria can be conducted in either isothermal, isobaric, temperature-swing, pressure-swing, or hybrid operation modes. The key criterion for hydrogen production is a net positive oxygen exchange ($\Delta\delta > 0$) between the reduction and oxidation steps, which directly determines the fuel yield. While Δδ can, in theory, be controlled through either pressure or temperature, operating solely in isothermal pressure-swing mode typically results in a limited oxygen exchange due to thermodynamic constraints [52,78–80]. For instance, at 1200 °C with a pressure swing from 1 mbar to 1 bar, Δδ reaches only about 0.0004. To improve redox performance, this work examines a combined temperature and pressure swing strategy. For example, operating the reduction step at 1500 °C and 1 mbar, and the oxidation step at 900 °C and 1 bar, can thermodynamically achieve Δδ values near 0.024, corresponding to significantly enhanced fuel output per cycle. However, the upper limit of the reduction temperature is bounded by the thermal stability of ceria. Sublimation of ceria has been observed above 2000 °C [15,49], imposing a practical ceiling on usable temperatures. Additionally, achieving low p_{O_2} during reduction necessitates the use of sweep gas, vacuum pumping, or usage of thermochemical oxygen pumps (TCOPs), all of which carry energetic penalties that constrain the viable operating window.

Kinetics

Ceria is an oxygen ion conductor [81,82], a property that facilitates rapid diffusion of oxygen through its lattice structure to and from reactive sites on the surface. This high oxygen mobility

underpins the material's characteristically fast redox kinetics during both reduction and oxidation steps [31,81,82]. In solar thermochemical reactors, the rate-limiting factor for porous ceria structures reduction is often not the intrinsic chemical kinetics but rather external parameters such as the heating rate or the effectiveness of oxygen removal during the reduction step. For instance, Welte et al. [17] reported that in a 2 kW_{th} solar aerosol reactor, the reduction extent of large ceria particles (> 200 μm) was constrained by heat transfer limitations. In contrast, smaller particles were limited by oxygen removal via gas-phase advection and an increase of 25% in δ was achieved simply by doubling the sweep gas flow rate to improve O_2 removal. Additionally supporting the conclusion that reduction kinetics are often governed by heat transfer in the reactor rather than material limitations, Furler et al. [83] showed the close agreement between experimentally measured δ values and thermodynamic equilibrium predictions in a 3.8 kW_{th} solar reactor.

Oxidation of ceria follows a surface-limited mechanism driven by oxygen vacancies and surface reactions. Arifin and Weimer [84] found that under conditions of 750–950 °C and 20–40% vol. H_2O, the oxidation exhibited an apparent first-order dependence on steam concentration, indicative of surface-controlled behaviour. Ackerman et al. [69] observed that bulk oxygen diffusion within ceria is sufficiently rapid that the overall oxidation rate is limited by surface reaction kinetics. As a result, ceria nanostructuring or texturing, can significantly enhance oxidation rates by exposing more active sites [85–87]. Zhao et al. [88], employed fine ceria nanopowder and reported hydrogen production rates an order of magnitude higher than those in prior thermochemical or chemical-looping studies. They proposed a two-step surface reaction model for oxidation, involving initial H_2O adsorption and dissociation followed by a charge-transfer process, linked through bulk-to-surface oxygen transport equilibrium. Additionally, catalytic enhancement using surface-deposited noble metals, such as rhodium, has been shown to accelerate oxidation kinetics [31,89].

2.2. Solar reactor concepts

The cornerstone technology of the solar thermochemical water splitting process is the solar reactor, where the redox reactions responsible for hydrogen production are carried out. Over the years, a wide array of reactor designs has been proposed and developed to enable the practical and efficient implementation of this process. These concepts vary significantly in their configuration, operating principles, and choice of redox material morphology. Solar reactors typically fall into two broad categories based on the mode of heating: direct irradiation of the redox material using concentrated solar energy [12–15], and indirect configurations where the heat is transferred via a heat exchanger or intermediate medium [16,17]. Additionally, a variety of redox material forms

have been employed, ranging from particles [13,17,18] and porous structures [6,7,20–26] to more novel approaches, such as ceramic membranes [90,91].

The most promising solar reactor designs in terms of solar-to-fuel efficiency integrate several performance-enhancing strategies. These include the recuperation of sensible heat from the redox material between the reduction and oxidation steps (through solid heat recovery sytems), continuous solar irradiation during the endothermic reduction reaction, and high utilisation of the redox material's oxygen exchange capacity. Other critical attributes include the potential for system scalability and the spatial separation of reaction zones; which includes separation of temperature, pressure, and gas species involved in each step of the redox cycle [18,92]. The subsequent sections provide an overview of the most significant solar reactor technologies developed for thermochemical water splitting. These are categorised according to the morphology of the redox material they employ, distinguishing between particle-based reactors and those utilising redox material structures. Each approach presents distinct advantages and technical challenges, which are discussed.

2.2.1. Particle-based reactors

Particle-based solar reactors utilise redox-active materials in granular or powder form. These designs offer the highest theoretical solar-to-fuel efficiencies, estimated at around 30% [18,92,93], and support continuous operation by enabling spatial separation of reduction and oxidation zones. Typically, such reactors incorporate continuous redox material flow and heat recuperation mechanisms. Several reactor concepts including fluidised particles [94,95], falling particle films [96] and moving beds along incline plates [97,98] have been studied. One notable design is the aerosol particle reactor, where alumina tubes, containing a downward flow of ceria particles counter to an inert sweep gas flow, are continuously irradiated (Figure 2.2 (a)). The opposing movement of gas and particles ensures that as the particles are heated, the local oxygen partial pressure declines, while offering enhanced heat and mass transfer [17,99]. Welte et al. [17] demonstrated such a reactor prototype in a solar simulator and estimated a peak solar-to-fuel efficiency of 0.56%, assuming complete re-oxidation, which was not experimentally verified. However, such systems face challenges in handling large particle flows at high temperatures and ensuring materials used for the solar tubular absorbers can withstand thermal stresses and oxidation by air.

An alternative vacuum-based reactor concept was proposed by Ermanoski et al. [92], utilising a packed bed of redox particles as pressure separation between the steps of the cycle. This design benefits from cascading pressure levels, which favour the reduction process [19]. Building on this idea, Singh et al. [100] proposed a technically feasible implementation, featuring a vertical particle transport system using a screw conveyor and direct irradiation of the reduction reactor through a quartz dome (Figure 2.2 (b)). More recently, Grobbel et al. [101] experimentally evaluated two

such reactors under vacuum in a solar simulator, focusing on horizontal motion conveying and component integration. While final reactor tests are ongoing, key technical challenges such as, including high-temperature mechanical motion under vacuum, sealing reliability, and the structural limitations of quartz windows, remain.

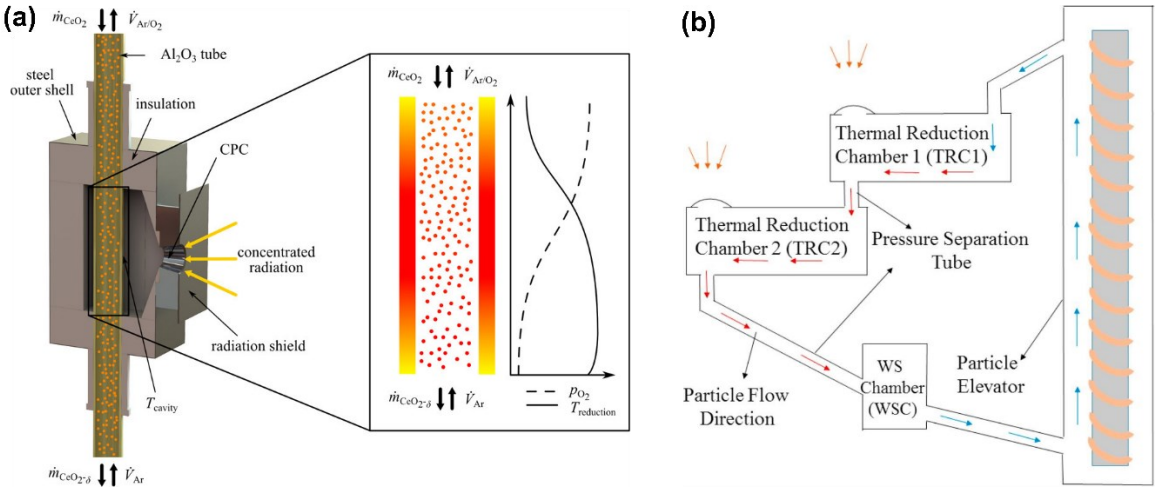

Figure 2.2: Particle-based solar thermochemical reactor concepts: (a) Solar aerosol reactor reproduced from Welte et al. [17] with permission of the American Chemical Society, (b) Cascading pressure reactor reproduced from Singh et al. [100] with permission of Elsevier Science & Technology Journals.

2.2.2. Structured reactors

Structured-reactor configurations for solar thermochemical water splitting can be broadly classified into stationary and moving concepts. Among these, the state-of-the-art system remains the cavity receiver-reactor demonstrated in the Sun-to-Liquid project, which achieved the highest reported solar-to-fuel efficiency of 4.1% for syngas production and 5.6% for CO production at a 50 kW scale (Figure 2.3 (a)) [6]. This reactor operates in batch mode using ceria RPCs and alternates between reduction under concentrated solar irradiation with vacuum pumping, and oxidation without solar irradiation. Despite its demonstrated performance, the absence of a heat recovery system limits its efficiency. Brendelberger et al. [102] modelled a 300 kW version incorporating thermal energy storage (TES) and reported up to 40% solar input reduction potential. A dual-TES approach predicted efficiency gains up to 51%, although experimental demonstration did not achieve actual heat recovery [103]. Practical implementation of heat recovery for this type of reactors remains challenging due to the high-temperature requirements of valves and thermal losses in the piping system. Another structured-reactor concept is the ASTOR/Hydrosol system, which replaces vacuum pumping with nitrogen sweep gas during the reduction step and has been experimentally demonstrated at a 250 kW scale [16,58]. Nevertheless, simulations suggest that scaling up the cavity receiver-reactor only would yield limited performance improvement, since only a small fraction near the surface of the ceria RPC is effectively utilised [104,105].

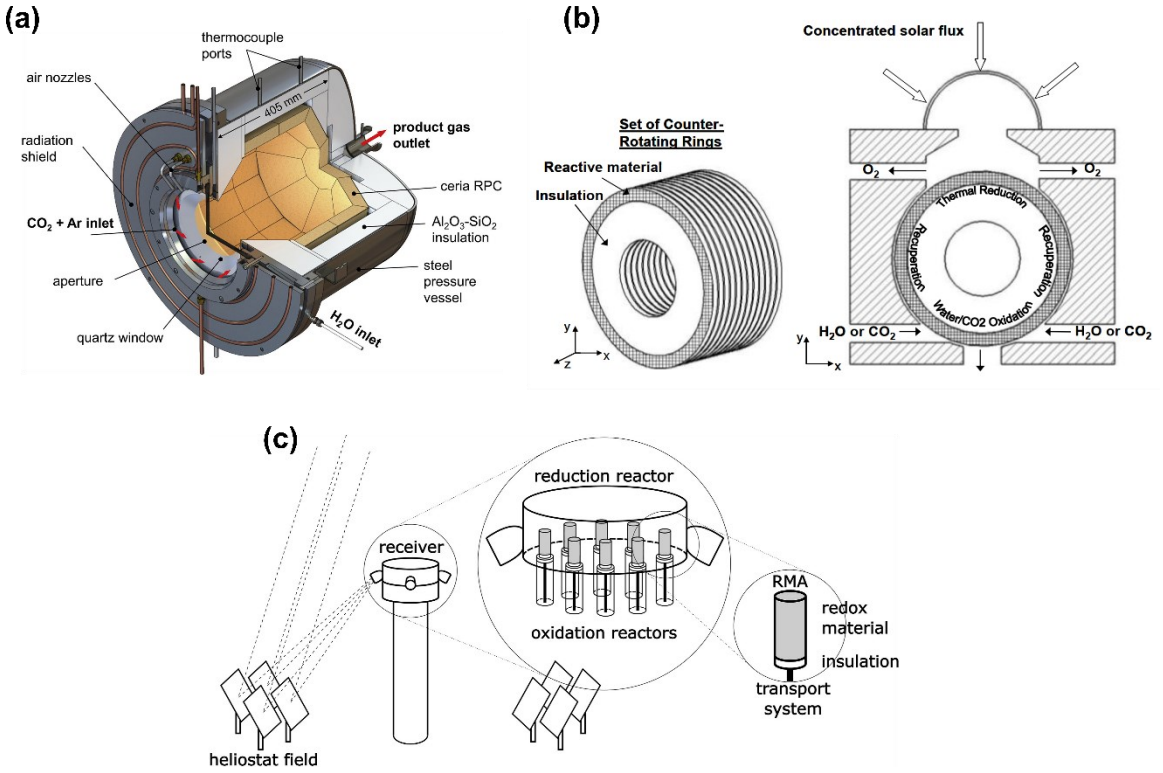

Figure 2.3: Structured solar thermochemical reactor concepts: (a) Cavity receiver-reactor reproduced from Zoller et al. [6] with permission of Elsevier Science & Technology Journals, (b) CR5 reactor reproduced from Diver et al. [106] with permission of Elsevier Science & Technology Journals, (c) R2Mx reactor reproduced from Brendelberger [26] with permission of Elsevier Science & Technology Journals.

Regardless of concept, one of the main sources of efficiency loss in stationary systems is the waste of sensible heat during temperature swing cycling. Solid heat recovery is therefore considered essential to improving reactor performance and several reactor concepts including moving brick designs [107,108] and the reactor train [109] have been proposed, unfortunately still without technical realisation. A notable exception is the counter rotating ring receiver-reactor-recuperator (CR5) (Figure 2.3 (b)), which is composed of a set of rotating rings made of redox material and was tested at a 16 kW scale achieving a peak efficiency of 1.7% [106,110]. At any time, one-quarter of each ring undergoes reduction, another oxidation, and the remaining halves serve for solid heat recovery, tightly coupling the durations of both redox steps. However, experimental challenges related to mechanical stability and high-temperature operation had the rings fracture at near 600 °C [106,110].

More recently, the receiver-reactor cavity system with multiple mobile redox units (R2Mx), has been proposed as a promising reactor design (Figure 2.3 (c)) [22,26]. The R2Mx system features a continuously irradiated cavity that serves as the reduction reactor and includes multiple apertures for solar input and a vacuum pump system. It also incorporates several mobile redox units (MRUs), each comprising a redox material assembly (RMA), a linear transport mechanism, an oxidation

reactor, and a sealing gate that separates the reaction zones. Each RMA consists of a structured redox material (ceria RPC) and an insulating interface to the transport system. The RMAs can be independently operated and moved vertically between the reduction and oxidation zones, enabling continuous on-sun operation of the reactor. The use of linear motion for the RMA transport eliminates many technical challenges associated with high-temperature rotating parts, thereby improving reliability and simplifying implementation. Furthermore, thanks to the spatial separation of the reduction and oxidation zones, the redox reactions can occur simultaneously and be decoupled in terms of duration and operating conditions, which supports a pressure and temperature swing operation of the thermochemical cycle. Between the reduction and oxidation chambers, a solid heat recovery unit can be installed using adjacent wall elements. A study indicated that already relatively simple versions of such a solid heat recovery system configuration could achieve heat recovery rates of 15–20% [22]. Furthermore, a numerical study predicted a peak solar-to-fuel efficiency values of about 17.6% for a multi-MW R2Mx system without solid heat recovery [26], underscoring its promising potential even at early development stages.

Nevertheless, one of the principal technical challenges that the R2Mx system faces, is ensuring robust atmospheric separation, or atmosphere control, between the reaction zones, particularly under high-temperature and vacuum conditions. Unlike conventional cavity receiver-reactor systems [6,15,19], which operate sequentially within a single reaction chamber and thus avoid the need for dynamic sealing in the reactor's main vessel, the R2Mx reactor necessitates, depending on the system design, continuous and cyclic pressure sealing. This requirement introduces a relatively unexplored aspect in solar thermochemical reactor design. A failure in the pressure sealing system could compromise the integrity of the reactor's operational environment, leading to system downtime or failure. Although the R2Mx concept remains under development, its advantages make it a compelling candidate for further investigation, and therefore this reactor system forms the basis of the detailed experimental and modelling investigations presented in this work.

2.3. Pressure and atmosphere control in solar reactors

Thermochemical solar reactors operate under highly specific pressure and gas compositions regimes, which are essential for driving the redox reactions efficiently. As reviewed, two-step thermochemical cycles for water splitting require a low p_{O_2} during the reduction step, and a 1 bar steam atmosphere during the subsequent oxidation step. Low p_{O_2} conditions can be achieved by using vacuum pumps, inert sweep gases, or TCOPs. Among these, vacuum pumps, being technologically more mature than TCOPs [111–113], and showing efficiency benefits over sweep gas systems [14,20], are the preferred choice in state-of-the-art systems and the R2Mx concept.

In conventional cavity receiver-reactor systems [6,16,20], the reactor vessel remains sealed throughout operation, typically using ultra-high vacuum copper gaskets. These gaskets can withstand high temperatures and are compatible with hot steam. Dynamic sealing is generally limited to valves used for switching gas streams, which are placed along the piping network and operate at low temperatures. Recently, Lidor et al. [103] highlighted the challenges of high-temperature gas flow control valves in heat recuperation systems for these type of reactors. Although technically feasible, high-temperature valve operation was associated with substantial thermal inefficiency and leakage, emphasising the ongoing challenge of flow control at elevated temperatures.

In contrast, the R2Mx concept features simultaneous reduction and oxidation reactions carried out in separate, parallel redox mobile units (MRUs). This operational mode demands precise control over pressure and atmosphere, not only between the reaction zones but also in relation to the ambient environment, to ensure an optimal StF efficiency. As a result, high-integrity sealing systems, capable of withstanding cyclic operation, high temperatures, and vacuum conditions, are essential. To meet these demands, a tailored pressure sealing system has been developed, comprising two components: a gate (valve) and a rod seal (Figure 2.4). The gate isolates the reduction reactor from steam and product gases, while allowing the movement of the solid RMA through the sealing boundary. Meanwhile, the rod seal continuously preserves the pressure differential between the reactor and its surroundings, even during the vertical displacement of the transport system. While a gate-based solution could theoretically replace the rod seal, the selected design prioritises the rod seal for its mechanical simplicity, compactness, and suitability for dynamic sealing.

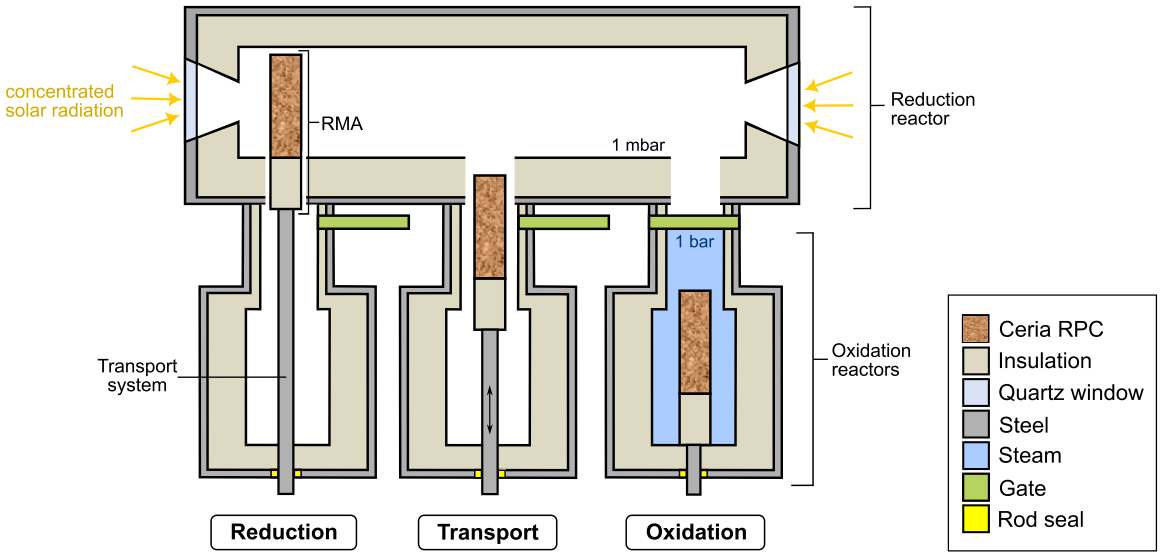

Figure 2.4: Schematic cross-sectional view of R2Mx type reactor system with multiple redox mobile units (MRU) each depicted at a different step in the fuel production cycle.

Given that the rod seal serves a well-defined function with relatively low design complexity, the following section concentrates on the gate mechanism, whose configuration poses greater technical challenges and presents a much broader design space. Furthermore, the gate design plays an influential role in determining the reactor's overall geometry, sealing materials temperature requirements, and system integration. Several generic valve configurations commonly used across various industries are reviewed and summarised in Table 2.1.

Table 2.1: Overview of different gate concepts for use in a reactor of type R2Mx.

Type of gate	**Sliding gate**	**Knife gate**	**Folding gate**	**Ball valve**
Mechanism	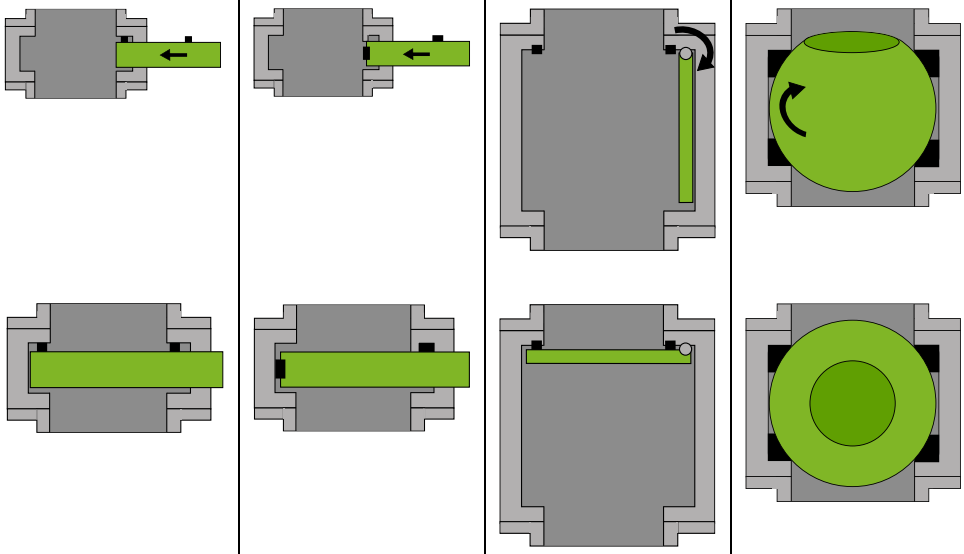			
Motion type	Linear or rotational	Linear	Rotational (hinged)	Rotational
Advantages	Compact profile, excellent sealing, simple actuation	Reduced friction, compact profile, excellent sealing, simple actuation	Simple design, good durability, few moving parts	Fast actuation, very low pressure drop
Limitations	Seal wear from repeated contact, needs precise alignment	Potentially large radiative heat transfer from RMA to seal, larger actuator force needed	Potentially large radiative heat transfer from RMA to seal, requires more space	High thermal inertia, bulky component
Sources	[114–116]	[117,118]	[119,120]	[114,121,122]

Sliding plate valves are widely used in vacuum systems due to their mechanical simplicity and effective sealing performance [114–116]. These valves consist of a flat plate that is pressed against a sealing surface, usually an elastomeric or metal seal, to close the flow path. The seal, which is typically an elastomeric O-ring, is commonly positioned on the upper surface of the moving plate, and actuation can be achieved either through linear or rotational motion (for pendulum valves) [115]. Nevertheless, this type of valves suffers from rapid seal wear and in order to ensure leak-tightness a precise alignment of the parts is required. Knife gate valves, also common in vacuum

applications, employ a plate that moves perpendicularly to the sealing interface [118]. In these designs, the elastomeric seal material is often located at the outer edge of the moving component, which might lead to increased temperature requirements for the seal as substantial radiative heat transfer from the RMA is expected during its transport. Folding or swing gate valves operate via a hinged plate mechanism and are valued for their mechanical robustness [119]. However, their relatively large spatial footprint would increase the overall height of the reactor, complicating compact system integration. This design also utilises an elastomeric O-ring as a seal and has a rather large radiative heat transfer between the hot RMA and the seal. Finally, full-bore ball valves offer advantageous flow characteristics and low pressure drop in the open state. One notable advantage is their compatibility with ultra-high-temperature graphite sealing elements. Nonetheless, thermal expansion mismatches may result in technical challenges [114]. Additionally, the significant mass of the steel ball may introduce substantial thermal inertia, thereby reducing the StF efficiency by using solar energy without contributing to the redox reaction. More sophisticated gate configurations, such as those employing double isolation valves with intermediate airlock chambers, are technically viable and can offer enhanced atmospheric isolation [114]. However, these solutions considerably increase system complexity, require precise synchronisation, and present additional challenges in terms of control, maintenance, and mechanical reliability under high-temperature cycling.

Regardless of the specific gate configuration selected, both the gate and rod seal in the R2Mx reactor are expected to operate under high thermal loads. A critical consideration for the reliable and long-term performance of the pressure sealing system is the degradation and eventual failure of the sealing materials. For polymer-based seals, in particular, high-temperature operation poses a significant engineering challenge. Accordingly, the following chapter provides a detailed overview of the sealing methods and materials investigated, considering their relevance to the successful operation of the pressure sealing system of the R2Mx reactor.

3. Sealing technology & fluoropolymers

As discussed in the previous chapter, the new generation of solar reactors is increasingly transitioning away from static configurations, placing greater demands on the efficiency and durability of sealing systems. In the R2Mx reactor, seals are specifically employed to isolate the reaction zones from one another and from the ambient, thereby enabling vacuum conditions essential for effective operation. In this chapter, the technological background required to design and evaluate the pressure sealing system of the R2Mx reactor is presented. Initially, leakage phenomena as well as detection methods are introduced. Next, the characteristics of O-rings and high-temperature resistance fluoroelastomers are discussed. Then, rod seals and PTFE attributes are examined. Finally, the regulatory context of fluoropolymers is discussed.

3.1. Leakage

Seals are critical components designed to inhibit the exchange of fluids, liquids or gases, between two separate environments. However, in reality an absolute leak-tightness is physically unattainable. A minimal degree of mass transport is always present due to factors such as surface roughness at the sealing interface, which can form micro-scale leakage pathways, or through molecular permeation of gases across the seal material itself [123,124]. In the context of vacuum systems, it is essential to define and adhere to an acceptable leakage threshold that ensures the system's functional integrity while allowing for minor, non-disruptive leakage.

Leakage across seals can be driven by several physical mechanisms, including pressure or concentration gradients, temperature differentials, viscous shear forces, molecular adhesion and cohesion, or body forces such as gravity or inertia [123]. A way of quantifying mass transport at the seal interface, and thus assess the sealing performance of a component is to evaluate its leakage rate q_l. It is usually expressed in $\mathrm{mbar \cdot l \cdot s^{-1}}$, and quantifies the rate of pressure change, Δp, in a sealed volume V, over time t, as per Eq. (3.1). It must be noted, that the leak rate depends on the type of gas.

$$q_l = \frac{\Delta p \cdot V}{\Delta t} \tag{3.1}$$

In polymer-based sealing materials, gas permeation is influenced by the solubility of the gas in the polymer matrix and its diffusion coefficient. The inclusion of fillers in the polymer formulation can reduce permeability by increasing the tortuosity of the diffusion path, thereby impeding the migration of gas molecules. For instance, Jung et al. [125] showed that hydrogen permeation in carbon black and silica-filled ethylene propylene diene monomer (EPDM) is inversely proportional to the filler content of the elastomer. In systems employing elastomeric seals, leakage is primarily governed by gas permeation through the material as long as the seal remains functionally intact. Failure, however, arises from the formation of additional leakage paths, for example when cracks are formed on the material's surface.

3.1.1. Vacuum leakage detection methods

Among the most commonly employed methods for leak detection in vacuum systems are helium leak detection and the pressure rise technique. Helium leak detectors offer exceptional sensitivity, often reaching detection limits below $1 \cdot 10^{-9}$ mbar·l·s^{-1}, making them particularly suitable for ultra-high vacuum (UHV) applications. Technological advancements in this area, such as those reported by Große Bley [126], have focused on improving signal stability and enhancing detection limits through software optimisation. Despite their high accuracy, helium-based systems are typically costly and require specialised equipment and handling procedures.

In contrast, the pressure rise method provides a more accessible and straightforward approach for assessing leakage in vacuum environments. This technique involves evacuating the system to its target pressure, subsequently isolating it from the pump, and monitoring the pressure increase over a defined time interval. While this method is less sensitive than helium-based detection and cannot localise leaks, it remains widely used due to its simplicity. One limitation of the pressure rise approach is its susceptibility to interference from outgassing, especially in systems with very large internal surface areas. A linear pressure increase over time generally indicates a real leak, whereas a decaying or non-linear pressure curve is typically attributed to outgassing phenomena (Figure 3.1). The total observed pressure rise in such tests results from two components: gas inflow due to leakage and gas release from outgassing. Outgassing may originate from: (1) evaporation of gases dependent on saturation vapour pressure and temperature; (2) desorption of gas molecules adsorbed onto the internal surfaces; and (3) diffusion of gases previously absorbed and dissolved within bulk materials into the vacuum environment. Consequently, to ensure that leakage measurements are not distorted by outgassing, it is recommended that the vacuum chamber is evacuated for long periods of time and that pressure rise measurements are performed until after

the non-linear desorption phase has stabilised, with the linear portion of the curve used to evaluate the leakage rate accurately.

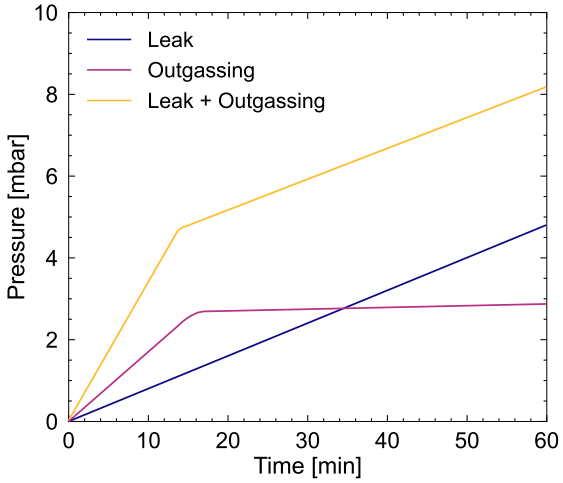

Figure 3.1: Pressure increase in a vessel under vacuum due to a leak, outgassing, and the combination of outgassing and a leak.

Gu and Huang [127] investigated leak detection by the pressure rise method and demonstrated that leakage rates measured across various vessel sizes and under differing pressures showed negligible variation. However, they noted that fluctuations in ambient temperature, as well as temperature differences between the test vessel and the leaking gas, could introduce measurement errors and proposed correction strategies to improve the accuracy of leakage rate evaluations under these conditions.

3.2. O-rings

O-rings are a common type of static seal, used in applications where the interfaces of the two separated boundaries do not move during operation. Static seals can be broadly categorised into two main types: seals, such as elastomeric O-rings, and gaskets. While O-rings rely on their elastic deformation to achieve sealing, gaskets, typically made from fibrous or composite materials, are clamped between flanges and require externally applied loads to establish a leak-resistant barrier [123]. Due to this difference in sealing mechanisms, O-rings generally require significantly lower assembly loads than gaskets [123]. This characteristic makes them particularly well suited for the R2Mx gate, which operates in a confined space, lacks bolted joints, and must undergo repeated opening and closing cycles. The following subsections examine the properties and performance of O-rings in greater detail, with a specific focus on their applicability within the R2Mx reactor system.

3.2.1. Fundamentals

The elastomeric O-ring is regarded as the most common type of general-purpose static seal and is typically installed within a specifically designed groove to achieve optimal sealing performance. Its sealing mechanism, known as automatic, relies on the elasticity and incompressibility of the elastomer material [123,128,129]. For instance, an O-ring with cross-section diameter d_1 is placed in its groove before installation as depicted in Figure 3.2 (a). During assembly (Figure 3.2 (b)), the O-ring is compressed to d_2, leading to a preload or contact stress σ_0 on the contacting surfaces. In operation (Figure 3.2 (c)), the fluid pressure p_{fluid} acts on the side face of the O-ring, effectively increasing the contact stress to σ_{max}, which can be simplified and approximated to:

$$\sigma_{\text{max}} \approx \sigma_0 + p_{\text{fluid}} \tag{3.2}$$

As the maximum contact stress σ_{max} is higher than the fluid pressure, leakage between the interstices of the elastomer and the housing can be virtually avoided. As per Eq. (3.2), it can be deduced that the seal inherently, or like its sealing mechanism suggests "automatically", adapts to changes in fluid pressure without external intervention.

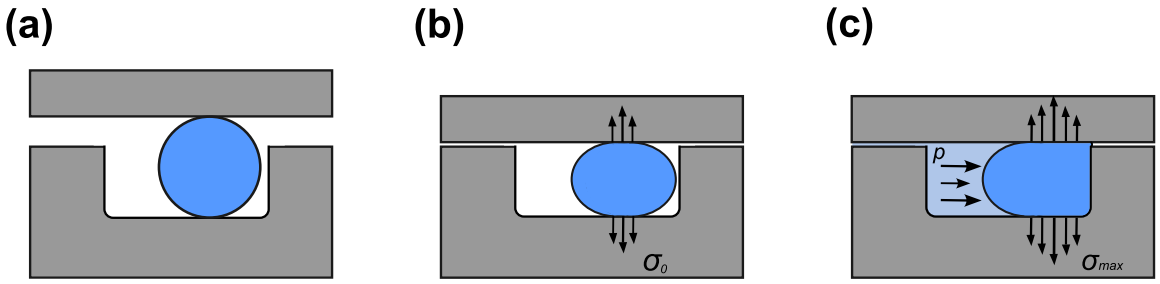

Figure 3.2: Cross-sectional view of the sealing action of an elastomeric O-ring; (a) before installation, (b) preload after installation, and (c) under operating pressure.

To ensure an effective seal operation, the seal preload and hence the groove dimensions have to be designed according to the application. The standard groove geometry is rectangular and extensive knowledge on groove design guidelines [128–130] and standards [131,132] exists. The O-ring initial deformation depends on the height of the groove and is approximately 15–30%, with the exact values varying between applications [128,130,133]. For mid-vacuum applications (~1 mbar), such as the one examined in this work, a 25% O-ring deformation is recommended [129,133]. This deformation is known in literature by a wide variety of names such as squeeze degree, compression rate, interference and nip [123,134,135]. For the purposes of this work, it will be referred to as squeeze degree (SD) and is defined as:

$$\mathrm{SD} = \frac{d_2 - d_1}{d_1} \cdot 100\% \tag{3.3}$$

In vacuum applications an increased SD can limit leakage by reducing permeability of the O-ring material as the path length that the gas has to travel is increased and the gas uptake area (groove depth) is reduced. Additionally, increasing the SD also forces the elastomer in the housing's surface irregularities, effectively preventing leakage around the seal.

3.2.2. Material selection

The performance and durability of O-rings in a sealing system depends significantly on material selection. Typically, material selection is performed on the basis of a multitude of factors including seal geometry and service lifetime, with the most prominent factors being operating temperature and pressure as well as fluid-seal chemical compatibility. Elastomers, as previously discussed, are by far the most widely used materials for O-rings, with an extensive range of elastomer types (> 15) being commercially available [128,130,133]. Two of the most renowned elastomers for their exceptional high-temperature resistance are fluoroelastomer (FKM) and perfluoroelastomer (FFKM). While FKM O-rings can typically withstand continuous service temperatures above 200°C, FFKM O-rings offer superior performance, withstanding temperatures up to 325°C. Making them notably better suited for demanding high-temperature applications than most other elastomers [128–130,133]. Detailed information on FKM and FFKM is provided in Chap. 3.2.3.

Other available materials for O-rings are plastics and metals. When referring to plastics used in O-rings, the most commonly used material is polytetrafluoroethylene (PTFE) due to its excellent chemical resistance to a wide variety of acids, fuels and solvents [136]. Nevertheless, plastic O-rings are seldom used due to their rapid loss of sealing force and higher (than elastomers') force requirement during assembly [123]. Up to date, the typical use of plastics in O-rings involves a PTFE sheath surrounding an elastomer O-ring where chemical compatibility might be an issue for elastomers [133]. Metal O-rings, on the other hand, are designed for extreme conditions, with operating temperatures ranging from cryogenic to up to 850 °C, are radiation tolerant and do not outgas in vacuum environments [123]. These O-rings rely on elastic deflection for sealing and usually do not exhibit full elastic recovery after disassembly, thus are considered to be single use only. Recent research has focused on increasing the elastic recovery of these seals by either using external aid such as Inconel springs [137] or by optimising the O-ring geometry [138]. Nevertheless, currently the commercially available designs only show limited recovery and therefore are not appropriate for the continuously opening and closing of the R2Mx reactor's gate.

3.2.3. Fluoro- and perfluoroelastomers

Fluoroelastomers, commonly abbreviated as FKM (according to ASTM D1418 [139] and DIN ISO 1629 [140]), are a class of synthetic rubbers known for their excellent thermal and chemical resistance. The abbreviation FKM is often used interchangeably with FPM, with both referring to the same family of fluorocarbon-based elastomers, also known as fluorocarbon rubbers. Structurally, FKMs are based on a saturated carbon backbone, which enhances their chemical and thermal stability. This stability is primarily attributed to the high bond energies of the carbon-fluorine (C–F) and carbon-hydrogen (C–H) bonds, reinforced by the electronegativity and shielding effect of fluorine atoms [141]. As a result, FKMs offer outstanding resistance to high temperatures (200 °C), fuels, oils, and a broad range of organic solvents and chemicals, making them suitable for demanding applications in the automotive, aerospace, chemical, medical, and food industries. However, their performance at low temperatures is limited, with typical lower service thresholds around -36 °C [130,133]. One of the notable advantages of FKMs is their low gas permeability, which makes them well-suited for vacuum sealing applications.

According to ASTM D1418 [139] classification, fluoroelastomers fall under the “M” class of rubbers, polymers with a polymethylene-type saturated backbone. These polymers incorporate vinylidene fluoride (VDF) as a comonomer and often include fluoroalkyl, perfluoroalkyl, or perfluoroalkoxy substituents along the chain [142,143]. They may also contain cure-site monomers (CSM) with reactive pendant groups to facilitate crosslinking. The molecular structures of commonly used monomers in FKM formulations, such as VDF, hexafluoropropylene (HFP), tetrafluoroethylene (TFE), and perfluoromethylvinyl ether (PMVE), are shown in Figure 3.3.

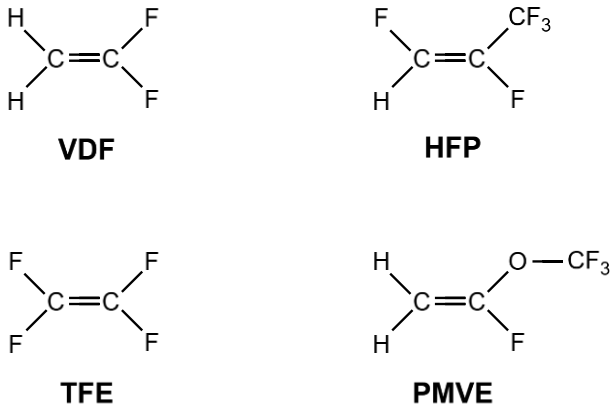

Figure 3.3: Chemical structures of monomers used in FKM and FFKM compounds.

FKMs are classified into different types according to their monomer composition (Table 3.1).

Table 3.1: FKM types as per ASTM D1418 [139].

FKM class	Monomers	Curing system	Fluorine content	Description	Sources
Type 1	VDF HFP	Bisphenol	65–66%	General purpose, good all-round properties, and the most common FKM.	[143–146]
Type 2	VDF HFP TFE CSM[a]	Bisphenol / Peroxide	66–70%	Improved heat resistance, best resistance to aromatic, and low molecular weight hydrocarbons.	[143,144,147]
Type 3	VDF TFE PMVE CSM[a]	Peroxide	62–67%	Improved low temperature resistance (-40 °C), at the cost of reduced chemical resistance.	[143,144,147]
Type 4	VDF Propylene TFE	Bisphenol	55–67%	Higher resistance to bases and amines, higher swelling in hydrocarbons, and decreased low temperature resistance	[142,145,146]
Type 5	VDF HFP TFE PMVE Ethylene CSM[a]	Peroxide	66–67%	Improved base resistance, low swelling in hydrocarbons	[142,143,145]

[a] CSM= cure site monomer, only included if the elastomer is peroxide cured.

The “M” class of rubbers, also includes perfluoroelastomers (FFKMs), sometimes designated as FFPMs [139]. Structurally, FFKMs are synthesised through the copolymerisation of TFE and PMVE, along with a small quantity of a CSM to enable cross-linking [143]. Making FKMs in essence, rubbery derivatives of polytetrafluoroethylene (PTFE) and are distinguished by their exceptional chemical inertness and thermal stability. Depending on the specific formulation, FFKM grades can tolerate continuous operating temperatures of up to 325 °C, making them the most heat-resistant rubber materials currently available [129,130,133]. Traditionally, their application was limited by poor low-temperature performance. However, recent advances in polymer chemistry have enabled the development of FFKM formulations capable of sealing at temperatures as low as -40 °C, thereby broadening their application range [146].

With a fluorine content exceeding 71%, FFKMs offer the highest level of chemical resistance among elastomeric materials, providing excellent performance in harsh chemical environments such as hot amines, steam, aggressive solvents, and hydrocarbons [133]. Their resistance is attributed both to the shielding effect of fluorine atoms around the carbon backbone and to the stability imparted by advanced vulcanisation systems [148–150]. Despite their superior performance characteristics, FFKMs do present some drawbacks. They exhibit relatively poor abrasion resistance and only moderate mechanical strength, which tends to degrade more rapidly at near 0 °C [143]. Additionally, certain FFKM formulations are incompatible with specific fluorinated refrigerants, and have a very high production cost [133].

Compounding

The formulation of FKM and FFKM, involves a complex mixture of ingredients tailored to impart specific mechanical, chemical, and processing properties to the final vulcanised material. Typically, an FKM compound consists of one or more fillers, acid scavengers, and a curing system [143]. Fillers are commonly added in the range of 10–30 parts per hundred rubber (phr) and may include reinforcing agents like carbon black, or non-black fillers such as silica, barium sulphate, calcium carbonate, and calcium metasilicate [151,152]. Acid acceptors, particularly magnesium oxide and calcium oxide, are incorporated to neutralise hydrogen fluoride generated either during vulcanisation or prolonged exposure to high temperatures [143]. Crosslinking of FKM is generally achieved through either ionic or free-radical curing systems, with bisphenol-based and peroxide-based chemistries being the most widely adopted approaches. Bisphenol crosslinking typically utilises Bisphenol AF in combination with an accelerator such as benzyltriphenylphosphonium chloride (BTPPC) and inorganic bases like calcium or magnesium hydroxide. In contrast, peroxide curing involves iodine or bromine functionalities in the polymer backbone and the use of a peroxide initiator alongside coagents such as triallyl isocyanurate (TAIC) or triallyl cyanurate (TAC) [152]. In addition, processing aids and plasticisers, including hydrocarbon esters, polyethylene, carnauba wax, and sulfone derivatives, are often incorporated to optimise flow properties during processing [143]. Notably, diphenyl sulfone (DPS) and dichlorodiphenyl sulfone (DCDPS) are frequently utilised in this context [153].

FFKM elastomer compounding follows a broadly similar formulation strategy, comprising fillers, curatives, and processing additives. Fillers may include carbon black, mineral-based agents, or polymeric fillers depending on the desired performance characteristics [152]. Two principal curing methods are prevalent for FFKM materials: peroxide crosslinking and nitrile-based systems. In peroxide curing, initiators such as 2,5-dimethyl-2,5-di(t-butylperoxy)hexane are combined with coagents like TAIC or trimethallyl isocyanurate (TMAIC), although crosslinking using bis-olefins alone is also possible [148–150]. Nitrile-curable FFKMs incorporate nitrile functional groups within the cure site monomer (CSM) and employ proprietary catalysts that promote the formation of stable triazine, benzoxazole, or benzimidazole structures within the crosslinked network [148,149]. Plasticisers and processing aids similar to those used in FKM formulations can also be found in FFKM compounds, with the addition of zinc oxide often improving compression set properties in peroxide-cured grades [149].

Relaxation and recovery behaviour

Polymers exhibit viscoelastic behaviour, combining the properties of elastic solids and viscous fluids. This rheological response is modelled in its simplest form using mechanical analogues involving a combination of purely elastic springs with elastic modulus E, purely viscous dampers with viscosity η, and retardation time $\tau = \eta/E$ [154]. Elastomers, being crosslinked polymer

networks, behave as solids and are typically described using the generalised Kelvin-Voigt model, which is an arrangement of springs and dampers in parallel, connected in series [155]. A single spring simulates the immediate elastic response, while multiple Voigt-Kelvin elements capture time-dependent effects. When an elastomer is held under constant deformation, such as in the case of a compressed O-ring seal, the stress and therefore force needed to maintain this deformation decreases over time due to stress relaxation (Figure 3.4 (a)). This occurs as the polymer chains rearrange towards a new equilibrium state as a result of the deformation. The degree of stress relaxation in a polymer depends on the material's formulation as well as on the initial mechanical loading and service temperature [150].

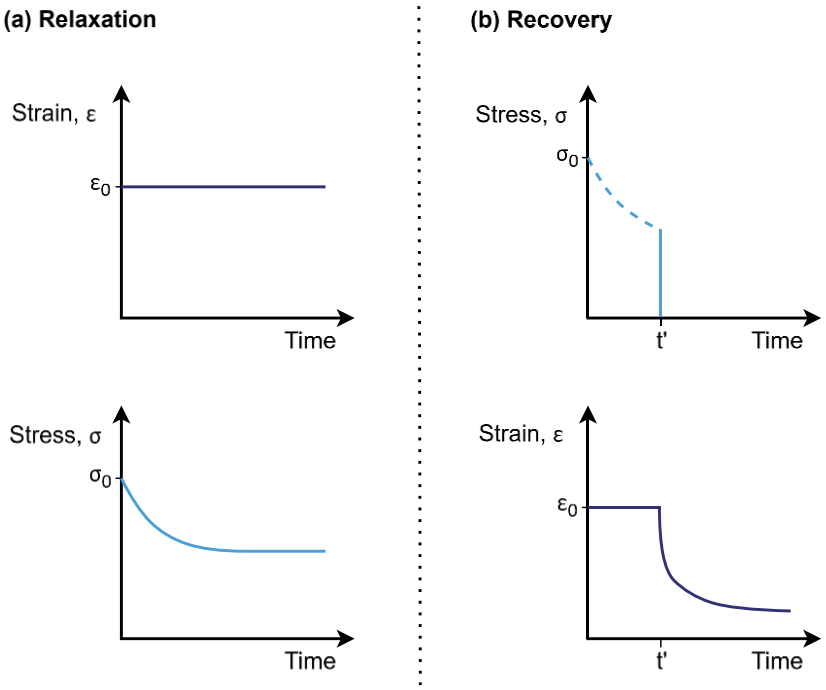

Figure 3.4: Relaxation and recovery behaviour of elastomers. (a) Stress relaxation, showing the time-dependent decline in stress under constant strain. (b) Recovery response, where following a period of constant strain, the elastomer progressively returns to its original shape upon stress removal at time t'.

The stress decay under constant strain can be mathematically expressed as:

$$\sigma(t) = \sigma_\infty + \sum_{1}^{n} \sigma_i \exp\left(-\frac{t}{\tau_i}\right) \tag{3.4}$$

where σ_∞ is the equilibrium stress at infinite time, σ_i is the initial stress contribution of a i-th Kelvin-Voigt element, and n is the number of Kelvin-Voigt elements in the generalised model. This model accurately describes stress relaxation under conditions dominated by physical processes, such as short-term loading at room temperature. However, at high temperatures and longer durations, ageing mechanisms, such as chain scission and additional crosslinking, become

significant. Under these conditions, the contact stress may decay to zero [156,157]. This could potentially compromise the sealing function, as O-rings rely on an “automatic” sealing mechanism.

When the stress is removed from a deformed elastomer, the elastic network of the elastomer allows it to recover, a process governed by both immediate and time-dependent mechanisms. This process can also be modelled by several Kelvin-Voigt elements with different retardation times. The recovery behaviour as a function of time, illustrated in Figure 3.4 (b), depends heavily on crosslink density: higher crosslinking promotes faster and more complete recovery [158]. Elastomers are entropy-elastic materials, where the thermodynamic driving force for recovery is the return of the chains to a higher entropy state.

For long-term deformation at high temperatures, compression set (CS) tests are used to evaluate recovery according to DIN ISO 7743 [159]. These tests reflect the combined influence of physical and chemical changes. During elastomer ageing, newly formed crosslinks may fix the deformed shape, while chain scission reduces the material’s ability to recover [160]. Kömmling et al. [161] showed that CS measurements typically show greater permanent deformation than short-term recovery at ambient conditions, and are regarded as suitable indicators of sealing performance degradation.

3.2.4. Elastomer ageing & O-ring failure

Investigating the failure modes of elastomeric O-rings is critical to ensure operational safety and improve their durability. The main reasons for failure may be traced back to degradation or loss of elastomeric properties due to thermal and/or chemical ageing of the material, operational procedures such as rapid gas decompression, and mechanical damage of the seal [123]. In general, a distinction can be made between physical and chemical ageing, with physical ageing referring to reversible processes such as crystallisation, chain arrangements and segregation [162]. Chemical ageing, on the other hand, leads to non-reversible reactions that may lead to changes in properties crucial for ensuring sealing performance and therefore has a significant effect on service lifetime.

Chemical ageing processes are inevitable, as polymers exist in a thermodynamically metastable state and they move towards a more stable energy configuration [143]. The type and rate of degradation depend on the polymer’s chemistry and its environment, with the most important external factors being heat, oxygen, ozone and radiation [141]. In elastomers, the primary chemical ageing mechanisms are chain scission and cross-linking, which often occur simultaneously, though typically one dominates depending on the material [162]. These degradation mechanisms affect the material macroscopic properties in different ways. For instance, chain scission can cause softening, stickiness and increase permeability by splitting the cross-links between chains created during vulcanisation. Main chain cleavage and increased cross-linking, result in material brittleness as the

chains have lower flowability. In both cases, the elastomer's elastic recovery deteriorates, diminishing the sealing force essential for reliable performance. Furthermore, these competing degradation mechanisms can significantly influence sealing performance, as cross-linking and chain scission may each temporarily enhance leak tightness by reducing permeability and improving conformity to surface roughness, respectively. However, over time, continued degradation often results in stiffening, shrinkage, and loss of elastic recovery, ultimately promoting the formation of leakage paths and compromising seal integrity. Ageing effects can be delayed by incorporating stabilisers (e.g., antioxidants or UV inhibitors), in the elastomer's formulations. For example, Maldonado Mangnere et al. [163] studied the influence of bismuth (III) oxide nanopowder on FKM blends and concluded that it is an excellent option to increase the gamma ray shielding properties of the elastomer. Nevertheless, in general, once the additives are depleted, after the so-called induction period, the ageing process accelerates.

Considering the ageing behaviour of FKM and FFKM elastomers at high temperatures in the range of 200–300 °C, there is limited data available. Nevertheless, existing studies provide some insight into the ageing mechanisms of these materials. FKM has been studied under various environmental conditions, including alkaline [164,165], geothermal [166,167], and hydrocarbon-rich media such as oils [168–172] and fuels [173,174]. Ageing in air between 150 °C and 200 °C has been associated with changes in mechanical and chemical properties attributed to dehydrofluorination and post-curing effects [168]. Simon et al. [175] further observed that peroxide-cured FKM begins to degrade at 250 °C through dehydrofluorination followed by chain scission. Interestingly, Zaghdoudi et al. [169] reported similar levels of compression set for FKM aged in both air and hydrogen at 150 °C, suggesting that the degradation mechanisms may not be strongly dependent on oxygen availability.

The ageing behaviour of FFKM is less thoroughly documented, though significant contributions have been made by Sandia and Brookhaven National Laboratories. Their studies [166,167] assessed the performance of both FKM and FFKM X-rings under geothermal conditions, subjecting the materials to 24-hour exposure at 300 °C in air and seven days in geothermal brine. At 150 °C, FKM exhibited the lowest compression set (CS) (12–17.5%), while FFKM displayed the highest values (130–220%). Despite this, FFKM demonstrated excellent resistance to the simulated geothermal environments. Further work by Reger et al. [148] evaluated various FFKM compounds with different crosslink densities in 6-week compression set tests, establishing material-specific service temperatures. Additionally, investigations into the thermo-oxidative ageing of FFKM at 150 °C identified preferential degradation at the crosslink sites of the TAIC curing network [176].

3.2.5. Lifetime prediction methods

In order to use O-ring seals effectively, it is essential to predict their service life, and replace them before performance degradation compromises the functionality of the system. Ageing tests under real operating conditions are often impractical due to the extended component lifetimes involved, which may span over years. Therefore, accelerated ageing is commonly employed, typically by increasing the temperature to speed up the degradation processes. Extrapolation techniques such as the Arrhenius approach or time-temperature shift (TTS) methods allow the data from these accelerated tests to be used for performing lifetime predictions under lower temperature service conditions. However, for the extrapolation to be valid, the degradation mechanisms at high temperatures must the same as those present at operational temperatures. No phase transitions (e.g., melting or glass transition) should occur within the tested range, and the dominant chemical reactions must remain consistent. The DIN ISO 11346 standard [177] recommends a maximum ageing-service temperature difference of 40 °C to maintain extrapolation accuracy.

Defining a clear end-of-life criterion is fundamental for performing service lifetime predictions. DIN ISO 11346 [177] suggests a 50% reduction in elongation at break as a generic threshold. However, this is not always relevant for seals, where leak tightness matters more than bulk mechanical properties. Recently, Kömmling et al. [178,179] have suggested CS in the range of 80–85% as a suitable end-of-life criterion for EPDM O-rings tested under rapid partial decompression conditions. CS is regarded as suitable property change measurement since it correlates well with the sealing function, however it is important to note that the only reliable indicator of sealing failure is leakage.

Arrhenius Approach

The Arrhenius equation models the temperature dependence of chemical reaction rates and is widely used in polymer ageing studies (Eq. (3.5)).

$$K(T) = A \exp\left(\frac{E_a}{R\,T}\right) \tag{3.5}$$

where K is the temperature dependant reaction rate, E_a is the apparent activation energy, R is the universal gas constant and T is the absolute temperature. The apparent activation energy is composed of the activation energies of the processes involved during degradation of the elastomer. Therefore, E_a may vary depending on the property being evaluated, as different properties are affected to varying extents by specific mechanisms or their combined effects [180,181].

In the Arrhenius approach, the logarithm of the time to reach the end-of-life criterion is plotted against the inverse absolute temperature. Ideally a straight line with the slope E_a/R results, which can be extrapolated to lower service temperatures to find the time at which the end-of-lifetime

criterion is reached. Deviations from linearity of the slope, caused by changes in dominant reaction mechanisms, may result in underestimated or overestimated lifetimes [182,183].

Time-temperature superposition

The time-temperature superposition (TTS) method relies on the principle that viscoelastic properties of polymers are dependant both on time and temperature [154]. In here, a property of a material that has been measured at several temperatures over an experimentally convenient time is superimposed to a reference temperature of interest (Figure 3.5). The curve created by superposition is called a master curve and represents the property of the material at the reference temperature. The data from the reference temperature is not shifted as it serves as the basis for superposing the other temperature curves. The corresponding factors of displacement in the time scale, denoted a_T, are determined empirically to provide optimal overlap of the data.

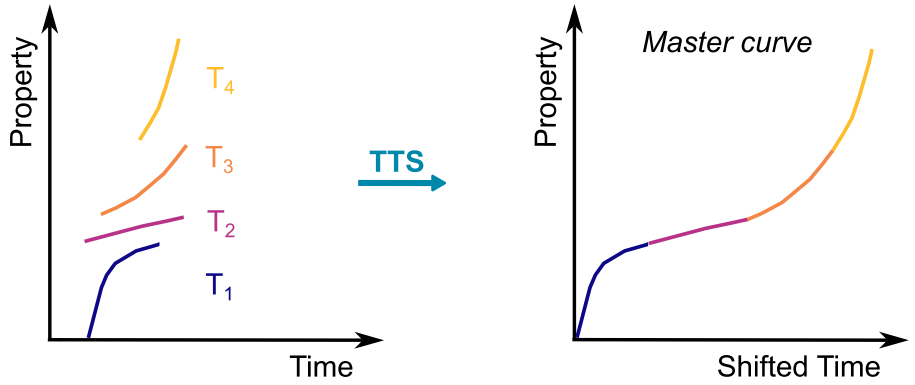

Figure 3.5: Time-temperature superposition (TTS) of a property across time, for testing temperatures 1 to 4.

This approach has become widely stablished extrapolation technique for service life prediction, as demonstrated by several investigations [156,183–186]. TTS is frequently employed in conjunction with the classical Arrhenius method. In this combined methodology, the logarithms of a_T derived from the TTS are plotted against the inverse absolute temperature in an Arrhenius-type diagram. If the resulting data points align linearly, this line may be extrapolated to estimate behaviour at an untested operating temperature, subject to the same limitations that apply to the Arrhenius approach. Without such extrapolation, TTS allows predictions only at the experimentally observed temperature range. In contrast to conventional approaches such as the Arrhenius method, TTS offers the advantage of incorporating the full set of time-dependent experimental data collected at each ageing temperature, thereby enabling a more robust and reliable lifetime prediction [154,187]. Additionally, the end-of-life criterion does not have to be reached at every temperature tested; a single reference temperature can be sufficient for extrapolation. However, for the TTS method to yield reliable results, the measured data must exhibit sufficient overlap across temperatures to allow for a consistent and unambiguous shift.

3.3. Rod seals

Dynamic sealing applications involve significant sliding along the seal boundary, this movement can be distinguished into two main categories: rotating and reciprocating. Both types of seals, rotating and reciprocating, are used in a wide range of equipment in several industries ranging from agricultural, construction, aeronautics, and automotive [188]. Depending on the installation type, reciprocating seals can be further divided into piston and rod seals. In this work, particular attention is given to reciprocating rod seals, which are necessary to achieve leak-tight operation of the transport system of a R2Mx solar reactor as introduced in Chap. 2.3, considering the RMA movement between reaction zones.

Reciprocating rod seals are generally manufactured from elastomers and thermoplastics, each displaying different advantages depending on the application's needs. Elastomeric rod seals are commonly used because of their self-sealing properties and wide availability. However, these materials usually require a lubricating film (typically provided by the fluid to be contained) to function effectively and, depending on the compound used, have a limited temperature resistance [123]. In contrast, thermoplastics such as polytetrafluoroethylene (PTFE) are preferred for more demanding applications, particularly where higher temperatures (200–260 °C) and high chemical resistance are required. Thermoplastic-based seals are also well-suited for dry running applications, as they form a self-lubricating film, reducing wear and friction. Material development for seals is an ongoing research topic, with several working groups focusing on wear resistant PTFE composites [189–192], carbon/carbon composites [193,194], polyimides [195–197], ultra-high molecular weight polyethylene (UHMW-PE) [198,199], and polyetheretherketone (PEEK) composites [197,200]. Up to date, PTFE in various compounds is the most widely used material in reciprocating seals and is therefore selected for application in the investigated solar reactor.

A wide variety of rod seal shapes has evolved over the years, with the most common shapes including U-cups, V-rings, rectangular seals, and lip seals. U-cups have been extensively researched in reciprocating motion, with investigations focusing either on the development of simulation models based on the inverse theory of hydrodynamic lubrication [201–203] and elastohydrodynamic lubrication [204,205] or empirical analyses on the friction of the seals [204,206–208]. PTFE lip seals, on the other hand, have been mainly employed in rotating shaft applications [209–212]. Despite their primary application in rotary systems, PTFE lip seals possess significant potential for applications in reciprocating motion in vacuum environments at high temperatures, as the one investigated in this work. Compared to U-cups, PTFE lip seals offer advantages such as lower friction due to a narrower contact area and better performance in dry-running conditions [123]. Therefore, the following subsections focus on the theoretical background of PTFE lip seals.

3.3.1. PTFE lip seals

A typical PTFE lip seal configuration is depicted in Figure 3.6 (a), where a relatively flat PTFE disk is clamped to a metal casing. The seal between the metal casing and the equipment's housing can be performed by metal-to-metal contact or by an O-ring. Before installation, the PTFE disk is relatively flat, but after installation it deforms to resemble a convectional lip seal as depicted in Figure 3.6. This deformation enables a bush-fitting sealing mechanism, where the leakage path is completely closed as the polymer conforms to the rod [123]. When in motion, a dynamic lubrication film separates the seal and rod surfaces. This lubrication film can be either from the fluid to be contained (e.g. lubricating oil) or, in dry running applications, from the seal material (PTFE) which forms a self-lubricating film on the rod's surface as it adheres to the metal [213,214]. A typical seal design has a lip contact width of 2–3 mm [123].

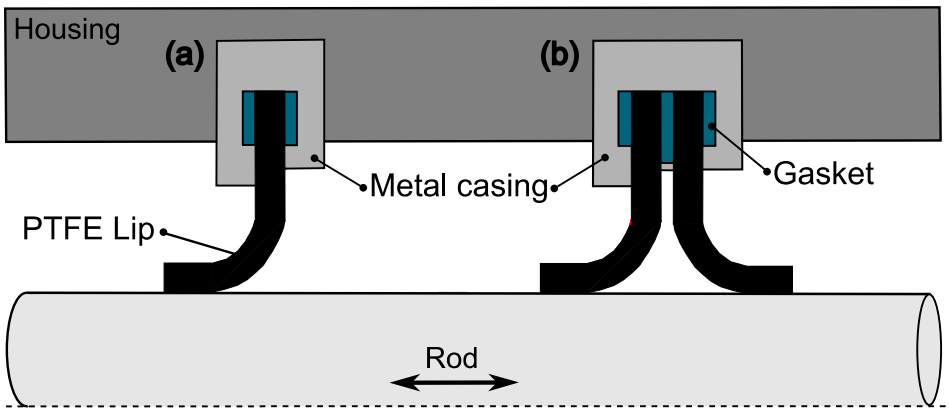

Figure 3.6: Schematic radial cross-section of: (a) single lip seal and (b) back-to-back double lip seal.

The sealing performance of a lip seal is influenced by several factors including seal profile design and operating conditions. The seal's preload or contact stress is a critical parameter as it influences the seal's ability to conform to the rod surface and is determined by the initial seal deformation and geometry. During operation, the fluid's pressure will also affect the working contact stress, which in turn influences the seal's friction and therefore the performance. Research suggests that PTFE lip seals' performance can be further enhanced by optimising the geometry of the sealing edge [209] or by incorporating a spiral form on the seal's face [215,216].

The seal's performance is also influenced by the rod's surface roughness and the fluid's viscosity. Several studies have performed numerical analyses of reciprocating rod seals coupled with different rod surfaces, such as honed [217], plunge ground [218], textured [219,220], and grooved [204], and it is generally agreed that a smooth rod surface leads to a decrease in seal wear. Furthermore, not only the surface roughness but also the geometric characteristics of the unevenness are relevant for the seal's leak tightness. Regarding the fluid's viscosity, a recent study

by Feuchtmüller et al. [221] showed that the wear of reciprocating rod seals was increased with lower viscosity and higher polarity oils. In vacuum conditions, where the fluid's viscosity is low, a hard rod surface (50–60 Rockwell C) with a fine surface finish (0.1–0.2 μm Ra) is usually recommended by seal manufacturers [123,222,223].

PTFE seals exist in several lip configurations including single, double, and triple lips; each one offering different advantages and disadvantages depending on the application's requirements. Multiple lip seals may use different lip arrangements such as back-to-back, reversed lip, and tandem [222,223]. Back-to-back seals (Figure 3.6 (b)) consist of two lips facing away from each other, ensuring sealing capability in both directions. These seals are particularly useful in applications where pressure differentials can occur in both directions and in conditions where alternating pressure exists. Nevertheless, due to the multiple sealing surfaces and increased contact area, back-to-back seal arrangements can lead to higher friction and wear. For the purposes of sealing the transport system of a R2Mx reactor a lip seal in back-to-back configuration is used.

3.3.2. PTFE and compounds

Polytetrafluoroethylene (PTFE) is a high-performance thermoplastic synthesised by the polymerisation of tetrafluoroethylene (TFE); TFE is depicted in Figure 3.3. PTFE was first commercialised by DuPont in the 1950s under the trademark Teflon® [224], and is distinguished by its unique molecular architecture and outstanding chemical stability. It is referred as the most chemically resistant polymer and one of the most thermally stable ones [143]. PTFE's exceptional properties can be attributed to its helical linear structure, in which fluorine atoms envelop a carbon-based chain, forming a cylindrical sheath that provides high chemical and thermal stability [143,225]. Individual helical cylinders can slide relative to each other, contributing to PTFE's propensity for cold flow under stress. Furthermore, the strong repulsion between adjacent fluorine atoms inhibits chain bending. The resulting molecular rigidity and low surface energy account for PTFE's well-known non-stick characteristics, excellent chemical inertness, and low coefficient of friction. Notably, PTFE's static and dynamic coefficients of friction are nearly equal, as no stick-slip occurs [226,227], but a temperature dependence of the coefficient of friction (μ) exists as reported by Pleskachevsky and Smurugov [228]. Furthermore, Blanchet and Kennedy [229] demonstrated that the μ for PTFE sliding against stainless steel is velocity-dependent, ranging from 0.02 to 0.18 under a contact pressure of 6.55 MPa and velocities between 0.01 and 0.2 $m \cdot s^{-1}$. Another study [210] observed a motion type-related variation in μ between 0.10 and 0.12 for tests involving a steel ball sliding on a PTFE disc. Overall, PTFE's coefficient of friction has been reported to vary significantly from as low as 0.02 to as high as 0.35 [210,228,230–232], depending on test configuration and tribological systems' operating conditions.

Structurally, PTFE exhibits a high degree of crystallinity (> 90%) in its virgin state, with a melting point of approximately 340 °C. Upon melting and subsequent recrystallisation, crystallinity may decrease to around 70%, and the melting point is slightly reduced [143]. Despite its many advantages, virgin PTFE is limited by poor wear resistance and a tendency to cold flow under load. To address these shortcomings, research has focused on the development of PTFE-based compounds with improved tribological and mechanical performance. Bageale et al. [233] conducted comparative wear analyses of virgin PTFE and filled composites under dry sliding conditions, and showed that the inclusion of fillers such as carbon and bronze significantly improves performance. Table 3.2 summarises commonly used inorganic fillers that have shown potential in enhancing PTFE's tribological behaviour. While not exhaustive, the list includes fillers capable of reducing wear rates of virgin PTFE by one or two orders of magnitude [233,234]. However, the effectiveness of these fillers is influenced by several factors, including their size and morphology, test conditions (such as load, velocity, and motion type), and the nature of the counterface material [232,235,236].

Table 3.2: Inorganic fillers used for PTFE compounds

Filler	Amount (% wt)	Comment	Sources
Glass fibres	15–40	Improved wear resistance by preventing surface failure [229]. Fibres perform better than glass beads and flakes [235].	[229,232, 235–237]
Graphite	0–50	Improved electrical conductivity. Optimal filler content is 10%, above 40% filler wear rate increases sharply [238]. Flakes can form [229].	[229,232, 237,238]
Carbon (fibres)	25–35	Improved mechanical strength [237]. Reduces creep and increases compressive strength and wear resistance.	[227,237, 239]
Bronze	40–60	Enhanced wear resistance and hardness. Wear rate decreases with increasing velocity, tendency to flake [229].	[229,232, 237]
MoS_2	0–50	Lowest friction coefficient. Above 40% filler wear rate increases sharply [238].	[231,232, 238]

3.3.3. Failure modes of PTFE seals

As discussed in Chap. 3.2.4, failure of the sealing system occurs when leakage exceeds a certain threshold value, rendering the seal ineffective in performing its intended function. Reasons for reciprocating rod seal failure are diverse, however the most common failure modes may be distinguished into wear, material degradation and mechanical damage. Mechanical damage of the seals is often associated with improper installation, where scratches and tears of the polymeric lip might occur as a result of the low resistance of the PTFE material to mechanical stress. Material degradation, on the other hand, results from the seal's exposure to harsh operating conditions, such as high temperatures, aggressive chemicals, and radiation. Thanks to its carbon-fluorine backbone and crystalline structure, PTFE is highly resistant to chemical attack and thermal degradation, and

its properties do not change significantly due to ageing [136,240,241]. Therefore, material ageing is not a major concern for PTFE seals, and wear plays a more substantial role in the failure of the sealing system [209]. Lip seal wear refers to the gradual removal of material from the PTFE lip due to the sliding motion along the rod's surface. The removal of lip material leads to an increase in the seal's contact width and a decrease in the lip thickness, which in turn reduce the contact pressure. If the contact pressure drops below the necessary threshold for effective sealing, large leakage can occur. Continuous wear may ultimately lead to the tearing of the seal, eventually resulting in the complete failure of the sealing system [209].

To model wear several approaches such as elastohydronamic analysis [242,243], finite element modelling [244,245] and the Archard wear model [246,247] are employed. The Archard's equation (Eq. (3.6)) is among the most commonly applied models and it describes the wear rate $\frac{dW}{dt}$ as being directly proportional to the contact pressure, p_c, and the relative sliding velocity between surfaces, v. The proportionality constant or wear coefficient, κ, is typically empirically determined.

$$\frac{dW}{dt} = \kappa\, p_c\, v \tag{3.6}$$

Furthermore, experimental testing often focuses on direct wear measuring by means of mass or height loss [248–250], while surface analysis is commonly used to determine wear mechanisms [210,251,252]. Wear is a complex phenomenon that involves several mechanisms or modes such as abrasion, adhesion, and fatigue [253,254]. Abrasive wear occurs when the rough surface of the harder steel rod scrapes against the softer PTFE lip, causing material to be worn away from the seal. Adhesive wear is caused as the frictional energy is dissipated by adhesive interaction and a polymer transfer film is formed on the rod's surface. In this case, the wear rate predominantly depends on the rheological properties of the transfer film, where if the strength of the bulk material is higher than the shear strength of the film, the wear rate will be low [255,256]. Fatigue wear arises from the cyclic loading of the seal, which leads to crack initiation and propagation in the PTFE material. Shibo et al. [210] found wear to be dependent on motion direction, with the higher wear mass loss obtained under linearly reciprocating motion. Generally tribological testing is performed on pin-on-disc apparatus to investigate the friction and wear behaviour of PTFE seals [247,257–259].

3.3.4. Lifetime prediction methods

Predicting the service lifetime of a rod seal is desirable in order to avoid unexpected failures and to plan maintenance schedules. Lifetime prediction extends beyond simple wear modelling by incorporating the degradation processes that seals experience in service, with sealing functionality.

Analytical approaches such as stochastic prediction models [260–262], and machine learning methods such as convolutional neural networks [263,264] have been employed in dynamic seals lifetime prediction. For instance, Sun et al. [265] predicted the service lifetime of mechanical seals operating in diesel using fractal geometry theory and a maximum allowable leakage rate, with in-field data validation confirming the model's predictive capability.

Due to the cost and time requirements of long-term field testing, empirical approaches often employ accelerated ageing protocols [266,267]. In accelerated ageing tests, the main parameter that affects the service lifetime of a component is used as a control variable. For O-rings the main parameter is the ageing temperature during thermo-oxidative conditions, while for tribological systems such as rod seals, the main parameter depends on the dominant wear mechanism [268]. According to Archard's wear equation (Eq.(3.6)), accelerated wear may be induced either by increasing the contact pressure or by modifying the wear coefficient. However, increasing the contact pressure may cause undesirable effects, such as seal deformation. Alternatively, the wear coefficient may be increased to accelerated wear. For examples, Lee et al. [247] developed an accelerated wear test of FKM rod seals by introducing 1 μm alumina particles into the lubricant, which increased the wear by a factor of 58 without significantly modifying the wear mechanism. Surface roughness also plays a role in wear acceleration. Kurita et al. [269] theoretically demonstrated that lip seal wear rates increase with a rougher shaft surface. More recently, condition monitoring techniques such as acoustic emission sensing have been employed to detect early-stage degradation and leakage onset in hydraulic seals [270]. These non-invasive diagnostics offer real-time insights and serve as useful complements to accelerated testing protocols. Despite these advancements, limited research exists on the lifetime prediction of PTFE-based reciprocating lip seals operating under vacuum conditions.

3.4. Fluoropolymers regulatory outlook

Fluoropolymers belong to the broader class of per- and polyfluoroalkyl substances (PFAS), a large (> 3000) and diverse group of synthetic compounds [271]. PFAS are typically classified into polymeric and non-polymeric substances and are characterised by the presence of strong carbon-fluorine bonds, which confer exceptional chemical and thermal stability, resistance to degradation, and surface-active properties such as water and oil repellence [271,272]. Due to these attributes, PFAS are widely used across almost all industries and many consumer products including textile impregnation, fire-fighting foam, and electroplating as highlighted by the extensive review of Glüge et al. [273]. However, growing concern surrounds the environmental and health implications of PFAS, as these substances are highly persistent, do not degrade naturally, and tend to accumulate in soil, water, and living organisms [274].

Among the most studied PFAS are the long-chain non-polymeric perfluoroalkyl acids (PFAAs), such as perfluorooctanoic acid (PFOA) and perfluorooctane sulfonate (PFOS), both of which have been found extensively in the environment and biota [271]. Furthermore, PFOA and PFOS have been classified as persistent, bioaccumulative, and toxic substances [275,276], prompting regulatory action in several jurisdictions to limit PFAAs manufacture and restrict the use of precursor substances that degrade into them [277,278]. Polymeric PFAS, on the other hand, are regarded as less toxic than non-polymeric PFAS, owing to their higher molecular weight, which limits their uptake into living cells. For instance, Henry et al. [279] reviewed extensive toxicological and biological data, and concluded that fluoropolymers meet established international criteria to be considered "polymers of low concern" and shall not be grouped with other classes of PFAS for hazard assessment or regulatory purposes. However, concerns remain, particularly regarding the full life cycle perspective of PFAS polymers. This, since their production and disposal may release more mobile and hazardous PFAS into the environment, posing risks including toxicity, contribution to climate change and ozone depletion, as well as hindered recyclability of products [280–282].

In response to these concerns, the European Union recently proposed the 2023 REACH regulation, which aims to ban most PFAS, including fluoropolymers, except for "essential uses" where no alternatives are available and for which time-limited derogations are foreseen [283]. Germany has backed strict regulatory measures, though industry groups have pushed back, citing the importance of fluoropolymers in critical technologies, including renewable energy systems, medical devices, and aerospace. Ongoing policy discussions are considering restriction options, other than a ban, for uses where the socio-economic impacts of a ban are likely to be disproportionate [284]. While a complete ban on fluoropolymers appears unlikely, it is probable that future regulations will impose stricter controls on production emissions and end-of-life management. Final decisions are expected as part of the Chemicals Industry Package in late 2025, with the goal of balancing environmental protection with the strategic industrial needs of key sectors across the EU [285].

4. Derivation of seals' operating conditions in an R2Mx reactor*

As reviewed, the development of more efficient water-splitting reactor technologies is crucial for advancing solar fuel production. The R2Mx technology is a promising approach to achieve this goal, incorporating key design advantages from the best-performing reactor concepts up to date. Despite its potential, the R2Mx technology is still in the early stages of development, with many aspects of the reactor's design and operation yet to be fully characterised. One of the key technical challenges of the concept lies in achieving reliable pressure sealing between reaction zones and to the external environment, particularly under high-temperature and vacuum conditions. However, detailed knowledge of the expected seal operating conditions is currently lacking. While it is anticipated that temperatures will be elevated, their magnitude and duration remain uncertain. This uncertainty is particularly critical given that polymer-based sealing materials exhibit limited

---

* **This chapter is partially derived from the following peer-reviewed publications authored and co-authored by the author of this work:**

Vega Puga, E., Brendelberger, S., Weber, A., and Sattler, C., "Modelling Development of a Receiver–Reactor of Type R2Mx for Thermochemical Water Splitting." Journal of Solar Energy Engineering Vol. 146 No. 5 (2024): 051011-1-051011-12. https://doi.org/10.1115/1.4065975.

Vega Puga, E., Brendelberger, S., Weber, A., and Sattler, C., "Modelling Development of a Receiver-Reactor of Type R2Mx for Thermochemical Water Splitting." *Proceedings of the ASME 2023 17th International Conference on Energy Sustainability*, Washington DC, USA, July 10–12 (2023) https://doi.org/10.1115/ES2023-107871.

Brendelberger, S., Holzemer-Zerhusen, P., Vega Puga, E., Roeb, M., and Sattler, C., "Study of a new receiver-reactor cavity system with multiple mobile redox units for solar thermochemical water splitting." *Solar Energy* Vol. 235 No. 5 (2022): pp. 118–128. https://doi.org/10.1016/j.solener.2022.02.013.

thermal stability at temperatures above 200 °C, making it essential to provide a first approximation of the thermal loads to ensure durable and effective sealing performance.

To bridge this gap, this chapter presents an initial R2Mx prototype and develops a novel finite element heat transfer model to analyse the system's thermal behaviour focusing on the pressure sealing system. The heat transfer model employs a newly developed simulation workflow, which enables the simulation of several consecutive water splitting cycles, in which ceria is reduced in a continuously heated reactor, oxidised in a separated reactor, and transported between reaction zones. With this model, the entire fuel production cycle is simulated for five consecutive cycles and operating temperatures across the cycles are derived for each component. The initial material selection is reviewed, and reactor design recommendations are given. The study centres on the understanding and derivation of realistic operating conditions for the pressure sealing system's main components, O-ring and rod seal, which represent important features of the R2Mx technology and are crucial to avoid system failure.

4.1. R2Mx prototype configuration

The reactor prototype employed in this work was conceived as one possible implementation pathway for enabling the experimental demonstration of the R2Mx concept. While future developments may lead to modifications, this design serves as a foundation for the proof-of-concept validation. The prototype, illustrated in Figure 4.1, incorporates all the key features characteristic of the R2Mx technology, while limiting the engineering complexity to the essential components required for initial functional testing. The system comprises a reduction reactor, a redox material assembly (RMA), an oxidation reactor, a gate, a rod seal, and a transport system.

Notably, unlike the scaled-up version of the concept [22,26], the prototype reactor does not have a solar interface for heating the redox material, but rather an electric heating unit, which surrounds the ceria RPC, and is incorporated in the reduction reactor. The heating unit in the reduction reactor serves as heat source to heat up the reactive redox material. This design choice favours simplicity and is regarded as a good approximation to the expected indirect heating cavity environment of the scaled-up concept [26]. The R2Mx concept foresees the use of a solid heat recovery system, which enables the transfer of sensible heat from a hot reduced redox material structure to an oxidised one. Since only one RMA is included in the R2Mx protype and the efficiency of the solid heat recovery system is highly influenced by numerous design and operational factors, this system has been omitted in the present study. However, given the modularity of the reactor design, the solid heat recovery system can be integrated in later development stages.

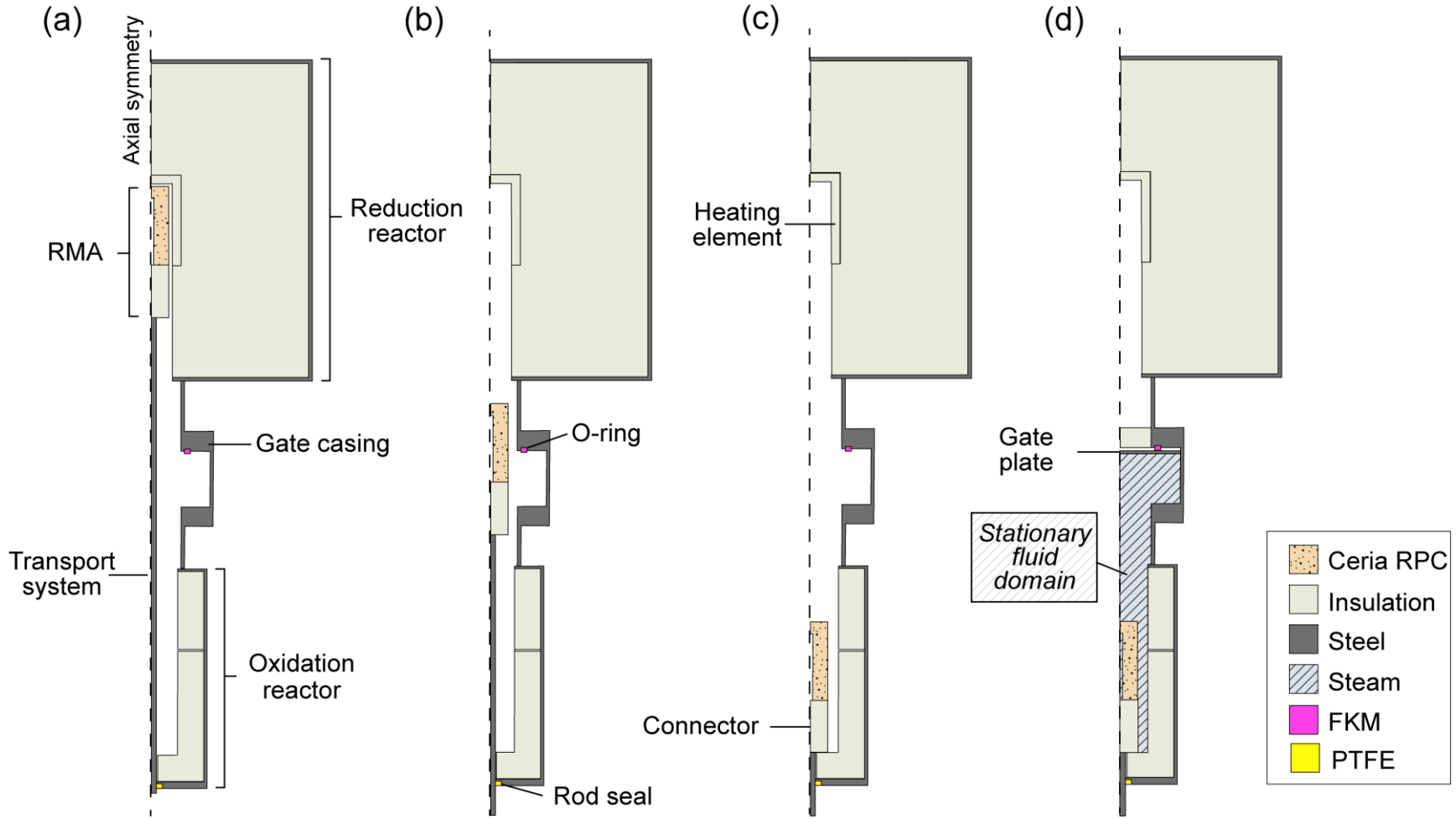

Figure 4.1: R2Mx prototype axisymmetric schematic design. (a) reduction step with RMA in the reduction reactor; (b) simplified transport step, with the RMA in the middle of its trajectory between reduction and oxidation reactor. The transport step includes several intermediate positions, which are not shown in this figure. The reader is referred to Figure 4.4 for a detailed illustration of the transport step. (c) RMA in the oxidation reactor, and (d) oxidation step with the oxidation reactor closed. For illustration purposes, the transport rod has been cropped in (b)–(d). Diagonal hatching denotes the stationary fluid domain, while all remaining components belong to the solid domain.

The R2Mx prototype incorporates one RMA, composed of a 1 kg ceria reticulated porous ceramic (RPC) and an aluminium silicate (Al_2O_3 – SiO2) Altraform KVR 164-502 [286] insulation connector, which acts as an interface to the transport system. Both, the ceria RPC and the connector, have a cylindrical form with an outer diameter of 70 mm and a height of 150 mm and 100 mm, respectively. While currently, the prototype design includes only one RMA, future development will require multiple RMAs to enable continuous on-sun operation of the R2Mx reactor and solid heat recovery.

In the computational model, several components have been simplified and remain generalised, reflecting on the early stage of the technology development. For instance, the reduction reactor is represented as a 5 mm-thick stainless steel (316L) chamber with an aluminium silicate insulation of 250 mm thickness, along with the heating unit. The transport system is modelled as a 20 mm outer diameter stainless steel rod responsible for moving the RMA between the reaction zones, without explicitly representing the motor assembly. Similarly, the oxidation reactor is depicted as a 420 mm-high cylindrical chamber, featuring a 60 mm-thick insulation layer and a 5 mm stainless steel shell. The oxidation reactor is equipped with radially distributed inlets for steam injection, outlets for product gas extraction, and a connection to the vacuum pump for pressure regulation. In the computational model, however, the specific locations of the gas inlets and outlets are not explicitly represented; instead, the gas flow path is simplified and depicted as an opening in the insulation layer of the oxidation reactor.

4.1.1. Pressure sealing system

The pressure sealing system is represented in greater detail in the heat transfer model due to its key role in the present work. This system consists of two sealing components, a gate and a rod seal, to ensure effective pressure management between the reaction zones. The gate prevents re-oxidation of the reduced redox material during cooling in the oxidation reactor, and during oxidation prevents steam and product gas from entering the reduction reactor. Two gate configurations, a sliding and a folding one, are considered for implementation in the prototype. In both cases, the seal is a high temperature resistance O-ring with a 3 mm-cord thickness and the gate plate is made of stainless steel and has a thickness of 5 mm. The O-ring material selection is an important design aspect and will be examined in more detail in Chap. 5. For the heat transfer model, the O-ring material is assumed to be an FKM elastomer under trade name Viton [287] given the wide availability of literature data on the material properties.

To achieve a more conservative estimate of the operating conditions of the sealing system, the folding valve configuration (Figure 4.2) is selected, as it is expected to lead to higher operating temperatures of the O-ring. The folding gate valve has a larger view factor between the O-ring and the hot RMA during the transport step and therefore significant radiative heat transfer is predicted.

In the prototype reactor, the closing process of the gate occurs in two stages. Initially, a linear actuator compresses the O-ring, achieving a squeeze degree (Eq. (3.3)) of 10–15%. In the second stage, the final compression of the O-ring, ranging from 20 to 25%, is induced by the pressure differential (1 bar) between the reduction and oxidation reactors, as steam is injected in the lower reactor during the oxidation step. To prevent the direct heating of the gate plate by the heating unit in the reduction reactor, a 10 mm-thick aluminium silicate insulation block is placed over the gate during oxidation. The insulation block may be either positioned directly on the gate plate or incorporated into a separate component, such a movable shutter; however, the final implementation will be determined in later design stages.

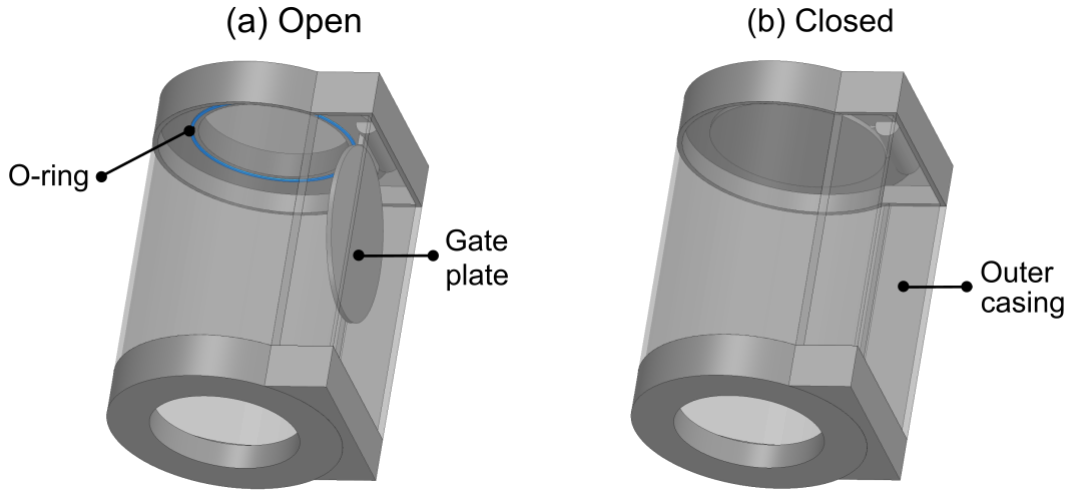

Figure 4.2: Computer-aided design of folding gate. Mid-outer casing section is depicted with higher transparency for illustration purposes.

In the computational model, when the gate is open, it is represented by its stainless-steel outer casing and O-ring, neglecting the movable steel plate, which is assumed to be one with the outer casing. For simplification purposes, the O-ring seal is modelled as a disk with a square cross section of a 3 mm side length and 90 mm inner diameter. This representation provides a conservative estimate of the maximum operating temperature, as it assumes increased surface contact with the hot gate casing, leading to higher conductive heat transfer. When the gate is closed (Figure 4.2 (b)), during the oxidation step, the movable gate plate is introduced, and it is represented by a 5 mm-thick stainless-steel plate. Additionally, only during oxidation (Figure 4.1 (d)), the 10-mm thick insulation block is represented on top of the closed gate plate.

The rod seal is integral to maintaining a pressure differential between the reactor prototype and the external environment through the entire thermochemical cycle. In the transport step, it facilitates dynamic sealing by accommodating the vertical displacement of the transport system's rod as it moves the RMA between reaction zones. During the oxidation step, the transport system remains

stationary and the rod seal functions as a critical barrier, preventing the escape of steam and product gases from the reactor, while simultaneously blocking the entry of ambient air. For the R2Mx reactor prototype an off-the-shelf PTFE lip seal in back-to-back configuration (Figure 4.3) is selected. This seal consists of a steel case and PTFE lips, which, upon contact with the transport system's rod, effectively prevent leakage.

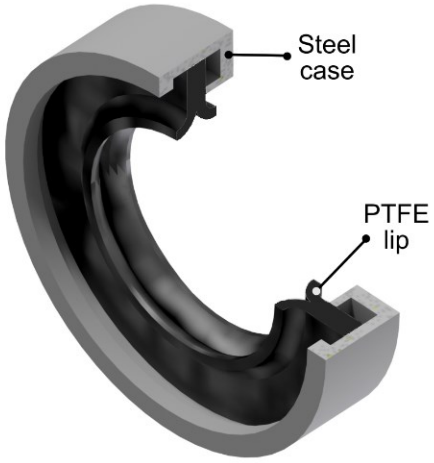

Figure 4.3: Computer-aided design of rod seal for usage in prototype R2Mx reactor.

In the heat transfer model, the geometry of the PTFE lips is simplified and represented by a disk. This simplification results in a conservative estimation of expected operating temperatures, as the larger contact area between the hot transport rod and the seal will lead to higher temperatures. However, it is important to note that the heat transfer model does not account for the heat produced because of friction between the lip seal and the rod. The rod seal is modelled as a disk with a thickness of 7.5 mm and a height of 8 mm, featuring a central hole to accommodate the moving transport rod.

4.2. Heat transfer analysis

The R2Mx prototype reactor, which is characterised by axial symmetry, was analysed using a two-dimensional axisymmetric heat transfer model implemented in ANSYS MECHANICAL 2022 R1 [288]. The simulation encompasses the entire sequence of operational steps necessary for cyclic hydrogen production and provides an initial approximation of the system's thermal behaviour. The objective of the simulation is to gain a first-order estimate of the temperature profiles within the reactor, recognising that many parameters remain uncertain and will ultimately depend on the specific design implementation of the prototype reactor. To enable this early-stage analysis, significant simplifications are applied, with the model primarily accounting for radiative heating of

the gate seal and conductive heating of the rod seal. Further details on the simulation procedure are outlined below.

4.2.1. Simulation workflow

The entire fuel production cycle in the R2Mx prototype is represented by a series of sequential simulations of the key operational steps. First, a reduction of the ceria RPC is simulated followed by RMA transport to the oxidation reactor, cooling, oxidation, RMA transport to the reduction reactor, and a new reduction. Figure 4.1 illustrates the geometry of the prototype during the different operational steps. By simulating the operational steps in the previously stated sequence, an accurate presentation of the operation of the R2Mx prototype is expected. This representation will allow the investigation of interaction and interdependencies between the different steps of the thermochemical water-splitting cycle in the prototype reactor. A full cycle consists of one reduction, one oxidation, and the intermediate transport and cooling steps. The simulation was performed for five cycles, under the operating conditions detailed in Table 4.1. The R2Mx prototype's operating conditions, such as reduction temperature, start of oxidation temperature, and specific steam flow rate, were derived from experimental data from prior studies of the state-of-the-art cavity receiver-reactor [6,7,104].

Table 4.1: Operational parameters of the fuel production cycle simulation

Variable	Value	Unit
Heating element temperature	1500	°C
Partial pressure of oxygen in reduction reactor	1	mbar
Steam flow rate	0.0135	$l \cdot s^{-1}$
Cooling duration	5.5	min
Oxidation duration	8	min

To initialise the simulation and establish realistic starting conditions, a first reduction using a steady-state heat transfer simulation is first performed with the RMA placed in the reduction reactor and the heating unit set to 1500 °C (Figure 4.1 (a)). This initial step provides the thermal baseline for the simulations that follow.

After the reduction step, the transport step is simulated. In this step, the RMA is moved from the reduction reactor to the oxidation reactor. In the simulation, RMA movement is approximated using a series of transient simulations at discrete intermediate positions along the full (785 mm) transport trajectory. For each intermediate transport position simulation, the resulting temperature distribution from the preceding position was used as the initial condition for the next calculation, thereby ensuring a thermally coupled and time-resolved representation of the RMA movement.

To optimise computational efficiency while maintaining accuracy, a separate sensitivity study (Appendix A) was conducted to assess the impact of transport trajectory discretisation. The results

indicated that using 4 positions provides a sufficiently accurate representation of the seal temperature profiles, including maximum temperatures, while significantly reducing computational demand. Figure 4.4 illustrates an example of this 4-position discretisation. The total RMA transfer time is assumed to be 4 s, based on the specifications of the foreseen motor of the transport system and the need to balance rapid transport with mechanical stability, preventing displacement or damage to the RMA during operation.

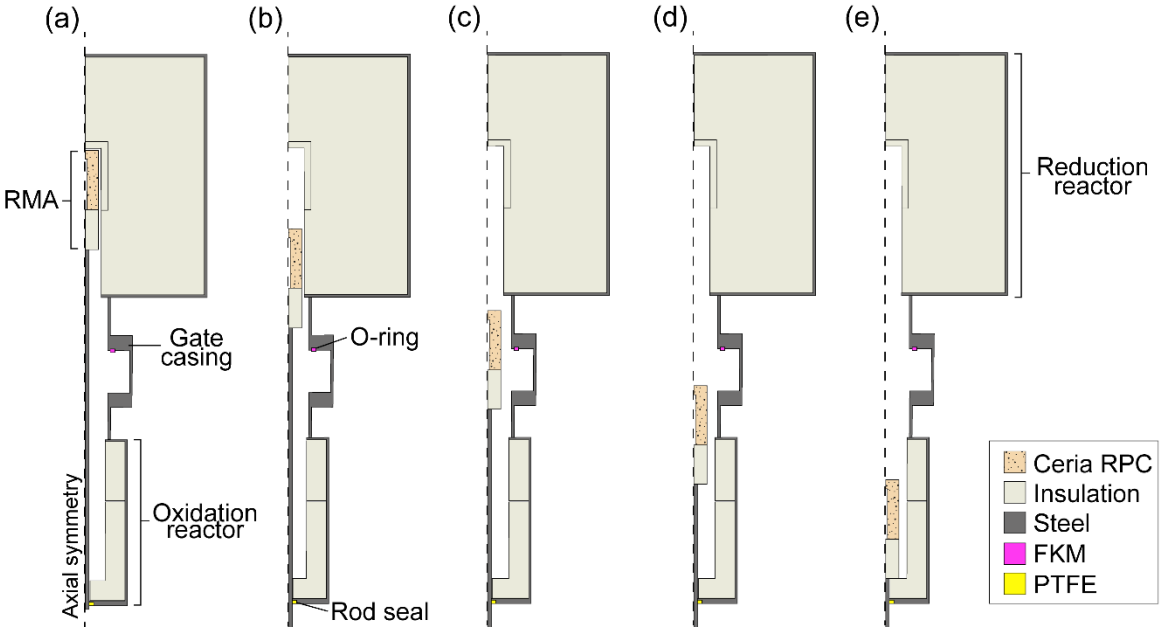

Figure 4.4: R2Mx prototype axisymmetric geometries employed for the simulation of the reduction and transport steps. (a) reduction, (b) transport position 1, (c) transport position 2, (d) transport position 3, and (e) transport position 4. For illustration purposes, the transport rod has been cropped in (b)–(e).

Upon completion of the transport step, when the RMA reaches the oxidation reactor, the ceria RPC is allowed to cool down before oxidation starts. The cooling step's primary target is to obtain a ceria RPC average temperature of about 900 °C to ensure favourable conditions for the oxidation step [7]. To achieve this, a cooling step duration of 5.5 min is derived for the first cycle, and maintained constant throughout all the subsequent cycles.

Once the cooling step is finalised, steam is injected into the oxidation reactor and the water-splitting (oxidation) reaction starts. During this step, the oxidation reactor operates in a steam atmosphere at a pressure of 1 bar, which is represented in the simulation by introducing a fluid phase (Figure 4.1 (d)). Both the injected steam and the newly introduced gate plate have an initial temperature of 150 °C. The initial temperature of the remaining components is the solution obtained the from the previous (cooling) simulation. The steam temperature is set to 150 °C to minimise condensation within the reactor. However, during the actual operation of the prototype, it is advisable to pressurise the oxidation reactor initially with an inert gas such as argon, to prevent

condensation caused by lower pressures in the reactor [6,7]. The steam flow rate is set to 0.0135 $l \cdot s^{-1}$, considering the prototype's ceria mass loading and literature data from experimental campaigns of two-step thermochemical fuel production [104].

Throughout the oxidation reaction, the gate is closed to isolate the atmospheres of the reduction and oxidation reactors. In the model, this is illustrated by inserting a stainless-steel plate in the gate, between the reactors. The oxidation step lasts 8 min, during which the electric heating unit in the reduction reactor is kept at 1500 °C, representing the continuous heat input in the reduction reactor. To avoid excessive heating of the gate plate and imminent damage to the O-ring seal, an insulation block is placed on top of the gate plate as a thermal system decoupling.

The oxidation process is simulated by a series of transient coupled simulations, where each subsequent simulation uses the solution from the previous one as its initial condition. A detailed computational fluid dynamics (CFD) analysis was not performed in this preliminary numerical study due to the lack of precise information regarding the exact positioning and geometry of the oxidation reactor's gas inlets and outlets. While it is known that the inlets and outlets are arranged radially within the oxidation reactor their specific locations and flow characteristics were not fully defined at this development stage. Therefore, a simplified approach was adopted, where the steam is modelled as a stationary fluid, and the effect of the oxidant fluid exchange is approximated by replacing the complete fluid volume by cool steam at each intermediary step in the simulation series. The frequency of this fluid replacement depends on factors such as the volumetric flow rate of steam, the free volume in the oxidation reactor, and the duration of the oxidation reaction. In the analysed case, the steam volume is replaced ten times. This strong simplification provides a partial representation of the enthalpy of the fluid streams entering and exiting the oxidation reactor. However, it does not account for flow dynamics, the influence of inlet and outlet geometries, or the effects of natural and forced convection. In future stages of the R2Mx technology development, this assumption will be replaced by detailed CFD simulations.

Once the oxidation step is finished, the gate plate and the steam volume are removed, and the RMA is transported back to the reduction reactor to begin a new cycle. The simulation of the RMA transport to the reduction reactor is performed in the same manner, previously described, as in its initial transport to the oxidation reactor. All reduction steps have a fixed duration of 8.6 min. This duration was determined on the basis a of previous study by the author [289], in which a newly defined metric, the energy conversion ratio, was utilised to identify an optimal reduction time for a reactor nearly identical to the one investigated in this work. The energy conversion ratio was defined as the ratio of the fuel produced to the energy demand required to maintain the reduction reactor at 1500 °C. It was found that the optimal reduction duration remained almost constant

(8.6 min) across five consecutive fuel production cycles, regardless of variations in oxygen partial pressure in the reduction reactor.

During the reduction, RMA transport, and cooling steps, the gas atmosphere is neglected in the heat transfer simulations, as the operation occurs under a 1 mbar vacuum. This simplification is supported by prior research [58,104], which indicated that convective heat transfer is negligible under comparable vacuum conditions. All reactor components, including the porous ceria RPC, are modelled as solid domains, whereas during oxidation, the steam is modelled as a stationary fluid domain.

4.2.2. Governing equations and boundary conditions

For both transport step and entire fuel production cycle simulations, the transient energy conservation equation (Eq. (4.1)) is solved using finite element analysis (FEA). The conservation equation within the solid domain is expressed as:

$$\nabla\,(k\,\nabla T)\; + Q_{\mathrm{conv}} + Q_{\mathrm{rad,amb}} + Q_{\mathrm{rad,sur}} = \rho c_{\mathrm{p}}\frac{\partial T}{\partial t} \tag{4.1}$$

where k represents the thermal conductivity, ρ the material density, c_{p} the material specific heat capacity, Q_{conv} the convective heat flux to the ambient as a boundary conditions, $Q_{\mathrm{rad,amb}}$ the radiative heat flux to the ambient as a boundary condition, and $Q_{\mathrm{rad,sur}}$ the radiative heat flux between surfaces inside the reactor prototype.

Thermal losses to the surroundings were considered at the outer stainless-steel shell of the reactor, accounting for both convective and radiative heat transfer. Convective heat loss to the ambient was modelled using Eq. (4.2), with a film coefficient, h, of 5 $\mathrm{W{\cdot}K^{-1}{\cdot}m^{-2}}$. Radiative heat loss to the ambient was implemented assuming a stainless-steel emissivity, $\varepsilon_{\mathrm{ss}}$, of 0.57 (Eq. (4.3)). In both cases the ambient temperature, T_{amb}, was set to 22 °C. Radiation exchange between internal reactor surfaces was incorporated using Eq. (4.4), considering a view factor analysis.

$$Q_{\mathrm{conv}} = \; h\,A\,(T_{\mathrm{ss}} - T_{\mathrm{amb}}) \tag{4.2}$$

$$Q_{\mathrm{rad,amb}} = \varepsilon_{\mathrm{ss}}\,\sigma\,A\left({T_{\mathrm{ss}}}^{4} - {T_{\mathrm{amb}}}^{4}\right) \tag{4.3}$$

$$Q_{\mathrm{rad,sur},i} = \varepsilon_i\,\sigma\,A\,{T_i}^{4} + \rho_i \sum_{j=1}^{N} F_{ij} Q_{\mathrm{rad_{out},}j} \tag{4.4}$$

where A is the area, ε is the emissivity, σ is the Stefan-Boltzmann constant, and F_{ij} is the view factor from surface i to surface j. All reactor components, with the exception of steam, were included in the radiative heat transfer calculations.

The energy conservation equation for the porous ceria RPC, treated as solid domain, is formulated as:

$$\nabla\,(k_{\mathrm{eff}}\,\nabla T)\; + Q_{\mathrm{rad,sur}} = \rho_{\mathrm{RPC}}\; c_{\mathrm{p,eff}}\; \frac{\partial T}{\partial t} \tag{4.5}$$

where k_{eff} denotes the effective thermal conductivity of the RPC, ρ_{RPC} represents the density of the redox material accounting for porosity, and $c_{\mathrm{p,eff}}$ corresponds to the modified specific heat capacity. Instead of explicitly defining the heat contribution from the chemical reaction as an additional source term, this effect is incorporated through a modified specific heat capacity for the ceria RPC [290]. The adjusted heat capacity, $c_{\mathrm{p,eff}}$, incorporates the change in non-stoichiometry, δ, the reduction enthalpy, and the energy required to heat one mole of ceria (Table 4.2).

For the fluid domain, which consists of stationary steam, the governing conservation equation is expressed as:

$$\nabla\,(k\,\nabla T) = \rho c_{\mathrm{p}}\,\frac{\partial T}{\partial t} \tag{4.6}$$

All interfaces between domains are assumed to exhibit ideal thermal conductance.

4.2.3. Material properties

The material properties of the ceria RPC are summarised in Table 4.2. To account for the porous nature of the ceria RPC, effective material properties are used. The radiative heat transfer within the RPC is approximated using the Rosseland diffusion model, which is incorporated into the radiative conductivity terms of the effective thermal conductivity, k_{eff}. This approach is chosen due to its reduced computational cost while maintaining reasonable accuracy, with an estimated error of approximately 2% when predicting ceria RPC temperatures, as shown by Lapp et al. [290]. Direct radiation penetration into the RPC's depth is not considered.

Table 4.2: Material properties of the ceria RPC

Variable	Correlation	Unit
Dual-scale porosity	$\Phi_{\text{dual}} = 0.7622$	-
Number of pores per inch	$\text{ppi} = 10$	ppi
Density RPC	$\rho_{\text{RPC}} = 1716.916$	$\text{kg}\cdot\text{m}^{-3}$
Emissivity [291]	$\varepsilon_{\text{RPC}} = 0.5$	-
Extinction coefficient [291]	$\beta = 390.962$	m^{-1}
Thermal conductivity CeO_2 [104]	$k_{CeO_2} = -1.723 \times 10^{-9} \cdot \text{T}^3 + 1.12 \times 10^{-5} \cdot \text{T}^2 - 0.024 \cdot \text{T} + 17.8$	$\text{W}\cdot\text{m}^{-1}\cdot\text{K}^{-1}$
Porous thermal conductivity [104]	$k_{\text{por}} = k_{\text{CeO2}}\,(1 - 0.6223\,\Phi_{\text{dual}})(1 - 1.055\,\Phi_{\text{dual}})$	$\text{W}\cdot\text{m}^{-1}\cdot\text{K}^{-1}$
Radiative conductivity [290]	$k_{\text{rad}} = \frac{16\,\sigma\,T^3}{3\,\beta}$	$\text{W}\cdot\text{m}^{-1}\cdot\text{K}^{-1}$
Effective thermal conductivity	$k_{\text{eff}} = k_{\text{por}} + k_{\text{rad}}$	$\text{W}\cdot\text{m}^{-1}\cdot\text{K}^{-1}$
Reaction enthalpy [104]	$\Delta\text{H}_\text{O} = 484.705 - 251.870\,(\Delta\delta)^{0.5}$	$\text{kJ}\cdot\text{mol}^{-1}$
CeO_2 specific heat capacity [104]	$c_{\text{p,mat}} = \frac{67.95 - 9.9 \times 10^5 \cdot T^2 + 0.0125 \cdot T}{M_{CeO_2}}$	$\text{J}\cdot\text{kg}^{-1}\cdot\text{K}^{-1}$
Heat capacity due to chemical reaction [292]	$c_{\text{p,chem}} = \frac{\text{d}Q_{\text{red}}}{\text{d}(\Delta\delta)} \cdot \frac{\text{d}(\Delta\delta)}{\text{d}T} = \Delta\text{H}_\text{O} \cdot \frac{\text{d}(\Delta\delta)}{\text{d}T}$	$\text{J}\cdot\text{kg}^{-1}\cdot\text{K}^{-1}$
Modified effective heat capacity [292]	$c_{\text{p,eff}} = c_{\text{p,mat}} + c_{\text{p,chem}}$	$\text{J}\cdot\text{kg}^{-1}\cdot\text{K}^{-1}$

The material properties used for all the different materials in this study, except for the porous ceria RPC, are provided in Table 4.3.

Table 4.3: Material properties used in the heat transfer model

Variable	Correlation / Value	Unit
FKM O-ring		
Density [293]	$\rho_{\mathrm{FKM}} = 1850$	kg·m^{-3}
Specific heat capacity [295]	$c_{\mathrm{p,FKM}} = 1650$	J·kg^{-1}·K^{-1}
Thermal conductivity[295]	$k_{\mathrm{FKM}} = 0.18$	W·m^{-1}·K^{-1}
Emissivity	$\varepsilon_{\mathrm{FKM}} = 0.9$	-
PTFE rod seal		
Density [293]	$\rho_{\mathrm{PTFE}} = 2250$	kg m^{-3}
Specific heat capacity [293]	$c_{\mathrm{p,PTFE}} = \begin{cases} 1.115, & T < 20\ °C \\ 7 \cdot 10^{-7}\,T^2 - 1 \cdot 10^{-5}\,T + 0.1802, & 20 \leq T \leq 150\ °C \\ 0.821, & T > 150\ °C \end{cases}$	J·kg^{-1}·K^{-1}
Thermal conductivity[293]	$k_{\mathrm{PTFE}} = 0.31$	W·m^{-1}·K^{-1}
Emissivity	$\varepsilon_{\mathrm{PTFE}} = 0.9$	-
Insulation Al_2O_3-SiO_2		
Density [286]	$\rho_{\mathrm{ins}} = 500$	kg·m^{-3}
Specific heat capacity [286]	$c_{\mathrm{p,ins}} = -3.09 \cdot 10^{-10}\,T^4 + 1.71 \cdot 10^{-6}\,T^3 - 3.48 \cdot 10^{-3}\,T^2 + 3.18 \cdot T + 101$	J·kg^{-1}·K^{-1}
Thermal conductivity [286]	$k_{\mathrm{ins}} = \begin{cases} 6 \cdot 10^{-11}\,T^3 - 1 \cdot 10^{-8}\,T^2 - 1 \cdot 10^{-5}\,T + 0.1802, & T < 1500\ °C \\ 0.29, & T \geq 1500\ °C \end{cases}$	W·m^{-1}·K^{-1}
Emissivity [296]	$\varepsilon_{\mathrm{ins}} = 0.28$	-
Stainless Steel 316L		
Density [288]	$\rho_{\mathrm{ss}} = 7850$	kg·m^{-3}
Specific heat capacity [288]	$c_{\mathrm{p,ss}} = 412 + 0.2 \cdot T - 2 \cdot 10^{-5}\,T^2$	J·kg^{-1}·K^{-1}
Thermal conductivity[288]	$k_{\mathrm{ss}} = 0.013 \cdot T + 11.45$	W·m^{-1}·K^{-1}
Emissivity [297]	$\varepsilon_{\mathrm{ss}} = 0.57$	-
Steam (150°C, 1 bar)		
Density [298]	$\rho_{\mathrm{st}} = 0.51634$	kg·m^{-3}
Specific heat capacity [298]	$c_{\mathrm{p,st}} = 1985.7$	J·kg^{-1}·K^{-1}
Thermal conductivity[298]	$k_{\mathrm{st}} = 0.0261$	W·m^{-1}·K^{-1}

4.2.4. Discretisation and numerical error

To discretise the governing equation in space, a mesh consisting of approximately 26,700 quadrilateral elements was employed. The O-ring has 1173 mesh elements with an average side length of 0.088 mm. While, the rod seal has 1197 squared mesh elements with a side length of 0.216 mm. Inflation layers were used on components where high thermal gradients were expected, and these were: ceria RPC, steam, and insulation of the oxidation reactor. The smallest mesh

elements located within the inflation layers, have a thickness of approximately 0.07 mm and a height of 2.5 mm. Conversely, the largest mesh elements in the model, featuring a square geometry with an edge length of 2.5 mm, are situated in the interior regions of the reduction reactor's insulation.

A two-dimensional axisymmetric mesh was utilised, leveraging radial symmetry for computational efficiency. To ensure mesh independence, a sensitivity analysis was conducted by comparing three mesh resolutions with approximately 12,500, 25,000, and 50,000 elements. The selected mesh configuration resulted in a deviation of only 0.2% at monitored points when compared to the finest mesh while significantly reducing computational times. Temporal discretisation was performed using the adaptive time-stepping approach, implemented via the program-controlled time-stepping feature to optimise computational times.

The numerical error associated with the simulation methodology is estimated at approximately 5.5%, consistent with findings from a similar FEA study using the same software [299]. This error arises primarily from heat equation imbalances due to the spatial and temporal discretisation of the model in the software. Furthermore, a negligible discrepancy (0.01%) was observed between the average temperature of exported results and that of imported data, which may be attributed to minor inconsistencies in mapping temperature profiles across different meshes. While the overall numerical error is relatively high, it remains within an acceptable range given the objectives of this study.

4.3. Results and discussion

The numerical model is a useful tool to understand the operating conditions of the pressure separation system and assess design choices in the R2Mx prototype. With it, the complete fuel production cycle was simulated considering all consecutive operational steps (reduction, transport, cooling, oxidation and transport) for a total of five cycles. To illustrate the expected temperature distribution of the R2Mx prototype during cyclic operation, two temperature contour plots are presented in Figure 4.5. These correspond to the conditions after the first reduction and at the end of the last (fifth) oxidation step.

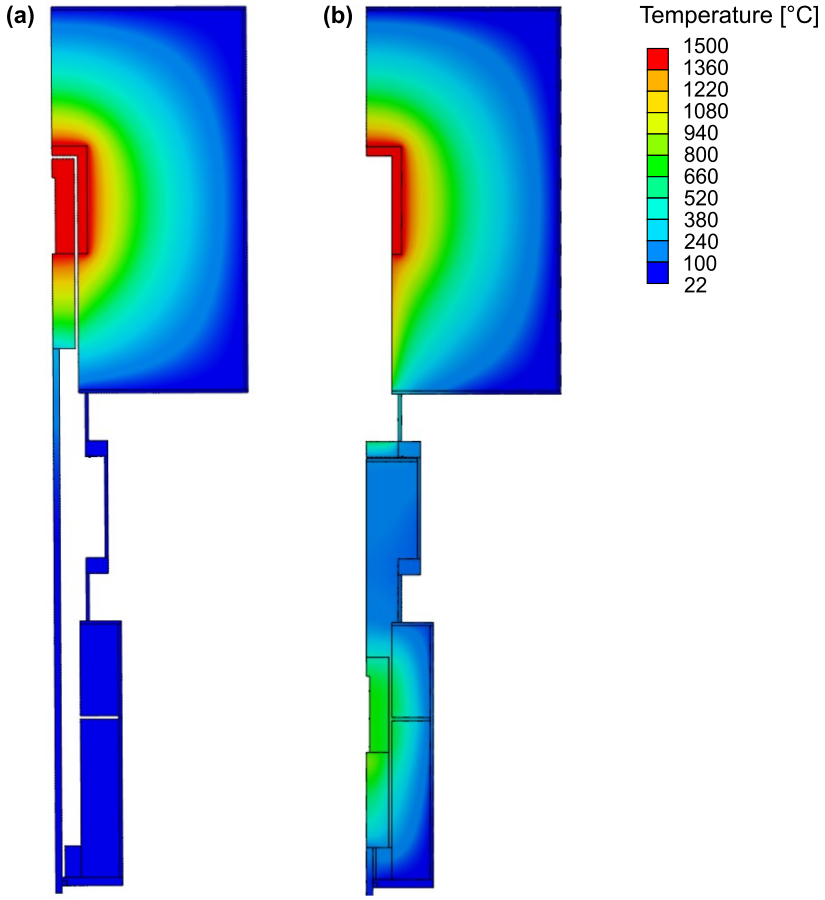

Figure 4.5: Temperature distribution of the R2Mx prototype: (a) after the first reduction and (b) at the end of the fifth oxidation step. The transport rod has been cropped vertically in (b) for illustration purposes.

The temperature evolution in the R2Mx prototype follows distinct trends across the different steps of the simulated fuel production cycles. Throughout all steps of the five simulated cycles, the heating element is uniformly kept at 1500 °C. Therefore, the reduction reactor's insulation exhibits the highest temperatures, maintaining a consistent maximum temperature of 1500 °C at the interface to the heating unit. During the reduction step (Figure 4.5 (a)), the RMA and transport rod experience their highest temperatures, whereas during the oxidation step (Figure 4.5 (b)), the oxidation reactor components and the gate casing achieve their highest temperatures. As the cycles progress, the gate casing, oxidation reactor's insulation, and steel shell exhibit a gradual increase in temperature, as expected. Notably, the transport step is particularly relevant for the pressure sealing system, as during this operation the seals experience their maximum temperatures. A detailed discussion on the seals' predicted operating temperatures follows in a subsequent section.

Focusing on the ceria RPC, the core of the thermochemical fuel production cycle, it experiences its peak temperatures during the reduction step. The gradual heating of the oxidation reactor's insulation over multiple cycles leads to an increase in the RPC's average post-cooling temperature, from 900 °C after the first cycle to 1000 °C after the fifth cycle. Similarly, and attributed to the

same effect, the RPC's post-oxidation temperature increases from 689.6 °C after the first oxidation step to 761.3 °C after the last oxidation step. An extrapolation of post-oxidation temperatures suggests that after ten cycles, the RPC's average post-oxidation temperature stabilises at approximately 764 °C [289]. Comparable literature on experimental campaigns of the state-of-the-art cavity receiver-reactor reports a nominal RPC temperature after oxidation of 500 °C for a 5 kW_{th} reactor [7] and 650 °C for a 50 kW_{th} reactor [6], indicating that the operational conditions predicted in the R2Mx prototype align with those observed in successful solar fuel production. Furthermore, these temperature trends are consistent with expectations for a two-step thermochemical cycle driven by pressure and temperature swing.

The thermal behaviour of the other reactor prototype's components aligns with their specific roles within the system and are detailed in Table 4.4. For instance, the insulation connector exhibits a temperature gradient, with its highest temperatures near the RPC and lower values towards the transport system. The transport rod shows moderate heating due to conduction from the connector and radiative exposure to the warmer oxidation reactor's insulation during reduction. Its highest temperature occurs at the interface with the insulation connector, and reaches 288.6 °C after the last examined reduction step. If a lower maximum temperature of the transport system would be desired, the length of the insulation connector could be increased. However, such modifications would alter the overall reactor geometry and should be carefully evaluated.

A steady temperature increase is observed in both the gate casing and the reduction reactor shell near the gate interface, with maximum recorded values of 250 °C and 390 °C, respectively. While these temperatures remain within operational limits for stainless steel, additional insulation may be required to optimise thermal management. Internal insulation could limit heat accumulation, while external insulation would help reduce thermal losses to the ambient and enhance operational safety. Lowering the temperature of the gate casing itself could also contribute to reducing the operating temperature the O-ring, thereby improving its durability. Additionally, the proximity of the steel components to the moving RMA influences their peak temperatures, a factor that warrants further investigation in future studies.

The oxidation reactor's insulation achieves its peak temperatures of about 1240 °C when the hot ceria RPC undergoes cooling within the oxidation reactor. This maximum temperature is confined to a very thin surface section, which only represents 0.15% of the insulation's total volume. Although the oxidation reactor's insulation does not experience temperatures as high as those in the reduction reactor and the connector, it is currently modelled using the same material as an initial approximation. Future studies may investigate the use of a more cost-effective insulation material with a lower classification temperature (currently 1600 °C), assessing its impact on the minimum ceria RPC temperature and overall cycle performance. Furthermore, investigations on the

insulation's geometry (e.g. thickness) and its influence on the prototype's thermal efficiency could be considered in subsequent stages of the technology development.

Table 4.4: Temperature data for selected R2Mx prototype components at relevant operating cycles and steps.

Component	Cycle step	Maximum temperature [°C]	Average temperature [°C]
Ceria RPC	1st reduction	1499.7	1492.3
	6th reduction	1494.7	1465.9
	1st oxidation	740.7	612.1
	5th oxidation	769.3	655.9
Connector	1st reduction	1465.2	943.5
	6th reduction	1423.0	777.6
	1st oxidation	870.8	499.1
	5th oxidation	842.1	488.9
Transport rod	1st reduction	250.5	48.7
	6th reduction	288.6	114.8
	1st oxidation	116.1	54.8
	5th oxidation	144.2	96.4
Rod seal	1st reduction	34.5	25.8
	6th reduction	120.1	77.2
	1st oxidation	76.1	54.6
	5th oxidation	110.8	89.1
Gate casing	1st reduction	45.3	41.9
	6th reduction	175.5	167.5
	1st oxidation	183.4	103.6
	5th oxidation	246.8	160.9
Gate plate	1st oxidation	136.2	126.1
	5th oxidation	192.9	189.9
O-ring	1st reduction	43.5	42.8
	6th reduction	171.8	169.9
	1st oxidation	142.2	125.4
	5th oxidation	198.1	191.6
Oxidation reactor's insulation	1st reduction	28.4	23.8
	6th reduction	418.8	181.9
	1st oxidation	630.1	256.5
	5th oxidation	681.1	314.5
Oxidation reactor's shell	1st reduction	29.8	23.3
	6th reduction	122.2	77.1
	1st oxidation	83.2	44.7
	5th oxidation	130.2	94.4
Reduction reactor's insulation	1st reduction	1500	340.2
	6th reduction	1500	352.9
	1st oxidation	1500	327.2
	5th oxidation	1500	335.35
Reduction reactor's shell	1st reduction	73.3	52.6
	6th reduction	208.6	72.6
	1st oxidation	335.6	74.7
	5th oxidation	389.1	84.6

O-ring temperature evolution

The O-ring, responsible for maintaining the pressure separation between the reduction and oxidation reactors during the cooling and oxidation steps, undergoes moderate temperature variations within each fuel production cycle. The O-ring experiences its peak instantaneous temperatures during the transport step when the hot RMA is moved to the oxidation reactor at the start of each cycle (Figure 4.6). The second transport stage, when the RMA is moved from the oxidation to the reduction reactor also shows a relevant increase in temperature of the O-ring, but is not as large as in the initial transport phase, given that the RMA has a lower temperature after oxidation and therefore the radiative heat transfer is not as pronounced. Over the course of the five simulated cycles, a progressive increase in the O-ring's maximum temperature is observed, attributed not only to the radiative heat exchange with the RMA but also to the gradual warming of surrounding components. Peak instantaneous temperatures during the initial transport step are in the range of 249 °C to 356°C from the first to the last cycle (Figure 4.6 (b)).

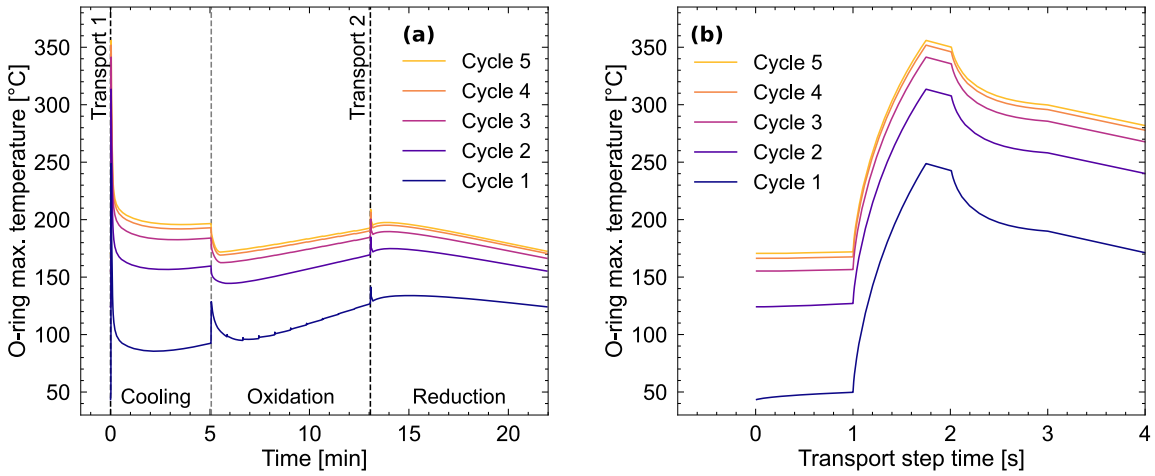

Figure 4.6: Maximum temperature of the O-ring during (a) the entire fuel production cycle and (b) the first transport step.

To investigate the O-ring's temperature distribution at peak temperature conditions, Figure 4.7 displays its cross-sectional temperature profile during the first transport stage of the first and fifth cycles, providing a detailed comparison of the temperature variations within the seal. Across the cycles, the general pattern of the temperature distribution remains consistent, with high temperatures concentrated near the lower half external surfaces of the O-ring, while the bulk of the material remains comparatively cool. As previously discussed, the overall O-ring temperatures in the fifth cycle are higher than in the first cycle, reflecting cumulative thermal effects. In both cycles, steep temperature gradients are observed from the highest temperatures located in the left lower corner of the seal to the inner material bulk temperature, likely as a result of the rubber's low thermal conductivity and short transport time (4 s) during which peak temperatures occur. The highest temperature area occurs where the proximity to the RMA is the closest and radiative heat

exchange is the most significant throughout the entire cycle (first transport step). The lower external regions of the seal exhibit moderate temperatures as a result of radiative heat exchange with the hot RMA, with the right regions of the seal displaying lower temperatures. The upper O-ring area, as well as the material bulk, remain at the lowest temperatures (~42 °C in the first cycle and ~175 °C in the fifth cycle), since both of these areas are shielded from direct radiative heat exchange and are in direct contact with the "cooler" stainless-steel gate casing.

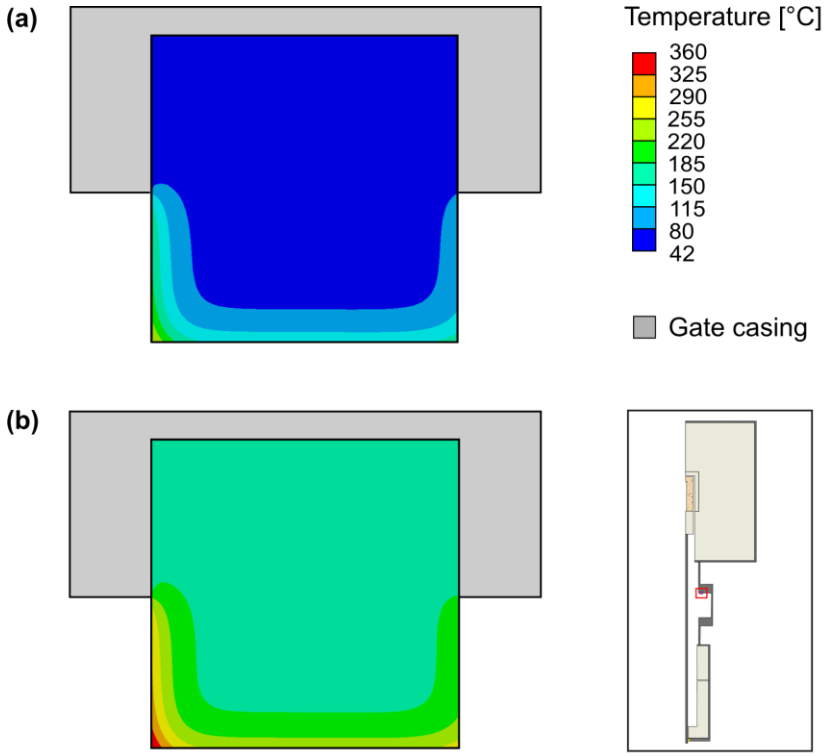

Figure 4.7: O-ring cross-sectional temperature profiles at the time when the peak temperature was evidenced for: (a) 1st cycle, (b) 5th cycle.

As reviewed, the maximum temperatures of the O-ring during the transport step are confined to a small area, leading to a significantly lower seal volume average temperatures (Figure 4.8). Except for the first cycle, the O-ring's average temperature remains almost constant during the cooling step, increases after the oxidation step, and decreases slightly after the reduction step. During oxidation, the O-ring's average temperature initially decreases and then as the oxidation reaction progresses, the O-ring heats up. This phenomenon is observed as from the second cycle onwards, the O-ring has a higher average temperature than the injected steam (150 °C). In the first cycle the O-ring experiences a large average temperature increase of about 80 °C, but as the operation progresses the average temperature does not exhibit large variations anymore. During the fifth cycle, the average temperature remains between 169 °C and 193 °C throughout the cycle.

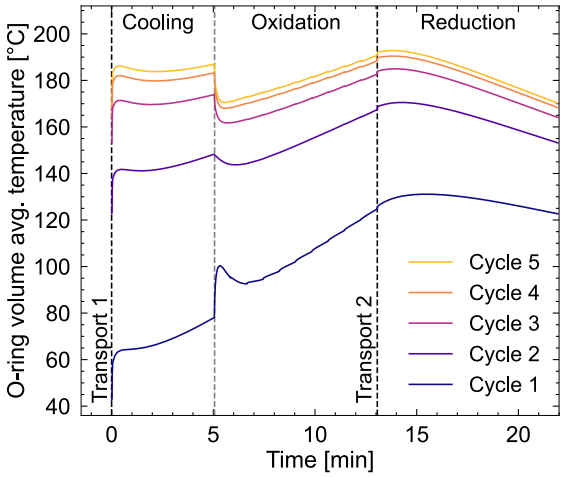

Figure 4.8: Volume average temperature of the O-ring during the entire fuel production cycle.

As reviewed, the maximum temperature of the O-ring tends to converge as the number of cycles increases, reflecting the fact that the oxidation reactor components are approaching steady-state temperatures (Figure 4.6). An estimate of the O-ring's maximum operating temperature was obtained by extrapolating the simulated maximum temperatures from five cycles to larger cycle numbers using an exponential fit (Figure 4.9). This approach was chosen to avoid the high computational and time cost associated with simulating more cycles. The exponential fit, based on five data points, exhibits a coefficient of determination, R^2, of 0.999, indicating a good correlation. The extrapolated results suggest that the O-ring's maximum temperature stabilises at approximately 360 °C after around 7 cycles. This temperature is relatively high for elastomeric O-rings, whose maximum recommended operating limits are approximately 325 °C for FFKM materials and 200 °C for the simulated FKM material.

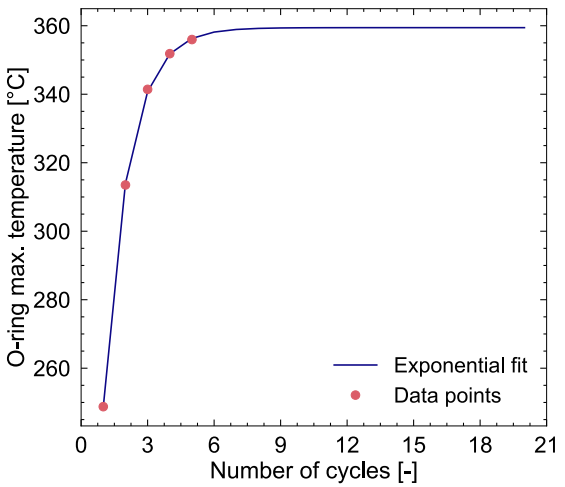

Figure 4.9: Fitting of the maximum temperature of the O-ring during the transport step with increasing number of cycles.

To mitigate excessive O-ring heating, several design modifications could be explored. One option is to increase the diameter of the gate valve, positioning the O-ring further from the hot RPC, thereby reducing radiative heat transfer. Alternatively, a different gate configuration, such as the previously introduced sliding plate gate, could offer improved thermal shielding by physically isolating the O-ring from direct radiative heat exchange. Increasing the RMA transport velocity may also lower the O-ring's peak temperature by reducing exposure time; however, care must be taken to ensure the mechanical stability of the RMA during movement. Lastly, incorporating active cooling within the gate presents a viable strategy for maintaining the O-ring temperatures within acceptable limits.

Rod seal temperature evolution

Figure 4.10 shows the maximum seal temperature as function of time for the five examined hydrogen production cycles. Similarly to the O-ring, the rod seal reaches its peak temperatures during the transport step, specifically at the end, when the hot transport rod comes into direct contact with the seal. During the cooling and oxidation steps the peak temperature of the rod seal decreases, and a second peak is observed during the second transport phase. The second peak arises from the hot transport rod coming into contact with the seal, however the second peak is lower than the first temperature peak, since during cooling and oxidation the transport rod was outside the reactor and had opportunity to cool down. Across the cycles, a temperature increase during all steps is observed. This temperature increase is attributed to both, a more homogenous heating of the transport rod due to heating through radiation of the insulation in the oxidation reactor, and the shell and components of the oxidation reactor becoming hotter. The rod seal's peak instantaneous temperatures increase from 146 °C in the first cycle to 203 °C in the fifth cycle.

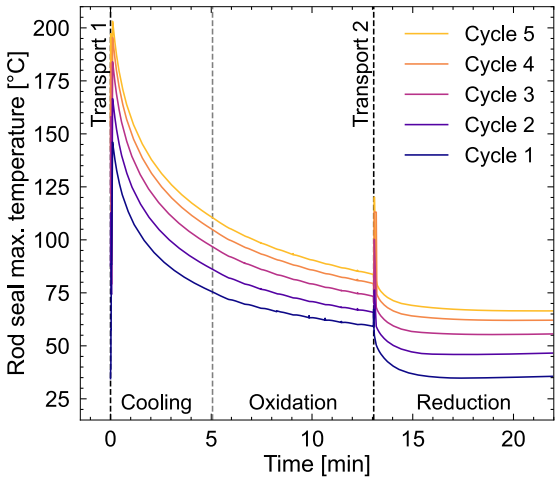

Figure 4.10: Maximum temperature of the rod seal during the entire fuel production cycle.

To analyse the temperature distribution of the rod seal at peak temperature conditions (at the end of the first transport step), Figure 4.11 presents cross-sectional temperature profiles in the first and fifth cycle. In both cases, a pronounced temperature gradient is observed across the seal, with elevated temperatures concentrated along the left-hand side in close proximity to the hot transport rod. As previously discussed, in the first cycle, the maximum temperature remains relatively low (146 °C), with the majority of the seal volume exhibiting temperatures below 100 °C. The thermal gradient indicates limited heat accumulation and lower overall thermal exposure during the early stages of operation. By the fifth cycle, however, a significant increase in thermal load is evident. The peak temperature rises notably (203 °C) and a larger portion of the seal is exposed to high temperatures, exceeding 200 °C in the hottest region near the rod interface. This progression highlights the cumulative nature of thermal loading over repeated cycles, which leads to heat build-up in the seal material due to limited time for cooling between cycles and the inherently low thermal conductivity of PTFE. In both examined cases, the outermost part of the seal remains significantly cooler, aligning with the oxidation reactor's steel shell temperature in that area.

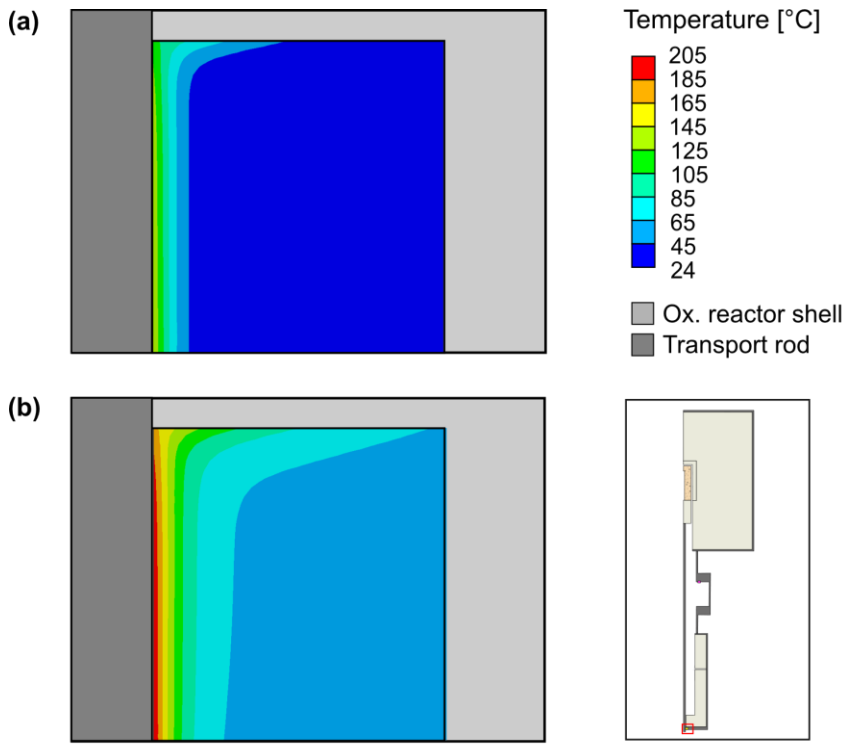

Figure 4.11: Rod seal cross-sectional temperature profiles at the time when the peak temperature was evidenced for: (a) 1st cycle, (b) 5th cycle.

The rod seal's volume average temperature was calculated across the cycles (Figure 4.12). Notably, the highest rod seal average temperature occurs during the cooling step, approximately

after 1.5 min, reaching a maximum of 100 °C in the fifth cycle. Subsequently, the average temperature of the rod seal decreases, initially slowly during the cooling and oxidation steps, before a more pronounced cooling rate is observed during the reduction step, when lower temperatures prevail. As observed for the O-ring, the rod seal's average temperature increases as the cycles progress, with the fifth cycle exhibiting the highest simulated average temperatures between 70 °C and 100 °C.

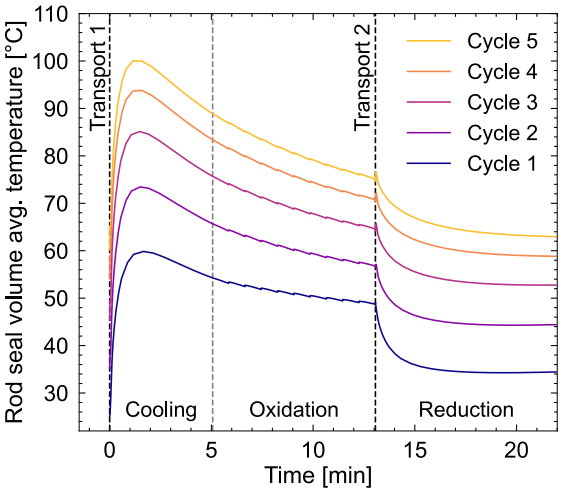

Figure 4.12: Volume average temperature of the rod seal during the entire fuel production cycle.

The maximum operating temperature of the rod seal was estimated by extrapolating the maximum temperatures obtained in the simulated five consecutive cycles to higher cycle iterations, representing conditions where both the reduction and oxidation reactors are expected to have reached quasi steady-state thermal operation. The developed exponential fit with an R^2 value of 0.983 is shown in Figure 4.13. Findings suggest that the rod seal's maximum temperature will converge to approximately 226 °C after around 18 operation cycles. This predicted maximum instantaneous temperature remains within the operating limits of PTFE seals. It should be noted that the current simulation does not account for frictional heating generated during rod movement. However, given the short duration of the transport step and the fact that the rod remains stationary for most of the cycle, this contribution is expected to be negligible.

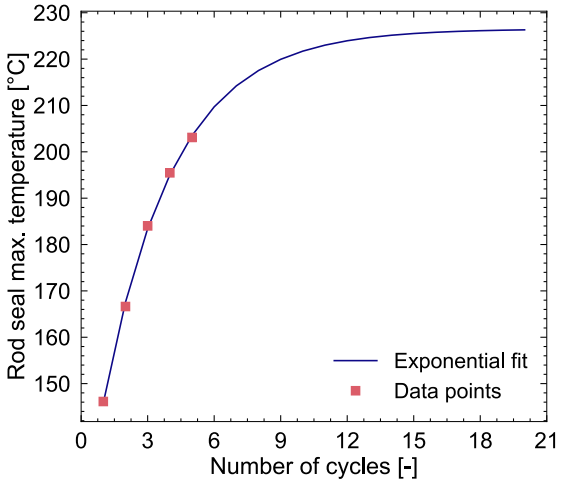

Figure 4.13: Fitting of the maximum temperature of the rod seal during the transport step with increasing number of cycles.

For the next stage of R2Mx technology development, design optimisations could aim to reduce the thermal mass cycled between the reactors. For instance, shortening the connector length could minimise sensible heat losses to passive components such as insulation, thereby improving overall thermal efficiency and making more energy available for the water-splitting reaction. However, such modifications are likely to increase the operating temperature of the transport rod, which would elevate the thermal load on the rod seal. This underscores the need for a more detailed evaluation of the seal's performance and long-term stability under elevated temperatures to ensure reliable operation in an optimised configuration. Moreover, in a scaled-up system, the present analysis estimating the operating conditions of the seals must be revisited. Increased ceria loading and a larger RMA will significantly affect the thermal exposure of the O-ring. Key parameters, such as RMA size, cycle time, and transport velocity, are expected to vary in a MW-scale R2Mx reactor, potentially altering the thermal loads on all sealing components. Nevertheless, the present study offers a valuable first-order estimate of expected temperatures and serves as a foundation for future design iterations.

4.4. Summary

In this chapter the design of a R2Mx prototype for solar thermochemical hydrogen production was presented and its thermal behaviour during continuous operation was analysed. A novel modelling workflow was developed in ANSYS Mechanical to efficiently couple a transient heat transfer analysis with the cyclic movement of the RMA during operation. The 2D axisymmetric transient model was employed to gain a deeper understanding of the system's thermal response during operation and to derive a first approximation of the seals' expected operating conditions.

Five consecutive fuel production cycles were simulated and material selection in the prototype reactor was assessed based on the resulting temperature profiles. For all simulated reactor parts, the initial material selection was confirmed to be appropriate. In particular, the insulation material in the oxidation reactor could be replaced with a lower classification temperature material, enabling a less conservative and more cost-effective design.

For both the O-ring and the rod seal, operating temperatures were found to increase progressively with the number of cycles, reflecting the thermal stabilisation of the system. Average operating temperatures during the fifth simulated cycle are about 200 °C for the O-ring and 100 °C for the rod seal. Furthermore, results showed that the maximum instantaneous temperature in the O-ring occurs at the lower corner of the seal, near the hot RPC, with a steep internal temperature gradient driven by the low thermal conductivity of the elastomer. For the rod seal, the highest instantaneous temperature occurs at the interface with the hot transport rod, particularly at the end of the transport step. The O-ring's maximum temperature was estimated to converge at approximately 360 °C after seven cycles, while the rod seal's maximum temperature was projected to reach 226 °C after about 18 cycles. These temperatures are relatively high for polymer-based seals, highlighting the need for further investigation into the long-term thermal stability and degradation behaviour of candidate sealing materials under these conditions.

5. O-ring degradation and lifetime prediction*

Achieving high performance in solar thermochemical reactors like the R2Mx extends beyond optimising redox material behaviour and energy conversion efficiency; it also demands operational reliability and long-term durability. A solar reactor that fails unpredictably due to the degradation of auxiliary components cannot be considered viable for continuous fuel production, therefore ensuring the robustness of critical subsystems is essential. Among these, gate's elastomeric O-ring plays a critical role in separating the reaction atmospheres and preventing product fuel loss under cyclic thermally demanding conditions. The thermal simulations presented in the previous chapter showed that the O-ring is subjected to significant thermal loads, with peak instantaneous temperatures reaching up to 360 °C and volume-average values around 200 °C during operation. These values exceed conventional thermal limits of elastomers and thus raise concerns regarding the long-term durability and reliability of these seals in solar reactor applications.

In response to this challenge, two high-temperature resistance elastomers, fluoroelastomer (FKM) and perfluoroelastomer (FFKM), were selected for further study. Both elastomers are known for their exceptional thermal and chemical resistance and are commonly employed in high-temperature sealing applications. However, the existing literature provides limited insight into their

---

* **This chapter is partially derived from the following peer-reviewed publications authored by the author of this work:**

Vega Puga, E., Brendelberger, S., Pierno, F., Wischek, J., and Sattler, C., "Sealability analysis of aged elastomer O-rings for usage in solar thermochemical water-splitting reactors." Key Engineering Materials Vol. 1007 (2025): pp. 37–48. https://doi.org/10.4028/p-p5fm2q.

Vega Puga, E., Wachtendorf, V., Kömmling, A., Brendelberger, S., Jaunich, M., and Sattler, C., "Lifetime prediction and degradation assessment of FKM and FFKM O-rings under high temperature thermo-oxidative ageing." Polymer Testing Vol. 147 (2025): pp. 1–17. https://doi.org/10.1016/j.polymertesting.2025.108820.

degradation behaviour and lifetime performance under thermo-oxidative ageing at high temperatures, particularly in the 200–300 °C range relevant to the R2Mx reactor. The degradation of elastomeric materials under such conditions can significantly alter their chemical structure and mechanical properties, potentially resulting in leakage and premature system failure. A systematic assessment of these effects is therefore essential for estimating seal durability and establishing realistic maintenance schedules that align with reactor availability and operational demands.

This chapter aims to characterise the degradation mechanisms and to predict the operational lifetime of FKM and FFKM O-ring exposed to high-temperature thermo-oxidative ageing. Building upon the temperature profiles derived in the previous chapter, this investigation focuses on experimentally relevant conditions that reflect the R2Mx reactor's expected operational conditions. Accelerated ageing studies were conducted on both O-ring seals and flat sheet specimens at defined temperature intervals (200–250 °C for FKM and 250–300 °C for FFKM). The chemical evolution of the materials was characterised using ATR-IR microscopy, while changes in weight, hardness, compression set (CS), and leakage rate were evaluated over ageing durations of up to 21 days. In addition, long-term compressive stress relaxation (CSR) was assessed through continuous testing at 200 °C over a five-month period.

A critical outcome of this work is the establishment of an end-of-life criterion based on the correlation between CS and a predefined leakage rate threshold, enabling a more direct and application-relevant definition of seal failure. This metric was subsequently used to derive lifetime predictions via time-temperature superposition (TTS), providing first-order estimates of service lifetimes under various operating temperatures. Through this integrated approach, the chapter contributes a practical and data-driven assessment of sealing performance at high temperatures, bridging a gap in current literature and supporting the design of more reliable pressure sealing systems for solar receiver-reactor systems.

5.1. Materials and methods

5.1.1. Materials

In the present study, two commercially available elastomer grades were evaluated: an FKM with bisphenol curing marketed as Vi655 [287] and a peroxide-cured FFKM marketed as Perlast G75B [300], both supplied by C. Otto Gehrckens GmbH & Co. (Pinneberg, Germany). A summary of the manufacturer-provided material properties for both elastomers is presented in Table 5.1.

Table 5.1: Manufacturer's data for tested FKM and FFKM elastomers [287,300].

Material	Operating temperature range [°C]+	Hardness [Shore A]		Curing system	Colour
FKM	-15 – 200	75 ± 5	DIN ISO 48	Bisphenol	Blue
FFKM	-15 – 325	76	ASTM D2240	Peroxide	Black

+ in air atmosphere

While the precise compositions of these proprietary materials remain undisclosed, general formulation characteristics can be inferred. The studied FKM belongs to Type 1 fluoroelastomers, and is a copolymer of vinylidene fluoride (VDF) and hexafluoropropylene (HFP), with a fluorine content of about 66% [139]. This FKM is characterised by a distinctive blue appearance, possibly achieved through the addition of inorganic pigments such as Stan-Tone D-4005, D-4006, and Cromophtal Blue 4GNP, stabilised with titanium dioxide (TiO_2) [152]. Given the blue appearance of the material, the absence of carbon black as a filler can be assumed. Conversely, the FFKM examined in this work is composed of tetrafluoroethylene (TFE), perfluoromethyl vinyl ether (PMVE), and a cure site monomer, with a fluorine content exceeding 71% [149]. Given its black coloration, the inclusion of carbon black as a filler is likely. Further details on general fluoroelastomers compounding can be found Chap. 3.2.3. The following Figure 5.1 depicts the schematic chemical structures of the studied FKM and FFKM elastomers.

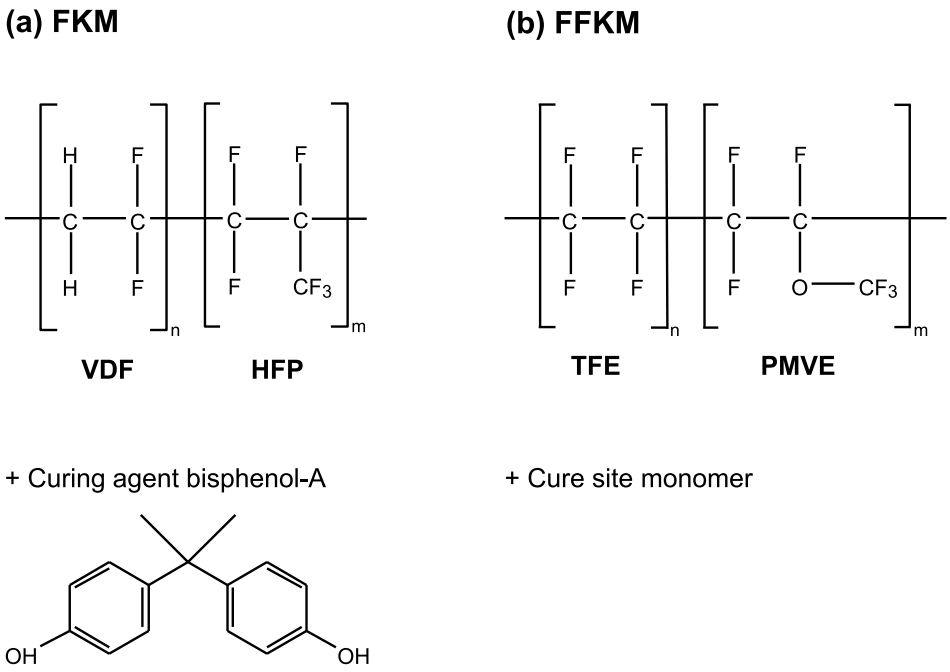

Figure 5.1: Schematic chemical structure of monomers of tested (a) FKM and (b) FFKM. Adapted from Vega Puga et al. [301] with the permission of Elsevier Science & Technology Journals.

For each elastomer type, both O-rings and 2-mm thick sheets were exposed to thermo-oxidative ageing in air. The 2-mm sheets were aged due to their suitability for hardness testing, offering a more homogenous surface compared to O-rings. The studied O-rings have a cross-sectional diameter of 3 mm and an outer diameter of 96 mm. This particular O-ring geometry was selected with regard to their intended usage in the gate of the R2Mx reactor. Additionally, the relatively small cross-sectional area of the O-rings was chosen to promote uniform oxidative ageing under elevated temperatures, ensuring sufficient oxygen penetration throughout the material bulk and minimising the risk of diffusion-limited oxidation (DLO) effects. The maximum sample thickness to ensure that oxidation is uniformly distributed across the sample, L_{90}, was calculated to be 7.8 mm for FKM at 200 °C. L_{90} represents the thickness at which 90% of the bulk oxidation corresponds to the surface oxidation and it was estimated using the following equation:

$$L_{90} = \left[\frac{K\ p\ P_{O_2}}{\varphi_{O_2}}\right]^{0.5} \tag{5.1}$$

where, p represents the partial pressure of oxygen surrounding the specimen, P_{O_2} is the material's oxygen permeability ($8 \cdot 10^{-7}$ ccsTP·cm^{-1}·s^{-1}·cmHg^{-1}), φ_{O_2} is the oxygen consumption rate ($1 \cdot 10^{-9}$ mol·g^{-1}·s^{-1}), and K is a rate constant valued at 2 for ageing of elastomers in air [182,302,303]. Since both the O-ring cross-sectional diameter (3 mm) and the sheet thickness (2 mm) are significantly below the estimated L_{90} value, all samples in this study were assumed to undergo ageing without significant DLO effects. Nevertheless, it is important to acknowledge that the parameters used for the estimation of L_{90} were sourced from literature and are based on a generic Type 1 FKM [182,302–304], and the specific characteristics of the materials under investigation may vary due to formulation differences.

5.1.2. Accelerated ageing protocol

The FKM and FFKM samples were thermally aged in an oven with a controlled air flow, in line with the DIN ISO 188 standard [305], which provides guidelines for accelerated ageing of rubber materials in air. Ageing of the O-rings was conducted in air, as it offers a practical and controlled environment while still capturing the dominant thermo-oxidative degradation mechanisms relevant to high-temperature operation. Although the R2Mx reactor will also expose seals to steam and hydrogen during real-world use, the influence of these environments warrants dedicated future investigation beyond the current scope. FKM samples were exposed to temperatures of 200 °C, 225 °C, and 250 °C, while FFKM samples were subjected to 250 °C, 275 °C, and 300 °C. These temperatures were selected to represent the upper operational limits of the materials, with particular attention given to exploring their sealing capabilities and durability under harsh thermal environments. Maximising the permissible operating temperature of the sealing materials is

beneficial for reducing the complexity of the pressure system design within the R2Mx reactor. At each temperature level, three O-rings, three sheets, and three O-ring segments of each elastomer type were aged to ensure reproducibility of the results. Exposure times were set at 1, 2, 4, 8, and 14 days. Additionally, the FKM O-rings aged at 225 °C underwent extended ageing for 21 days to provide enhanced data density for service lifetime prediction estimations.

The O-rings were aged in compression using compression set (CS) fixtures designed to apply a 25% squeeze degree (SD) (Eq. (3.3)), aligning with the expected in-service deformation. This SD was applied at ambient conditions; however, it is expected that the deformation of the O-rings increases during high-temperature ageing due to the thermal expansion of the elastomeric materials. After each exposure time, the O-rings were removed from the fixtures for evaluation of CS and leakage rate. To prevent adhesion between the seals and the aluminium plates of the fixtures, a silicone oil lubricant was applied. The influence of the lubricant on CS measurements is regarded as negligible, as confirmed by existing literature [181]. Following each test cycle, the O-rings were reassembled into the fixtures and returned to the oven for continued ageing. The ageing procedure for O-rings was concluded once seal failure was observed, indicated by the inability to maintain a vacuum within the test volume.

The elastomer sheets (2 mm thickness) were aged on a perforated metal support to facilitate even circulation of hot air around the samples. After hardness measurements, the samples were returned to the oven for continued ageing until the next measurement cycle. Similarly to the elastomer sheets, the O-ring segments were aged on a perforated metal support and uncompressed. The O-ring segments were exclusively utilised for weight loss measurements, and after these were performed, the samples were returned to the oven for further ageing.

5.1.3. Analysis methods

Optical microscopy

Optical microscopy was employed to examine and document the morphological changes in the aged O-rings. This non-destructive characterisation technique enabled the assessment of changes in surface appearance, texture, and the presence of defects. A SteREO Discovery V20 light microscope (Carl Zeiss AG, Oberkochen, Germany) equipped with an LED-based reflected light source, electronic zoom control, and an AxioCam digital camera was used for this investigation.

ATR-IR microscopy

To monitor chemical modifications induced by thermal ageing, attenuated total reflectance infrared (ATR-IR) microscopy was utilised. The measurements were conducted using a LUMOS II microscope (Bruker Co., Ettlingen, Germany). Detailed measurement parameters are summarised in Table 5.2.

Table 5.2: Measurement conditions

Parameter type	Value / Note
Geometry	Attenuated total reflectance (ATR)
ATR-tip material	Germanium
No. of accumulated scans	Sample: 256, Background: 64
ATR-tip pressure setting	Medium
ATR-tip cleaning	After each measurement point for heterogeneities like visible spots and
Wavenumber range	4000–600 cm^{-1}
IR resolution	4 cm^{-1}
Detector	Mercury cadmium telluride (MCT) sensor cooled with liquid nitrogen
VIS lens magnification	x8
Sample geometry	O-ring, the measurement was realised on the crest of round-shaped
IR sample detection area	Square shaped knife-edge limited aperture, 50 µm width
Corrections used	Atmospheric correction for CO_2 bands. Simple ATR correction Baseline correction: rubber band
Normalisation	No normalisation was employed
Acquisition and data manipulation software	Bruker OPUS, version 8.7

Mass change

The mass of the O-ring segments was determined prior to ageing and following each exposure time using a Sartorius Analytic AC 210 S balance, providing a measurement accuracy of 0.1 mg. O-ring segments with an approximate initial mass of 0.6 g were employed for this analysis. Prior to weighting, all samples were subjected to a cleaning procedure in an ultrasonic bath for 7 minutes to remove any adhering dust or surface contaminants that could affect the measurement accuracy. The progression of mass loss in the O-ring segments as a result of ageing was calculated and subsequently normalised as per Eq. (5.2).

$$\mathrm{w_L} = \left(1 - \frac{m_\mathrm{f}}{m_\mathrm{i}}\right) \cdot 100\% \tag{5.2}$$

where w_L represents the percentage weight loss of the sample, m_i denotes the initial mass of the sample prior to ageing, and m_f corresponds to the mass of the sample after the specified ageing time.

Hardness

The hardness of the aged materials was assessed in accordance with DIN ISO 48-4 [306], using a Shore A durometer. The tests were performed on stacks of three 2-mm thick elastomer sheets. At each exposure time, hardness measurements were carried out at five different locations on the samples' surface. To avoid bias, different locations on the sheet surface were tested after each exposure time. The reported values represent the average of the five hardness measurements, along with the corresponding standard deviation.

Compression Set (CS)

Compression set testing provides insight into the ability of an elastomer to recover its original dimensions following prolonged deformation under a load. The CS value was calculated as per Eq. (5.3).

$$\mathrm{CS} = \frac{h_0 - h_2}{h_0 - h_1} \cdot 100\% \tag{5.3}$$

where h_0 is the original height of the O-ring, h_1 is the compressed height, and h_2 is the recovered height after release. A CS of 0% denotes complete recovery, whereas 100% corresponds to permanent deformation and loss of sealing capability.

Measurements were taken at 8 positions around each O-ring. Although the DIN ISO 815-1 standard (Method B) recommends measuring h_2 after 30 ± 3 minutes of recovery at room temperature [307], this short period may not sufficiently account for time-dependent viscoelastic relaxation phenomena, leading to potential inaccuracies. Therefore, in line with previous studies [179,181,183], equilibrium CS values were adopted in this work. To obtain these, the samples were tempered at 100 °C for 2 hours. To validate that equilibrium was achieved, a subset of samples was subjected to an additional 6-hour tempering, resulting in a negligible further change in CS (< 2%), which is minor compared to the changes observed (~ 10%) due to initial tempering and the measurement error of about ± 3%. In this work, all CS values refer to equilibrium CS unless otherwise stated.

Compression Stress Relaxation (CSR)

CSR testing was conducted to evaluate the loss of sealing force in O-rings over time under thermal and compressive stress. The experiments were carried out at 200 °C for both FKM and FFKM O-ring segments, with an approximate length of 45 mm. Three samples per material were tested over a duration of up to 5 months using EB 02 stress relaxation rigs placed within an EB 22 cell oven (Elastocon, Brämhult, Sweden). A SD of 25% was applied at room temperature, following mechanical and thermal pre-conditioning as outlined in DIN ISO 3384 [308]. The sealing force was recorded at 10-second intervals during the first hour, every minute for the next 24 hours, and subsequently every 10 minutes, without altering the applied strain. The initial force (F_0) was determined 30 minutes after the onset of compression, in accordance with DIN ISO 3384 [308].

Leakage rate determination

The sealing performance of O-rings aged under thermo-oxidative conditions was experimentally assessed as a function of exposure time. The leakage rate (q_l) was determined using the pressure rise method and calculated utilising Eq. (3.1). A test rig was specifically developed for this purpose and it is illustrated in Figure 5.2 [301,309]. The test setup comprises two vacuum chambers

connected via a spacer flange housing the O-ring within a dedicated groove and a custom gate. The custom-designed gate system, featuring two steel surfaces, a spring-loaded mechanism, and a linear actuator, is used to apply a compressive load on the O-ring. During leakage rate testing, first both chambers, A and B, are evacuated to 0.1 mbar with the vent valve V1 closed. Next, the gate (V2) is closed to a position which exerts a load of 445 N to the seal (about 10% SD). Immediately after, the upstream chamber is vented to ambient pressure by opening valve V1, generating a differential pressure across the O-ring to facilitate sealing and achieve a SD of 20–25%. The maximum attainable SD of the O-ring within the experimental setup is limited to 25%, given that the groove height is 2.25 mm. The operation of the leakage rate test rig has been designed to replicate the foreseen operation of the gate, thereby reflecting mechanical stresses the O-ring would experience in the R2Mx reactor, as described in Chap. 4.1.1. The pressure rise in the Chamber A is monitored over a 45-minute period using a precision pressure sensor (Inficon, Bad Ragaz, Switzerland), with a measurement range of 10^{-4} to 10 mbar and an accuracy of 1%. Leakage rate testing was conducted on O-rings previously subjected to equilibrium CS measurements and aged in a compressed state. Three independent measurements were performed per ageing condition, with the average leakage rate and standard deviation reported for each ageing temperature and duration.

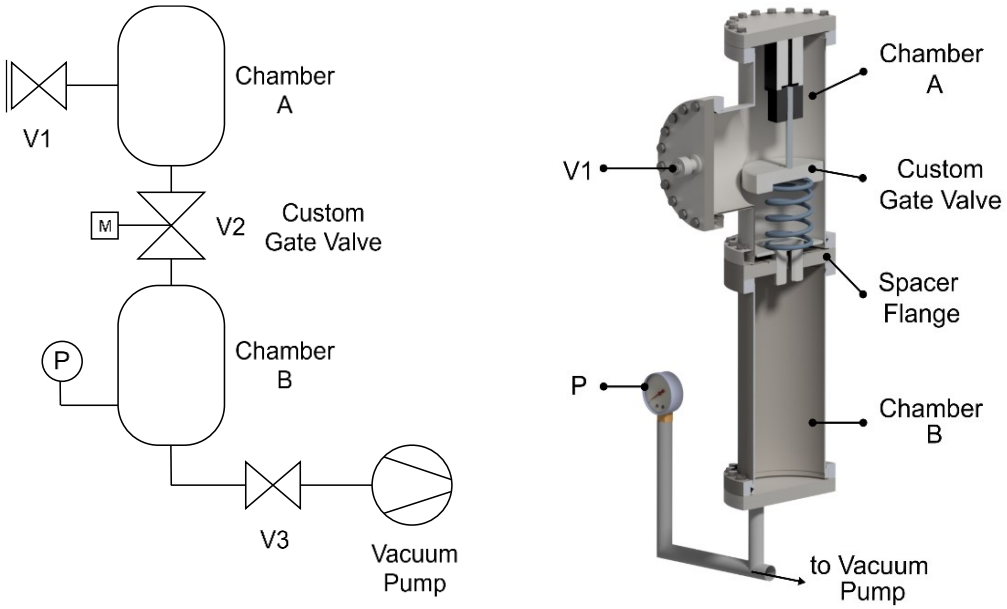

Figure 5.2: Schematic representation and computer-aided design (CAD) model of the test rig employed for leakage rate measurements. Reproduced from Vega Puga et al. [301] with permission of Elsevier Science & Technology Journals.

5.2. Results and discussion

This section presents the results of each analysis method to provide insights into the ageing behaviour and degradation mechanisms of the elastomeric O-rings. Furthermore, the lifetime

prediction of both, FKM and FFKM, O-rings at the different tested temperatures (200–300°C) is performed.

5.2.1. Optical microscopy

Microscopic imaging was employed to characterise the morphological evolution of elastomeric O-rings subjected to thermo-oxidative ageing, enabling the visual assessment of surface changes and degradation phenomena. Figure 5.3 presents a series of optical micrographs depicting both unexposed and aged FKM O-rings (exposed to the highest ageing temperature of 250 °C) for varying durations. To facilitate the observation of the most pronounced morphological changes, the highest ageing temperature has been selected.

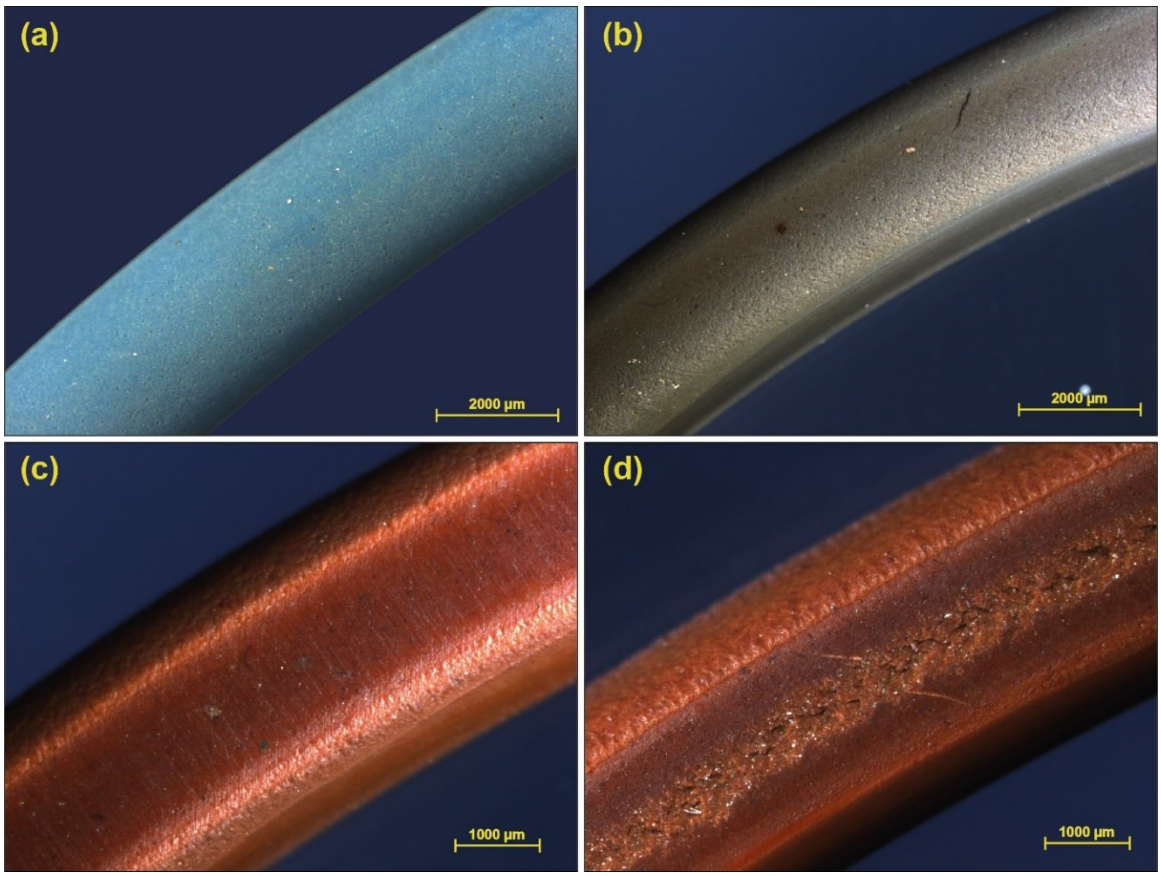

Figure 5.3: Optical micrographs of FKM O-rings exposed to different thermo-oxidative ageing conditions: (a) unexposed reference sample, (b) aged at 250 °C for 2 days, (c) aged at 250 °C for 8 days, (d) aged at 250 °C for 8 days showing evidence of crack formation. Reproduced from Vega Puga et al. [301] with permission of Elsevier Science & Technology Journals.

The unexposed FKM sample (Figure 5.3 (a)) exhibits a uniform blue appearance, a circular cross-sectional geometry, and a slightly porous surface texture. Following thermo-oxidative ageing for 2 days at 250 °C (Figure 5.3 (b)), the material undergoes a noticeable colour transition towards a grey hue, accompanied by the emergence of surface heterogeneities, such as darkened spots and lines. These heterogeneities persist throughout subsequent ageing stages. Furthermore,

compression-induced deformation is evident, with the originally circular cross-section becoming visibly flattened due to the O-ring being aged in a compressed state between the metal fixtures.

Prolonged exposure of the FKM O-rings to 250 °C for 8 days (Figure 5.3 (c) and (d)) results in further colour transition, with the samples acquiring a brownish tint. This change in colour is plausibly attributed to the degradation of the blue pigment, polymer degradation, or a combination of both. Polymer degradation may involve the formation of carbonyl functionalities, which in turn could alter the UV-VIS absorption via extended conjugated double bonds. Filler degradation is considered an unlikely contributor to the observed colour changes, given the known thermal stability of the suspected filler materials at the tested temperatures. The flattened region of the O-ring becomes increasingly pronounced with ageing, displaying parallel linear markings, likely corresponding to the surface finish of the metal fixtures, which have imparted a permanent impression on the elastomer. Additionally, the outer perimeter of the O-ring exhibits increased surface roughness and irregularities relative to the smoother sealing face. This phenomenon may arise due to compressive forces mitigating surface roughness development in the sealing face or the metal fixtures restricting the escape of degradation products, unlike in the free surfaces. Alternatively, the free surfaces may experience enhanced oxidative degradation due to greater oxygen availability, compounded by tensile stresses induced by compression deformation.

Notably, in Figure 5.3 (d) significant surface roughening in the middle of the sealing area of the O-ring is observed, suggestive of adhesive interactions between the elastomer and the metal surface. This behaviour is indicative of chain scission reactions leading to the O-ring sticking to the metal fixture. When the adhesive forces at the interface exceed the cohesive strength of the FKM, material rupture occurs upon disassembly, resulting in the observed surface roughness. Consistently, remnants of rubber material were found adhering to the metal fixtures upon removal of the aged O-rings. However, this effect was only observed at the highest ageing temperature and longest exposure time (8 days).

Considering the second examined material, FFKM, optical micrographs of unaged and thermo-oxidatively aged O-rings exposed to 300 °C for different durations are presented in Figure 5.4. The unexposed FFKM O-ring has a black coloration, a circular cross-section, and exhibits reduced surface porosity relative to its FKM counterpart. After 2 days of ageing at 300 °C under compression (Figure 5.4 (b)), the FFKM O-ring shows a flattened cross-section framed by raised material lines. These lines form at the interface between the elastomer, ambient air, and the metal fixture. After 8 days of ageing at 300 °C (Figure 5.4 (c) and (d)), the flattened O-ring region enlarges, reflecting increased deformation and a corresponding loss of elastic recovery capacity. Similar to the FKM samples, parallel lines attributed to the metal surface finish are apparent on the

compressed region. Moreover, the edges of the sealing surface develop pronounced, irregular bulges of material.

Figure 5.4 (d) displays a severely degraded FFKM O-ring exhibiting pronounced surface distortion and material damage after 8 days of ageing. A crack is observed, accompanied by localised diameter expansion, indicative of material softening due to polymer chain scission. The presence of further parallel lines within this region underscores the substantial change in the O-ring's geometry. Adjacent to the crack, within the inner diameter region, a distinct line composed of raised material bulges is apparent, further corroborating significant material softening. Additionally, a small brownish spot is observed, likely corresponding to metallic contamination resulting from the detachment of galvanised material from bolts in contact with this particular O-ring during testing.

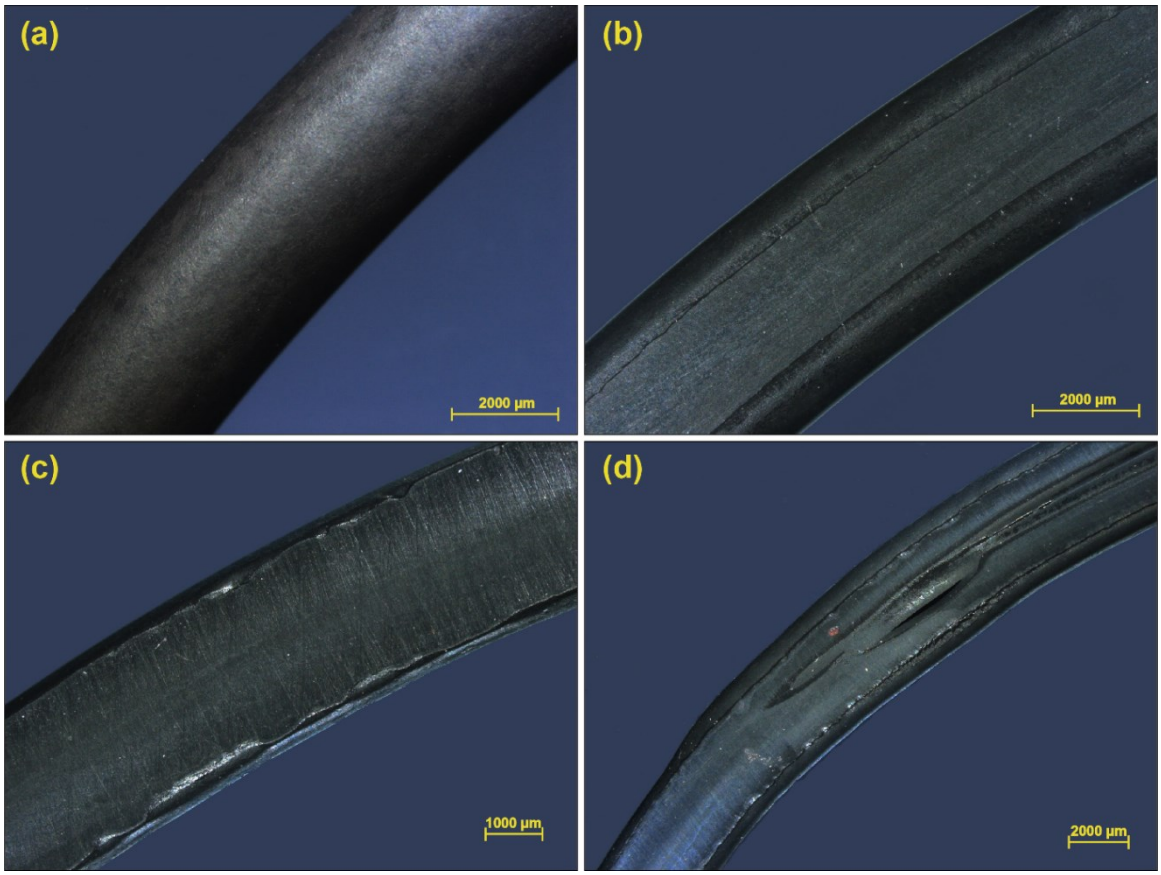

Figure 5.4: Optical micrographs of FFKM O-rings subjected to varying thermo-oxidative ageing conditions: (a) unexposed reference sample, (b) aged at 300 °C for 2 days, (c) aged at 300 °C for 8 days, (d) aged at 300 °C for 8 days exhibiting pronounced deformation and crack formation. Reproduced from Vega Puga et al. [301] with permission of Elsevier Science & Technology Journals.

5.2.2. ATR-IR microscopy

The chemical structure evolution of the FKM elastomer subjected to ageing at several temperatures and durations was examined using ATR-IR microscopy. Based on the obtained data,

a proposed reaction scheme illustrating the plausible degradation mechanisms of FKM under thermo-oxidative conditions is presented in Figure 5.5.

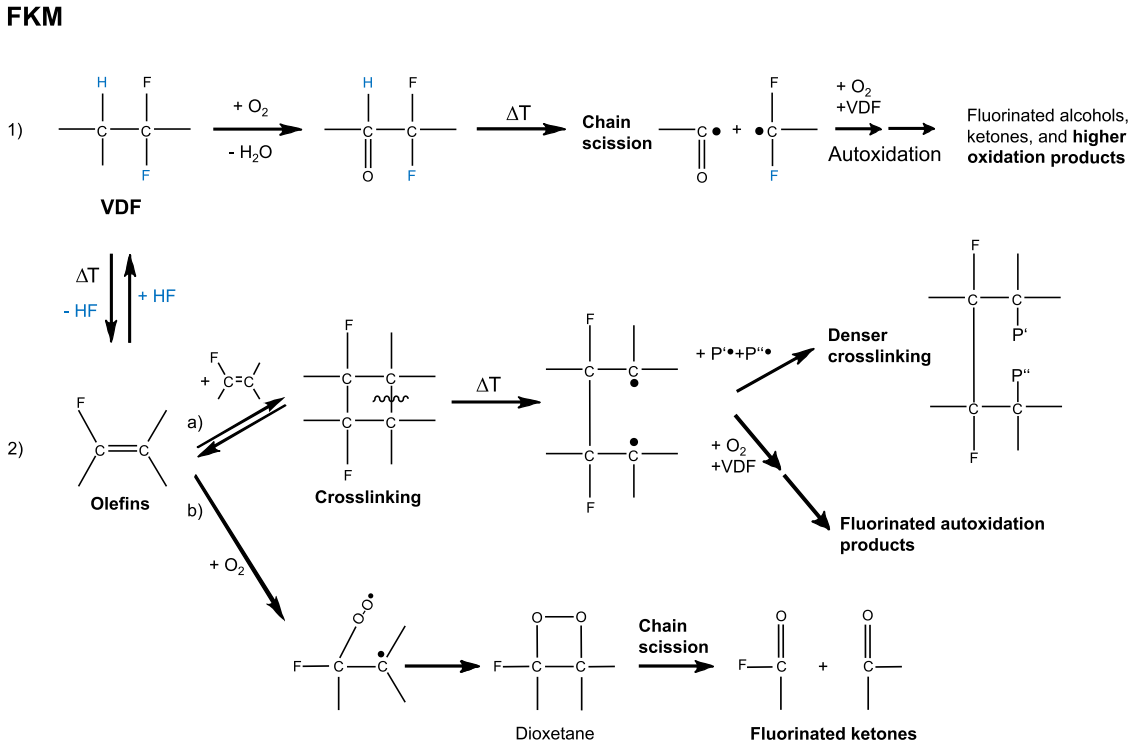

Figure 5.5: Proposed reaction scheme for the thermo-oxidative degradation of FKM. 1) Elimination of hydrogen fluoride (HF) from the vinylidene fluoride (VDF) segments results in the reversible formation of fluorinated olefins. Alternatively, autoxidation of the VDF monomer leads to oxidised products. 2) The fluorinated olefins may react either with themselves reversibly leading to crosslinking, or react with molecular oxygen to form dioxetane. The scission of dioxetane yields fluorinated ketones and chain scission. Reproduced from Vega Puga et al. [301] with permission of Elsevier Science & Technology Journals.

ATR-IR measurements of unexposed and thermo-oxidatively aged O-rings are shown in Figure 5.6. The wavenumber assignments used in this analysis are consistent with those reported in literature [168,175,310,311]. However, in contrast to previous studies, no spectral normalisation procedure was applied in the present work. This decision was based on the absence of an invariant species, unaffected by thermal exposure, which could be used reliably for normalisation. Furthermore, the absorbance values obtained across multiple measurements demonstrated excellent reproducibility and remained within a narrow margin of error, thereby mitigating the need for further normalisation associated with sample-to-tip contact variability.

As shown in Figure 5.6 (a), thermo-oxidative ageing of FKM induced pronounced changes in the absorption bands around 1085 cm^{-1}, attributed to the vibrational modes of CF_2 groups. For the unexposed FKM specimen, this band initially appears as a shoulder; however, after ageing at 200 °C for 14 days, the absorbance rises to a distinct peak, remaining stable for the sample aged at

225 °C for 14 days. Notably, at the highest ageing condition (250 °C for 8 days), the intensity of the 1085 cm^{-1} band decreases below that of the unexposed material. In contrast, the absorbance bands associated with CF vibrations at 1394 cm^{-1} and CF_3 groups at 882 cm^{-1} remained relatively unchanged throughout all thermo-oxidative ageing conditions.

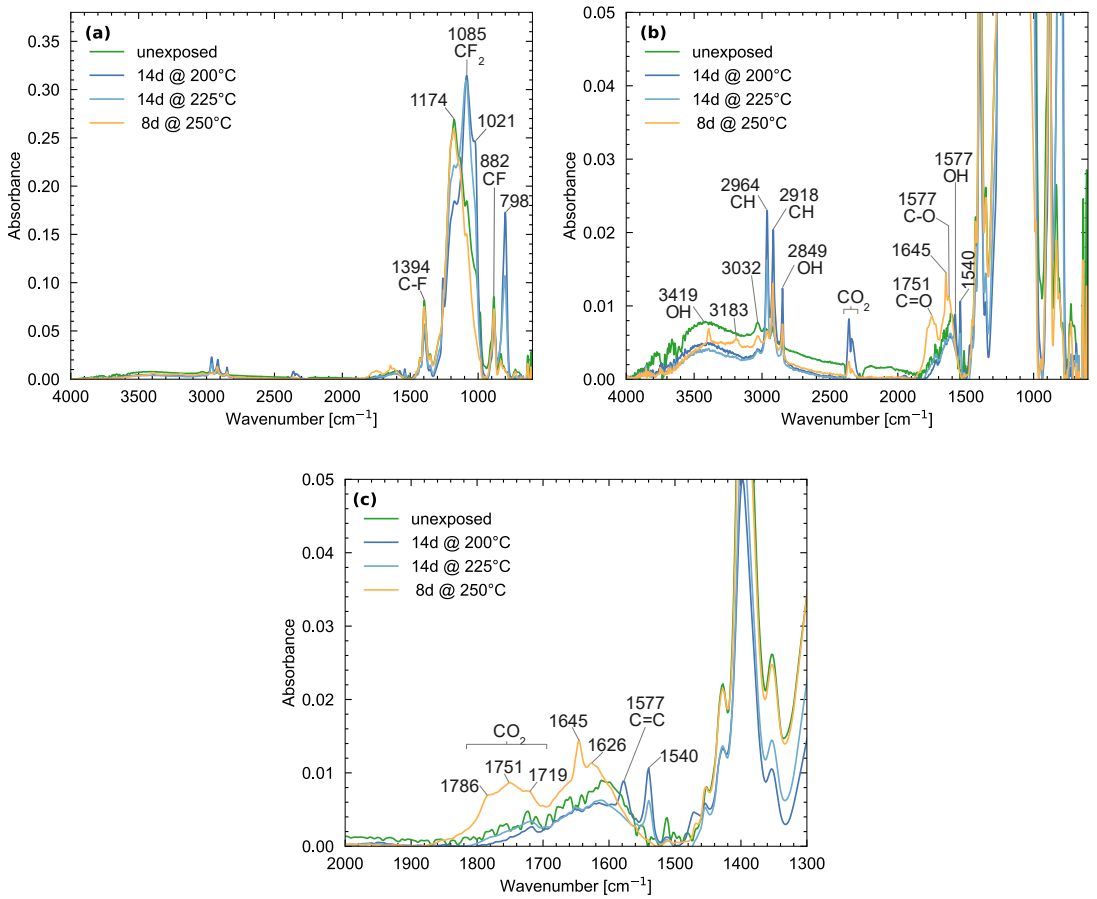

Figure 5.6: ATR-IR spectra of aged FKM at varying ageing temperature and duration, (a) spectral region from 4000 cm^{-1} to 600 cm^{-1}, (b) magnified view of the absorbance axis, (c) spectral region from 2000 cm^{-1} to 1300 cm^{-1}. Reproduced from Vega Puga et al. [301] with permission of Elsevier Science & Technology Journals.

These observations are in agreement with previous research [168,175,310] on the degradation mechanisms of fluorinated elastomers, where thermally activated elimination of hydrofluoric acid (HF) from the $–CF_2$ group occurs. This reaction pathway results in the formation of a C=C double bond, the development of which is further evidenced in Figure 5.6 (c). Specifically, a new absorption band emerges at 1577 cm^{-1}, assigned to the absorption of C=C double bonds. This band is absent in the unexposed material but becomes visible and reaches a peak following ageing at 200 °C, subsequently diminishing at higher temperatures (225 °C and 250 °C). This trend suggests that once formed, the C=C double bonds are prone to further reaction, particularly oxidation in the presence of oxygen.

The subsequent oxidation of C=C double bonds leads to the formation of carbonyl-containing species, including ketones, aldehydes, acids, and esters. This is evidenced by the emergence of new absorbance features in the 1700–1850 cm^{-1} region, as depicted in Figure 5.6 (b). The absorbance of these carbonyl-associated bands, located at approximately 1719 cm^{-1}, 1751 cm^{-1}, and 1786 cm^{-1}, is the most pronounced in the sample exposed to 250 °C. In contrast, only a weak baseline absorbance is observed for the unexposed sample, likely attributable to the material's prior thermal processing history. The formation of carbonyl groups through oxidative degradation is associated with chain scission and backbone cleavage within the elastomer network. These processes are expected to contribute directly to the deterioration of mechanical strength [176].

The evolution of the C=C double bond absorption band at 1577 cm^{-1}, relative to the unexposed reference material, initially increases, reaching a maximum upon ageing at 200 °C, before subsequently declining at higher ageing temperatures. This behaviour can be explained by considering the competing reaction pathways involving C=C double bonds during thermo-oxidative ageing. Specifically, while double bonds are formed as a result of HF elimination from the polymer backbone, they are simultaneously susceptible to consumption via oxidative degradation or through the formation of new C–C crosslinks. The relative predominance of these mechanisms is highly dependent on temperature. In addition to oxidation, C=C double bonds may undergo crosslinking reactions, particularly through the recombination of two unsaturated sites. However, the detection of such crosslinking events by IR microscopy is inherently challenging, as these processes rarely result in the appearance of new absorption bands but rather manifest as subtle changes in existing spectral features. It is also plausible that during the initial stages of thermal exposure, post-curing reactions may occur, further contributing to the chemical evolution of the material.

The quantitative development of key functional groups, namely carbonyl species, C=C double bonds, and CF_2 groups, was assessed through peak area analysis. This analysis provides a measure proportional to the concentration of the respective group, with results shown in Figure 5.7. The methodology applied for baseline correction and integration of peak areas is illustrated in Figure 5.7 (d).

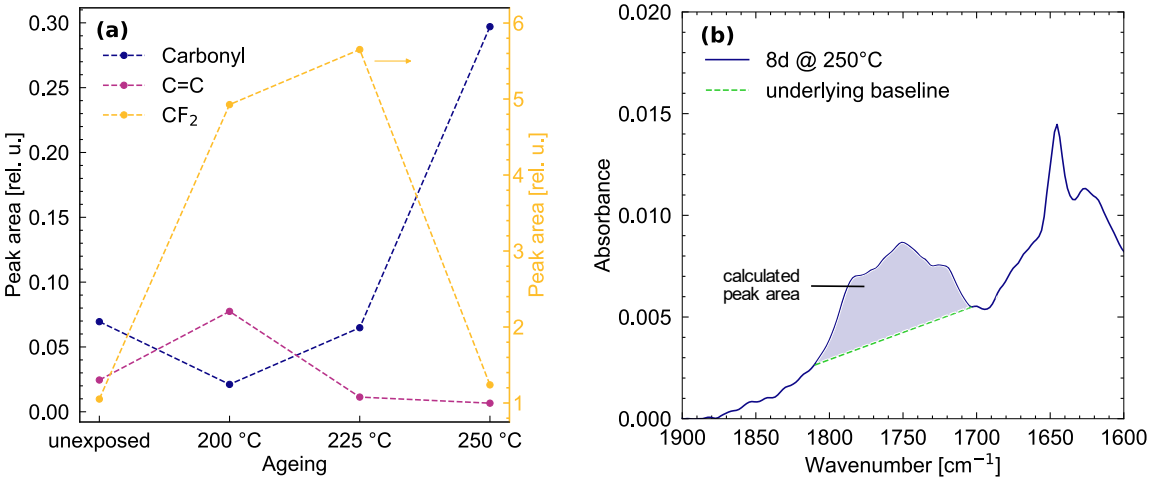

Figure 5.7: Evolution of the peak area in FKM elastomer as a function of thermo-oxidative ageing, with baseline correction applied: (a) carbonyl within 1703–1810 cm^{-1}, C=C double bond within 1562–1600 cm^{-1}, and CF_2 groups within 1040–1150 cm^{-1}. (b) Schematic illustration of peak area determination method, for carbonyl functionalities between 1703–1810 cm^{-1} of the FKM sample aged at 250 °C for 8 days.

Beyond monitoring bulk chemical changes in the FKM surface, an investigation of the heterogeneities such as dark spots and lines that emerged on the surface of aged samples was also undertaken. Representative images of such features, observed after ageing at 250 °C for 8 days, are shown in Figure 5.8. Comparison of the ATR-IR spectra of heterogeneities and the adjacent uniform brownish polymer region was performed without applying spectral normalisation. This approach was necessary due to the absence of a suitable invariant band across all the analysed regions. Consequently, comparisons were made using absolute absorbance values.

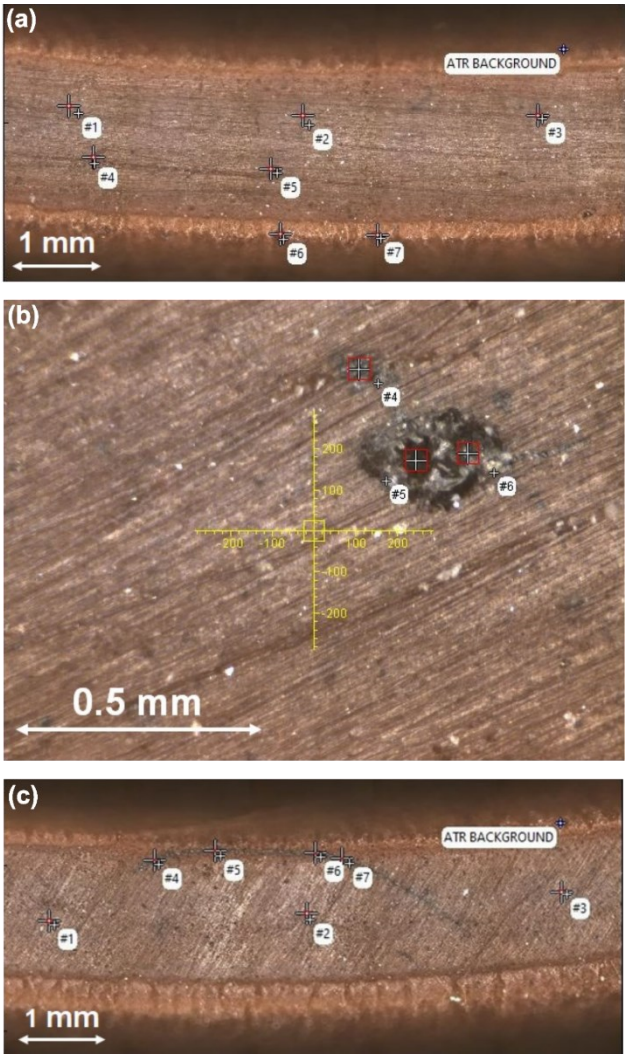

Figure 5.8: Micrographs and ATR-IR measurement positions of the three investigated heterogeneities: (a) line, (b) spot 1 with micrometre scale as yellow cross, and (c) spot 2.

Figure 5.9 presents selected wavenumber regions to highlight the spectral differences between the unexposed reference sample and the heterogeneities observed in the 250 °C aged specimen. Spot 1 exhibits spectral characteristics largely consistent with its surrounding uniform brownish background. The dark line also shares similarities with the homogenous background with the difference being a lower intensity of CF_x-associated bands and higher concentration of carbonyl species. These dark line's characteristics are indicative of more advanced thermo-oxidative degradation. In contrast, Spot 2 displays markedly different spectral features across all wavenumber regions examined. Notably, the spectra of Spot 2 did not exhibit typical markers of thermo-oxidative degradation products but rather suggests the presence of an entirely different sample. A spectral library search identified this substance as poly(dimethylsiloxane) (PDMS) rubber with high certainty [312]. PDMS is commonly employed as a lubricant during rubber processing and could be linked to the production history of the FKM sample. The characteristic Si-absorption bands associated with PDMS are labelled accordingly within Figure 5.9 (b).

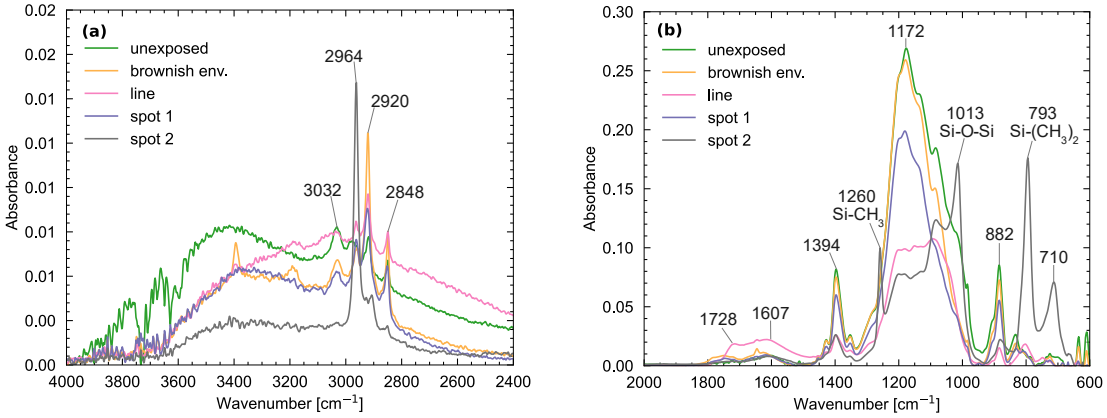

Figure 5.9: ATR-IR spectra of thermo-oxidatively aged FKM at 250 °C for 8 days. Comparison of heterogeneities (dark spots and line), brownish homogenous region, and unexposed reference sample, (a) in the spectral region 4000–2400 cm^{-1}, (b) in the spectral region 2000–600 cm^{-1}. Reproduced from Vega Puga et al. [301] with permission of Elsevier Science & Technology Journals.

The evolution of the chemical structure of the FFKM elastomer as a result of thermo-oxidative ageing was also investigated utilising ATR-IR microscopy. In accordance to the obtained data, proposed degradation pathways and mechanisms governing the thermo-oxidative ageing behaviour of FFKM are summarised in the following Figure 5.10.

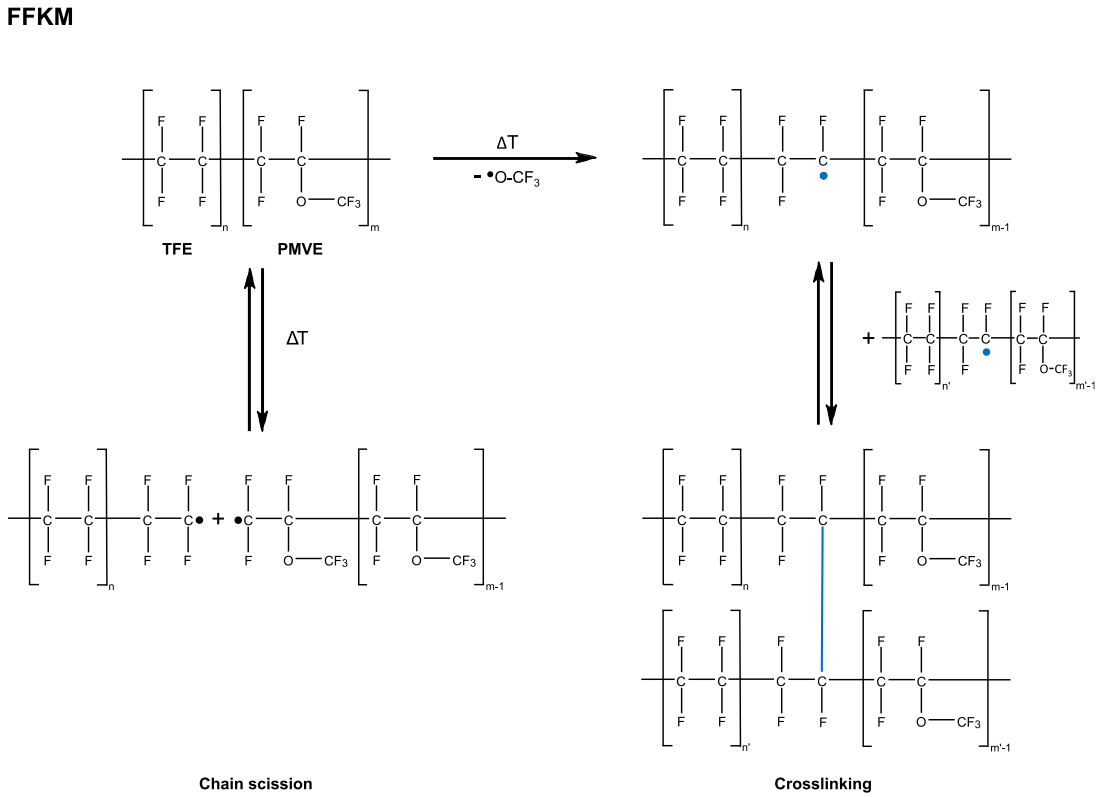

Figure 5.10: Proposed reaction scheme for the degradation of FFKM under thermo-oxidative conditions. Either cleavage of a C–C bond within the main polymer chain produces two radicals, resulting in irreversible chain scission. Or the elimination of a trifluoromethylether radical (•OCF$_3$) from the perfluoromethylvinyl ether (PVME) monomer generates a polymer radical that can reversibly recombine itself to form crosslinked structures. Reproduced from Vega Puga et al. [301] with permission of Elsevier Science & Tech. Journals.

ATR-IR measurements of FFKM samples prior and following thermo-oxidative ageing are presented in Figure 5.11. Consistent with the approach used for FKM, no spectral normalisation was performed in this analysis, as no invariant reference signal could be reliably identified. The primary peak assignments for the unaged FFKM were adopted from Mihaly et al. [313], while those corresponding to the aged material were based on Zhuo et al. [176], and specific features associated with perfluoromethyl vinyl ether (PMVE) segments were drawn from Trisna et al. [314].

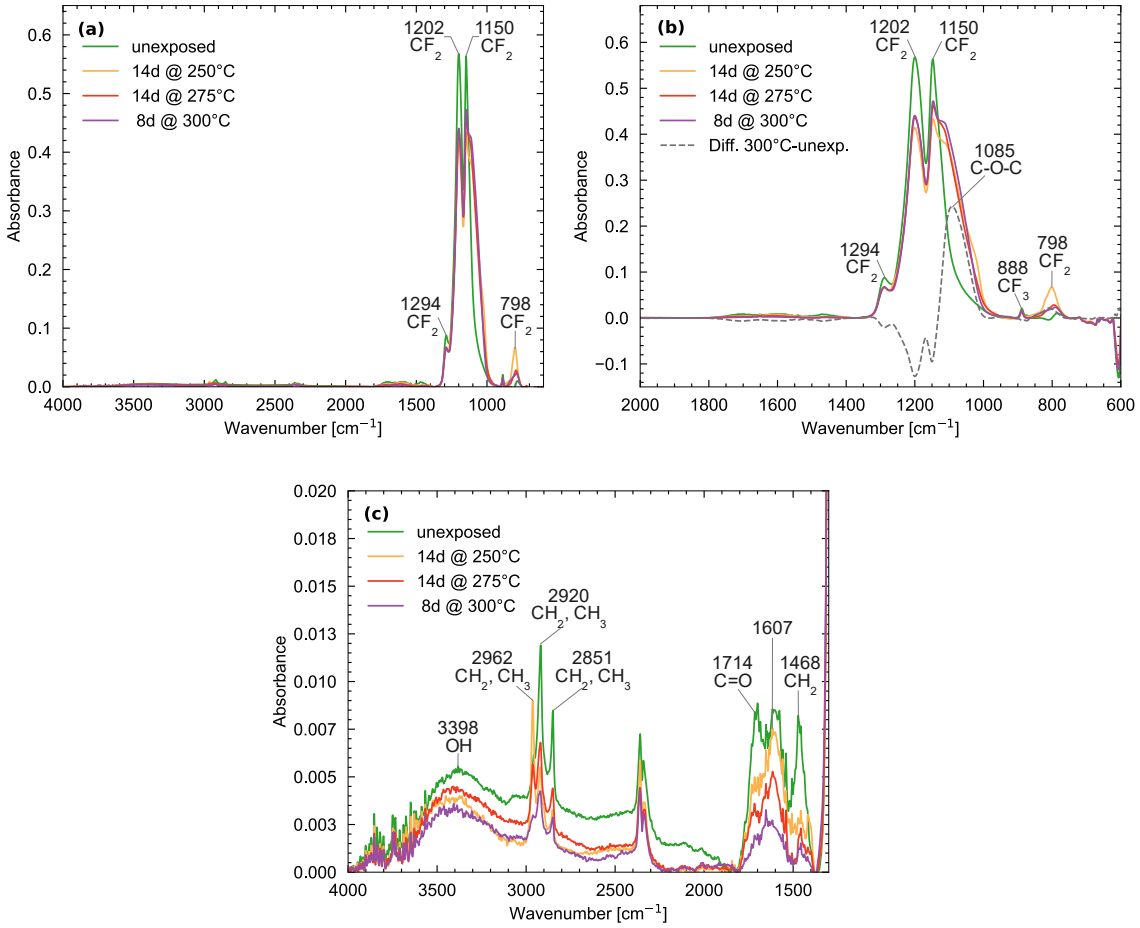

Figure 5.11: ATR-IR spectra of aged FFKM at varying ageing temperature and duration, (a) spectral region 4000–600 cm^{-1}, (b) spectral region 2000–600 cm^{-1} with the addition of the difference spectrum (between unexposed and aged at 300 °C for 8 days samples) depicted as a grey dashed line, (c) in the spectral region 4000–1300 cm^{-1}. Reproduced from Vega Puga et al. [301] with permission of Elsevier Science & Technology Journals.

As shown in Figure 5.11 (a), the most pronounced chemical alterations induced by thermo-oxidative ageing are localised within the wavenumber range of approximately 900 cm^{-1} to 1300 cm^{-1}, corresponding to various C–F bonds. This region is shown in greater detail in Figure 5.11 (b). In the unexposed FFKM sample, two prominent peaks are observed at 1202 cm^{-1} and 1150 cm^{-1}, characteristic of CF_2 groups and typically present in poly(tetrafluoroethylene) (PTFE)-like structures. Upon ageing at 250 °C, a significant reduction in the intensity of these absorption

bands is evident, with a further gradual decrease observed for samples aged at 275 °C and 300 °C. This decline is attributed to a thermally induced elimination of CF_2, which in turn is likely to involve a C–C bond break within the polymer backbone. This results in the formation of radical species and enables molecular rearrangements, which lead to degradation of the mechanical strength of the material.

With increasing ageing temperature, the emergence of a shoulder at 1085 cm^{-1} becomes apparent in the sample aged at 250 °C, with only a slight further increase observed for samples aged at 275 °C and 300 °C. In the difference spectrum (obtained by subtracting the unexposed sample's spectrum from that of the sample aged at 300 °C), this shoulder feature becomes more distinct, appearing as a peak centred at 1085 cm^{-1}. This absorption band may be indicative of the presence of C–O–C or C–F_x bonds. Hiltz [315] conducted pyrolysis gas chromatography and mass spectrometry analysis of a chemically related fluoroelastomer (a terpolymer comprising HFP, tetrafluoroethylene (TFE), PMVE, and VDF, which contains C–H bonds) at temperatures between 700 °C and 900 °C. He suggested that the degradation pathway involves the elimination of a $^{+}\bullet OCF_3$ fragment from the ether bond in the PMVE segment, and that the majority of the degradation products are linked to the PMVE component. In the present study, a similar degradation mechanism may be responsible for the formation of the shoulder at 1085 cm^{-1}. However, due to the fully perfluorinated nature of the FFKM investigated here, no evidence of hydrofluoric acid elimination or associated C=C double bond formation is observed, as this would typically require the presence of hydrogen atoms. Additionally, the increase in the absorption band at approximately 798 cm^{-1} (788 cm^{-1} in the unexposed state) from the unexposed state to aged at 300 °C is attributed to CF_2 groups.

The evolution of minor absorption bands in the wavenumber region between 4000 cm^{-1} and 1300 cm^{-1}, with an absorbance axis magnification is shown in Figure 5.11 (c). In this region, very weak signals corresponding to CH_2 and CH_3 vibrational modes are detected. Ideally, such absorptions would not be present in a fully perfluorinated polymer; their occurrence here is most likely attributed to the presence of residual crosslinking agents. The intensity of these bands systematically decreases with increasing ageing temperature, from the unexposed material through to samples aged at 300 °C, suggesting the possibility of ongoing post-curing reactions. A comparable trend is also observed for the carbonyl absorption band at 1714 cm^{-1} and the broad OH stretching band around 3400 cm^{-1}. These features are suggested to belong to an additional component, such as the cure site monomer.

5.2.3. Weight loss

Weight loss during thermo-oxidative ageing of elastomeric materials is acknowledged as a macroscopic indicator of chemical degradation processes, as it provides valuable insights into the

extent and rate of material deterioration. Figure 5.12 shows the percentage weight loss, relative to the unexposed state, for FKM and FFKM O-ring segments subjected to prolonged thermo-oxidative ageing over at temperatures between 200 °C and 300 °C.

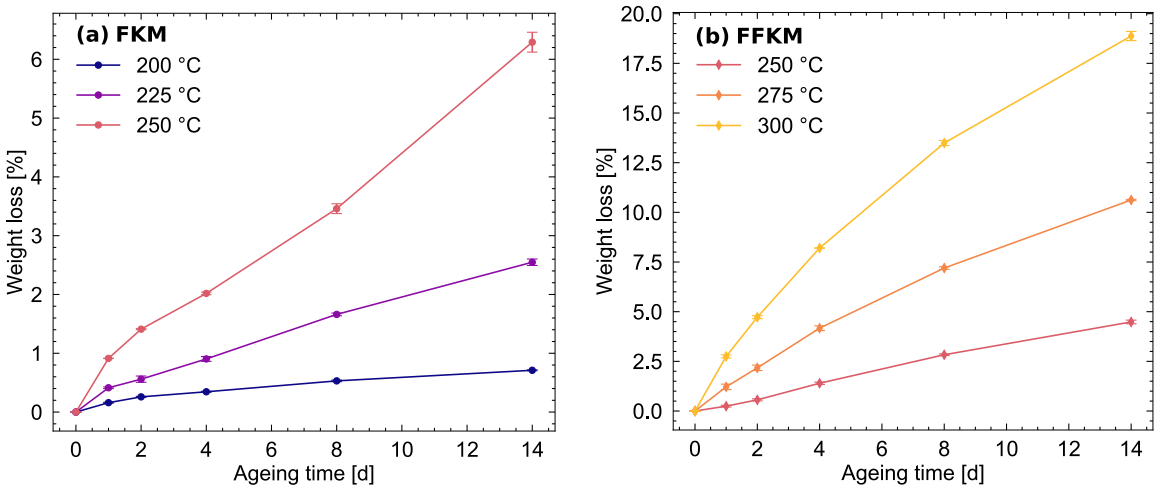

Figure 5.12: Weight loss of thermo-oxidatively aged (a) FKM and (b) FFKM O-ring segments as a function of temperature and time.

Both elastomer types exhibit a two-stage weight loss profile. The initial phase is marked by a rapid decline in weight, followed by a secondary phase with progressively slower weight loss. This behaviour aligns with autocatalytic degradation models, where reaction rates depend on evolving activation energies and competing chain scission/crosslinking processes. These findings are consistent with a previous study on a triallyl isocyanurate (TAIC)-cured FKM, which suggests that the non-linear weight loss behaviour observed with increasing ageing time may reflect a complex degradation mechanism involving multiple, sequential reactions occurring at distinct stages of the ageing process [175].

Weight loss in aged fluoroelastomers can arise from several contributing factors, including moisture loss, volatilisation of plasticisers or additives, and the generation of low molecular weight species as a consequence of thermo-oxidative degradation. As discussed in the ATR-IR microscopy analysis (Chap. 5.2.2), aged FKM O-rings show clear spectral evidence of chain scission, crosslinking, and oxidation. For instance, the loss of HF and subsequent formation of C=C bonds, along with increased carbonyl and ether functionalities, point to cleavage of the backbone followed by oxidative reactions. These findings are corroborated by the initial rapid phase of weight loss, which can be attributed to the release of volatile degradation products formed as a direct consequence of chain scission.

In the case of FFKM, the degradation mechanism similarly involves chain scission, likely associated with the elimination of trifluoromethylether fragments from the PMVE segments, as

well as concurrent crosslinking reactions. The appearance of new IR bands and the reduction in CF_2-related absorption support this interpretation. While chain scission leads to mass loss due to the volatilisation of degradation products, crosslinking can act to suppress further weight loss by immobilising reactive fragments within the polymer network, thereby reducing their volatility. This crosslinking effect is most evident in the second, slower phase of the weight loss profile.

For both examined elastomers an increase in the ageing temperature results in an enhanced weight loss rate, highlighting the thermally activated nature of the degradation processes. High temperatures facilitate both chain scission and the diffusion of degradation products, compounding the extent of weight loss. It is noteworthy that FFKM displays approximately 30% lower weight loss than FKM at a comparable ageing temperature of 250 °C. This superior resistance to thermal degradation can be attributed to the fully fluorinated backbone of FFKM, where the predominance of strong C–F bonds enhances thermal stability and reduces the susceptibility to chain cleavage. In contrast, FKM contains C–H bonds, which are more prone to thermally induced cleavage, contributing to its comparatively higher weight loss.

Interestingly, under the studied conditions, FKM samples exhibited a lower overall weight loss percentage than FFKM, despite being aged at temperatures exceeding the manufacturer's recommended maximum operating temperature. However, this apparent discrepancy can be rationalised by considering that FFKM was subjected to higher absolute ageing temperatures, which would promote the diffusion of volatile degradation products and enhance the weight loss rate. While, weight loss analysis and ATR-IR clearly reveal chemical modifications arising from thermo-oxidative ageing, the implications of these changes for the material's mechanical performance will be examined in the subsequent sections.

5.2.4. Hardness

The hardness of FKM and FFKM samples was evaluated prior and following thermo-oxidative ageing, using three stacked sheets of 2 mm thickness. Initial measurements revealed that unexposed FKM samples exhibited an average hardness of 75.8 Shore A, whereas unexposed FFKM samples demonstrated a higher hardness of 85 Shore A, exceeding the manufacturer's specified value. The evolution of hardness for both materials, as a function of ageing temperature and time, is presented in Figure 5.13.

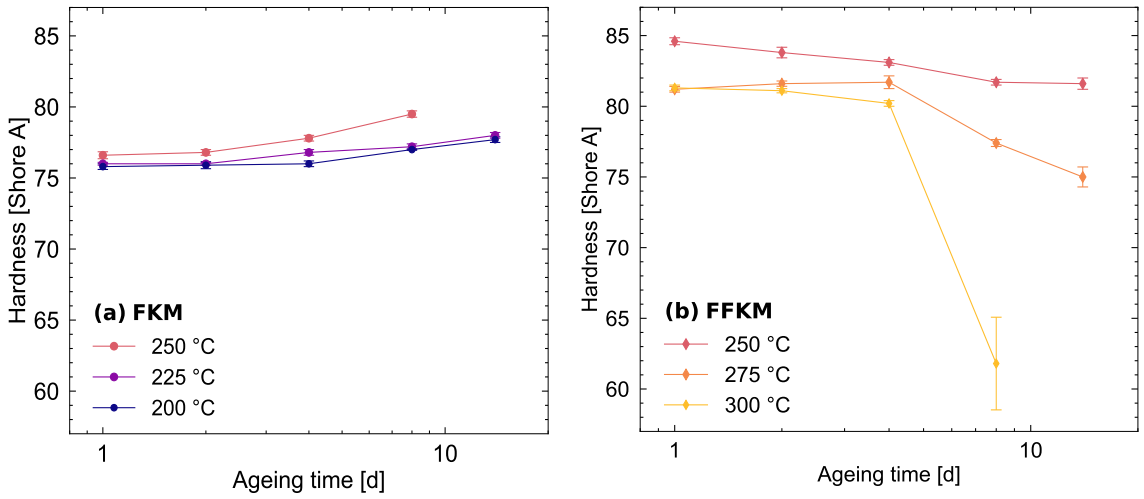

Figure 5.13: Measured hardness of thermo-oxidatively aged (a) FKM and (b) FFKM sheets.

For the FKM material, a slight increase in hardness was observed with prolonged ageing durations and higher temperatures. This phenomenon is likely associated with post-curing reactions and the degradation or volatilisation of plasticisers and lubricants, as also supported by the previously discussed weight loss plots. The limited increase in hardness observed for aged FKM samples may also be attributed to the so-called cage effect, which is observed in heavily fluorinated polymers. This effect restricts the mobility of free radicals, promoting their recombination within the polymer matrix, and consequently suppressing the progression of degradation reactions and limiting irreversible structural damage [156,316,317]. Nonetheless, at higher temperatures where polymer chain mobility is significantly enhanced, the ability of radicals to recombine diminishes, leading to more pronounced material degradation [156]. Previous FKM studies [181,318], which have investigated the degradation of this elastomer type within lower temperature ranges (75 – 150 °C), have also found similar hardness trends. However, to further substantiate the hypothesis that increased hardness in FKM results from post-curing processes during thermo-oxidative ageing, future investigations could focus on quantifying the degree of crosslinking in aged samples, thereby providing direct experimental evidence for this proposed mechanism.

In contrast to FKM, the FFKM material exhibits a marked reduction in hardness with increasing ageing temperature and exposure time. This pronounced decrease in hardness suggests that chain scission reactions are the dominant degradation mechanism during ageing, in agreement with the breakage of C–C bonds in the polymer backbone as identified through the presented ATR-IR analysis. Previous research investigating the thermo-oxidative ageing behaviour of peroxide-cured FFKM within the temperature range of 90 °C to 150 °C has proposed that material degradation proceeds via two concurrent processes: post-curing reactions and the breakdown of the TAIC crosslinking network, with the latter becoming increasingly significant at higher temperatures

[176]. Furthermore, the higher ageing temperatures applied to FFKM in this study may have further hindered the recombination of free radicals due to enhanced molecular mobility. At the most severe ageing state for FFKM (300 °C, 8 days) a substantial reduction in hardness was observed. It is worth noting, however, that hardness measurements under these conditions were subject to considerable uncertainty, as the elastomer samples adhered to the perforated metal support on which they were aged. Consequently, an imprint of the perforated metal was visible on the sample surface, and the hardness value varied depending on the specific location on the sample where the measurement was conducted.

5.2.5. Compression Set

The measured CS values for FKM and FFKM O-rings subjected to various ageing temperatures and durations are presented in Figure 5.14. Both materials exhibited an increase in CS with increasing ageing temperature and time. However, FFKM exhibits a relatively high CS after only 1 day of ageing across all tested temperatures. This behaviour is particularly interesting given that the ageing temperatures for FFKM remained below the manufacturer's maximum recommended limit, while FKM was aged beyond its specified maximum operating temperature. Additionally, it is important to highlight that CS testing was conducted on O-rings that had a deformation (SD) of 25% in the CS fixtures at ambient temperature prior to exposure to high temperatures. Given that FFKM possesses a coefficient of thermal expansion approximately 30% greater than that of FKM at similar filler content [149], and that FFKM samples were exposed to temperatures 50 °C higher than FKM, the effective deformation of FFKM O-rings during thermal ageing would have been greater than that of the FKM ones. This increased deformation likely resulted in higher internal stresses within the FFKM samples, contributing to the initially elevated CS values.

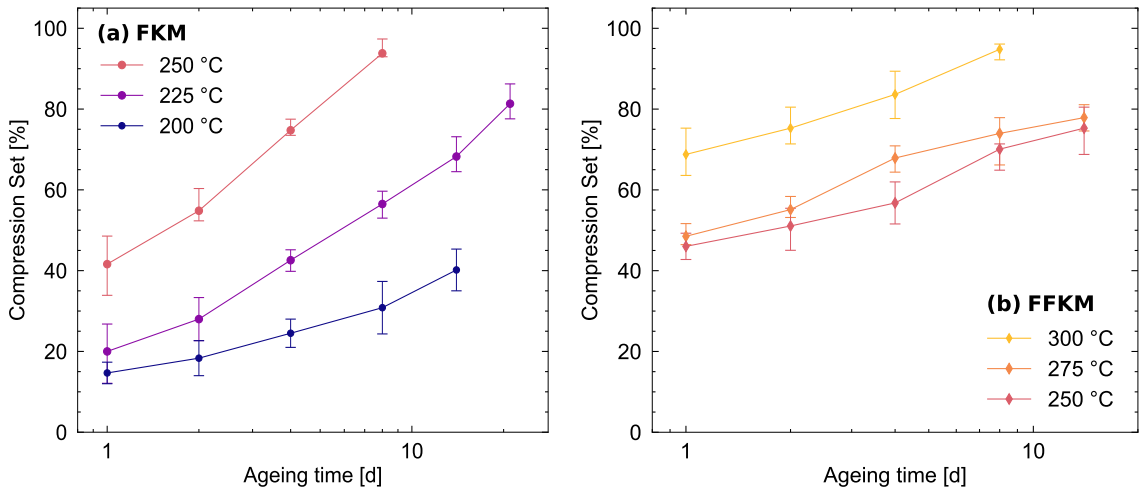

Figure 5.14: Measured compression set of thermo-oxidatively aged (a) FKM and (b) FFKM O-rings.

For instance, at an ageing temperature of 250 °C and an exposure time of 1 day, FKM exhibits superior recovery behaviour than FFKM, with a slightly lower CS value. Nevertheless, for longer exposure durations (> 2 days) at the same temperature, the CS of FKM surpasses that of FFKM. The significantly higher CS observed in FKM at longer exposure times indicates a more advanced degradation state, thus reinforcing the superior thermal resistance of FFKM. While an initial SD of 18% for FFKM O-rings could be adopted to achieve approximately 25% SD at 325 °C [148], the present study employed a standardised 25% deformation (SD) in accordance with the DIN ISO 815-1 standard to ensure methodological consistency [307].

Moreover, it is evident that for both FKM and FFKM, CS measurements capture material degradation more sensitively than hardness testing. For example, FKM aged at 250 °C for 14 days exhibited only a modest increase in hardness of approximately 3 Shore A units, whereas the equilibrium CS indicated a 95% reduction in resilience. This discrepancy may be attributed to the previously discussed cage effect (Chap. 5.2.4), where free radical recombination within the polymer matrix mitigates permanent damage [317]. In the sheet samples used for hardness testing, this effect may be more pronounced due to reduced mechanical stresses compared to the O-rings aged under compression. In compressed O-rings, fragmented chain ends generated by chain scission may have relaxed and separated, hindering recombination and promoting further degradation.

An alternative, though less probable, explanation is the concurrent occurrence of chain scission and post-curing-induced crosslinking during thermo-oxidative ageing. While these processes exert opposing influences on hardness, their combined effects may offset one another in hardness measurements while contributing additively to increased CS values [160,161,319]. Generally, chain scission leads to a reduction in hardness, whereas crosslinking enhances it; thus, the net hardness change reflects the dominant process and may not fully capture the extent of the material degradation. In contrast, CS is exacerbated by both mechanisms: chain scission diminishes the material's ability to recover by breaking molecular bonds, while additional crosslinking fixes the deformed geometry of the O-ring by creating new bonds [169].

5.2.6. Compressive stress relaxation

Compression stress relaxation (CSR) experiments were carried out on FKM and FFKM O-ring segments at 200 °C. The evolution of the normalised force (F/F_0), where F_0 represents the initial sealing force of the respective elastomer, is presented in Figure 5.15 as a function of ageing time. For each material, three curves corresponding to the tested samples are shown. It should be noted that one measurement for both FKM and FFKM was terminated after approximately two months due to technical malfunctions of the testing apparatus.

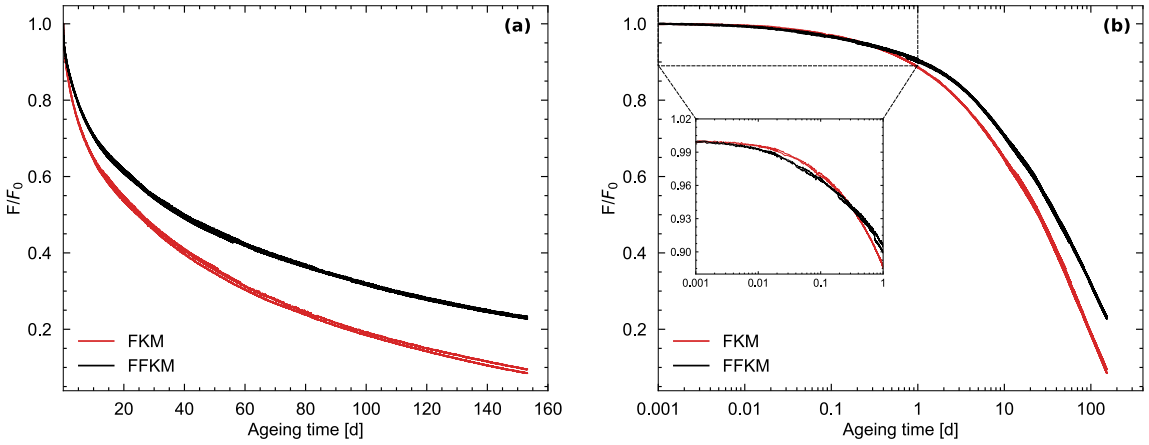

Figure 5.15: Compressive stress relaxation of FKM and FFKM O-ring segments at 200 °C in (a) linear and (b) logarithmic time scale. Reproduced from Vega Puga et al. [301] with permission of Elsevier Science & Technology Journals.

Both elastomers exhibit a reduction in sealing force with increasing ageing time. Initially, a rapid decline in force is observed (on the linear time scale), which subsequently transitions to a slower, more gradual decrease as the ageing duration increases. This behaviour is consistent with findings from previous studies [319–321], which attribute the early-stage force relaxation predominantly to physical processes (e.g. relaxation of polymer chain units or movement of entanglements), while the more dominant force decrease at extended ageing times is associated with chemical relaxation mechanisms (e.g. oxidative chain scissions). The experimental results indicate that FFKM has a slightly greater degree of relaxation during the initial physical phase, whereas FKM displays higher force loss in the chemical phase. The substantial decrease in sealing force observed for FKM at prolonged exposure times is indicative of progressive thermo-oxidative degradation of its molecular structure. Conversely, FFKM demonstrates enhanced thermal stability at 200 °C, maintaining a higher proportion of its sealing force over extended ageing durations.

The CSR results further corroborate the CS measurements, as an inverse correlation between CSR and CS could be determined for FKM. Nevertheless, such a direct comparison could not be established for FFKM, since the CSR tests were conducted at 200 °C, an ageing temperature lower than those employed for the CS measurements. This temperature constraint was dictated by the operational limitations of the CSR testing equipment. Similar to CS, CSR testing provides a more sensitive measure of material degradation than hardness testing. This is attributed to the cumulative reduction in sealing force arising from both chain scission and crosslinking reactions during ageing, while the cage effect, which promotes free radical recombination, may be less effective under compressive strain. Consequently, CSR and CS are considered more reliable indicators of structural degradation than hardness measurements, rendering them particularly valuable for the accurate prediction of O-ring lifetimes under thermo-oxidative conditions.

5.2.7. Leakage rate

Leakage in elastomeric sealing systems may arise through two principal mechanisms: permeation of the fluid through the bulk of the elastomer material and secondary leakage, which occurs via micro-channels at the interface between the seal and the adjoining surface. Among the various properties used to assess seal performance, leakage is the most direct and critical indicator of functional failure, and therefore serves as a reliable end-of-life criterion for O-rings. In this context, the leakage rates of FKM and FFKM O-rings subjected to thermo-oxidative ageing at different temperatures and durations were experimentally tested and are presented in Figure 5.16. Given that absolute leak-tightness is rarely achievable under practical operating conditions, engineering standards typically define an acceptable threshold leakage rate, q_L, determined by the specific requirements of the application [322]. In the present study, the threshold leakage rate, or maximum allowable leakage rate, was conservatively defined as a tenfold increase relative to the leakage rate of unexposed O-rings. This threshold, indicated by a black dash dotted line in Figure 5.16, was selected to reflect both the sensitivity of the R2Mx system to leakage and to align with criteria commonly adopted in vacuum technology, where such an increase is considered indicative of significant performance degradation [323].

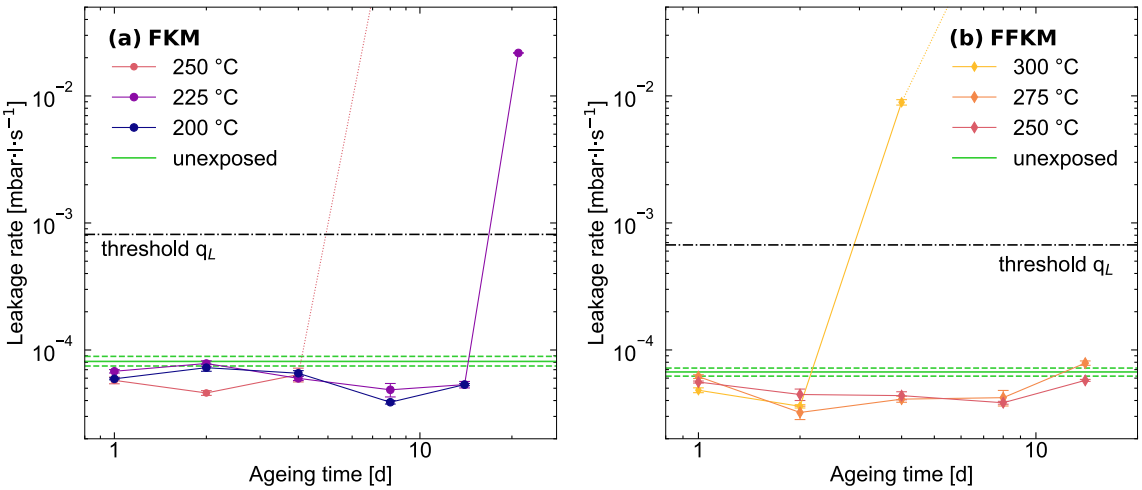

Figure 5.16: Leakage rates of aged O-rings for (a) FKM and (b) FFKM. The measurement uncertainty for the leakage rate measurements of the unexposed O-rings is shown by dashed light blue lines. The threshold leakage is marked by a black dot dashed line. In instances where it was not possible to establish vacuum in the chamber A of the test setup, leakage rate is assumed infinite and is depicted outside the diagram box with a dotted line.

Failure of the FKM O-rings was identified at a leakage rate of $2.2 \cdot 10^{-2}$ mbar·l·s^{-1}, corresponding to 21 days of ageing at 225 °C, exceeding the predefined leakage threshold ($8.1 \cdot 10^{-4}$ mbar·l·s^{-1}) and being two orders of magnitude larger than the leakage rate from the unexposed samples. Similarly, FFKM O-rings' failure was observed after 4 days of ageing at 300 °C, at a leakage rate of $8.9 \cdot 10^{-3}$ mbar·l·s^{-1}. For the FFKM O-ring the leakage rate threshold

was set at $6.7 \cdot 10^{-4}$ mbar·l·s^{-1}. Notably, attempts to measure leakage in FKM samples aged for 8 days at 250 °C, as well as FFKM samples aged for 8 days at 300 °C, were unsuccessful due to the inability to establish a vacuum, indicating catastrophic failure of the seal. In all instances, seal failure occurred abruptly rather than progressively, a phenomenon consistent with previous observations reported in the literature for elastomeric seals undergoing thermo-oxidative degradation [156,178,181,183].

Throughout the ageing process, some variability was observed in the measured leakage rates for both elastomer types. While a superficial interpretation may attribute this to a reduction in material permeability, a prior investigation [169] demonstrated that the permeability of FKM remained essentially unchanged after 100 days of ageing at 150 °C. Moreover, given that the predominant degradation mechanism in both FKM and FFKM is chain scission, a decrease in permeability is unlikely. It is therefore more plausible that the observed variability in leakage rate is attributable to experimental factors, including outgassing of the O-rings or experimental setup components, as well as variations in ambient conditions such as temperature and pressure during testing.

Previous research [156,178,181,183] has shown that despite advanced material degradation, elastomeric O-rings are able to maintain leak-tightness due to adhesive interactions with mating surface under static conditions. However, this behaviour does not adequately represent dynamic applications, where the seal-to-surface contact is repeatedly disrupted. To address this limitation and avoid potential artefacts from adhesion effects, the current study employed a testing protocol where O-rings were aged compressed in lubricated fixtures and subsequently removed with care prior to leakage measurement. This methodology ensures that the reported leakage rates more accurately reflect the intrinsic sealing capability of the aged material, independent of surface adhesion, and thus provide a conservative yet realistic assessment of the seal performance under conditions relevant to dynamic service environments.

5.2.8. Service lifetime prediction

To estimate the operational lifetime of FKM and FFKM O-rings within the studied application, the time-temperature superposition (TTS) methodology, described in Chap. 3.2.5 is employed. In this study, CS measurements were selected to construct the TTS master curves, given their high sensitivity to material degradation, as discussed in Chap. 5.2.5, and the greater quantity of data available compared to the equally suited CSR. The resulting master curves and shift factors for FKM and FFKM are presented in Figure 5.17. For FKM, a reference temperature of 200 °C was selected, while for FFKM, 250 °C was chosen, in accordance with their respective ageing conditions. Additionally, leakage rate measurements corresponding to the shifted ageing times are plotted on a secondary axis, facilitating the correlation between the leakage performance of O-rings at a given ageing state and their associated CS values.

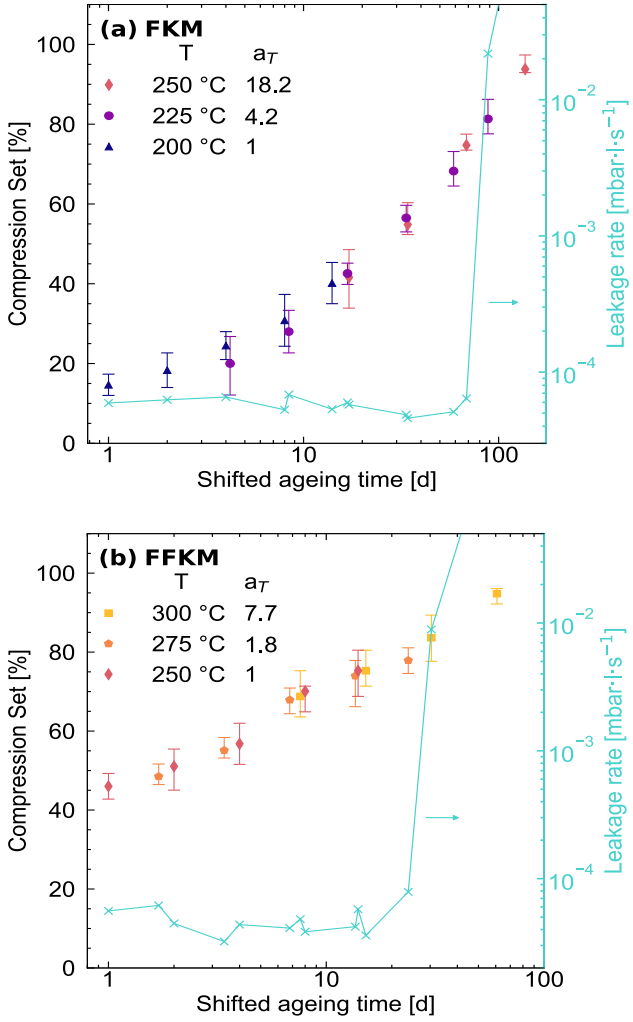

Figure 5.17: Time-temperature superposition and shift factors (a_T) of CS data, along with corresponding measured leakage rates on the secondary axis. The reference temperature for (a) FKM is 200 °C, and for (b) FFKM is 250 °C.

The CS data for both materials exhibited satisfactory superposition within the investigated time and temperature domains. Seal failure, defined by the leakage rate exceeding the pre-established threshold, was observed when the CS reached approximately 81% for FKM and 83% for FFKM. Adjacent measurements, wherein the O-rings remained leak-tight, corresponded to CS values of 75% for FKM and 78% for FFKM. Consequently, a conservative CS value of 75% was adopted in this work as the end-of-life criterion for both elastomers. Previous investigations [178,179] have proposed that CS in the range of 80–85% constitutes a suitable end-of-life criterion for ethylene propylene diene monomer (EPDM) O-rings, particularly in dynamic leakage testing involving rapid partial decompression of the seal after static ageing without seal removal. The lower end-of-life criterion identified in this study may be attributed to the experimental methodology employed, specifically, the frequent interruption of the ageing process for intermediate characterisation of the samples. As the O-rings were repeatedly removed from the metal fixtures for testing, adhesion

between the seal and the mating surface was minimised. Consequently, elevated leakage rates were observed at lower degradation levels than those reported in studies where the seal remained undisturbed during ageing.

To gain further insight into the underlying degradation mechanisms, a plot of the logarithm of the shift factors versus the inverse absolute temperature was constructed (Figure 5.18), enabling an Arrhenius-type analysis. If the shift factors align linearly across the studied temperature range, it may be inferred that a single dominant degradation mechanism is operative. For FKM, the data exhibited a highly linear trend, yielding an apparent activation energy (E_a) of 116 kJ·mol^{-1}. This value exceeds those reported in literature, such as an E_a of 78 kJ·mol^{-1} for bisphenol-cured FKM based on equilibrium CS data in the 75–150 °C range [179], and approximately 82 kJ·mol^{-1} derived from stress relaxation measurements for a type 2 FKM aged between 150–275 °C [324]. More recent studies employing a "power law" model reported E_a values ranging from 117 to 151 kJ·mol^{-1} for FKM O-rings, with end-of-life criteria between 50–80% CS and testing temperatures of 100–200 °C [325]. These discrepancies in E_a values are largely attributable to the differing test methodologies, which significantly influence the derived parameters, rendering direct comparison of results between studies inappropriate [180,318].

For FFKM, a less satisfactory linear fit was obtained, resulting in an E_a of 110 kJ·mol^{-1}. To enhance the interpretation of this result and ascertain whether changes in the prevailing degradation mechanisms occur within the studied temperature range, further experiments at additional ageing temperatures (e.g., 225 °C or 325 °C) are recommended. Such investigations would also clarify whether the observed non-linear behaviour persists and whether a power-law model provides a more suitable description of the temperature-dependent degradation processes. A previously reported E_a value for a high-temperature-resistant FFKM was 251 kJ·mol^{-1}, determined via thermogravimetric analysis (TGA) corresponding to a 5% mass loss in the temperature range of 350–416 °C [149]. As with the FKM data, direct comparison of this reported E_a with that of the present work is not appropriate due to the fundamentally different testing methods and significant variation in temperature ranges, given that polymeric materials typically exhibit multiple apparent activation energies across broad temperature intervals. Overall, the apparent activation energies determined for FKM (116 kJ·mol^{-1}) and FFKM (110 kJ·mol^{-1}) in this study illustrate that a higher activation energy does not necessarily result in a longer service lifetime. This conclusion is also supported by prior research [179]. Instead, the findings indicate that directly measurable parameters, such as CS, offer a more reliable basis for lifetime prediction of elastomeric seals than activation energy alone.

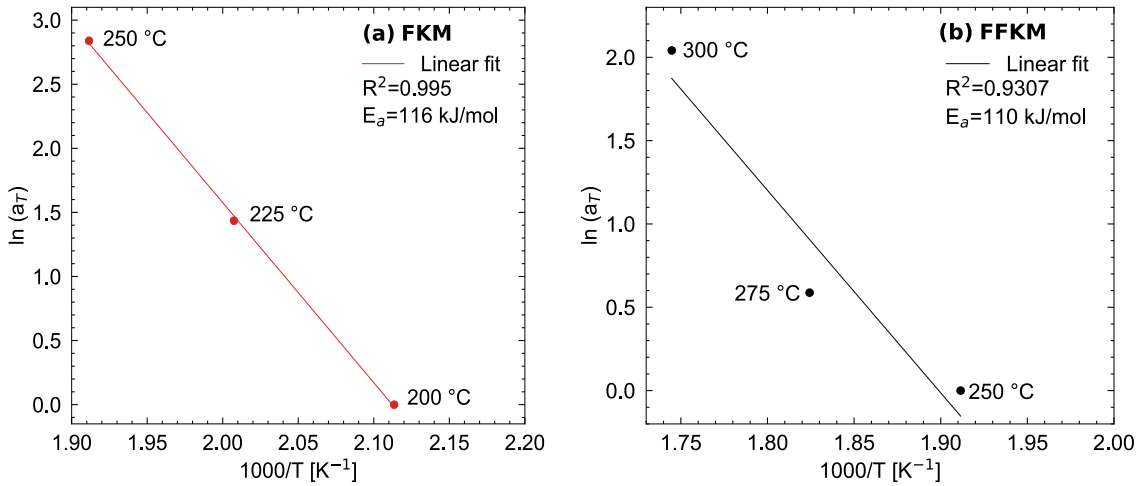

Figure 5.18: Arrhenius diagrams of shift factors, a_T, for (a) FKM and (b) FFKM. Reproduced from Vega Puga et al. [301] with permission of Elsevier Science & Technology Journals.

Building upon the Arrhenius diagrams previously discussed, it is important to emphasise that the lifetime prediction presented herein does not rely on the derived apparent activation energies nor on extrapolation towards lower temperatures. Instead, TTS methodology, based on CS data, has been applied to provide a more direct and robust estimation of service lifetime within the experimentally investigated temperature range. Utilising the previously established end-of-life criterion of 75% CS, the projected service duration of the O-ring seals may be determined not only at the temperatures where leakage was experimentally observed but also across the other ageing temperatures. While the DIN ISO 11346 standard [177] permits extrapolation of degradation curves by up to 30–40 °C beyond the highest tested temperature, the present study conservatively restricts the lifetime prediction to the experimentally tested temperatures to ensure greater reliability and accuracy.

Table 5.3 details the empirically derived and predicted times required for FKM and FFKM O-rings to reach 75% CS, representing the end of their operational life. In addition, the estimated service lifetime of FKM and FFKM O-rings at 200 °C, determined from long-term CSR tests, is included for comparison. The lifetime corresponding to the CSR data reflects the time required for the sealing force to decrease to 25% of its initial value, a condition analogous to the 75% CS failure criterion. The predicted service lives of FKM O-rings aged at 200 °C, obtained via both the TTS and CSR methodologies, exhibit good agreement, differing by only 5% (73 days vs. 77 days). This consistency reinforces the validity of the applied methods. Notably, the use of TTS enables a more rapid assessment of long-term performance by utilising accelerated ageing protocols, at the cost of a marginally more conservative lifetime estimate.

Table 5.3: Experimentally derived and predicted service lifetimes of FKM and FFKM O-rings at different operating temperatures

Material	Service lifetime [d]*					
	200 °C		*225 °C*	*250 °C*	*275 °C*	*300 °C*
FKM	73	77+	17	4		
FFKM		135+		16	9	2

*considering 75% CS as end-of-life criterion
+ measured time to reach 25% of initial sealing force using CSR

The lifetimes reported in Table 5.3 assume continuous operation of the O-ring seals over a 24-hour cycle. However, in the context of the intended solar receiver-reactor application, operational hours are limited to approximately 8 hours per day, corresponding to the availability of solar irradiation. Accordingly, the following Table 5.4 presents lifetime predictions of the O-rings in *operational days*, where one operational day is defined as an 8-hour active thermal exposure period. It is important to note, that the temperatures used in ageing tests reflect constant exposure, and therefore should not be directly equated with O-ring peak temperatures reported in Chap. 4. As previously discussed, the instantaneous peak temperatures, estimated to reach 360 °C, are highly localised and transient, typically lasting less than 1 second. In contrast, the temperatures used for thermo-oxidative ageing and lifetime prediction of O-rings are more representative of the volume-averaged temperatures derived in Chap. 4, which better reflect the bulk temperature of the elastomer. This approach provides a conservative yet realistic estimate of long-term thermal degradation under sustained operational conditions.

Table 5.4: Predicted service lifetimes of FKM and FFKM O-rings under thermo-oxidative ageing. Lifetime is expressed in operational days, where one day corresponds to 8 hours of continuous solar reactor activity.

Material	Service lifetime [Operational days (8h/day)]				
	200 °C	*225 °C*	*250 °C*	*275 °C*	*300 °C*
FKM	219	51	12		
FFKM	405		48	27	6

Continuously operating the O-ring seals at temperatures exceeding 200 °C would necessitate frequent maintenance interventions, potentially on a monthly or bimonthly basis, which may not be feasible from either an economic or operational perspective, particularly given that maintenance would need to be scheduled during night-time periods. Consequently, an operational continuous temperature limit of 200 °C is recommended for both FKM and FFKM seals to minimise replacement frequency. While based on the derived service lifetimes of FFKM at 200 °C and 250 °C, operation at 225 °C may be feasible, the absence of experimental data at this temperature warrants a conservative approach. Therefore, 200 °C has been selected as the recommended continuous operating temperature. Both elastomeric materials, FKM and FFKM, demonstrated satisfactory thermal stability and performance at this temperature, permitting the development of a material selection strategy that balances lower maintenance requirements against the higher

procurement cost of FFKM. Maintaining the O-ring at a relatively low temperature of approximately 200 °C within the foreseen gate application presents a significant design challenge and requires further optimisation. Several parameters can be adjusted to reduce radiative heat exchange from the hot RMA, including increasing the transport speed of the RMA, increasing the distance between the RMA and the seal, incorporating thermal shielding to limit radiative heat transfer, and implementing active cooling strategies.

This study provides a foundational understanding of the thermo-oxidative ageing behaviour of FKM and FFKM O-ring seals under continuous high-temperature exposure for usage in a solar receiver-reactor. Nevertheless, further research is necessary to evaluate the impact of thermal cycling during reactor operation. In particular, the effects of repeated daily heating and cooling between stand-by (at night) and operational temperatures on the long-term performance of the O-rings remain insufficiently understood. Furthermore, the influence of brief but extreme temperature (360 °C) peaks, localised on the surface of the O-ring warrants closer examination. Although short-lived, these very high surface temperatures may lead to accelerated ageing on the elastomer surface, potentially changing surface roughness and initiating leakage channels, thereby compromising seal integrity and reducing service lifetime. Understanding these effects are fundamental to developing more accurate O-ring lifetime predictions under real-world operating conditions. Additionally, it is important to note that the results presented herein are specific to the particular FKM and FFKM materials, O-ring geometries, and test conditions employed in this study. Further validation is recommended to confirm the applicability of these findings to other elastomer types and seal configurations.

5.3. Summary

In this chapter, the high-temperature degradation behaviour of FKM and FFKM O-rings within the temperature range of 200 °C to 300 °C has been investigated by examining chemical and mechanical property changes induced by thermo-oxidative ageing. In the case of FKM O-rings, progressive discolouration was observed, with the original blue hue fading to grey and eventually dark brown at the most severe ageing conditions. Furthermore, aged samples exhibited increasing surface heterogeneities, softening, adhesion, and pronounced roughening of the surface texture. Infrared (IR) microscopy analysis indicated that the degradation mechanism of FKM is primarily governed by the thermally activated elimination of hydrogen fluoride (HF) from the $–CF_2$ group, leading to the formation of C=C double bonds. Subsequent oxidation of these unsaturated sites to carbonyl groups was detected, which is associated with chain scission events and backbone cleavage. Weight loss measurements suggest that chain scission predominates in the early stages of ageing, contributing significantly to volatile formation and mass loss, whereas crosslinking

becomes more prominent in later stages, attenuating further weight loss by stabilising the polymer structure. Mechanically, the accelerated ageing programme revealed only a minor increase in hardness, while compression set (CS) values increased substantially with higher ageing temperatures and prolonged exposure times.

For FFKM O-rings, thermo-oxidative ageing was characterised by material softening, evidenced by bulging at the edges of the seal. At failure, deformation of the O-ring diameter and the formation of crevices were observed, indicative of substantial material deterioration. IR microscopy suggested that degradation proceeds via the elimination of CF_2 groups following C–C bond scission within the polymer backbone. Additionally, radical-driven reactions and post-curing phenomena, resulting in further crosslinking, may also occur during ageing. Similarly to FKM, FFKM weight loss was observed to occur in two stages: an initial rapid weight loss stage followed by a less pronounced weight reduction phase. Chain scission reactions contributed to the observed decrease in hardness of aged FFKM samples. Despite exhibiting higher CS values at short exposure times compared to FKM, FFKM demonstrated superior thermal resistance at elevated temperatures, particularly at 250 °C. Long-term compression stress relaxation (CSR) tests conducted over five months at 200 °C confirmed the enhanced ageing resistance of FFKM relative to FKM.

Leakage rate tests performed on thermo-oxidatively aged O-rings revealed that seal failure occurs abruptly rather than progressively, underscoring the critical importance of accurate lifetime prediction. The experimental CS data were analysed using the time–temperature superposition (TTS) method, enabling the derivation of a conservative end-of-life criterion, defined as 75% CS. This criterion provided a direct correlation between the CS evolution of the elastomers and leakage rates exceeding an acceptable threshold. The predetermined leakage rate threshold was about $7 \cdot 10^{-4}$ mbar·l·s^{-1} and it was defined as an order of magnitude increase from the leakage rate of the unexposed samples.

Service lifetime predictions based on the TTS master curves indicated that FKM O-rings exhibit lifetimes of approximately 73, 17, and 4 days at 200 °C, 225 °C, and 250 °C, respectively. Correspondingly, FFKM O-rings demonstrated lifetimes of 135 days (determined via CSR) at 200 °C, and 16, 9, and 2 days at 250 °C, 275 °C, and 300 °C, respectively. It is conceivable that these lifetimes may be extended by optimising O-ring deformation (specially FFKM) at elevated temperatures, thereby reducing mechanical stresses during operation. Considering the specific application in a solar receiver-reactor, where daily operation is typically limited to an 8-hour window, the predicted service lifetimes increase substantially. Under these conditions, lifetimes of approximately 200 days for FKM and 400 days for FFKM are attainable at continuous 200 °C operation, rendering both materials suitable candidates for this application. Continuous gate operation at temperatures exceeding 200 °C is not recommended due to the markedly reduced

lifetimes of the seals, which would necessitate highly frequent maintenance interventions, which would present significant economic and logistical challenges for the reliable and cost-effective operation of the R2Mx reactor.

6. Rod seal degradation and lifetime prediction

The design and operation of the R2Mx solar reactor impose unique and demanding operating conditions on its sealing components, particularly the dynamic rod seals responsible for maintaining vacuum integrity during high-frequency, high-temperature actuation cycles. Thermal simulations presented in earlier chapters revealed that the transport rod, and by extension the rod seals, are exposed to temperatures reaching up to 300 °C during standard operation. These high temperatures, combined with cyclic mechanical loads and vacuum conditions, motivate a deeper investigation into the degradation mechanisms and service lifetimes of the selected rod seals. This mirrors the approach taken in the previous Chap. 5 for O-ring seals, but introduces additional complexities associated with dynamic sealing performance and wear.

In literature, the application of PTFE-based lip seals under vacuum and high temperature conditions remains relatively underexplored, particularly in reciprocating motion systems like the transport system of the R2Mx reactor. Furthermore, the testing conducted in this study intentionally extends beyond the manufacturer's maximum recommended operating temperatures for these seals, in order to assess their practical limitations and gain insight into possible failure modes under extreme conditions. To address this, an experimental programme was developed to characterise both the material degradation and tribological behaviour of the rod seals. The study begins with thermo-oxidative ageing tests of the PTFE compound used in the lip seals, providing a baseline understanding of its stability under prolonged high-temperature (250–300 °C) exposure.

Next, the performance of lip seals is examined using a custom-built test rig designed to mimic the R2Mx reactor's operating conditions. Two main scenarios were investigated: ambient temperature operation, in which two different rod surface roughness were evaluated, and high-temperature operation (250–300 °C), where testing was performed exclusively with rough rods to accelerate the degradation of the seals. Throughout testing a comprehensive set of tribological tests was carried out, including wear (mechanism type and weight loss), lip seal deformation, leakage rate under vacuum, and force measurements. Finally, a methodology for predicting the service lifetime of the rod seals was developed, using the wear and leakage rate data obtained during testing. A conservative end-of-life criterion of 1% weight loss was proposed, based on observations

at failure points at 275 °C and 300 °C. Lifetime estimations were then extrapolated to operational metrics relevant to the R2Mx system, such as cycle count and operational days, providing a practical tool for maintenance scheduling and design optimisation.

6.1. Materials and methods

6.1.1. PTFE lip seals and sheets

The investigated rod seals (Figure 4.3) are a commercially available lip seals under the trade name TEDIMA Multiseal double lip in a back-to-back configuration supplied by TEDIMA GmbH (Krefeld, Germany) [222]. The lip seal is made of a proprietary PTFE compound with brand name TEDEX-B, and as such, detailed knowledge on the material properties is limited. The available data sheet only provides the operating temperature range, which spans from -90 °C to 260 °C; a temperature range characteristic of PTFE-based materials. Due to the black colouration of the PTFE compound, possible fillers include carbon black and graphite. As per the manufacturer's information, the material has a considerable memory effect, high elasticity, low friction, and good wear resistance. Therefore, a spring is not required to energise the lip seal. In total, ten PTFE lip seals with inner diameter 20 mm, outer diameter 35 mm, and steel case height 8 mm were tested. This seal geometry was selected considering its application in the transport system of the R2Mx solar reactor.

Given the limited information available on the material properties of the utilised PTFE compound, TEDEX-B flat sheets were used in an accelerated ageing program aimed at evaluating the material property changes as a result of thermo-oxidative ageing. Twelve 2-mm thickness and 5-cm diameter flat samples were aged and utilised to perform hardness and mass loss measurements.

6.1.2. Accelerated ageing protocol

The 2-mm thickness PTFE compound sheets were aged inside an oven with forced air circulation according to the DIN ISO 188 standard [305]. The ageing temperatures are 250 °C, 275 °C, and 300 °C and the exposure times are 1, 2, 4, 8, and 14 days. Three flat samples were aged per temperature on a meshed rack to ensure inhibited air circulation around material. The ageing was repeatedly interrupted after the aforementioned exposure times to perform hardness and mass loss tests necessary to evaluate the changes in material properties. After these tests were completed, the PTFE flat samples were returned to the oven to continue ageing.

6.1.3. Hardness

Hardness measurements were performed using a Shore D durometer on a stack of three PTFE sheets, in accordance with the DIN ISO 48-4 standard [306]. After each exposure time, five separate

measurements were carried out at different locations to avoid localised effects. The resulting average hardness and standard deviation are detailed in Chap. 6.2.1.

6.1.4. Mass change and wear

The mass of the PTFE flat samples was measured before ageing and after each exposure time. Each flat sample had an initial weight of approximately 2 g. The lip seals (~13 g) were also weighted before and after testing in the dedicated test rig at defined time intervals. In both cases, the mass measurements were performed using an analytical balance (Satorius Analytic, Model AC 210 S) with a precision of 0.1 mg. Prior weighting, all samples (sheets and lip seals) were cleaned in an ultrasonic bath for seven minutes to remove any dust particles or wear debris that could affect the mass measurement. The weight loss evolution of the samples is calculated according to Eq. (5.2). In the case of lip seals the mass loss is directly associated with wear, as shown in previous investigations [210,251,257,326,327] and therefore in this study it is only referred as wear.

6.1.5. Test rig for seal performance evaluation

To evaluate the performance of several lip seals under varying temperatures and rod roughness, a custom test rig was designed and built. The test rig (Figure 6.1) mimics the expected seal operating conditions in the R2Mx reactor and consists of a vacuum chamber, a reciprocating rod, and a load cell to measure the friction force. The lip seal is mounted on a flange of the vacuum chamber and the sealing between the flange and the lip seal's steel case is performed by an FKM O-ring lubricated with vacuum grease. On the contrary, between the lip seal and the rod no vacuum grease was applied, as this allows for a direct measurement of the actual leakage rates and ensures that the wear assessment reflects dry sliding conditions. While lubrication can reduce wear, its exclusion here provides a clearer understanding of the rod seal's intrinsic performance. Previous studies [211,328] have explored how various lubricants affect the seals and counterface wear, and this tribological correlations could be further investigated in future stages of the research.

The rod is driven in a reciprocating motion by an electric linear actuator, which consists of a servo motor and a lead screw setup, allowing for precise control of the stroke length and frequency. A linear ball bearing is mounted on the vacuum chamber's flange to ensure that the rod remains properly aligned during motion, reducing strain on the seal. Furthermore, the test rig is equipped with a heating system which consists of an HMT-450 heating jacket (Horst GmbH, Lorsch, Germany) placed around the vacuum chamber and a temperature controller capable of maintaining a set temperature with a ± 2 °C accuracy. To control the temperature of the test rig two thermocouples are installed at the midpoint of the flange's thickness where the lip seal is mounted at approximately 5 mm distance from the lip seal's steel case.

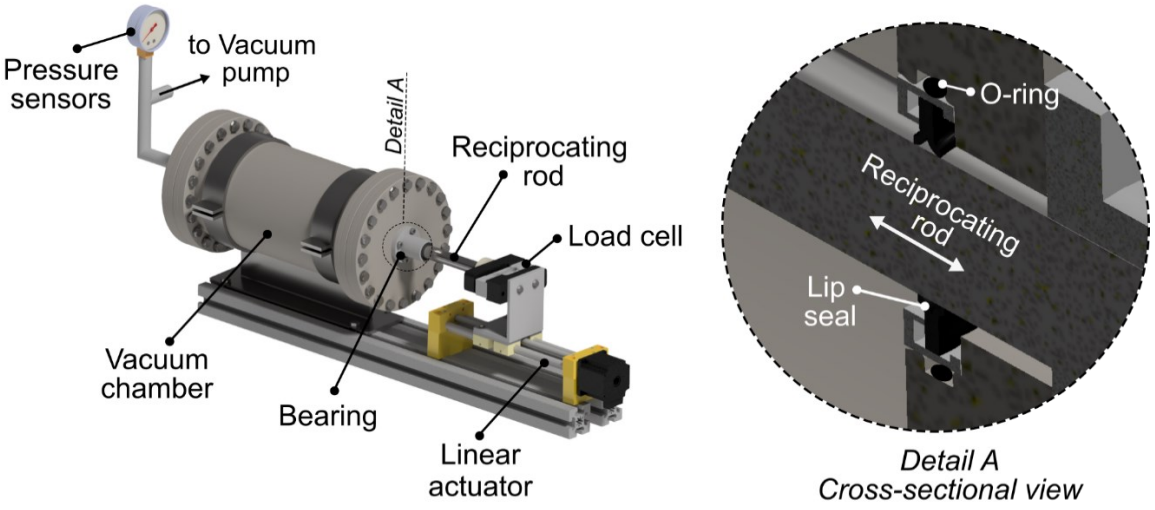

Figure 6.1: Computer aided design (CAD) of the test rig utilised. The heating system is not shown for illustration purposes. *Detail A* shows the cross-sectional view of the flange of the vacuum chamber, where the rod seal is mounted.

Initially, the rod is inserted through the lip seal, and then this assembly is mounted on the vacuum chamber. For each lip seal test a new rod is used, to avoid cross-contamination of wear particles. During testing, the vacuum chamber is first evacuated to 0.5 mbar utilising a vacuum pump, and with the rod stationary the pressure rise within the chamber is evaluated for 45 min to determine the leakage rate according to Eq. (3.1). In tests where a high temperature is required, the system is allowed to heat to the desired temperature, and then the static leakage rate measurement is performed again at high temperature for 45 min. While the temperature is kept constant at the desired value, the reciprocating motion of the rod initiates and remains continuous for 6 or 12 consecutive hours (6 hours during ambient temperature testing). During this time, the pressure in the vacuum chamber is monitored to evaluate the leakage rate of the seal. After the specified period of reciprocating motion is completed, the vacuum chamber is once again evacuated to 0.5 mbar, and the leakage rate of the seal with the stationary rod is determined. This procedure is repeated according to the experimental plan, which foresees wear and deformation measurements of the lip seal at different time intervals. To perform these measurements, the lip seal and rod are dismounted from the vacuum chamber, and after the measurements are completed, they are reinstalled in the test rig with a new FKM O-ring.

During static and reciprocating motion testing, the pressure rise in the vacuum chamber is measured using two sensors: a pirani gauge (Inficon, Bad Ragaz, Switzerland) with a measuring range of $1 \cdot 10^{-4}$ to 10 mbar and an accuracy of 1%, and a full range gauge PKR 361 (Pfeiffer Vacuum, Aßlar, Germany) measuring range of $1 \cdot 10^{-9}$ to 1000 mbar and accuracy of 30%. The friction force is measured continuously using a 10 kg load cell (Antratek, Bremen, Germany). The

background leakage of the test rig is measured by replacing the lip seal with a steel disk and performing the same test procedure. The background leakage of the test rig was found to be negligible compared to the static and dynamic leakage of the lip seal. Additionally, the static O-ring is expected to contribute at least an order of magnitude less to the overall leakage than the lip seal. Although the O-ring is also subjected to high temperatures, adhesive interactions with the mating surface under static conditions allow it to maintain sealing integrity even after advanced material degradation, as shown in previous studies [156,178,181,183].

6.1.6. Rods

Several carbon alloy steel rods of grade CF53 [329] with two surface roughness, polished and rough, were tested. Both types of rods have a 60 HRC hardness, an outer diameter of 20 mm, and a length of 200 mm. The diameter of the rods coincides with the geometry of the foreseen transport system of the R2Mx reactor prototype, however the length of the rods is five times shorter than in the intended application. In the experimental setup, the rod has a horizontal reciprocating motion, therefore its length was reduced to minimise bending moments and ensure concentricity with the seal. However, in the R2Mx reactor, the rod will move vertically, minimising the bending moments and allowing for a larger rod length. The rod's polished surface was obtained by utilising a rotary polishing machine with polishing pads, while the rough surface was achieved by grinding the rods in a radial direction without axial feed (to produce parallel scratches) with a 300-grit silicon carbide sandpaper.

The 2D topography of the rods was measured at eight axially and circumferentially equidistant points using a CVR-135 surface roughness tester (Bowers Group, Camberly, UK). To ensure the accuracy and repeatability of the measurements, the diamond needle of the surface roughness tester was always placed on the crest of the horizontally positioned rods. The following Table 6.1 details the average surface roughness parameters of the used rods and the recommended rod roughness as specified by the manufacturer of the lip seals.

Table 6.1: Surface roughness parameters of the tested rods and those recommended by the lip seals' manufacturer [222].

	R_a [µm]	R_z [µm]
Manufacturer's specifications	0.1 – 0.4	0.65 – 2.5
Polished rods	0.08	0.63
Rough rods	0.37	2.8

6.1.7. Testing conditions

All the lip seals were tested in the previously described test rig, utilising the same experimental procedure, however parameters such as temperature, rod roughness and duration were varied. The following Table 6.2 summarises the testing conditions employed.

Table 6.2: Overview of testing conditions.

Test	Rod type	Amount of seals tested	Temperature [°C]	Test duration [d]
A1	Polished	2	22	4
A2	Rough	2	22	4
B1	Rough	2	250	8
B2	Rough	2	275	8
B3	Rough	2	300	8

For all experiments, the speed of the rod was kept constant at 100 $mm \cdot s^{-1}$. Prior the main testing phase, a short run-in time of 1 hour at 50 $mm \cdot s^{-1}$ was carried out. The influence of this initial phase on the wear of the seals was found to be negligible, as also reported in literature [266].

6.1.8. Optical microscopy of lip seals

To examine the morphological changes of the lip seals before and after testing, optical microscopy was employed. This analysis method in particular was used to evaluate and compare the wear patterns and mechanisms of the lip seals under different operating conditions. After the specified testing intervals in the experimental plan were completed, the lip seals were dissembled from the test rig and examined utilising a SteREO Discovery V20 light microscope (Carl Zeiss AG, Oberkochen, Germany) equipped with an AxioCam digital microscope camera.

6.1.9. 3D scanning of lip seals

The deformation of the lip seals was evaluated utilising a 3D optical scanner, allowing for non-invasive and accurate measurements at several time intervals during testing. The seals were disassembled from the test rig and cleaned with isopropanol in an ultrasonic bath. 3D scanning was performed exactly one day after disassembly from the test rig, to allow the lip seals to return to their original shape and minimise possible time-dependant viscoelastic effects. The scanning was performed using an ATOS Q 12M (Carl Zeiss AG) system, with 12 million points per scan, a point distance of 0.029 mm, and over a measuring field of 100 x 70 x 60 mm. To capture the entire 360° geometry of the seal, the samples were placed on an electric rotating table GOM ROT 640 and scans were performed at 18 evenly spaced positions on both sides. The 3D scanning data was post-processed using the GOM Inspect software package.

The lip seal's complex configuration, comprising black polymeric lips and a polished steel case, presented a challenge for 3D scanning. The significant contrast between these two materials resulted in a substantial difference between the intensity of the reflected light, making it difficult to capture a complete high-resolution scan of the seal. Therefore, the scanning was focused on capturing the PTFE lips to the highest degree of accuracy, as they represent the most critical part of the seal.

6.2. Results and discussion

This section presents the results of the experimental investigation into the degradation behaviour and performance of PTFE-based rod seals under operating conditions representative of the R2Mx solar reactor. Initially the results of the accelerated ageing tests conducted on PTFE flat samples, aimed at assessing changes in key material properties resulting from prolonged thermo-oxidative exposure are presented. These tests provide foundational insights into the chemical and physical stability of the material under high temperatures (250–300 °C). Subsequently, the performance of lip seals is examined using a dedicated test rig designed to simulate real-world operating conditions. Two main scenarios are considered: ambient temperature operation, in which two different rod surface roughness are evaluated, and high-temperature operation (250–300 °C), where testing is performed exclusively with rough rods to accelerate degradation of the seals. Measured seal characteristics such as friction force, wear behaviour (weight loss and wear type), lip seal deformation, and leakage rate are reported and discussed. Finally, based on the experimental findings, a methodology for predicting the service lifetime of the rod seals in the R2Mx reactor, which incorporates a predefined leakage rate threshold, is proposed.

6.2.1. PTFE compound thermo-oxidative ageing

Weight loss is considered a measure of material degradation, particularly in the context of thermo-oxidative ageing. The percentage weight loss of the PTFE compound flat samples as a function of ageing time and temperature, relative to the unexposed state, is shown in Figure 6.2.

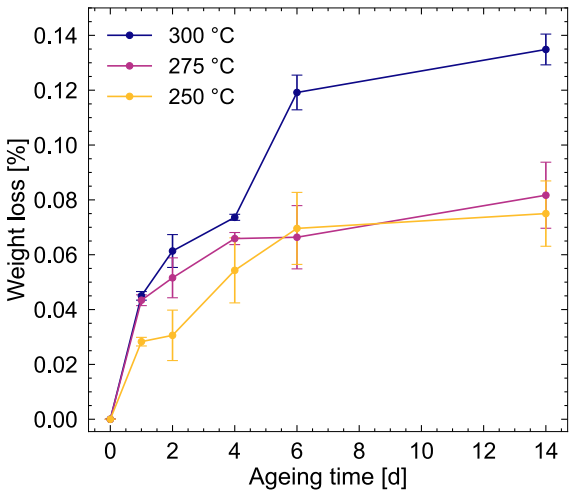

Figure 6.2: Weight loss of thermo-oxidative aged PTFE compound flat samples as a function of ageing time and temperature.

The tested PTFE compound exhibits a characteristic degradation profile: an initial phase of relatively rapid weight loss, followed by a slower rate of mass reduction as ageing time increases. This trend suggests that the degradation process slows over time, potentially due to initial depletion

of residual moisture or volatile components. As expected, weight loss is more pronounced at elevated temperatures, confirming that thermal exposure accelerates the degradation process. However, even at the highest tested temperature of 300 °C and the longest ageing duration (14 days), the total weight loss remains minimal, reaching only 0.13%. This indicates a high degree of thermal stability for the PTFE compound under the tested conditions.

Weight loss in aged PTFE materials may arise from the evaporation of residual moisture, plasticisers, or processing additives, as well as from the formation and release of volatile products as a result of thermal degradation. The dominant degradation mechanism for PTFE during thermo-oxidative ageing is generally considered to be chain scission, which leads to the formation of difluorocarbon radicals (CF_2•) and the generation of tetrafluoroethylene (TFE) monomers [136,240,241]. These volatile species evaporate during heating, resulting in a measurable mass loss. The small observed weight loss of the studied PTFE compound suggests that thermal degradation of the polymer at the tested temperatures is limited and is consistent with previous research. Simon and Kaminsky [136] reported that virgin PTFE undergoes slow decomposition above 260 °C, with more pronounced degradation only occurring beyond 400 °C. Similarly, Huang et al. [240] found negligible weight loss during thermo-oxidative ageing of PTFE between 340–400 °C up to 100 h and fast weight loss at 450 °C with the samples losing almost half of their initial weight after 50 h of ageing. Teyssedre et al. [330] found a 5% weight loss at 250 °C and 300 °C after approximately 263 and 85 days, respectively.

To evaluate the effect of thermo-oxidative ageing on the mechanical properties of the PTFE compound, the hardness of the flat samples was measured before and after ageing. Figure 6.3 presents the Shore D hardness values of the PTFE compound as a function of ageing time and temperature. The initial hardness of all unexposed samples was 63 Shore D, indicating uniformity across the batch prior to thermal ageing. Throughout the ageing protocol, the hardness of the PTFE compound remained relatively stable. A slight variation of ±0.2 Shore D points was observed in samples aged at 250 °C and 275 °C, which falls within the expected measurement uncertainty. A more notable decrease of approximately 3 Shore D points was recorded after 14 days of ageing at the highest temperature of 300 °C. A reduction in hardness is typically indicative of polymer degradation via chain scission, which is in line with the previously discussed and widely accepted dominant degradation mechanism of PTFE.

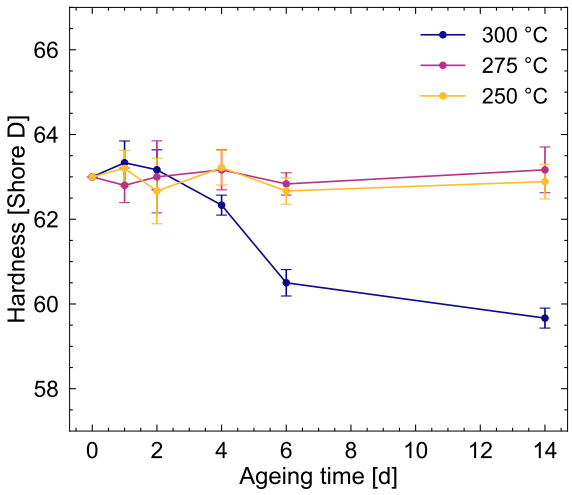

Figure 6.3: Hardness of PTFE compound flat samples as a function of thermo-oxidative ageing time and temperature.

While the literature on the hardness change of PTFE subjected to thermo-oxidative ageing is limited, existing studies suggest that PTFE hardness remains unaffected by degradation. For instance, García Tuero et al. [331] reported only a minor decrease in PTFE hardness (-4 Shore D points) after 672 hours of ageing in automatic transmission fluid. Similarly, Hasseb et al. [332] observed no measurable change in PTFE hardness following 1000 hours of exposure to diesel and biodiesel at room temperature. Other studies, such as those by Ucar and Basdogan [333] and Feyzullahoğlu [334], have found that polymers with high hardness exhibited better wear resistance and anti-extrusion ability. These findings highlight the suitability of PTFE as sealing material in the context of a lip seal at high operating temperatures. Based on the weight loss and hardness data obtained in this study, it can be concluded that the tested PTFE compound (TEDEX-B) demonstrates behaviour consistent with that of standard PTFE material, namely, high thermal resistance and minimal degradation under the applied conditions.

6.2.2. Lip seal performance at ambient temperature

Given that the TEDEX-B material exhibits behaviour consistent with standard PTFE, and that the changes in material properties due to thermo-oxidative ageing are minimal, wear and tribological factors become significantly more influential in determining the service life of the lip seals. Accurate life prediction of seals is highly desirable; however, the time and cost associated with obtaining failure data from field testing can be extremely large, and therefore, accelerated life testing methods are often employed. These methods typically use the main parameter that affects the life of the component as a control variable to simulate and expedite degradation processes [335]. In tribological systems, the selection of an appropriate accelerated testing parameter depends on the predominant wear mechanism [268].

In this work, the effect of using a roughened rod surface to accelerate lip seal wear was investigated. The performance of the lip seal at ambient temperature was evaluated using several analysis techniques such as optical microscopy, seal deformation analysis, force measurements, weight loss due to wear, and leakage rate monitoring. By comparing the results of tests conducted with both a polished and a rough rod surface, an acceleration factor can be derived, and the feasibility of this approach for lifetime prediction assessed. Both tests were conducted over a duration of 4 days under ambient conditions.

Deformation analysis

3D scanning was used to qualitatively evaluate the geometry changes of the lip seals after testing with the reciprocating rods. The following Figure 6.4 shows radial cross-sectional outlines of lip seals after testing with rough and polished rods at different time intervals. For the tested seals the 3D scans were performed after removing the rod from the middle of the sample, and thus letting it go back to its original shape for 1 day. For both testing conditions, rough and polished rod, the lips exhibit a gradual opening and hence creep as the testing duration progresses. The initial lip seal outline (0 days) shows a seal geometry in an as-is from the manufacturing state and is later deformed to fit the 20 mm-diameter rod. After 2 days of testing, the lip seal is able to recuperate near its original shape but there is evidence of plastic deformation as the geometry does not completely come back to the initial one. The lips' thickness decreases either because of wear or the lips are being opened for which the material has to become thinner to accommodate the increase in length. After 4 days of testing, the lip seal becomes slightly wider, as a sign of creep under constant contact stress with the rod. Here, it is possible to observe a slower steadier deformation compared to that seen from 0 to 2 days of testing. In service and testing conditions the lip seal is radially pressed against the reciprocating rod, leading to relaxation over time and plastic flow of the material. Both of which result in the edges of the lip becoming further apart from each other. Notably, both rough and polish rod, lead to almost identical deformation profiles of the lip seal. This suggests that macro-scale deformation and creep are not significantly influenced by micro-scale surface over the testing durations examined in this study. The deformation seems to be driven by contact stresses and material response rather than by wear and surface-driven interactions.

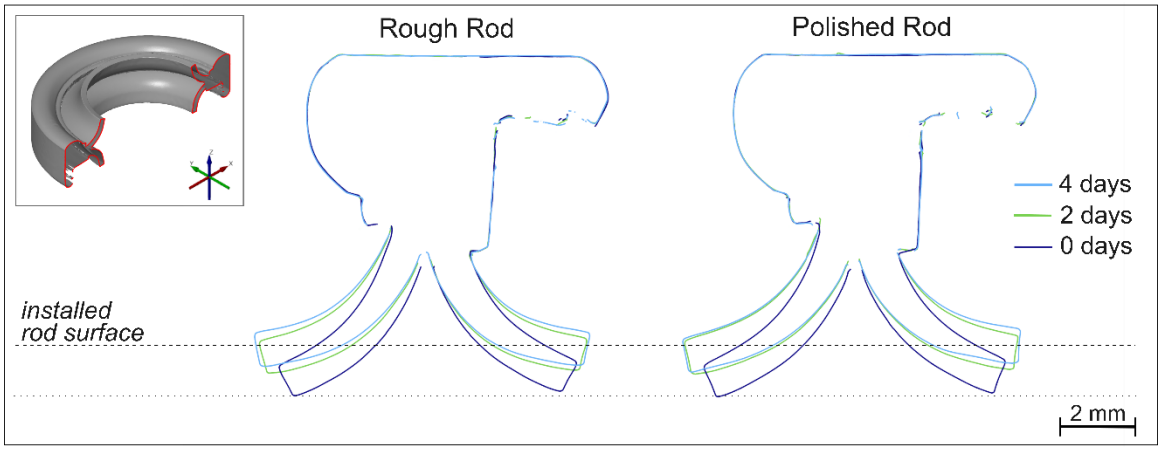

Figure 6.4: Cross-sectional outlines of lip seals after testing with rough and polished rods for varying times.

Force measurements

Throughout the testing, a load cell was employed to measure the force exerted on the rod, with its placement illustrated in Figure 6.1. The force measurements conducted under static rod conditions are presented in Figure 6.5. During these measurements, the vacuum chamber was initially set to a pressure of 0.5 mbar. The recorded force comprises several contributions: the vacuum-induced load on the rod (resulting from the pressure differential), frictional forces by the lip seal, and stresses due to mechanical and thermal expansion. At the start of the static condition measurement, the vacuum-induced force was approximately 31 N; however, as leakage occurred, the pressure, and thus the force changed. Due to the complexity and variability of these interactions, the force data are presented as total values without decomposition into individual contributions.

In the plot, it is evident that the force exerted on the polished rod remains nearly constant throughout the test, with a slight decrease observed after 15 km. This reduction likely corresponds to the development of a well-formed transfer film, leading to a reduction in friction. In contrast, the force for the rough rod starts similarly to the polished rod at around 60 N (up to 15 km) but increases as the sliding distance increases, with the final recorded value being 67 N. This increase can be attributed to micro-mechanical interlocking between the PTFE material and the rod surface, and disruption of the transfer film. A dark transfer film was observed on both rods; however, in the case of the rough rod, the film appeared more disrupted and less uniform, likely due to interference from surface asperities. The continuous disturbance of the film suggests a less stable tribological interface compared to the polished surface.

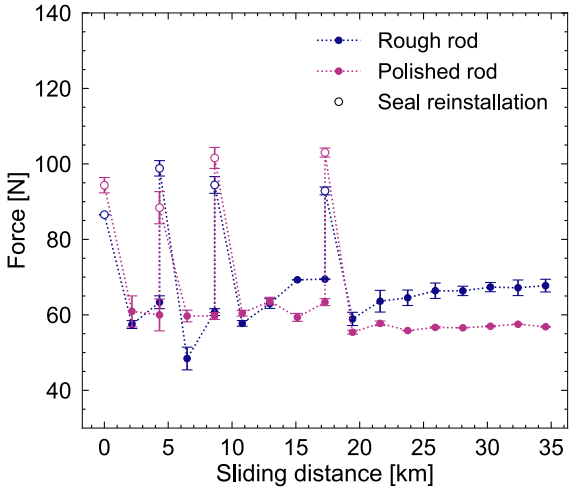

Figure 6.5: Static force measurements as function of sliding distance and rod type. Unfilled markers represent the measurements performed directly after reinstallation of the lip seal in the test rig.

Notably, in both cases, force peaks were observed throughout the sliding distance. These peaks occurred following the initiation of a new testing series, particularly after the rod seal was reinstalled. A high friction force was recorded immediately after reinstallation, likely due to static friction caused by seal deformation and sticking. Despite the system being stationary, the friction force remained significant, requiring a large motor to overcome the initial breakaway force, evident in the sharp force peaks at the start of each series. Overall, the effect of surface roughness resulted in a maximum force difference of approximately 20% towards the end of the test. It is important to note that the vacuum-induced force, which contributes approximately half of the total force, remained independent of the surface characteristics.

Wear

Wear of the lip seals was assessed through optical microscopy and weight loss measurements. Figure 6.6 shows optical microscopy images of the lip seal surface where the polymer interfaces with the moving rod, for a new seal, a seal tested with a polished rod, and a seal tested with a rough rod. The new sample Figure 6.6 (a) exhibits a uniform surface appearance, with no visible wear marks or deformation. Its texture appears slightly porous and homogeneous across the contact region, indicative of the as-manufactured state. The lip seal tested with the polished rod (Figure 6.6 (b)) shows a darkened wear zone at the lip edge, precisely where contact with the moving rod occurred. This darkened area presents a rougher surface texture than the rest of the seal, suggesting initial material displacement. Fine ploughing marks in the direction of the rod motion are evident, consistent with abrasive wear mechanisms [210,253,254]. Furthermore, during testing, the formation of a dark transfer film on the rod was observed, characteristic of adhesive wear processes (Appendix B). The blurred appearance at the edge of the lip seal further suggests mild adhesive wear [253,254]. In contrast, the lip seal tested with the rough rod (Figure 6.6 (c)) displays a more

pronounced darkened contact band with visibly deeper ploughing marks, indicating more severe abrasive wear and aggressive material removal. In addition, material bulges are observed near the trailing edge of the contact zone. These may have resulted from abrasive wear and lateral displacement of the PTFE due to repeated rod movement, potentially exacerbated by localised thermal softening. As with the polished rod, transfer film formation was also noted, suggesting concurrent adhesive wear. However, abrasive wear appears to be the dominant wear mechanism under these test conditions.

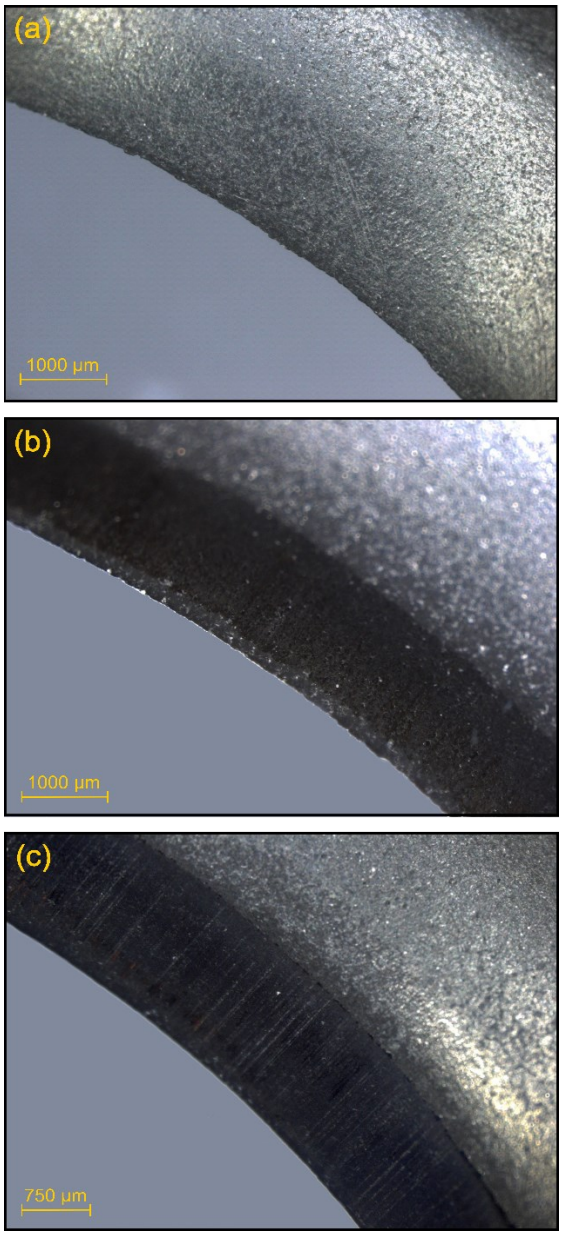

Figure 6.6: Optical micrographs of the inner side of PTFE lip seals, where the polymer meets the moving rod: (a) before testing, (b) after 4 days of testing using a polished rod, and (c) after 4 days of testing using a rough rod.

The weight loss associated with the wear of the tested lip seals in shown in Figure 6.7. Both the polished and rough rod configurations exhibit a similar overall wear trend, characterised by an initial phase of rapid weight loss followed by phase with a decreased weight reduction rate. The initial high wear rate is attributed to severe ploughing and tearing of the polymer surface, occurring before the formation of a stabilised PTFE transfer film. As the contact surfaces adapt and the transfer film gradually forms on the rods' surface, the wear rate stabilises and decreases significantly. The use of a polished rod results in consistently low wear, even after a sliding distance of 35 km. In contrast, testing with a rough rod leads to approximately double the material loss, with a maximum recorded wear of 0.6%. This level of wear is considered mild and is consistent with the findings of Zhao et al. [248], who reported a 0.7% weight loss in hydraulic seals as indicative of mild wear. The increased wear observed with the rough rod is primarily attributed to enhanced abrasive action, difficulty in forming a stable transfer film, and the presence of localised stress concentrations. These factors collectively exploit PTFE's inherent softness and relatively low abrasion resistance, accelerating the material removal process under these more aggressive conditions.

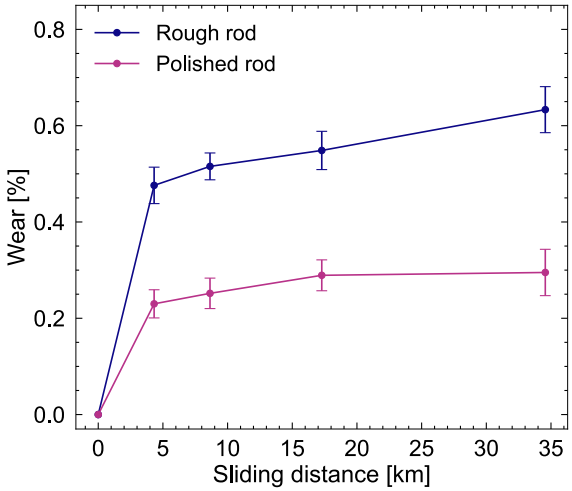

Figure 6.7: Wear of lip seals as a function of sliding distance and rod's surface finish.

Leakage rate

Among the various parameters used to assess seal functionality, leakage represents the most direct and critical indicator of performance failure. Accordingly, in this study, leakage was experimentally measured at defined intervals throughout the testing period. The experimental setup enabled the evaluation of both dynamic and static leakage rates of the lip seals. However, in the context of the R2Mx solar reactor prototype, dynamic leakage, occurring during the transport step, lasts for only approximately 4 seconds, whereas static leakage is expected to occur during the oxidation and reduction reactions, each lasting between 6 and 8 minutes. Given this operational profile, the focus of this investigation is on static leakage performance, as it is anticipated to be the

more critical factor for the reactor's long-term efficiency performance. While dynamic leakage rates are inherently higher, their impact is mitigated by their short-term occurrence.

Figure 6.8 shows the leakage rate of lip seals tested with both polished and rough rods as a function of sliding distance. In both cases, the leakage rate is initially at its lowest, $6.5 \cdot 10^{-4}$ mbar·l·s^{-1} for the polished rods and $2.3 \cdot 10^{-3}$ mbar·l·s^{-1} for the rough rods. After approximately 5 km of sliding, the leakage rate stabilises and remains nearly constant for the remainder of the test duration at $2 \cdot 10^{-3}$ mbar·l·s^{-1} for the polished rod and $5 \cdot 10^{-3}$ mbar·l·s^{-1} for the rough rod. This trend closely mirrors the wear behaviour discussed earlier, where a high initial wear rate is followed by a more stable wear regime. The rough rod results in a leakage rate approximately 2.4 times greater than that observed with the polished rod. This increased leakage is attributed to the surface finish of the rod; higher surface roughness reduces the conformal contact between the lip seal and the rod surface, promoting the formation of microchannels through which fluid can enter the vacuum chamber. At this stage of the investigation, due to the relatively low degree of wear observed, the higher leakage rate of the rough rod cannot be attributed to material degradation and wear of the lip seal. Instead, it is likely governed by the inherent surface characteristics of the rod that compromise the seal interface.

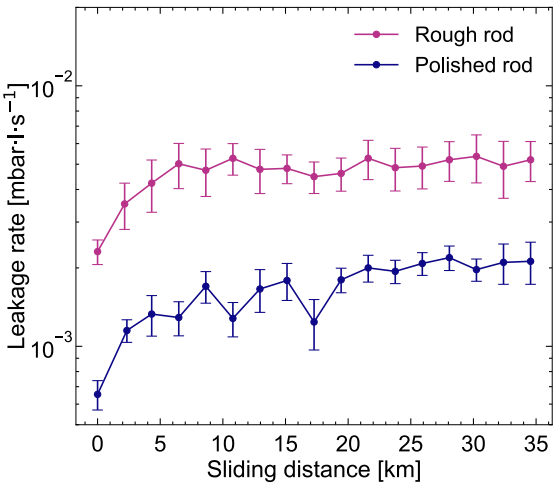

Figure 6.8: Static leakage rate of lip seals as a function of sliding distance and rod type.

6.2.3. Lip seal performance at high temperature

Having examined the influence of using a rough rod to accelerate the lifetime testing of lip seals at ambient temperature, the next section of this study focuses on high-temperature testing of the rod seals. Tests were conducted at three temperatures, namely, 250 °C, 275 °C, and 300 °C, using the same experimental setup over a duration of 8 days. All high-temperature tests were performed with rough rods to promote wear and facilitate the assessment of thermal and tribological performance under more severe operating conditions.

Deformation analysis

Figure 6.9 illustrates the cross-sectional geometry of lip seals tested at temperatures between 250 °C and 300 °C with a rough rod. For all tested temperatures, the lip seals exhibit a progressive opening of the lips, indicative of time and temperature dependent creep. The initial seal profile (0 days) represents the undeformed, as-is geometry, which is radially compressed when installed onto the 20 mm-diameter rod. After 2 days of testing and subsequent 1 day of recuperation, the lip seals begin to recover their original shape, but all profiles, including the lowest tested temperature, show clear evidence of incomplete elastic recovery, highlighting the onset of plastic deformation. At 250 °C, the deformation is relatively minor, with the lips still approximating their initial position, though a slight permanent opening is present. This deformation is comparable to the one observed at ambient temperatures. At 275 °C and 300 °C, the lips open more noticeably, with the deformation increasing steadily from 2 days to 8 days of testing. The outer lip tips move further outward, and the overall width of the seal profile increases, consistent with creep under continuous thermal and contact stress. At 300 °C, the deformation becomes more pronounced, and the seal geometry exhibits signs of asymmetry and contour loss, suggesting the beginning of thermal degradation or viscoplastic flow. These permanent deformations may reduce the radial interference fit against the rod, potentially compromising sealing performance. The similarity in deformation patterns across different temperatures, particularly between 275 °C and 300 °C, further suggests that temperature is the dominant factor influencing deformation.

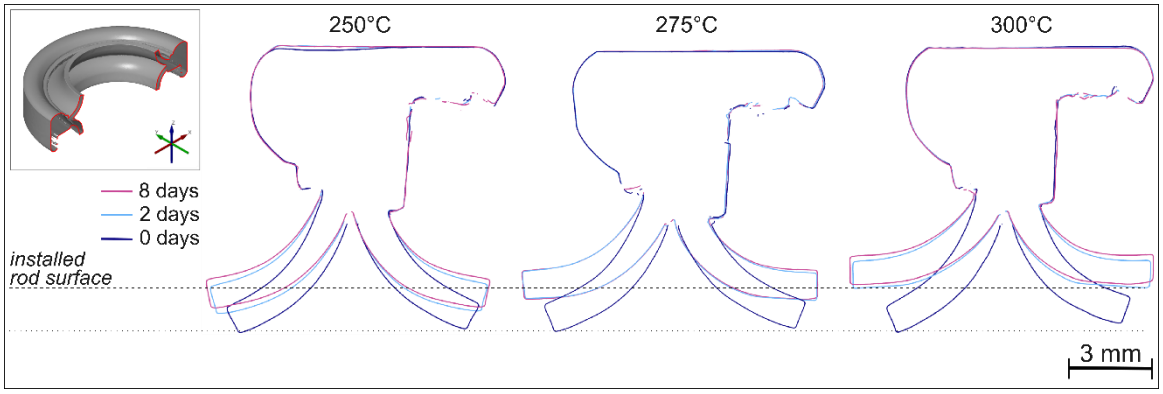

Figure 6.9: Cross-sectional outlines of lip seals tested at 250 °C, 275 °C and 300 °C for varying times.

Force measurements

Similarly to the ambient temperature testing, the axial force acting on the reciprocating rod was recorded as a function of sliding distance for each of the testing temperatures (Figure 6.10). The reported force includes contributions from the vacuum pressure differential (~31 N at ambient temperature), frictional interactions between the seal and rod, as well as thermally induced stresses. Initially, all seals tested between 250 °C and 300 °C exhibit high friction forces, with peak values ranging from approximately 100 N to 120 N, indicating strong interference between the lip seal and

the rod, potentially indicating polymer bedding-in effects. Furthermore, the force recorded during high temperature testing are noticeably higher than those reported for ambient testing. This is likely attributed to the thermal expansion of the rod and seal, which increases radial interference and thus friction. Another explanation could be the instability of the transfer film due to high temperature operation, which could similarly lead to increased friction.

As sliding progresses, the force gradually declines, more noticeably at the highest testing temperature, 300 °C. This reduction can be attributed to a combination of material wear-in, contact surface adaptation, and relaxation of radial sealing pressure due to creep. For 250 °C and 275 °C, the force stabilises after approximately 20–30 km of sliding, indicating a transition into a steady-state friction regime, with a force reduction observed for 275 °C only towards the end of the test. In contrast, at 300 °C, the force decreases more rapidly and continuously, eventually reaching values below 60 N, which may signal a substantial loss of sealing pressure due to accelerated creep or softening of the material due to the high operating temperature. Points marked with open symbols indicate seal reinstallation, which leads to a temporary increase in force, likely due to the reestablishment of lip-rod interference. Overall, this data confirms that elevated temperatures promote both material softening and creep, which in turn reduce sealing forces over time, potentially undermining long-term sealing performance.

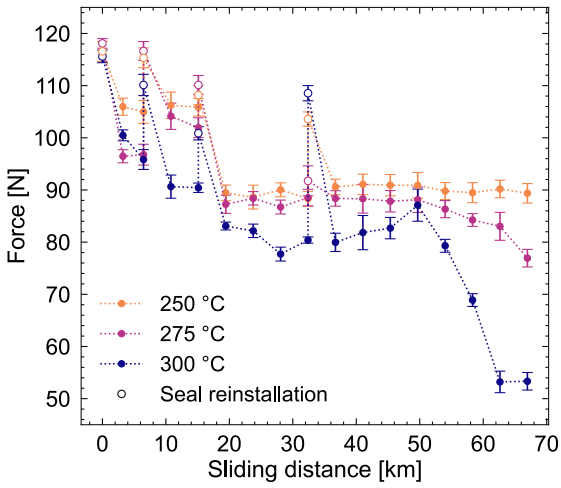

Figure 6.10: Force measurements during static position of the rod, as a function of testing temperature and sliding distance.

Wear

Wear in the lip seals tested at high temperatures with a rough rod was initially assessed by utilising optical microscopy. The optical microscopy images presented in Figure 6.11 show the inner area of the PTFE lip seals tested under reciprocating motion for a duration of 8 days. The darkened band in each image corresponds to the rod contact region, where direct tribological

interaction and material deformation occur. At 250 °C, the wear track appears relatively uniform and sharply defined, with parallel ploughing marks aligned in the sliding direction. This indicates a predominantly abrasive wear mechanism, where micro-asperities on the rod's surface plough into the PTFE, producing consistent material removal without substantial surface degradation. At 275 °C testing temperature, the wear band remains distinguishable but becomes more blurred, with reduced contrast and a slightly smoother appearance. This suggests a transition toward adhesive wear, where increased temperature softens the PTFE matrix, promoting localised material transfer or smearing and reducing the severity of abrasion. The nature of the contact suggests the transfer film might be less stable or patchy, leading to intermittent adhesion and mild smearing.

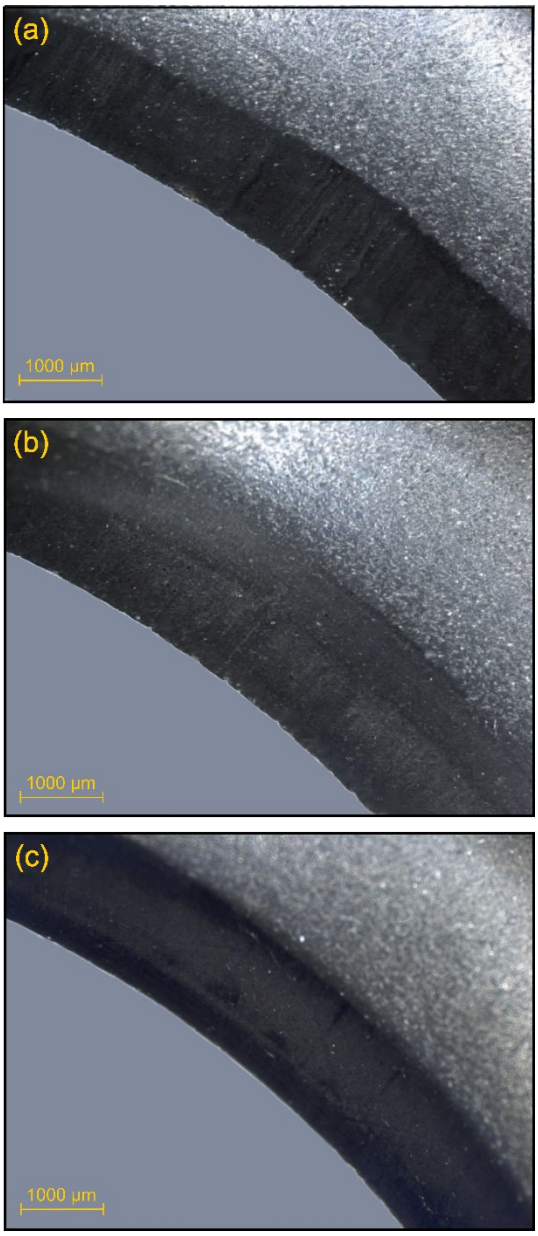

Figure 6.11: Optical micrographs of the inner side of PTFE lip seals, where the polymer in contact the moving rough rod, for a testing duration of 8 days at different testing temperatures: (a) 250 °C (b) 275 °C, and (c) 300 °C.

At 300 °C (Figure 6.11 (c)), the wear track exhibits pronounced darkening, blurred boundary edges, and surface waviness, all indicative of significant material softening and viscoplastic flow. These morphological changes suggest that PTFE has reached a regime where its mechanical response is dominated by creep deformation, coupled with the onset of thermal degradation. The testing temperature, 300 °C measured near the seal's casing, suggests that flash temperatures at the seal-rod interface could be even higher during reciprocating motion, potentially exceeding the PTFE's softening point and approaching its melting range. Such high flash temperatures are consistent with those reported in literature [259,336] and can lead to creep-assisted deformation and loss of mechanical integrity at the contact surface as PTFE approaches its crystalline relaxation and thermal stability limits. Under these conditions, interfacial stresses can lead to delamination of the surface layers of the lip seal. This phenomenon is consistent with the observed irregularities and micro-shearing features on the worn lip surface. Furthermore, at very high temperatures (> 320 °C) the polymer's crystalline regions begin to relax or partially melt, leading to a substantial reduction in modulus and dimensional stability [143,225]. Consequently, the PTFE's ability to form and maintain a coherent transfer film is compromised, resulting in an unstable film that accumulates in lumps, as evidenced during testing. Such an inhomogeneous transfer film, instead of acting as a protective layer, may increase friction and localised heating leading to further degradation [255,256]. Overall, the progressive darkening and broadening of the wear track with increasing testing temperature reflects a shift in dominant wear mechanisms, from abrasion at lower temperatures, to adhesion and smearing at intermediate temperatures, and finally to thermally activated flow and creep at the highest tested temperature.

Wear was further assessed through weight loss measurements as a function of testing temperature and sliding distance, as illustrated in Figure 6.12. Consistent with observations from ambient temperature testing, all tested temperatures exhibit an initially high wear rate during the early phase (< 5 km), which subsequently stabilises and remains relatively constant over the remainder of the test duration. The wear behaviour of the PTFE lip seals demonstrates a clear temperature dependence, particularly beyond 250 °C. While, the percentage weight loss due to wear remains relatively stable from ambient conditions up to 250 °C, only showing a marginal increase, a pronounced increase in wear is observed at higher temperatures. Specifically, the wear rate increases by 55% between 250 °C and 275 °C, and 78% between 275 °C and 300 °C. This trend reflects the thermal limitations of PTFE, especially as the material approaches and exceeds its crystalline relaxation threshold. At these elevated temperatures, the polymer becomes increasingly prone to viscoplastic deformation and surface flow under mechanical stress. Additionally, high temperatures hinder the formation and stability of a protective transfer film, resulting in increased frictional heating and localised thermal softening. After 66 km of testing at 275 °C, a 1.1% weight

loss was recorded, which is indicative of moderate wear, as highlighted in a previous study of hydraulic seals [248]. However, under vacuum conditions, such levels of wear may already compromise sealing performance due to the higher sensitivity of vacuum systems to dimensional and surface integrity. At 300 °C, degradation mechanisms are further intensified, contributing to a significant increase in wear, with a recorded weight loss of 1.75% after 8 days of testing (66 km sliding distance). Such wear levels are likely to adversely affect the sealing efficiency and long-term durability of the lip seals in high-temperature vacuum applications.

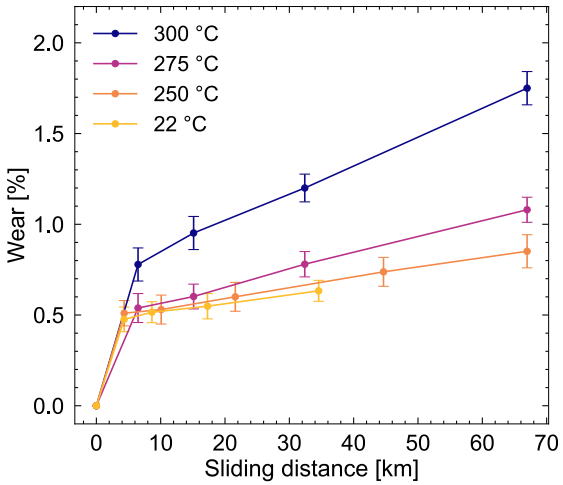

Figure 6.12: PTFE lip seals' wear as a function of sliding distance and testing temperature.

Leakage rate

In order to assess the performance of the rod seals, the leakage rates of the PTFE lip seals tested at high temperatures were recorded and are depicted in Figure 6.13. Similarly as with the ambient temperature case, static leakage rates are reported. Furthermore, a threshold or maximum acceptable leakage rate has been defined considering the specific requirements of the application as well as criteria commonly adopted in vacuum technology [323]. As in the previously discussed O-rings investigation (Chap. 5), the threshold leakage rate was conservatively defined as a tenfold increase relative to the leakage rate of the new lip seals. In Figure 6.13, the threshold leakage rate (q_L) is $1.2 \cdot 10^{-2}$ mbar·l·s^{-1} and is represented by a black dash dot line.

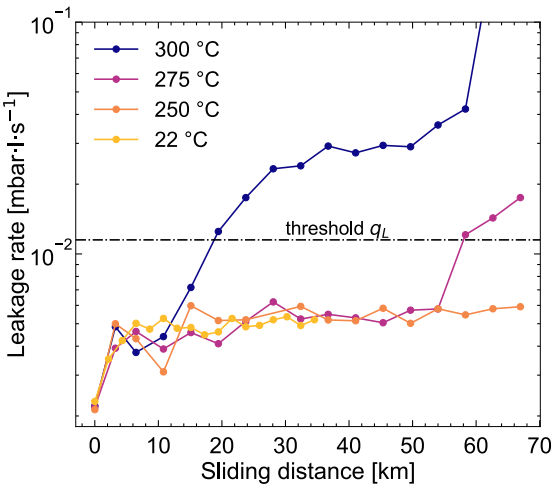

Figure 6.13: Leakage rate of PTFE lip seals as a function of testing temperature and sliding distance. Threshold leakage value is represented by a black dash dot line. Error bars are not displayed for illustration purposes, however a version of this figure with error bars and a table containing the detailed data set including the standard deviation of each data point are provided in Appendix B.

The leakage rate trends across all tested temperatures exhibit a similar shape with an initially low leakage phase ($1.2 \cdot 10^{-3}$ mbar·l·s^{-1}), followed by an increased leakage rate period which remains stable ($5 \cdot 10^{-3}$ mbar·l·s^{-1}), and, in higher temperature cases, a subsequent increase beyond failure leakage rates. At 22 °C and 250 °C, the leakage rate starts with a low leakage phase and then stabilises well below q_L, maintaining consistent sealing performance throughout the entire test. At 275 °C, a similar early stabilisation phase is observed, but after about 50 km, the leakage rate begins to rise steadily, ultimately surpassing q_L, with failure evidenced at approximately 58 km. In the 300 °C case, the leakage remains low at first, stabilises momentarily, but then shows a large increase beyond q_L after only about 19 km, indicating failure and rapid seal degradation due to high thermal stress. Failure of the sealing system is considered to occur once the leakage rate of the seals has increased beyond q_L. At both testing temperatures where failure was observed, 275 °C and 300 °C, the leakage increase occurred in progressive manner, contrary to the abrupt failure that was observed for O-rings. This phenomenon is consistent with previous investigations that also report progressive increase in leakage of rod seals [260,337,338]. Furthermore, it is important to highlight that the leakage rates reported in this study refer to reciprocating motion in dry conditions. In practical applications, vacuum grease could be used in order to reduce wear and leakage.

Service lifetime prediction

Predicting the service lifetime of rod seals is essential for optimising maintenance schedules and ensuring sustained efficiency of the R2Mx reactor system. According to literature, wear is identified as the primary factor influencing sealing performance of rod seals under reciprocating motion [209,260,338]. Accordingly, this study defines seal failure criterion based on empirically measured leakage rates and the corresponding seal's weight loss due to wear. From the

experimental results, it can be deduced that seal failure at 275 °C occurs at approximately 58 km of sliding distance, corresponding to a wear of 0.99%. Similarly, at 300 °C, failure is observed at around 19 km, also coinciding with a 1.01% wear. These results suggest that, for the system studied, a 1% weight loss may serve as a practical end-of-lifetime criterion.

It is important to note that time-temperature superposition (TTS) is not applicable when the dominant wear mechanisms vary with temperature. In this study, this is evidenced by the transition in wear behaviour observed across the tested temperature range. Since failure was experimentally observed at 275 °C and 300 °C, the only testing condition for which failure must be estimated is at 250 °C. For this case, the wear curve presented in Figure 6.12 is extrapolated to identify the point at which 1% wear occurs, providing an estimate of the service lifetime. This approach, while straightforward, has limitations. Leakage is not solely a function of weight loss due to wear; it is also influenced by changes in contact pressure arising from material removal and at high temperatures such as the ones tested, creep also becomes a significant factor. Finite element analysis (FEA) by Avanzini and Donzella [339] demonstrates that leakage increases non-linearly as wear alters the seal lip contact profile. This non-linear relationship is corroborated by Figure 6.7 and Figure 6.8, which show that although wear increases steadily, the leakage rate remains relatively constant at 250 °C but rises abruptly at 300 °C. Moreover, a 1% weight loss at 250 °C may not correspond to failure if the wear is more uniformly distributed compared to the more localised or severe degradation seen at higher temperatures. Despite these uncertainties, the 1% wear end-of-lifetime criterion is adopted here as a reasonable approximation for failure in the absence of direct leakage rate measurements at this temperature. The data points and linear fit used to extrapolate the wear failure point of the lip seals tested at 250 °C are shown in Figure 6.14. A linear regression was performed on the second phase of the wear curve, where the wear rate remains constant, achieving a very satisfactory fit with a coefficient of determination of 0.998. Findings suggest that after sliding for 92.8 km at 250 °C, the PTFE lip seal will have a 1% wear and therefore a leakage rate higher than q_L, exhibiting failure.

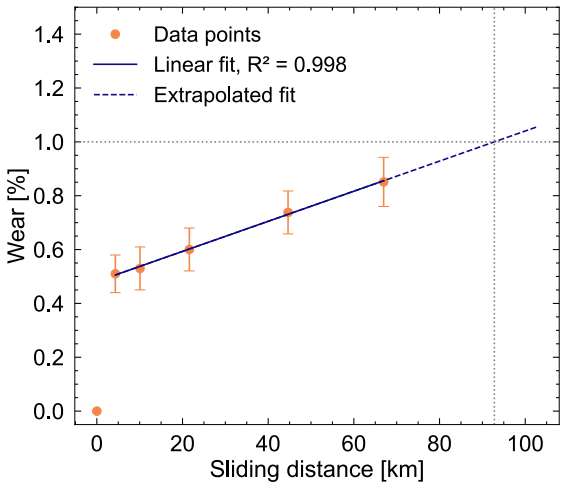

Figure 6.14: Wear of lip seals tested at 250 °C as a function of sliding distance. Linear fit performed on the experimental data and extrapolated beyond the measured sliding distance to estimate when wear reaches 1%. The corresponding distance at which wear equals 1% is 92.8 km.

The estimated service lifetimes of the PTFE lip seals tested with rough rods, originally expressed in terms of sliding distance (km), can be converted into operational days by considering the stroke length of the transport rod in the R2Mx reactor (1.2 m) and the cycle duration. The total time it takes to complete one thermochemical fuel production cycle can vary significantly depending on the size of the reactor and the operational strategy. To ensure a conservative and representative estimate, reaction step durations were based on the modelling work of Brendelberger [26], who developed a plant model for a MW-scaled version of the R2Mx reactor and evaluated the system's performance over a wide parameter space. For the purposes of this service lifetime assessment, the so-called "peak efficiency set", which refers to the parameter set that leads to the highest average annual plant efficiency, was selected. Within the peak efficiency set (provided in Appendix C), the optimal reduction step duration is 100 s, and therefore in this work it is assumed that a complete fuel production cycle will also incorporate two transport steps each lasting 4 s and a oxidation step assumed to have a similar duration as the reduction step. Additionally, as outlined in Chap. 6.2.8, the solar reactor is expected to operate for 8 hours per day, reflecting the sun availability. Considering these assumptions, the service lifetimes of the PTFE lip seals have been converted from sliding distance into the corresponding number of cycles and operational days. These results are summarised in Table 6.3, presenting both the experimentally measured and predicted service lifetimes.

Table 6.3: Measured and predicted service lifetime of rod seals operating in reciprocating motion with a rough rod at several temperatures.

Temperature	**Service lifetime**		
[°C]	*Sliding distance [km]*	*Operational cycles [-]*	*Operational days [8h/d]*
250	92.8	30933	223
275	58.2	19400	140
300	19.4	6466	47

Findings suggest that continuous operation of the rod seals at 250 °C and 275 °C results in technically feasible maintenance intervals, approximately annual at the lower temperature and quarterly at the higher temperature. In contrast, operation at 300 °C is not recommended, as the seals would require replacement on an almost monthly basis, which may be impractical from both an operational and economic perspective. However, it should be emphasised that all data presented refer to seals tested against rough rods under dry conditions, which were intentionally employed to accelerate wear. At ambient temperature, the use of a rough rod resulted in approximately twice the seal wear compared to a polished rod under equivalent sliding distances. Nevertheless, as the dominant wear mechanisms transition from abrasive at lower temperatures to adhesive and eventually thermally-induced degradation at elevated temperatures, the validity of this twofold acceleration factor becomes uncertain across the full temperature range. Consequently, a conservative approach has been adopted, and lifetime estimations have not been extrapolated to polished rod conditions. Future investigations are therefore recommended to experimentally assess the durability of lip seals under realistic conditions using polished rods.

The methodology developed to estimate the service lifetime, based on a 1% weight loss due to wear as the end-of-life criterion, is especially relevant for highly dynamic systems where wear is regarded as the primarily failure factor, driven by sliding contact. However, if the R2Mx reactor were to be operated with longer reaction cycles and extended periods of static rod conditions, the dominant failure mode might shift. In such cases, time-dependent phenomena such as creep and stress relaxation would become more significant than sliding wear alone, necessitating an alternative lifetime prediction framework. To that end, additional experimental work is recommended to validate the suitability of the 1% wear threshold at 250 °C through long-term testing.

This study provides an initial framework for understanding the high-temperature wear behaviour of PTFE-based rod seals under continuous reciprocating motion and thermal exposure, representative of prolonged operation within the R2Mx reactor. However, it is important to acknowledge that the experimental conditions reflect continuous high-temperature use, without accounting for the effects of thermal cycling. In real-world reactor operation, the system is subject to daily heating and cooling cycles as it transitions between ambient conditions and high operational temperatures. Additionally, to that, and as outlined in Chap. 5, the rod seal is subject to cyclic

thermal loads as a result of the nature of the thermochemical fuel production cycle. These continuous thermal cycles can introduce additional ageing mechanisms, such as thermomechanical fatigue, creep recovery, and microstructural degradation, which may significantly influence the long-term sealing performance. As such, further research is required to investigate how these cyclic thermal stresses affect the service life and integrity of rod seals. Such investigations are essential for developing more robust and realistic lifetime prediction models that reflect real-world operating conditions. Moreover, the results presented in this work are specific to the PTFE compound, seal geometry, and testing configuration used, and further validation is needed to ensure the applicability of these findings to other polymer formulations and sealing arrangements.

6.3. Summary

This chapter presented a comprehensive investigation into the tribological performance and service lifetime prediction of PTFE-based double lip rod seals for use in a high-temperature solar reactor for thermochemical fuel production.

Initially, the proprietary PTFE-compound (TEDEX-B) was thermo-oxidatively aged to confirm its behaviour was consistent with standard PTFE material and no compound-specific effects must be considered during testing. Next, the influence of surface roughness on the sealing performance of the investigated lip seals was explored by performing tests with polished and rough stainless-steel rods. Deformation analysis of seals tested at ambient temperature indicated minimal geometric alteration in both cases, while force measurements revealed a relatively constant friction profile for the polished rod, whereas the rough rod exhibited an increase in friction over time, likely due to transfer film disruption and micro-mechanical interlocking. The effect of surface roughness resulted in a maximum force difference of approximately 20% towards the end of the test. Wear mechanisms for both rods were predominantly abrasive, with uniform surface wear observed and minimal lip distortion. Also, in both cases the wear behaviour was primarily characterised by an initial high wear rate due to polymer ploughing, followed by a stabilised wear regime once a PTFE transfer film developed on the rod's surface. Leakage rate testing under vacuum conditions revealed an initially low leakage rate that later stabilises into a slightly higher one for both rod types. However, the rough rod exhibited leakage rates approximately twice as high as the polished rod due to reduced seal conformality and microchannel formation at the seal-rod interface. Notably, leakage remained constant after the first 5 km of sliding, consistent with the stabilised wear regime.

The study then investigated seal behaviour at high temperatures of 250 °C, 275 °C, and 300 °C, using rough rods to accelerate failure. Deformation analysis revealed significant permanent deformation of the lip geometry leading increased opening and width of the seal profile at 275 °C and 300 °C. Force measurements showed an overall rise in friction with temperature due to thermal

expansion and a marked decrease in force as the seals approached failure conditions. As temperature increased, wear behaviour transitioned from abrasive to adhesive and finally to thermally dominated mechanisms. Weight loss due to wear increased substantially beyond 250 °C, by 55% at 275 °C and a further 78% at 300 °C, reflecting PTFE's increased susceptibility to viscoplastic flow and surface deformation near its crystalline relaxation point. Transfer film instability and increased frictional heating further exacerbated wear at high temperatures.

Leakage rate measurements under high-temperature conditions showed a sharp increase for seals tested at 275 °C and 300 °C, whereas seals at 250 °C maintained low, stable leakage rates throughout testing. Failure conditions of seals tested at 275 °C and 300 °C were evidenced as their leakage rates surpassed a predetermined leakage threshold ($1.2 \cdot 10^{-2}$ mbar·l·s^{-1}). Based on this data, an end-of-life criterion (1% wear) correlating the onset of increased leakage and wear was defined and used to predict the service lifetime of seals at 250 °C. Findings suggest that continuous operation of rod seals with rough rods at 200 °C and 250 °C will lead to service lifetimes of 223 and 140 operational days, respectively, making these operating temperatures technically feasible. Conversely, continuous operation of the rod seals at 300 °C is deemed unsuitable, as the lifetime is considerably reduced resulting in high maintenance frequency that would have adverse implications for the cost-effective R2Mx reactor performance. The reported seal lifetimes represent conservative estimates, as they are based on tests conducted with rough rods and under dry conditions. In practical applications, the use of polished rods and appropriate lubrication is expected to significantly enhance seal durability. To refine lifetime predictions and broaden their applicability, further long-term testing under high temperatures, thermal cycling, and with polished rods is recommended.

7. Effect of leakage on reactor efficiency

The previous chapters presented an extensive experimental characterisation of the relevant sealing components: Chap. 5 evaluated the degradation and leakage rate development of O-rings under thermo-oxidative conditions, while Chap. 6 addressed the degradation and leakage of the rod seal under dry sliding conditions. The present chapter builds on these findings by integrating the experimentally determined leakage rates into a numerical model of the R2Mx reactor, with the goal of quantifying the impact of leakage on system-level performance.

Leakage in thermochemical reactors remains a relatively underexplored topic, largely because most conventional systems do not require dynamic atmosphere separation at high temperatures. For example, in the state-of-the-art cavity receiver-reactor [6,7,20], where reduction and oxidation reactions occur sequentially within a single reactor chamber, the use of dynamic seals is typically unnecessary in the main vessel. In contrast, the R2Mx architecture demands high sealing integrity to ensure independent atmosphere conditions in each reaction zone. Thus, introducing new operational challenges, particularly related to maintaining vacuum and preventing fuel losses, which in turn critically affect the solar reactor's performance.

This chapter addresses this research gap by developing a numerical model of a generic R2Mx reactor system in order to assess the effects of sealings' leakage rates on the reactor's efficiency. Leakage is incorporated at each step of the redox cycle, reduction, cooling, and oxidation, where it influences the energy demand of the vacuum pump, leads to re-oxidation of reduced ceria, alters gas mixture composition during oxidation, and contributes to fuel loss. The utilised leakage rates are based on the experimental findings of this work and therefore represent realistic values expected in a solar reactor of type R2Mx. By quantifying the loss in solar-to-fuel (StF) efficiency across a range of leakage scenarios, this study establishes a critical link between component-level seal degradation and reactor-scale performance. Insights into the relative impact of the different sealing components and design considerations for future high-performance solar reactors are provided.

7.1. Leakage in an R2Mx reactor

To investigate the influence of leakage on the performance of an R2Mx solar reactor system, this study focuses on a generic reactor model adapted from the work of Brendelberger [26]. The system under consideration features a MW-scale solar irradiated reduction reactor, large amount of independently operated cylindrical redox material assemblies (RMA), and one oxidation reactor per RMA (Figure 2.3 (c)). It is assumed that the pressure separation between reactor zones and ambient is realised by means of a gate with an O-ring and a rod seal, as discussed in Chap. 4. The previous Chaps. 5 and 6 presented an in-depth experimental investigation into the degradation behaviour of these sealing components under representative operating conditions. Their experimentally derived leakage rates serve as the basis for assessing the impact of seal degradation and eventual failure on reactor performance.

Leakage in the R2Mx reactor may originate from either the rod seal or the gate seal, and its impact on reactor efficiency varies depending on the specific step of the thermochemical fuel production cycle. The overall reactor efficiency, commonly referred to as the solar-to-fuel (StF) efficiency, is defined as the ratio of the energy content of the fuel produced to the energy input required to operate the reactor (Eq. (1.3)) [27]. Leakage can significantly impair the StF efficiency by either increasing parasitic energy consumption or reducing fuel yield, motivating a further system evaluation. This modelling work considers solely ceria-based thermochemical hydrogen production, with the three principal process steps being: (1) high-temperature reduction of ceria, (2) its subsequent cooling in the oxidation reactor, and (3) oxidation of ceria with steam to produce hydrogen. The brief transport phases between zones are excluded from the model due to their short duration and negligible impact on the StF efficiency. Figure 7.1 schematically illustrates the three main process steps along with the corresponding leakage paths and gas flows associated with pressure sealing system's leakage.

During the reduction step, leakage through the rod seal allows ingress of ambient air into the reactor, thereby increasing the vacuum pump's energy demand to maintain the 1 mbar target pressure. This additional auxiliary energy consumption directly reduces the StF efficiency. In the cooling step, air inflow via the rod seal may lead to partial re-oxidation of the previously reduced ceria. This decreases the non-stoichiometry, δ, thereby diminishing the hydrogen yield in the subsequent oxidation step and ultimately reducing reactor efficiency. During the oxidation step, both the rod and gate seals are relevant. Rod seal leakage allows ambient air ingress, which may shift the oxidation reaction dynamics thus hindering hydrogen production. Simultaneously, gate seal leakage permits the loss of hydrogen and other process gases into the reduction reactor, directly decreasing fuel yield. Therefore, these three scenarios are incorporated into the numerical model of

the generic R2Mx system to comprehensively assess the implications of leakage on reactor performance.

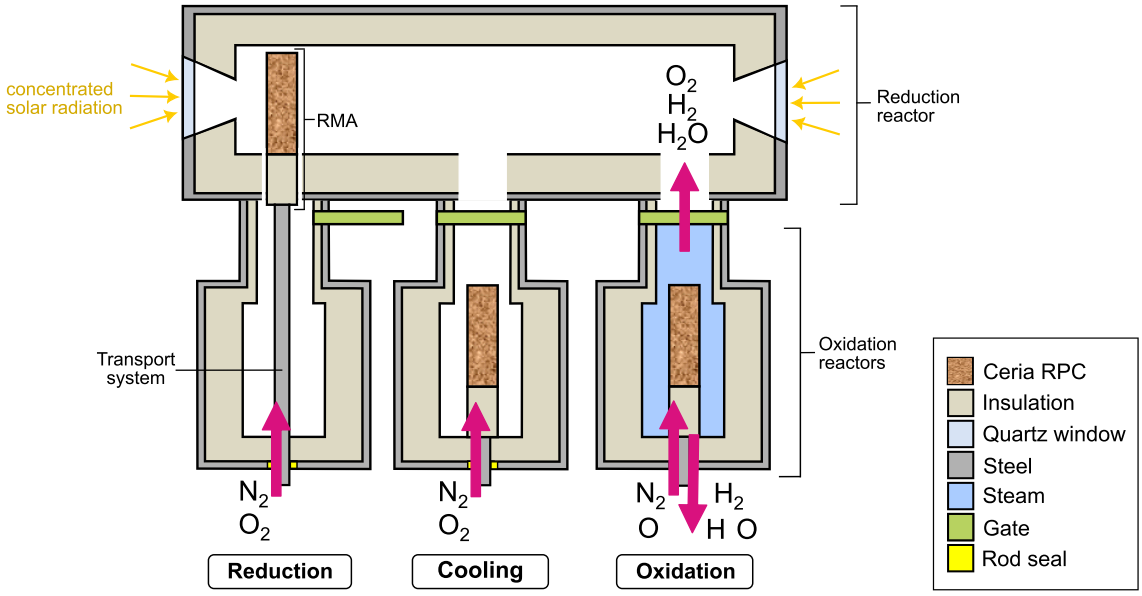

Figure 7.1: Schematic of R2Mx type reactor system with multiple redox mobile units (MRU) each depicted at a different step in the fuel production cycle. Gas flows which result from leakage of the pressure sealing system are highlighted by pink arrows.

7.2. Numerical model

Two modelling approaches are employed to evaluate the impact of leakage on reactor efficiency. The first addresses the reduction step, while the second examines the cooling and oxidation steps. Both models were developed using Python (version 3.11.4) [340] and, in light of the study's objectives, adopt simplified representations of the reactor geometry and operating modes to capture the dominant effects of leakage. Key assumptions and approximations corresponding to each model are outlined in the subsequent sections.

7.2.1. Reduction

To assess the change in StF efficiency as a function of leakage during the reduction step, a simplified numerical model is developed, building on the plant model and findings of Brendelberger [26]. The data corresponding to the "peak efficiency set" from said study, provided in Appendix C, is used as a reference point for evaluating the reactor's performance. The herein developed model calculates the additional energy demand imposed on the vacuum pump system due to rod seal leakage by assuming mass conservation, where air entering the reactor as a result of seal leakage is instantaneously evacuated by the vacuum pump arrangement to maintain a constant target oxygen partial pressure of 1 mbar. The corresponding additional energy consumption is estimated using a scaled, piecewise linear interpolation of the values of vacuum pump power

demand, P, and pumping speed, S, reported in literature for a realistic large-scale pump arrangement with 3 stages [102,113]. These vacuum pump's performance values are detailed in Table 7.1.

Table 7.1: Properties of vacuum pump arrangement, extracted from [102].

Variable	Unit	Value								
$\mathrm{Log}_{10}(p/p_0)$	[-]	0	1.05	1.53	2.06	2.5	2.9	3.6	4.4	5
$S \cdot 10^3$	[$m^3\,h^{-1}$]	44.3	56.3	59.1	55.3	49.6	23.6	7.1	3	2
P	[kW]	70	75	81	102	148	111	85	76	70

The increased vacuum pumping requirement is initially expressed as a heat equivalent, then converted into electrical power using the pump number and the number of RMAs in the system. This value is then used to update the energy loses due to the auxiliary systems, allowing for the calculation of the revised system efficiency.

The air amount, which the vacuum pump must remove, is derived from the rod seal's experimentally measured leakage rates reported in Chap. 6. Specifically, the lowest observed leakage rate when the rod seals were new was $1 \cdot 10^{-3}$ mbar·l·s^{-1}, and the failure threshold was defined at $1 \cdot 10^{-2}$ mbar·l·s^{-1}. To encompass worst-case scenarios, the model considers rod seal's leakage rates up to an order of magnitude above this threshold. Furthermore, it is important to note that the experimental leakage rates of aged samples were obtained at temperatures below those experienced within the reactor cavity during reduction. Therefore, the temperature dependence of the gas flow through the leakage path must be considered, and is approximated as per:

$$q_{l,T_{\mathrm{red}}} = q_{l,T_{\mathrm{exp}}} \cdot \frac{T_{\mathrm{red}}}{T_{\mathrm{exp}}} \tag{7.1}$$

where $q_{l,T_{\mathrm{red}}}$ is the leakage rate at the reduction temperature (T_{red}), and $q_{l,T_{\mathrm{exp}}}$ is the leakage rate measured at the experimental temperature (T_{exp}). For all investigated gas flows, associated with rod seal leakage rates, laminar flow is assumed given their magnitudes. Key parameters employed in the model are summarised in Table 7.2.

Table 7.2: Parameters used in the reduction step modelling.

Parameter	Symbol	Value	Unit
Reduction temperature	T_{red}	2100	K
Hydrogen higher heating value [341]	$\mathrm{HHV}_{\mathrm{H_2}}$	286	kJ·mol^{-1}
Partial pressure oxygen in reactor	$p_{\mathrm{O_2}}$	1.05	mbar
Ambient pressure	p_{amb}	1	bar
Rod seal leakage	$q_{\mathrm{rs},T_{\mathrm{exp}}}$	$1 \cdot 10^{-1}$–$1 \cdot 10^{-3}$	mbar·l·s^{-1}

7.2.2. Cooling and oxidation

During the cooling phase, the reduced ceria is cooled at a rate of 1.82 $K \cdot s^{-1}$ over a period of 440 s. This cooling rate was derived from the thermal simulations reported in Chap. 4 and literature [23], to reflect reasonable operating conditions. The initial partial pressure of oxygen is set at 1.05 mbar, and the starting temperature, corresponding to the reduction temperature, is 1800 °C. As in the reduction step, leakage through the rod seal is modelled as an inflow of ambient air (a combination of oxygen and nitrogen) into the reactor, and the same leakage rate range as in the reduction step is examined.

Upon completion of the cooling step, the oxidation step commences. During oxidation, a steam flow of 0.0135 $l \cdot s^{-1}$ is introduced into the oxidation reactor, based on operational data from previous experimental campaigns on state-of-the-art cavity receiver-reactor [6,7,104]. Steam injection continues until the total oxidation reactor pressure reaches 1 bar. Thereafter, a balance between the incoming steam flow and the outgoing gas mixture flow is maintained to capture the continuous flow conditions. An important simplification in the model is the assumption of a constant oxidation at 1000 °C, which allows pressure changes to be attributed solely to variations in gas composition, without the added complexity of temperature-dependent effects. In practice, the temperature of ceria would decrease as the oxidation reaction proceeds due to the cooling effect of the injected steam.

Throughout the oxidation step, leakage through both the rod seal and the gate is considered. Rod seal leakage is modelled as ambient air inflow into the reactor, while gate leakage allows hydrogen and other gases to escape from the oxidation reactor into the reduction reactor. Rod seal leakage rates are consistent with those used in the reduction and cooling steps, whereas gate leakage rates are based on experimental O-ring degradation results (Chap. 5), taking the average between the FKM and FFKM compounds. Since new O-rings' leakage rates corresponded to $7 \cdot 10^{-5}$ $mbar \cdot l \cdot s^{-1}$ and the failure threshold was defined at $7 \cdot 10^{-4}$ $mbar \cdot l \cdot s^{-1}$, leakage rates up to $7 \cdot 10^{-3}$ $mbar \cdot l \cdot s^{-1}$ are examined to provide conservative estimates.

The numerical model considers a single mobile redox unit (MRU), as all MRUs within the R2Mx reactor are assumed to operate identically under equivalent conditions, making the behaviour of one, representative of the entire system. Furthermore, the fuel produced as well as the leakage are proportional to the number MRUs. The examined RMA has a ceria mass loading of 0.88 kg, with geometric dimensions derived from the work of Brendelberger [26]. All operational parameters employed in the cooling and oxidation model are summarised in Table 7.3.

Table 7.3: Parameters used in the cooling and oxidation model

Parameter	Symbol	Value	Unit
Reduction temperature	T_{red}	1800	°C
Oxidation temperature	T_{ox}	1000	°C
Partial pressure oxygen at start of cooling	p_{O_2}	1.05	mbar
Ambient pressure	p_{amb}	1	bar
Rod seal leakage	$q_{rs,T_{exp}}$	$1 \cdot 10^{-1}$–$1 \cdot 10^{-3}$	mbar·l·s^{-1}
Gate O-ring leakage	$q_{O,T_{amb}}$	$7 \cdot 10^{-3}$–$7 \cdot 10^{-5}$	mbar·l·s^{-1}
Steam flow rate per RMA	$\dot{V}_{H_2O}$	0.0135	l·s^{-1}
Ceria mass loading per RMA	m_{CeO_2}	0.88	kg
Volume of oxidation reactor	V	0.11	m^3
Cooling duration		440	s
Oxidation duration		600	s
Dynamic viscosity of air [341]	μ_{air}	18.20	µPa·s^{-1}
Dynamic viscosity of oxygen [341]	μ_{O_2}	20.24	µPa·s^{-1}
Dynamic viscosity of nitrogen [341]	μ_{N_2}	17.68	µPa·s^{-1}
Dynamic viscosity of hydrogen [341]	μ_{H_2}	19.53	µPa·s^{-1}

Throughout cooling and oxidation, it is assumed that the reduced ceria remains in thermodynamic equilibrium with the evolving oxidation reactor atmosphere. This assumption is justified by the rapid oxygen vacancy diffusion and fast redox kinetics characteristic of ceria at high temperatures (> 1000 °C) relevant for the cooling step [52]. Additionally, during the cooling step, the applied cooling rate is sufficiently low relative to vacancy migration timescales, and the stability of the fluorite structure throughout the relevant temperature range prevents any phase changes that might inhibit equilibrium. On the other hand, the thermodynamic equilibrium assumption in the oxidation step should be made under more careful consideration, since at temperatures between 750–950 °C and 20–40% vol H_2O, the oxidation reaction has been described as controlled by surface process with apparent first order dependence towards steam concentration [84]. Nevertheless, experimental studies suggest that oxidation at 1000 °C is highly exothermic and surface-limited, with 90% hydrogen production achieved within 2 minutes [52]. Given that the R2Mx reactor uses reticulated porous ceramic (RPC) ceria structures with high surface area and dual-scale porosity [53,342], a rapid equilibrium between the redox material and the surrounding atmosphere is expected, supporting the validity of the equilibrium assumption during oxidation under the examined conditions.

The 0D numerical model used to simulate the cooling and oxidation steps is based on the validated framework developed by Pein et al. [343] for thermochemical oxygen pump systems, and it predicts the evolution of the gases' pressure and oxygen non-stoichiometry, δ, over time. While ceria remains out of equilibrium with the gas phase, it continuously reacts with available oxygen until thermodynamic equilibrium is attained. This dynamic alters δ, which, in turn, affects the

equilibrium partial pressure of oxygen, p_{O_2}. The relationship between p_{O_2}, temperature, and enthalpy, ΔH, and entropy of reaction, ΔS, is described by Eqs. (7.2) and (7.3) [11].

$$\frac{p_{O_2}}{p} = A \cdot \exp\left(\frac{-2 \cdot \Delta H^0}{R \cdot T}\right), \qquad A = \exp\left(\frac{2 \cdot \Delta S^0}{R}\right) \tag{7.2}$$

$$\Delta S^0(\delta) = \delta\left(\frac{1}{2}S_{O_2} + \Delta S_{ph}\right) + \Delta S_{con}(\delta) \tag{7.3}$$

where R is the ideal gas constant, S_{O_2} the entropy of the oxygen gas, ΔS_{ph} the change in vibrational state, and $\Delta S_{con}(\delta)$ the configuration entropy. Variations in δ thus influence the partial pressure of oxygen, and if the equilibrium p_{O_2} is lower than that of the surrounding atmosphere, ceria undergoes oxidation, thus reducing the p_{O_2} of the surrounding atmosphere accordingly. Following Eq. (7.4) quantifies the variation in the oxygen partial pressure within the reactor atmosphere resulting from a change in the reduction extent of ceria, considering the ideal gas law [343].

$$p_{r,O_2} = p_{r,O_2,start} + n_{CeO_2} \cdot \frac{d\delta}{2} \cdot \frac{RT}{V} \tag{7.4}$$

where, $p_{r,O_2,start}$ is the oxygen partial pressure in the reactor atmosphere prior the change in δ, n_{CeO_2} is the molar quantity of ceria, and V is the volume of the oxidation reactor. Oxygen exchange between the redox material and the surrounding atmosphere will proceed until a new thermodynamic equilibrium is attained, defined by:

$$p_{r,O_2} = p_{O_2}(\delta + d\delta, T) \tag{7.5}$$

By rearranging this expression with respect to $d\delta$, the molar flux of oxygen over a discrete time step dt can be derived, enabling a time-resolved thermodynamic description of the redox reaction.

$$\dot{N}_O = \left(\frac{dn_{CeO_2}}{dt}\right)_{p,T} = \frac{n_{CeO_2}}{2}\left(\frac{d\delta}{dt}\right) \tag{7.6}$$

During the oxidation step, the gas mixture within the oxidation reactor consists of 12 species. The Cantera Python package [344], an open-source computational toolkit for the modelling of chemical kinetics, thermodynamic properties, and multicomponent transport, is employed to compute the equilibrium composition of the gas mixture under the specified conditions in the oxidation reactor at each time step. The gas species considered in the model are: H_2, H_2O, O, O_2,

N, NO, NO_2, NH_3, H, OH, H_2O_2, HO_2. These species were selected as they showed the most significant concentrations under the examined conditions. At each time step, the molar flux of oxygen, nitrogen, steam and hydrogen, arising the from the oxidation reaction and seal leakages, are calculated and used to update the gas mixture composition.

Experimentally measured leakage rates for the seals are adjusted for temperature dependence using Eq. (7.1). Since the seals' leakage rates were obtained in air, the conversion to the gases of interest such as hydrogen, oxygen, and nitrogen, is performed according to the Hagen-Poiseuille's equation (Eq. (7.7)), which assumes laminar flow conditions.

$$q_{l,\mathrm{air}} = q_{l,\mathrm{j}} \cdot \frac{\mu_{\mathrm{j}}}{\mu_{\mathrm{air}}} \tag{7.7}$$

where, $q_{l,\mathrm{j}}$ is the leakage rate of gas *j* and μ_j is its dynamic viscosity.

7.3. Results and discussion

In the following section, the results of the numerical model are presented and discussed in the frame of a generic R2Mx system. Figure 7.2 illustrates the variation in StF efficiency as a result of rod seal leakage during the reduction step. The efficiency of a no-leakage condition case is derived from literature [26] and is indicated by a blue dashed line in the plot. Results suggest that rod seal leakage during the reduction step has a relatively limited effect on the StF efficiency. Specifically, as the StF efficiency is reduced by 0.004% at the lowest leakage rate investigated of $1 \cdot 10^{-3}$ mbar·l·s^{-1}, when the rod seal is new. Even at the highest leakage conditions modelled, the efficiency reduction does not exceed 0.4%. This limited impact is attributed to the fact that the oxygen released by the redox material during the reduction reaction far exceeds the quantity of air entering the reactor due to rod seal's leakage, where the average oxygen release rate for one ceria RPC during reduction is about 105 mbar·l·s^{-1}. Consequently, the additional energy required by the vacuum pump remains relatively minimal, and overall reactor efficiency is only marginally affected.

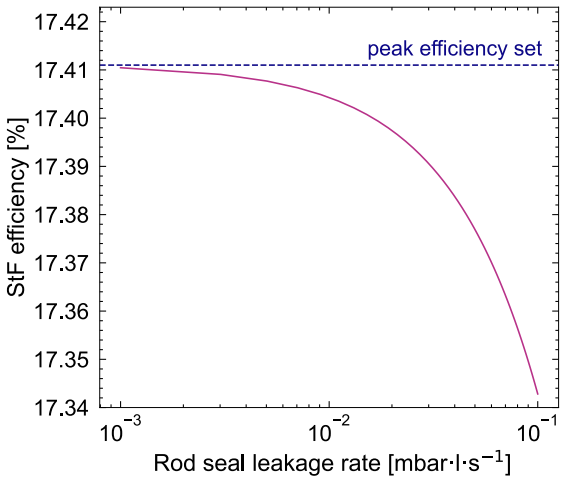

Figure 7.2: Solar-to-fuel (StF) efficiency as a function of leakage rate of the rod seal during the reduction step only. The StF efficiency of the highest efficiency set from [26], which does not consider leakage is depicted by a dashed blue line.

Next, the effect of leakage on reactor performance during the cooling and oxidation steps is investigated. Figure 7.3 displays the evolution of the non-stoichiometry of ceria during the cooling step at the different examined rod seal leakage rates. The blue line represents the no-leakage condition. As leakage of the rod seal increases, the non-stoichiometry at the end of the cooling step decreases, indicating more pronounced re-oxidation of ceria. This reduction in oxygen vacancy concentration translates directly into a diminished hydrogen yield during subsequent oxidation, thereby reducing the StF efficiency. At a leakage rate of $1 \cdot 10^{-3}$ mbar·l·s^{-1}, the reduction extent decreases by approximately 0.05%, and by 4.73% at $1 \cdot 10^{-1}$ mbar·l·s^{-1}, the highest leakage rate investigated.

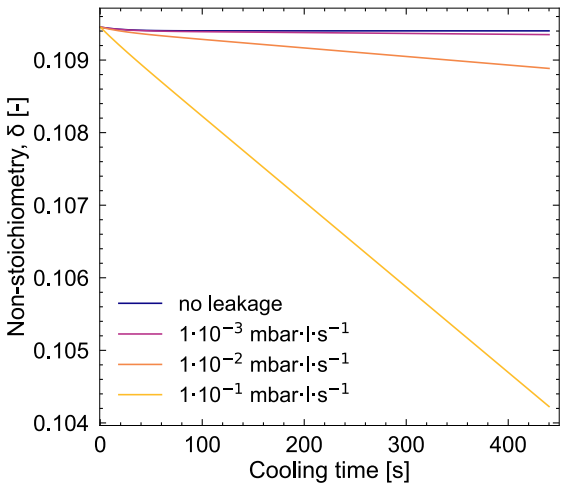

Figure 7.3: Non-stoichiometry of ceria as a function of rod seal leakage and cooling time.

During the oxidation step, the evolution of gas species pressures and the ceria non-stoichiometry is shown in Figure 7.4 for a representative case with intermediate leakage rates from both the rod seal and the gate O-ring. Of the 12 gas species modelled, only six are depicted due to the negligible concentrations of the remainder. Only steam injection is accounted for, until a total pressure in the oxidation reactor of 1 bar is reached, at approximately 110 seconds. Beyond this point, the gas mixture is removed at the same rate at which steam is added to simulate the continuous flow in the system. This results in a continued rise in H_2O partial pressure, while other gas species begin to stabilise or decrease. The majority of hydrogen is produced at the start of the oxidation step, as a result of the thermodynamic equilibrium assumption of the model. Then, H_2 is gradually removed from the reactor; however, a portion also escapes into the reduction reactor due to gate leakage. This hydrogen loss to the reduction reactor is treated as a reduction in fuel yield, directly impacting the StF reactor efficiency. Throughout the oxidation step, the ceria undergoes further oxidation, as evidenced by the decreasing non-stoichiometry illustrated by the green line in Figure 7.4. Over the course of 10 min, the non-stoichiometry decreases by approximately 85%.

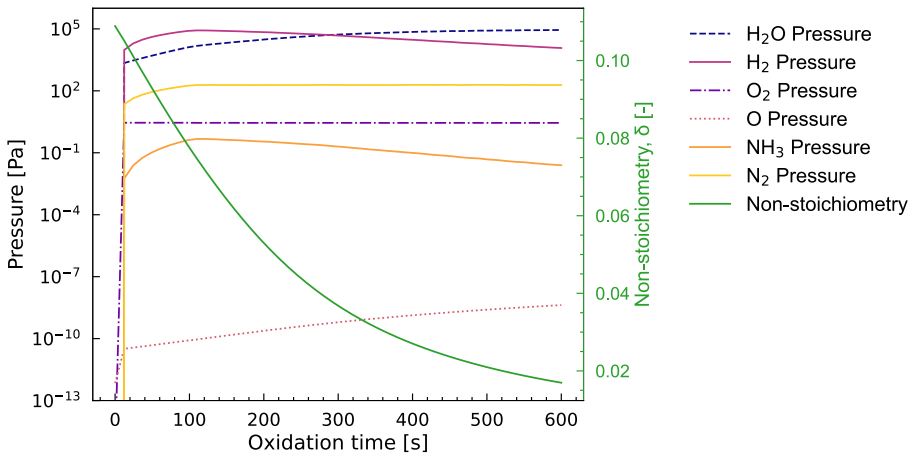

Figure 7.4: Gas pressures and non-stoichiometry evolution as a function of oxidation reaction time. Exemplary case for a gate O-ring leakage rate of $7 \cdot 10^{-4}$ mbar·l·s^{-1} and rod seal leakage rate of $1 \cdot 10^{-2}$ mbar·l·s^{-1}.

Notably, when leakage effects are considered, the formation of ammonia in the oxidation reactor becomes apparent. As ambient air enters the oxidation reactor via the rod seal, nitrogen can react with hydrogen, producing small quantities of ammonia, a reaction absent in the no-leakage scenario. Although the amount of ammonia formed is minimal, it may be operationally relevant, as its formation consumes hydrogen, the intended fuel product, and may also contribute to corrosive conditions and/or deposits forming in the oxidation reactor. Given that ammonia has recently gained interest as an energy carrier, its formation could also be interpreted in a more positive light, highlighting the production of not only one energy carrier, hydrogen, but two, within one

thermochemical cycle. Nevertheless, ammonia production is beyond the scope of this study and is not further examined here. Future research may address this topic in order to better understand the possible effects of these reactions in the R2Mx reactor and/or other reactor concepts such as the ASTOR/Hydrosol system [16,58] and the SOMPIHR concept [345], which utilise nitrogen as sweep gas during reduction.

Figure 7.5 presents the cumulative effect seal leakage, from the rod seal and the gate O-ring, on the reactor's StF efficiency throughout the full thermochemical cycle. At the lowest leakage levels (when the seals are new), a 3.8% decrease in StF efficiency is observed. While, at the predefined threshold leakage rates, the efficiency drops by about 5.6%. The highest considered leakage scenario leads to a reduction of approximately 17.4%, showing a substantial efficiency loss that could severely impact the reactor performance. Among the two sealing components, the rod seal has a significantly greater influence on the StF efficiency's decrease within the studied conditions. This stems from the rod seal's higher leakage rate, which is approximately two orders of magnitude greater than that of the gate O-ring, arising from the fact that it is a dynamic seal, and that is was tested under dry sliding conditions. Moreover, the used rod seal's leakage data was derived from testing with a rough rod; which at ambient conditions is approximately 2.4 times higher than that of a polished rod (Chap. 6.2.2). Nonetheless, even a rod seal operated with a polished rod would remain the dominant contributor to leakage losses. To mitigate this, future R2Mx systems could incorporate leakage reduction strategies such as vacuum grease usage, multiple lip seals arranged in series, or active cooling of the rod seal via a heat transfer fluid within the transport rod. However, the necessity of such measures should be evaluated, as the overall impact of rod seal leakage in system performance appears to be relatively minor.

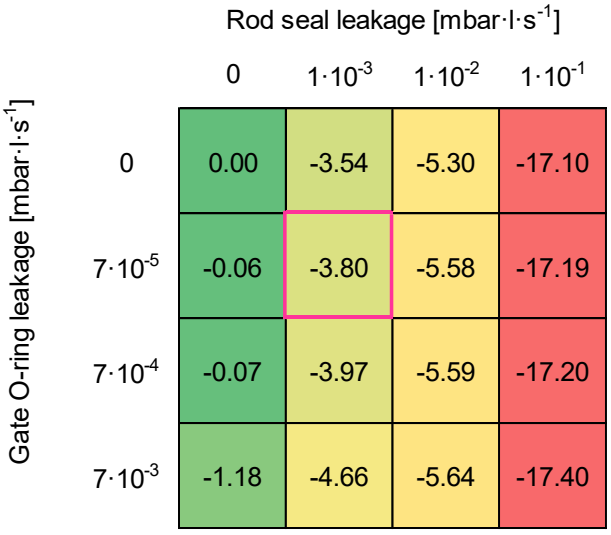

Figure 7.5: Solar-to-fuel (StF) efficiency percentage change matrix as a function of rod seal leakage and gate O-ring leakage. Negative values indicate performance decrease.

Particularly relevant is that O-ring failure can occur in a catastrophic manner, potentially resulting in an unbounded increase in leakage (Chap. 5.2.7). In such a case, reactor operation would become impractical, as the MRU where the failed occurred may become inoperable, and therefore the StF would be significantly reduced. Although the present study limits O-ring leakage rates to one order of magnitude above the defined failure threshold, real-world failure could exceed this, underscoring the importance of an effective design of the gate and timely maintenance intervals. Conversely, the rod seal is not expected to fail catastrophically but rather to degrade progressively, with leakage increasing as a continuous function of time, thus allowing for more operational flexibility (Chap. 6.2.3).

7.4. Summary

This chapter presented a detailed numerical investigation of the effect of pressure sealing system leakage on the performance of a solar thermochemical reactor of type R2Mx, focusing on the entire thermochemical fuel production process. The analysis specifically considered leakage from the two key pressure sealing components: the rod seal and the gate O-ring.

For the reduction step, a simplified numerical approach was used to assess the effect of rod seal leakage on the solar-to-fuel (StF) efficiency. The model assumed a constant oxygen partial pressure maintained by a vacuum pump and evaluated the increase in vacuum pump energy demand as a function of leakage rate. Results demonstrated that, even at elevated leakage rates (up to 0.1 $mbar \cdot l \cdot s^{-1}$), the impact on the StF efficiency remained minor, with a maximum reduction of 0.4%. This limited impact was attributed to the relatively high rate of oxygen evolution during ceria reduction compared to the air inflow through leakage of the rod seal, resulting in a reduced additional electric load.

For the subsequent cooling and oxidation steps, a more complex model assuming thermodynamic equilibrium was employed. A total of 12 gas species were modelled to evaluate the evolving gas composition in the oxidation reactor, while leakage rates were corrected for temperature and gas species under the assumption of laminar flow. Results from the cooling step show that increased rod seal leakage leads to partial re-oxidation of the reduced ceria, as evidenced by a decrease in the ceria non-stoichiometry. This in turn lowers the amount of hydrogen that can be produced in the subsequent oxidation step, thereby decreasing the StF efficiency.

In the oxidation step, the leakage of both the rod seal and gate O-ring was modelled. Rod seal leakage introduced nitrogen, which in combination with hydrogen, led to minor ammonia formation. While the quantities are small, this phenomenon consumes fuel and poses potential risks

to reactor longevity and safety through deposit formation and corrosion. Additionally, gate leakage allowed hydrogen to escape into the reduction chamber, representing a direct loss of fuel.

Finally, cumulative efficiency losses throughout the entire fuel production cycle were mapped across combinations of leakage rates for both seals. At minimum leakage conditions based on measured values of new samples, a 3.8% efficiency drop is observed, while a 17% efficiency decrease is expected at the highest modelled leakage rates. Notably, rod seal leakage plays a dominant role in efficiency reduction due to its significantly higher leakage rates. However, the gate O-ring, while more leakage-tight, may fail catastrophically, potentially rendering the specific RMU inoperable and therefore strongly decrease the reactor's efficiency. These findings underscore the importance of robust pressure sealing system design and operation to mitigate the solar reactor's performance degradation associated with gas leakage.

8. Conclusions and outlook

This thesis investigated the thermal behaviour, degradation mechanisms, and performance implications of polymer-based sealing components, specifically elastomeric O-rings and polytetrafluoroethylene (PTFE) rod seals, for usage in the R2Mx solar thermochemical reactor for hydrogen production. The research combined a multi-disciplinary approach including detailed thermal modelling, experimental characterisation of seal degradation at high temperatures, and numerical modelling of the reactor's solar-to-fuel (StF) efficiency to provide a holistic understanding of seal durability and leakage impact under reactor-relevant conditions. This final chapter summarises the principal findings, discusses their broader significance, and outlines potential directions for future research.

Initial efforts focused on thermally characterising an R2Mx prototype utilising a 2D axisymmetric transient heat transfer model in ANSYS Mechanical. This model captures the heat transfer dynamics and provided an understanding of the evolution of the temperature distribution of components during continuous cyclic reactor operation. A novel approach to couple thermal simulations with the movement of the redox material assembly (RMA) was developed to accurately reflect the system's thermal response during consecutive fuel production cycles. The simulation findings revealed that the gate O-ring would operate at average temperatures of about 200 °C, but reach peak instantaneous temperatures of about 360 °C. The rod seal, on the other hand, is expected to operate at average temperatures of about 100 °C and experience peak instantaneous temperatures of approximately 230 °C. While material selection analysis confirmed the suitability of most reactor components under operational conditions, the sealing materials were identified as potential points of concern due to exposure to temperatures exceeding standard polymer seal recommendations. Recognising the inherent trade-off between maintaining low seal temperatures and increasing engineering complexity, it became essential to understand nor only the thermal tolerance of the polymeric materials but also their failure modes and thresholds.

Targeted sealing material degradation studies were performed to characterise long-term behaviour of O-rings and rod seals under thermo-oxidative conditions, intentionally exceeding manufacturer-specified temperature limits to evaluate worst-case scenarios. Initially, two elastomeric sealing materials, fluoroelastomer (FKM) and perfluoroelastomer (FFKM), were

subjected to an accelerated ageing campaign at temperatures between 200 °C and 300 °C. A combination of techniques including IR and optical microscopy, mass loss analysis, hardness measurements, compression set (CS), compressive stress relaxation (CSR), and leakage rate evaluation provided insights into the underlying degradation mechanisms and the associated property changes. IR analysis revealed that FKM undergoes thermally activated dehydrofluorination, leading to the formation of C=C double bonds, which upon oxidation yield carbonyl-containing degradation products. FFKM degradation, on the other hand, is driven by main-chain scission, which leads to CF_2 groups elimination. CS and CSR testing, highlighted FFKM's superior thermal resilience, showing better performance than FKM at high temperatures.

For reliable service lifetime predictions, an end-of-life criterion is required to determine the point at which a seal can no longer perform its intended function. In this study, seal failure was defined as the onset of leakage exceeding a pre-established threshold ($7 \cdot 10^{-4}$ mbar·l·s^{-1}), specifically, a tenfold increase over the leakage rate of the unexposed samples. The leakage threshold was initially defined according to standard practice; however, this value may be further refined by utilising the model presented in Chap. 7 to account for system-specific behaviour. Results showed that both FKM and FFKM elastomers undergo abrupt failure at advanced degradation states, highlighting the need for accurate lifetime estimation. Since CS is highly sensitive to degradation and strongly linked to sealing performance, it was identified as a suitable predictor of service life. The failure point of the O-rings was found to correspond to a CS value of approximately 75%, which was adopted as the end-of-life criterion. Using time-temperature superposition (TTS) of CS data, service lifetimes were predicted at all tested temperatures. Results showed that under continuous 200 °C operation, FKM and FFKM O-rings could last for approximately 220 and 400 operational days respectively, assuming 8-hour daily solar reactor operation. However, seal durability declined sharply at higher temperatures. These predictions are conservative, as lifetime could potentially be extended, particularly for FFKM, by reducing initial O-ring compression and thereby lowering operational mechanical stresses. These findings emphasise the importance of maintaining seal operating temperatures at or below 200 °C to minimise maintenance frequency and preserve system performance. While, it is likely that maintaining the O-ring at approximately 200 °C solely through gate design will be challenging, certain parameters may be adjusted to reduce the radiative heat transfer to the seal. These include increasing the transport speed of the hot RMA, increasing the distance between the RMA and the seal, incorporating a thermal shield, and introducing active cooling mechanisms.

Next, a dedicated experimental campaign was performed to assess the degradation and wear characteristics of PTFE double-lip rod seals, used for sealing at the interface of the transport system in the R2Mx reactor. Rod seal testing was conducted in a custom-built test rig at ambient conditions

using polished and rough rods, and at high temperatures (250–300 °C) using exclusively rough rods to accelerate degradation. In both cases a comprehensive set of tribological tests, including wear analysis, lip seal deformation, force measurements and leakage rate tests, was used to characterise the seals' performance. At ambient conditions, the rough rods accelerated wear due to reduced surface conformality and increased abrasive interaction, but showed the same wear mechanism as polished rods. Optical and deformation analysis revealed minor geometric changes without a distinctive effect of the rod surface. Leakage rate testing under vacuum conditions demonstrated low initial leakage that stabilised after 5 km of sliding, consistent with wear behaviour. However, rough rods exhibited leakage rates nearly twice as high as polished rods. At high temperatures, rod seals exhibited accelerated degradation. Notable permanent deformation of the seal profile occurred at ≥ 275 °C, and the wear mechanism transitioned from abrasive to adhesive and finally thermally driven failure. Weight loss due to wear increased substantially beyond 250 °C, as transfer film instability and frictional heating exacerbated wear at high temperatures.

Leakage rates increased progressively with testing time until failure of the rod seals was evidenced. Seals tested at the highest temperatures exhibited leakage above the predefined failure threshold ($1 \cdot 10^{-2}$ mbar·l·s^{-1}). Following a similar approach to the O-ring investigation, an end-of-life criterion was defined for the rod seals, this time, based in wear-induced weight loss as it was identified as the most relevant indicator of seal degradation in this context. A 1% wear was selected as the end-of-life criterion given its correlation with the onset of increased leakage. Service lifetime predictions for rough rod seals suggested lifetimes of about 220 days at 250 °C and 140 days at 275 °C, under realistic 8-hour daily operation of the solar reactor. The 300 °C case proved unsustainable, with failures predicted in under 40 days. While results are conservative due to testing under dry and accelerated wear conditions, they nonetheless provide critical benchmarks for seal durability. Improved lifetimes are anticipated with lubrication and smoother rods, as employed in real-world operation.

In order to integrate and contextualise the experimental results within the broader reactor performance framework, a numerical model was developed to evaluate the impact of seal leakage on the R2Mx system's StF efficiency. Experimentally measured gate O-ring and rod seal leakage rates were incorporated into the reactor model. For the reduction step, vacuum pump energy consumption was calculated based on air inflow resulting from rod seal leakage. Even at worst-case leakage rates, the efficiency drop was limited to 0.4%, primarily due to the high oxygen evolution during ceria reduction, which dominated over the comparatively minor leakage inflow. In contrast, the cooling and oxidation steps exhibited greater sensitivity to leakage. Rod seal leakage during cooling led to partial re-oxidation of the reduced ceria, reducing hydrogen yield in the subsequent oxidation step. During oxidation, rod seal leakage introduced nitrogen into the reactor,

enabling ammonia formation, a reaction with undesired safety and efficiency implications. Gate leakage contributed to direct hydrogen loss to the reduction reactor.

The combined effects of leakage from both sealing components throughout the entire fuel production cycle were evaluated across a matrix of leakage scenarios. At minimum leakage rates, when seals are new, a 3.8% StF efficiency loss was observed, while when seals were operated at predefined leakage rate failure thresholds the efficiency decreased by 5.6%. High leakage scenarios (above predefined failure thresholds) led to a 17% StF efficiency drop. These findings suggest that, provided the seals operate within conservative service lifetime limits, leakage remains manageable and is unlikely to significantly impair reactor performance. Among the two sealing components, rod seal leakage was the dominant contributor to reactor efficiency loss due to its inherently higher leakage rates. However, this can be mitigated by implementing design improvements, such as using polished rods and applying vacuum grease, given that the leakage rates used in the model were based on testing with rough rods under dry conditions. The operating temperature may also be reduced by incorporating active cooling in the transport arm. In contrast, the gate O-ring, although exhibiting tighter sealing performance, presents the risk of catastrophic failure, which could immediately render the specific mobile reactor unit (MRU) inoperable and severely decrease reactor efficiency. This risk is compounded by the limited thermal durability of the O-rings, particularly above 200 °C, as previously demonstrated through ageing studies. Consequently, precise thermal control for the gate becomes essential to ensure sealing integrity and system reliability.

In summary, this work demonstrates that high operating temperatures in the solar reactor, though essential for thermochemical efficiency, impose significant limitations on polymer seal durability. A key outcome of this research is the in-depth understanding of the high-temperature degradation behaviour of FKM, FFKM, and PTFE sealing materials, which holds relevance across a range of engineering applications. Moreover, the development of experimentally validated end-of-life criteria for these seals represents a significant contribution, offering a practical and transferable methodology for service lifetime prediction. This approach can be readily adapted for use in other thermally demanding sectors, such as aerospace, chemical processing, and advanced energy systems, where seal reliability is critical to system integrity and performance. Furthermore, the assessment of how leakage impacts reactor efficiency, provides a valuable toolset for design optimisation of future high-performance solar water-splitting reactors.

While the findings of this study establish key design and material guidelines, further investigation is warranted to bridge the gap between controlled laboratory conditions and dynamic real-world reactor operation. In particular, the effects of thermal cycling, representative of daily start up and shutdown as well as of operationally short-lived temperature peaks, on seal degradation

and leakage remain to be explored. Future studies should also validate the proposed end-of-life criteria across a broader range of materials, geometries, and sealing configurations, given that in polymers, and elastomers in particular, degradation is highly dependent on formulation. The development of probabilistic models accounting for abrupt failure of O-rings could also be developed to further assess reactor availability and risk. In the case of rod seals, extended high-temperature testing with polished rods under lubricated conditions would yield more accurate service lifetime predictions. Future investigations should consider the influence of more representative operating atmospheres for the ageing of both seals, given that in the present study only thermo-oxidative ageing in air was examined. In particular, exposure to steam and hydrogen, conditions relevant for operation in the R2Mx reactor during the oxidation step, may introduce chemical ageing pathways not captured in this work. Additionally, as the R2Mx reactor advances towards larger-scale implementation, real-time leakage monitoring and seal condition diagnostics could be developed to enable predictive maintenance strategies. Ultimately, integrating these findings into holistic reactor system design will be essential to ensure operational stability, minimise downtime, and maximise long-term energy efficiency.

References

[1] European Union, “Directive (EU) 2023/2413 of the European Parliament and of the Council of 4 October 2023 on the promotion of renewable energy.” Official Journal of the European Union, 2023, https://eur-lex.europa.eu/eli/dir/2023/2413/oj/eng.

[2] European Council of the European Union, “Renewable energy: Council adopts new rules.”, [Online], 2023, https://www.consilium.europa.eu/en/press/press-releases/2023/10/09/renewable-energy-council-adopts-new-rules/, [January 06, 2025].

[3] Eurostat, “Renewable energy statistics.”, Statistics Explained, 2024, https://ec.europa.eu/eurostat/statistics-explained/index.php?title=Renewable_energy_statistics, [January 06, 2025].

[4] United Nations Framework Convention on Climate Change, “Adoption of the Paris Agreement.”, 21st Conference of the Parties, United Nations, Paris, 2015, https://unfccc.int/resource/docs/2015/cop21/eng/l09r01.pdf, [January 09, 2025].

[5] Rissman, J., Bataille, C., Masanet, E., Aden, N., Morrow, W. R., Zhou, N., Elliott, N., Dell, R., Heeren, N., Huckestein, B., Cresko, J., Miller, S. A., Roy, J., Fennell, P., Cremmins, B., Koch Blank, T., Hone, D., Williams, E. D., La Rue Can, S., Sisson, B., Williams, M., Katzenberger, J., Burtraw, D., Sethi, G., Ping, H., Danielson, D., Lu, H., Lorber, T., Dinkel, J., and Helseth, J., “Technologies and policies to decarbonize global industry: Review and assessment of mitigation drivers through 2070.” *Applied Energy* Vol. 266 (2020): 114848-11-14848-32. https://doi.org/10.1016/j.apenergy.2020.114848.

[6] Zoller, S., Koepf, E., Nizamian, D., Stephan, M., Patané, A., Haueter, P., Romero, M., González-Aguilar, J., Lieftink, D., Wit, E. de, Brendelberger, S., Sizmann, A., and Steinfeld, A., “A solar tower fuel plant for the thermochemical production of kerosene from H2O and CO2.” *Joule* Vol. 6 No. 7 (2022): pp. 1606–1616. https://doi.org/10.1016/j.joule.2022.06.012.

[7] Schäppi, R., Rutz, D., Dähler, F., Muroyama, A., Haueter, P., Lilliestam, J., Patt, A., Furler, P., and Steinfeld, A., “Drop-in fuels from sunlight and air.” *Nature* Vol. 601 No. 7891 (2022): pp. 63–68. https://doi.org/10.1038/s41586-021-04174-y.

[8] Baykara, S. Z., "Experimental solar water thermolysis." *International Journal of Hydrogen Energy* Vol. 29 No. 14 (2004): pp. 1459–1469. https://doi.org/10.1016/j.ijhydene.2004.02.011.

[9] Boudesocque, N., Vandensteendam, C., Lafon, C., Girold, C., and Baronnet, J. M., "Hydrogen production by thermal water splitting using a thermal plasma.". *16th World Hydrogen Energy Conference, Lyon, France, June 13-16*.

[10] Roeb, M., Neises, M., Säck, J. P., Rietbrock, P., Monnerie, N., Dersch, J., Schmitz, M., and Sattler, C., "Operational strategy of a two-step thermochemical process for solar hydrogen production." *International Journal of Hydrogen Energy* Vol. 34 No. 10 (2009): pp. 4537–4545. https://doi.org/10.1016/j.ijhydene.2008.08.049.

[11] Bulfin, B., Vieten, J., Agrafiotis, C., Roeb, M., and Sattler, C., "Applications and limitations of two step metal oxide thermochemical redox cycles; a review." *Journal of Materials Chemistry A* Vol. 5 No. 36 (2017): pp. 18951–18966. https://doi.org/10.1039/C7TA05025A.

[12] Abanades, S., "A Review of Oxygen Carrier Materials and Related Thermochemical Redox Processes for Concentrating Solar Thermal Applications." *Materials* Vol. 16 No. 9 (2023): p. 3582. https://doi.org/10.3390/ma16093582.

[13] Koepf, E., Zoller, S., Luque, S., Thelen, M., Brendelberger, S., González-Aguilar, J., Romero, M., and Steinfeld, A., "Liquid fuels from concentrated sunlight: An overview on development and integration of a 50 kW solar thermochemical reactor and high concentration solar field for the SUN-to-LIQUID project.", *SolarPACES*, 2126, p. 180012, Casablanca, Morocco, October 2-5, 2018. https://doi.org/10.1063/1.5117692.

[14] Ermanoski, I., Siegel, N. P., and Stechel, E. B., "A New Reactor Concept for Efficient Solar-Thermochemical Fuel Production." *J. Sol. Energy Eng* Vol. 135 No. 3 (2013): p. 031002. https://doi.org/10.1115/1.4023356.

[15] Abanades, S. and Flamant, G., "Thermochemical hydrogen production from a two-step solar-driven water-splitting cycle based on cerium oxides." *Solar Energy* Vol. 80 No. 12 (2006): pp. 1611–1623. https://doi.org/10.1016/j.solener.2005.12.005.

[16] Thanda, V. K., Fend, Th., Laaber, D., Lidor, A., Storch, H. von, Säck, J. P., Hertel, J., Lampe, J., Menz, S., Piesche, G., Berger, S., Lorentzou, S., Syrigou, M., Denk, Th., Gonzales-Pardo, A., Vidal, A., Roeb, M., and Sattler, Ch., "Experimental investigation of the applicability of a 250 kW ceria receiver/reactor for solar thermochemical hydrogen generation." *Renewable Energy* Vol. 198 No. 18 (2022): pp. 389–398. https://doi.org/10.1016/j.renene.2022.08.010.

[17] Welte, M., Barhoumi, R., Zbinden, A., Scheffe, J. R., and Steinfeld, A., "Experimental Demonstration of the Thermochemical Reduction of Ceria in a Solar Aerosol Reactor."

Industrial & Engineering Chemistry Research Vol. 55 No. 40 (2016): pp. 10618–10625. https://doi.org/10.1021/acs.iecr.6b02853.

[18] Brendelberger, S. and Sattler, C., "Concept analysis of an indirect particle-based redox process for solar-driven H2O/CO2 splitting." *Solar Energy* Vol. 113 No. 3 (2015): pp. 158–170. https://doi.org/10.1016/j.solener.2014.12.035.

[19] Ermanoski, I., Grobbel, J., Singh, A., Lapp, J., Brendelberger, S., Roeb, M., Sattler, C., Whaley, J., McDaniel, A., and Siegel, N. P., "Design and construction of a cascading pressure reactor prototype for solar-thermochemical hydrogen production.", *SolarPACES*, 1734, Cape Town, South Africa, October 13-16, 2016. https://doi.org/10.1063/1.4949203.

[20] Marxer, D., Furler, P., Takacs, M., and Steinfeld, A., "Solar thermochemical splitting of CO2 into separate streams of CO and O2 with high selectivity, stability, conversion, and efficiency." *Energy & Environmental Science* Vol. 10 No. 5 (2017): pp. 1142–1149. https://doi.org/10.1039/C6EE03776C.

[21] Patankar, A. S., Wu, X., Chao, W., Tuller, Harry L., and Ghoniem, A., "A Reactor Train System for Efficient Solar Thermochemical Fuel Production." *J. Sol. Energy Eng* Vol. 144 No. 6 (2022): p. 061014. https://doi.org/10.1115/1.4055298.

[22] Brendelberger, S., Holzemer-Zerhusen, P., Vega Puga, E., Roeb, M., and Sattler, C., "Study of a new receiver-reactor cavity system with multiple mobile redox units for solar thermochemical water splitting." *Solar Energy* Vol. 235 No. 5 (2022): pp. 118–128. https://doi.org/10.1016/j.solener.2022.02.013.

[23] Vega Puga, E., Brendelberger, S., Weber, A., and Sattler, C., "Modelling Development of a Receiver–Reactor of Type R2Mx for Thermochemical Water Splitting." *Journal of Solar Energy Engineering* Vol. 146 No. 5 (2024): 051011-1-051011-12. https://doi.org/10.1115/1.4065975.

[24] Vega Puga, E., Brendelberger, S., Weber, A., and Sattler, C., "Modelling Development of a Receiver-Reactor of Type R2Mx for Thermochemical Water Splitting.". ASME 2023 17th International Conference on Energy Sustainability, Washington DC, USA, July 10–12. https://doi.org/10.1115/ES2023-107871.

[25] Diver, R. B., Miller, J. E., Siegel, N. P., and Moss, Timothy A., "Testing of a CR5 Solar Thermochemical Heat Engine Prototype.", *ASME International Conference on Energy Sustainability*, 2, Phoenix, Arizona, USA, May 17-22, 2010. https://doi.org/10.1115/ES2010-90093.

[26] Brendelberger, S., "R2Mx plant model for solar thermochemical hydrogen production at MW scale." *International Journal of Hydrogen Energy* Vol. 91 (2024): pp. 1407–1421. https://doi.org/10.1016/j.ijhydene.2024.10.050.

[27] Bulfin, B., Miranda, M., and Steinfeld, A., "Performance Indicators for Benchmarking Solar Thermochemical Fuel Processes and Reactors." *Frontiers in Energy Research* Vol. 9 (2021): p. 677980. https://doi.org/10.3929/ETHZ-B-000497079.

[28] Kodama, T. and Gokon, N., "Thermochemical Cycles for High-Temperature Solar Hydrogen Production." *Chemical Reviews* Vol. 107 No. 10 (2007): pp. 4048–4077. https://doi.org/10.1021/cr050188a.

[29] Funk, J. E., "Thermochemical hydrogen production: past and present." *International Journal of Hydrogen Energy* Vol. 26 No. 3 (2001): pp. 185–190. https://doi.org/10.1016/S0360-3199(00)00062-8.

[30] Yalçin, S., "A review of nuclear hydrogen production." *International Journal of Hydrogen Energy* Vol. 14 No. 8 (1989): pp. 551–561. https://doi.org/10.1016/0360-3199(89)90113-4.

[31] Chueh, W. C. and Haile, S. M., "A thermochemical study of ceria: exploiting an old material for new modes of energy conversion and CO2 mitigation." *Philosophical Transactions of the Royal Society A: Mathematical, Physical and Engineering Sciences* Vol. 368 No. 1923 (2010): pp. 3269–3294. https://doi.org/10.1098/rsta.2010.0114.

[32] Wild, M., Folini, D., Schär, C., Loeb, N., Dutton, E. G., and König-Langlo, G., "The global energy balance from a surface perspective." *Climate Dynamics* Vol. 40 No. 11 (2013): pp. 3107–3134. https://doi.org/10.1007/s00382-012-1569-8.

[33] MSCI Sustainability Institute, "Global primary energy consumption in 2023.", 2023, https://www.msci-institute.com/charts/global-primary-energy-consumption-generation-in-2023/, [April 05, 2025].

[34] Steinfeld, A., "Solar hydrogen production via a two-step water-splitting thermochemical cycle based on Zn/ZnO redox reactions." *International Journal of Hydrogen Energy* Vol. 27 No. 6 (2002): pp. 611–619. https://doi.org/10.1016/S0360-3199(01)00177-X.

[35] Perkins, C., Lichty, P. R., and Weimer, A. W., "Thermal ZnO dissociation in a rapid aerosol reactor as part of a solar hydrogen production cycle." *International Journal of Hydrogen Energy* Vol. 33 No. 2 (2008): pp. 499–510. https://doi.org/10.1016/j.ijhydene.2007.10.021.

[36] Loutzenhiser, P. G., Meier, A., and Steinfeld, A., "Review of the Two-Step H2O/CO2-Splitting Solar Thermochemical Cycle Based on Zn/ZnO Redox Reactions." *Materials* Vol. 3 No. 11 (2010): pp. 4922–4938. https://doi.org/10.3390/ma3114922.

[37] Koepf, E., Advani, S. G., Prasad, A. K., and Steinfeld, A., "Experimental Investigation of the Carbothermal Reduction of ZnO Using a Beam-Down, Gravity-Fed Solar Reactor." *Industrial & Engineering Chemistry Research* Vol. 54 No. 33 (2015): pp. 8319–8332. https://doi.org/10.1021/acs.iecr.5b01249.

[38] Brkic, M., Koepf, E., and Meier, A., "Continuous Solar Carbothermal Reduction of Aerosolized ZnO Particles Under Vacuum in a Directly Irradiated Vertical-Tube Reactor." *Journal of Solar Energy Engineering* Vol. 138 No. 2 (2016). https://doi.org/10.1115/1.4032685.

[39] Allen, K. M., Coker, E. N., Auyeung, N., and Klausner, J. F., "Cobalt Ferrite in YSZ for Use as Reactive Material in Solar Thermochemical Water and Carbon Dioxide Splitting, Part I: Material Characterization." *JOM* Vol. 65 No. 12 (2013): pp. 1670–1681. https://doi.org/10.1007/s11837-013-0704-2.

[40] Kodama, T., Kondoh, Y., Yamamoto, R., Andou, H., and Satou, N., "Thermochemical hydrogen production by a redox system of ZrO2-supported Co(II)-ferrite." *Solar Energy* Vol. 78 No. 5 (2005): pp. 623–631. https://doi.org/10.1016/j.solener.2004.04.008.

[41] Scheffe, J. R., McDaniel, A. H., Allendorf, M. D., and Weimer, A. W., "Kinetics and mechanism of solar-thermochemical H2 production by oxidation of a cobalt ferrite–zirconia composite." *Energy & Environmental Science* Vol. 6 No. 3 (2013): pp. 963–973. https://doi.org/10.1039/C3EE23568H.

[42] Charvin, P., Abanades, S., Flamant, G., and Lemort, F., "Two-step water splitting thermochemical cycle based on iron oxide redox pair for solar hydrogen production." *Energy* Vol. 32 No. 7 (2007): pp. 1124–1133. https://doi.org/10.1016/j.energy.2006.07.023.

[43] Kodama, T., Nakamuro, Y., and Mizuno, T., "A Two-Step Thermochemical Water Splitting by Iron-Oxide on Stabilized Zirconia." *Journal of Solar Energy Engineering* Vol. 128 No. 1 (2004): pp. 3–7. https://doi.org/10.1115/1.1878852.

[44] Neises, M., Roeb, M., Schmücker, M., Sattler, C., and Pitz-Paal, R., "Kinetic investigations of the hydrogen production step of a thermochemical cycle using mixed iron oxides coated on ceramic substrates." *International Journal of Energy Research* Vol. 34 No. 8 (2010): pp. 651–661. https://doi.org/10.1002/er.1565.

[45] Loutzenhiser, P. G., Gálvez, M. E., Hischier, I., Stamatiou, A., Frei, A., and Steinfeld, A., "CO2 Splitting via Two-Step Solar Thermochemical Cycles with Zn/ZnO and FeO/Fe3O4 Redox Reactions II: Kinetic Analysis." *Energy & Fuels* Vol. 23 No. 5 (2009): pp. 2832–2839. https://doi.org/10.1021/ef801142b.

[46] Scheffe, J. R., Weibel, D., and Steinfeld, A., "Lanthanum–Strontium–Manganese Perovskites as Redox Materials for Solar Thermochemical Splitting of H2O and CO2." *Energy & Fuels* Vol. 27 No. 8 (2013): pp. 4250–4257. https://doi.org/10.1021/ef301923h.

[47] McDaniel, A., Miller, E. C., Arifin, D., Ambrosini, A., Coker, E. N., O'Hayre, R., Chueh, W. C., and Tong, J., "Sr- and Mn-doped LaAlO3−δ for solar thermochemical H2 and CO

production." *Energy & Environmental Science* Vol. 6 No. 8 (2013): pp. 2424–2428. https://doi.org/10.1039/C3EE41372A.

[48] Takacs, M., Hoes, M., Caduff, M., Cooper, T., Scheffe, J. R., and Steinfeld, A., "Oxygen nonstoichiometry, defect equilibria, and thermodynamic characterization of LaMnO3 perovskites with Ca/Sr A-site and Al B-site doping." *Acta Materialia* Vol. 103 (2016): pp. 700–710. https://doi.org/10.1016/j.actamat.2015.10.026.

[49] Abanades, S., Legal, A., Cordier, A., Peraudeau, G., Flamant, G., and Julbe, A., "Investigation of reactive cerium-based oxides for H2 production by thermochemical two-step water-splitting." *Journal of Materials Science* Vol. 45 No. 15 (2010): pp. 4163–4173. https://doi.org/10.1007/s10853-010-4506-4.

[50] Hoes, M., Muhich, C. L., Jacot, R., Patzke, G. R., and Steinfeld, A., "Thermodynamics of paired charge-compensating doped ceria with superior redox performance for solar thermochemical splitting of H2O and CO2." *Journal of Materials Chemistry A* Vol. 5 No. 36 (2017): pp. 19476–19484. https://doi.org/10.1039/C7TA05824A.

[51] Haeussler, A., Abanades, S., Jouannaux, J., Drobek, M., Ayral, A., and Julbe, A., "Recent progress on ceria doping and shaping strategies for solar thermochemical water and CO2 splitting cycles." *AIMS Materials Science* Vol. 6 No. 5 (2019): pp. 657–684. https://doi.org/10.3934/matersci.2019.5.657.

[52] Chueh, W. C., Falter, C., Abbott, M., Scipio, D., Furler, P., Haile, S. M., and Steinfeld, A., "High-Flux Solar-Driven Thermochemical Dissociation of CO2 and H2O Using Nonstoichiometric Ceria." *Science* Vol. 330 No. 6012 (2010): pp. 1797–1801. https://doi.org/10.1126/science.1197834.

[53] Furler, P., Scheffe, J., Marxer, D., Gorbar, M., Bonk, A., Vogt, U., and Steinfeld, A., "Thermochemical CO2 splitting via redox cycling of ceria reticulated foam structures with dual-scale porosities." *Physical Chemistry Chemical Physics* Vol. 16 No. 22 (2014): pp. 10503–10511. https://doi.org/10.1039/C4CP01172D.

[54] Bulfin, B., Lowe, A. J., Keogh, K. A., Murphy, B. E., Lübben, O., Krasnikov, S. A., and Shvets, I. V., "Analytical Model of CeO2 Oxidation and Reduction." *The Journal of Physical Chemistry C* Vol. 117 No. 46 (2013): pp. 24129–24137. https://doi.org/10.1021/jp406578z.

[55] Villafán-Vidales, H. I., Arancibia-Bulnes, C. A., Riveros-Rosas, D., Romero-Paredes, H., and Estrada, C. A., "An overview of the solar thermochemical processes for hydrogen and syngas production: Reactors, and facilities." *Renewable and Sustainable Energy Reviews* Vol. 75 (2017): pp. 894–908. https://doi.org/10.1016/j.rser.2016.11.070.

[56] Schunk, L. O., Lipiński, W., and Steinfeld, A., "Heat transfer model of a solar receiver-reactor for the thermal dissociation of ZnO—Experimental validation at 10kW and scale-

up to 1MW." *Chemical Engineering Journal* Vol. 150 No. 2 (2009): pp. 502–508. https://doi.org/10.1016/j.cej.2009.03.012.

[57] Koepf, E., Villasmil, W., and Meier, A., "Pilot-scale solar reactor operation and characterization for fuel production via the Zn/ZnO thermochemical cycle." *Applied Energy* Vol. 165 (2016): pp. 1004–1023. https://doi.org/10.1016/j.apenergy.2015.12.106.

[58] Säck, J.-P., Breuer, S., Cotelli, P., Houaijia, A., Lange, M., Wullenkord, M., Spenke, C., Roeb, M., and Sattler, C., "High temperature hydrogen production: Design of a 750KW demonstration plant for a two step thermochemical cycle." *Solar Energy* Vol. 135 No. 13 (2016): pp. 232–241. https://doi.org/10.1016/j.solener.2016.05.059.

[59] Lorentzou, S., Zygogianni, A., Pagkoura, C., Karagiannakis, G., Konstandopoulos, A. G., Saeck, J. P., Breuer, S., Lange, M., Lapp, J., Fend, T., Roeb, M., Gonzalez, A. J., Delgado, A., Brouwer, J. P., Makkus, R. C., and Kiartzis, S. J., "HYDROSOL-PLANT: Structured redox reactors for H2 production from solar thermochemical H2O splitting." *AIP Conference Proceedings* Vol. 2033 No. 1 (2018): p. 130010. https://doi.org/10.1063/1.5067144.

[60] Carrillo, A. J., Bork, A. H., Moser, T., Sediva, E., Hood, Z. D., and Rupp, J. L. M., "Modifying La0.6Sr0.4MnO3 Perovskites with Cr Incorporation for Fast Isothermal CO2-Splitting Kinetics in Solar-Driven Thermochemical Cycles." *Advanced Energy Materials* Vol. 9 No. 28 (2019): p. 1803886. https://doi.org/10.1002/aenm.201803886.

[61] Barcellos, D., Sanders, M. D., Tong, J., McDaniel, A. H., and O'Hayre, R. P., "BaCe0.25Mn0.75O3−δ—a promising perovskite-type oxide for solar thermochemical hydrogen production." *Energy & Environmental Science* Vol. 11 No. 11 (2018): pp. 3256–3265. https://doi.org/10.1039/C8EE01989D.

[62] Fernandes Cauduro, A. L., Gager, E., King, K. A., McCord, D., McDaniel, A. H., Scheffe, J., Nino, J., and El Gabaly, F., "Stabilization of Catalytically Active Surface Defects on Ga-doped La–Sr–Mn Perovskites for Improved Solar Thermochemical Generation of Hydrogen." *Topics in Catalysis* Vol. 67 No. 13 (2024): pp. 900–908. https://doi.org/10.1007/s11244-024-01940-w.

[63] Bare, Z. J. L., Morelock, R. J., and Musgrave, C. B., "A Computational Framework to Accelerate the Discovery of Perovskites for Solar Thermochemical Hydrogen Production: Identification of Gd Perovskite Oxide Redox Mediators." *Advanced Functional Materials* Vol. 32 No. 25 (2022): p. 2200201. https://doi.org/10.1002/adfm.202200201.

[64] Vieten, J., Bulfin, B., Huck, P., Horton, M., Guban, D., Zhu, L., Lu, Y., Persson, K. A., Roeb, M., and Sattler, C., "Materials design of perovskite solid solutions for thermochemical applications." *Energy & Environmental Science* Vol. 12 No. 4 (2019): pp. 1369–1384. https://doi.org/10.1039/C9EE00085B.

[65] Emery, A. A., Saal, J. E., Kirklin, S., Hegde, V. I., and Wolverton, C., "High-Throughput Computational Screening of Perovskites for Thermochemical Water Splitting Applications." *Chemistry of Materials* Vol. 28 No. 16 (2016): pp. 5621–5634. https://doi.org/10.1021/acs.chemmater.6b01182.

[66] Bartel, C. J., Sutton, C., Goldsmith, B. R., Ouyang, R., Musgrave, C. B., Ghiringhelli, L. M., and Scheffler, M., "New tolerance factor to predict the stability of perovskite oxides and halides." *Science Advances* Vol. 5 No. 2: eaav0693. https://doi.org/10.1126/sciadv.aav0693.

[67] Meredig, B., Agrawal, A., Kirklin, S., Saal, J. E., Doak, J. W., Thompson, A., Zhang, K., Choudhary, A., and Wolverton, C., "Combinatorial screening for new materials in unconstrained composition space with machine learning." *Physical Review B* Vol. 89 No. 9 (2014): p. 94104. https://doi.org/10.1103/PhysRevB.89.094104.

[68] Panlener, R. J., Blumenthal, R. N., and Garnier, J. E., "A thermodynamic study of nonstoichiometric cerium dioxide." *Journal of Physics and Chemistry of Solids* Vol. 36 No. 11 (1975): pp. 1213–1222. https://doi.org/10.1016/0022-3697(75)90192-4.

[69] Ackermann, S., Scheffe, J. R., and Steinfeld, A., "Diffusion of Oxygen in Ceria at Elevated Temperatures and Its Application to H2O/CO2 Splitting Thermochemical Redox Cycles." *The Journal of Physical Chemistry C* Vol. 118 No. 10 (2014): pp. 5216–5225. https://doi.org/10.1021/jp500755t.

[70] Mogensen, M., Sammes, N. M., and Tompsett, G. A., "Physical, chemical and electrochemical properties of pure and doped ceria." *Solid State Ionics* Vol. 129 No. 1 (2000): pp. 63–94. https://doi.org/10.1016/S0167-2738(99)00318-5.

[71] Ackermann, S., Sauvin, L., Castiglioni, R., Rupp, J. L. M., Scheffe, J. R., and Steinfeld, A., "Kinetics of CO2 Reduction over Nonstoichiometric Ceria." *The Journal of Physical Chemistry C* Vol. 119 No. 29 (2015): pp. 16452–16461. https://doi.org/10.1021/acs.jpcc.5b03464.

[72] Knoblauch, N., Dörrer, L., Fielitz, P., Schmücker, M., and Borchardt, G., "Surface controlled reduction kinetics of nominally undoped polycrystalline CeO2." *Physical Chemistry Chemical Physics* Vol. 17 No. 8 (2015): pp. 5849–5860. https://doi.org/10.1039/C4CP05742B.

[73] Sørensen, O. T., "Thermodynamic studies of the phase relationships of nonstoichiometric cerium oxides at higher temperatures." *Journal of Solid State Chemistry* Vol. 18 No. 3 (1976): pp. 217–233. https://doi.org/10.1016/0022-4596(76)90099-2.

[74] Haxel, G. *Rare earth elements: critical resources for high technology* US Department of the Interior, US Geological Survey (2002).

[75] Takacs, M., Ackermann, S., Bonk, A., Neises-von Puttkamer, M., Haueter, Ph., Scheffe, J. R., Vogt, U. F., and Steinfeld, A., "Splitting CO2 with a ceria-based redox cycle in a solar-driven thermogravimetric analyzer." *AIChE Journal* Vol. 63 No. 4 (2017): pp. 1263–1271. https://doi.org/10.1002/aic.15501.

[76] Brendelberger, S., Roeb, M., Lange, M., and Sattler, C., "Counter flow sweep gas demand for the ceria redox cycle." *Solar Energy* Vol. 122 (2015): pp. 1011–1022. https://doi.org/10.1016/j.solener.2015.10.036.

[77] Tran, J. T., Warren, K. J., Wilson, S. A., Muhich, C. L., Musgrave, C. B., and Weimer, A. W., "An updated review and perspective on efficient hydrogen generation via solar thermal water splitting." *WIREs Energy and Environment* Vol. 13 No. 4 (2024): e528. https://doi.org/10.1002/wene.528.

[78] Bayon, A., La Calle, A., Stechel, E. B., and Muhich, C. L., "Operational Limits of Redox Metal Oxides Performing Thermochemical Water Splitting." *Energy Technology* Vol. 10 No. 1 (2022): p. 2100222. https://doi.org/10.1002/ente.202100222.

[79] Ermanoski, I., Miller, J. E., and Allendorf, M. D., "Efficiency maximization in solar-thermochemical fuel production: challenging the concept of isothermal water splitting." *Physical Chemistry Chemical Physics* Vol. 16 No. 18 (2014): pp. 8418–8427. https://doi.org/10.1039/C4CP00978A.

[80] Bader, R., Venstrom, L., Davidson, J. H., and Lipiński, W., "Thermodynamic Analysis of Isothermal Redox Cycling of Ceria for Solar Fuel Production." *Energy & Fuels* Vol. 27 No. 9 (2013): pp. 5533–5544. https://doi.org/10.1021/ef400132d.

[81] Bulfin, B., Call, F., Vieten, J., Roeb, M., Sattler, C., and Shvets, I. V., "Oxidation and Reduction Reaction Kinetics of Mixed Cerium Zirconium Oxides." *The Journal of Physical Chemistry C* Vol. 120 No. 4 (2016): pp. 2027–2035. https://doi.org/10.1021/acs.jpcc.5b08729.

[82] Subbarao, E. C. and Maiti, H. S., "Solid electrolytes with oxygen ion conduction." *Solid State Ionics* Vol. 11 No. 4 (1984): pp. 317–338. https://doi.org/10.1016/0167-2738(84)90024-9.

[83] Furler, P., Scheffe, J., Gorbar, M., Moes, L., Vogt, U., and Steinfeld, A., "Solar Thermochemical CO2 Splitting Utilizing a Reticulated Porous Ceria Redox System." *Energy & Fuels* Vol. 26 No. 11 (2012): pp. 7051–7059. https://doi.org/10.1021/ef3013757.

[84] Arifin, D. and Weimer, A. W., "Kinetics and mechanism of solar-thermochemical H2 and CO production by oxidation of reduced CeO2." *Solar Energy* Vol. 160 (2018): pp. 178–185. https://doi.org/10.1016/j.solener.2017.11.075.

[85] Pullar, R. C., Novais, R. M., Caetano, A. P. F., Barreiros, M. A., Abanades, S., and Oliveira, F. A., "A Review of Solar Thermochemical CO(2) Splitting Using Ceria-Based Ceramics With Designed Morphologies and Microstructures." *Frontiers in chemistry* Vol. 7 (2019): p. 601. https://doi.org/10.3389/fchem.2019.00601.

[86] Tran, J. T., Warren, K., Wilson, S., Muhich, C. L., Musgrave, C. B., and Weimer, A. W., "An updated review and perspective on efficient hydrogen generation via solar thermal water splitting." *WIREs Energy and Environment* Vol. 13 No. 4 (2024): e528. https://doi.org/10.1002/wene.528.

[87] Venstrom, L. J., Petkovich, N., Rudisill, S., Stein, A., and Davidson, J. H., "The Effects of Morphology on the Oxidation of Ceria by Water and Carbon Dioxide." *Journal of Solar Energy Engineering* Vol. 134 No. 1 (2011). https://doi.org/10.1115/1.4005119.

[88] Zhao, Z., Uddi, M., Tsvetkov, N., Yildiz, B., and Ghoniem, A. F., "Redox Kinetics Study of Fuel Reduced Ceria for Chemical-Looping Water Splitting." *The Journal of Physical Chemistry C* Vol. 120 No. 30 (2016): pp. 16271–16289. https://doi.org/10.1021/acs.jpcc.6b01847.

[89] Coronado, J. M. and Bayón, A., "Catalytic enhancement of production of solar thermochemical fuels: opportunities and limitations." *Physical Chemistry Chemical Physics* Vol. 25 No. 26 (2023): pp. 17092–17106. https://doi.org/10.1039/D3CP00609C.

[90] Abanades, S., Haeussler, A., and Julbe, A., "Thermochemical solar-driven reduction of CO2 into separate streams of CO and O2 via an isothermal oxygen-conducting ceria membrane reactor." *Chemical Engineering Journal* Vol. 422 (2021): p. 130026. https://doi.org/10.1016/j.cej.2021.130026.

[91] Tou, M., Jin, J., Hao, Y., Steinfeld, A., and Michalsky, R., "Solar-driven co-thermolysis of CO2 and H2O promoted by in situ oxygen removal across a non-stoichiometric ceria membrane." *Reaction Chemistry & Engineering* Vol. 4 No. 8 (2019): pp. 1431–1438. https://doi.org/10.1039/C8RE00218E.

[92] Ermanoski, I., Siegel, N. P., and Stechel, E. B., "A New Reactor Concept for Efficient Solar-Thermochemical Fuel Production." *Journal of Solar Energy Engineering* Vol. 135 No. 3 (2013). https://doi.org/10.1115/1.4023356.

[93] de la Calle, A. and Bayon, A., "Annual performance of a thermochemical solar syngas production plant based on non-stoichiometric CeO2." *International Journal of Hydrogen Energy* Vol. 44 No. 3 (2019): pp. 1409–1424. https://doi.org/10.1016/j.ijhydene.2018.11.076.

[94] Meier, A., Ganz, J., and Steinfeld, A., "Modeling of a novel high-temperature solar chemical reactor." *Chemical Engineering Science* Vol. 51 No. 11 (1996): pp. 3181–3186. https://doi.org/10.1016/0009-2509(96)00217-5.

[95] Kodama, T., Cho, H. S., Inoue, K., Saito, T., Watanabe, S., Gokon, N., and Bellan, S., "Particles fluidized bed receiver/reactor with a beam-down solar concentrating optics: First performance test on two-step water splitting with ceria using a Miyazaki solar concentrating system." *AIP Conference Proceedings* Vol. 2126 No. 1 (2019): p. 180011. https://doi.org/10.1063/1.5117691.

[96] Oles, A. S. and Jackson, G. S., "Modeling of a concentrated-solar, falling-particle receiver for ceria reduction." *Solar Energy* Vol. 122 (2015): pp. 126–147. https://doi.org/10.1016/j.solener.2015.08.009.

[97] Koepf, E., Advani, S. G., Steinfeld, A., and Prasad, A. K., "A novel beam-down, gravity-fed, solar thermochemical receiver/reactor for direct solid particle decomposition: Design, modeling, and experimentation." *International Journal of Hydrogen Energy* Vol. 37 No. 22 (2012): pp. 16871–16887. https://doi.org/10.1016/j.ijhydene.2012.08.086.

[98] Schrader, A. J., Dominicis, G. de, Schieber, G. L., and Loutzenhiser, P. G., "Solar electricity via an Air Brayton cycle with an integrated two-step thermochemical cycle for heat storage based on Co3O4/CoO redox reactions III: Solar thermochemical reactor design and modeling." *Solar Energy* Vol. 150 (2017): pp. 584–595. https://doi.org/10.1016/j.solener.2017.05.003.

[99] Scheffe, J. R., Welte, M., and Steinfeld, A., "Thermal Reduction of Ceria within an Aerosol Reactor for H2O and CO2 Splitting." *Industrial & Engineering Chemistry Research* Vol. 53 No. 6 (2014): pp. 2175–2182. https://doi.org/10.1021/ie402620k.

[100] Singh, A., Lapp, J., Grobbel, J., Brendelberger, S., Reinhold, J. P., de Olivera, L., Ermanoski, I., Siegel, N. P., McDaniel, A., Roeb, M., and Sattler, C., "Design of a pilot scale directly irradiated, high temperature, and low pressure moving particle cavity chamber for metal oxide reduction." *Solar Energy* Vol. 157 (2017): pp. 365–376. https://doi.org/10.1016/j.solener.2017.08.040.

[101] Grobbel, J., McDaniel, A., Giljanovic, A., Lorreyte, C., Müller, J. H., Thomey, D., and Sattler, C., "Experimental Investigation of a System of Two Vacuum Solar Receivers for the Continuous Reduction of Ceria Particles." *SolarPACES Conference Proceedings* Vol. 1 (2024). https://doi.org/10.52825/solarpaces.v1i.732.

[102] Brendelberger, S., Rosenstiel, A., Lopez-Roman, A., Prieto, C., and Sattler, C., "Performance analysis of operational strategies for monolithic receiver-reactor arrays in solar thermochemical hydrogen production plants." *International Journal of Hydrogen Energy* Vol. 45 No. 49 (2020): pp. 26104–26116. https://doi.org/10.1016/j.ijhydene.2020.06.191.

[103] Lidor, A., Aschwanden, Y., Häseli, J., Reckinger, P., Haueter, P., and Steinfeld, A., "High-temperature heat recovery from a solar reactor for the thermochemical redox

splitting of H2O and CO2." *Applied Energy* Vol. 329 No. 1 (2023): p. 120211. https://doi.org/10.1016/j.apenergy.2022.120211.

[104] Zoller, S., Koepf, E., Roos, P., and Steinfeld, A., "Heat Transfer Model of a 50 kW Solar Receiver–Reactor for Thermochemical Redox Cycling Using Cerium Dioxide." *J. Sol. Energy Eng* Vol. 141 No. 2 (2019): p. 021014. https://doi.org/10.1115/1.4042059.

[105] Kyrimis, S., Le Clercq, P., and Brendelberger, S., "3D modelling of a solar thermochemical reactor for MW scaling-up studies." *AIP Conference Proceedings* Vol. 2126 No. 1 (2019): p. 180013. https://doi.org/10.1063/1.5117693.

[106] Diver, R. B., Miller, J. E., Siegel, N. P., and Moss, Timothy A., "Testing of a CR5 Solar Thermochemical Heat Engine Prototype.", *ASME International Conference on Energy Sustainability*, 2, Phoenix, Arizona, USA, May 17-22, 2010. https://doi.org/10.1115/ES2010-90093.

[107] Falter, C. P., Sizmann, A., and Pitz-Paal, R., "Modular reactor model for the solar thermochemical production of syngas incorporating counter-flow solid heat exchange." *Solar Energy* Vol. 122 No. 12 (2015): pp. 1296–1308. https://doi.org/10.1016/j.solener.2015.10.042.

[108] Siegrist, S., Storch, H. von, Roeb, M., and Sattler, C., "Moving Brick Receiver–Reactor: A Solar Thermochemical Reactor and Process Design With a Solid–Solid Heat Exchanger and On-Demand Production of Hydrogen and/or Carbon Monoxide." *J. Sol. Energy Eng* Vol. 141 No. 2 (2019): p. 021009. https://doi.org/10.1115/1.4042069.

[109] Patankar, A. S., Wu, X., Chao, W., Tuller, Harry L., and Ghoniem, A., "A Reactor Train System for Efficient Solar Thermochemical Fuel Production." *J. Sol. Energy Eng* Vol. 144 No. 6 (2022): p. 061014. https://doi.org/10.1115/1.4055298.

[110] Miller, J. E., Allendorf, M. D., Ambrosini, A., Chen, K. S., Coker, E. N., Dedrick, D. E., Diver, R. B., Hogan, R. E., Ermanoski, I., and Johnson, T. A., "Final Report— Reimagining Liquid Transportation Fuels: Sunshine to Petrol." *Sandia National Laboratories Report No. SAND2012-0307* (2012). https://doi.org/10.2172/1035344.

[111] Kawabe, M., Ono, H., Sano, T., Tsuji, M., and Tamaura, Y., "Thermochemical oxygen pump with praseodymium oxides using a temperature-swing at 403–873 K." *Energy* Vol. 22 No. 11 (1997): pp. 1041–1049. https://doi.org/10.1016/S0360-5442(97)00044-3.

[112] Ezbiri, M., Allen, K. M., Gàlvez, M. E., Michalsky, R., and Steinfeld, A., "Design Principles of Perovskites for Thermochemical Oxygen Separation." *ChemSusChem* Vol. 8 No. 11 (2015): pp. 1966–1971. https://doi.org/10.1002/cssc.201500239.

[113] Brendelberger, S., Storch, H. von, Bulfin, B., and Sattler, C., "Vacuum pumping options for application in solar thermochemical redox cycles – Assessment of mechanical-, jet-

and thermochemical pumping systems." *Solar Energy* Vol. 141 (2017): pp. 91–102. https://doi.org/10.1016/j.solener.2016.11.023.

[114] P. Smith and Zappe, R. W. *Valve selection handbook* Gulf Professional Publishing, Burlington, MA, USA (2004).

[115] Schütte Industrieservice GmbH, "Pressure-/vacuum swing gate valve KU-HP+PAM.", Germany, 2025, https://www.schuette-is.com/en/bulk-material-valves/swing-valve/pressure-vacuum-swing-gate-valve-ku-hp/, [June 18, 2025].

[116] VAT Group AG, "HV Control Gate Valve: For High Cycle Vacuum Control and Isolation.", Switzerland, 2025, https://www.vatgroup.com/series/high-vacuum-control-gate-valve, [June 18, 2025].

[117] VAT Group AG, "Mini UHV Gate Valve: The General Purpose Isolation Valve for Demanding Applications.", Switzerland, 2025, https://www.vatgroup.com/series/mini-uhv-gate-valve, [June 18, 2025].

[118] Mule, A., Patil, Y. R., Abhyankar, P., and Hingane, A., "Design of a Knife Valve and Stress Analysis using Finite Element Analysis." *International Journal of Science Technology & Engineering* Vol. 3 No. 02 (2016): pp. 165–168.

[119] Anderson, C. N., Bosserman, B. E., Morris, C. D., Cadrecha, C., Lescovich, J. E., Taylor, H. W., and Vuncannon, J., "Chapter 5 - Valves.". *Pumping Station Design (Third Edition)*. Butterworth-Heinemann, Burlington (2008): 5.1-5.32.

[120] McElhaney, K. L., "Failure Modes and Causes for Swing and Lift Type Check Valves.", United States, 1997.

[121] Tameson, "Ball Valves For Vacuum Applications.", Netherlands, 2021, https://tameson.com/pages/vacuum-ball-valve, [June 18, 2025].

[122] Pfeiffer Vacuum, "Ball Valves.", Germany, 2025, https://vacuum-shop.com/shop/en_US/category/2073463/ball-valves.html, [June 18, 2025].

[123] Flitney, R. *Seals and Sealing Handbook* Butterworth-Heinemann, Oxford, UK (2014).

[124] Jousten, K., Jitschin, W., Lachenmann, R., Jünemann, A., Friedrichsen, U., Lippelt, E., Kossek, B., Grave, H., Galda, K., Bernhardt, K., and Livesey, G. *Wutz Handbuch Vakuumtechnik: Theorie und Praxis* Vieweg+Teubner (2004).

[125] Jung, J. K., Lee, Chang H., Baek, U. B., Choi, M. C., and Bae, J. W., "Filler Influence on H(2) Permeation Properties in Sulfur-CrossLinked Ethylene Propylene Diene Monomer Polymers Blended with Different Concentrations of Carbon Black and Silica Fillers." *Polymers* Vol. 14 No. 3 (2022). https://doi.org/10.3390/polym14030592.

[126] Große Bley, W., "Industrial vacuum leak detection with intelligent gas leak detectors: Not just a mass spectrometer." *Vakuum in Forschung und Praxis* Vol. 18 S1 (2006): pp. 24–29. https://doi.org/10.1002/vipr.200690027.

[127] Gu, B. and Huang, X., “Investigation of leak detection method by means of measuring the pressure increment in vacuum.” *Vacuum* Vol. 80 No. 9 (2006): pp. 996–1002. https://doi.org/10.1016/j.vacuum.2006.01.005.

[128] Trelleborg Sealing Solutions, “O-rings and Back-up Rings.” (2024), https://www.trelleborg.com/-/media/tss-media-repository/tss_website/pdf-and-other-literature/catalogs/o_ring_gb_en.pdf.

[129] EKIS, “Technical Handbook of O-rings.” (2024), https://o-ring.info/en/technical-info/technical-o-ring-handbook/.

[130] C. Otto Gehrckens GmbH & Co. KG, “O-ring Basics: Everything about O-rings.”. COG, Pinnenberg, Germany (2022), https://www.cog.de/fileadmin/dokumente/Broschueren/COG_Broschuere_O-Ring_1x1_EN.pdf.

[131] ISO 3601-2:2016, “Fluid power systems — O-rings: Part 2: Housing dimensions for general applications.” International Organization for Standarization, Geneva, Switzerland, https://www.iso.org/standard/80469.html.

[132] AS568F, “Aerospace size standard for O-rings.” SAE International, Pennsylvannia, USA, 2020, https://www.sae.org/standards/content/as568f/.

[133] Parker Hannifin Corporation, “Parker O-ring Handbook: ORD 5700.”, Cleveland, USA (2021), https://www.parker.com/content/dam/Parker-com/Literature/O-Ring-Division-Literature/ORD-5700.pdf.

[134] Battini, D., Donzella, G., Avanzini, A., Zenoni, A., Ferrari, M., Donzella, A., Pandini, S., Bignotti, F., Andrighetto, A., and Monetti, A., “Experimental testing and numerical simulations for life prediction of gate valve O-rings exposed to mixed neutron and gamma fields.” *Materials & Design* Vol. 156 (2018): pp. 514–527. https://doi.org/10.1016/j.matdes.2018.07.020.

[135] Müller, H. K. and Nau, B. *Fluid sealing technology: Principles and applications*, Mechanical Engineering Marcel Dekker, New York, USA (1998).

[136] Simon, C. M. and Kaminsky, W., “Chemical recycling of polytetrafluoroethylene by pyrolysis.” *Polymer Degradation and Stability* Vol. 62 No. 1 (1998): pp. 1–7. https://doi.org/10.1016/S0141-3910(97)00097-9.

[137] Ma, K., Guan, K., and Cai, R., “Compression recovery performance of spring energized C-rings.” *Proceedings of the Institution of Mechanical Engineers, Part E* Vol. 230 No. 1 (2014): pp. 18–25. https://doi.org/10.1177/0954408914535572.

[138] Kim, G. H., Lee, Y. S., and Yang, H. L., “A new design concept of metal O-ring seal for long-term performance.” *Vacuum* Vol. 123 (2016): pp. 54–61. https://doi.org/10.1016/j.vacuum.2015.10.014.

[139] ASTM D 1418:2022, “Standard Practice for Rubber and Rubber Latices-Nomenclature.” ASTM International, USA, 2022.

[140] ISO 1629:2025, “Rubber and latices - Nomenclature.” International Organization for Standarization, Geneva, Switzerland, https://www.iso.org/standard/88692.html.

[141] Banks, R. E. *Fluorocarbons and their Derivatives* Macdonald & Company (1970).

[142] Drobny, J. G. *Fluoroelastomers Handbook: The definitive user's guide* William Andrew Publishing, Oxford, UK (2016).

[143] Drobny, J. G. and Ebnesajjad, S. *Technology of Fluoropolymers: A Concise Handbook* CRC Press, Boca Raton (2023).

[144] McKeen, L. W., Ed. *Permeability Properties of Plastics and Elastomers (Third Edition) Plastics Design Library* William Andrew Publishing, Oxford (2012).

[145] J-Flex rubber Products, “So, just what are Fluoroelastomers?”, 2025, https://www.j-flex.com/so-just-what-are-fluoroelastomers/.

[146] ERIKS Group, “FKM and FPM Elastomer.”, 2020, https://eriks.com/en/what-we-do/rubber-materials-overview/fkm/, [May 14, 2025].

[147] Patil, R. D., “Elastomers: Fluorinated.”. *Encyclopedia of Materials: Science and Technology*. Elsevier, Oxford (2001): pp. 2463–2465.

[148] Reger, T. S. and Reichl, G. J., “Science of Sealing: Advanced Materials for High-Temperature Applications.”, *31st Annual SEMI Advanced Semiconductor Manufacturing Conference (ASMC), p.* 1–5, Saratoga Springs, NY, USA, August 24–26, 2020. https://doi.org/10.1109/ASMC49169.2020.9185380.

[149] Verschuere, A. and Cole, E., “FFKM to overcome new challenges: An introduction to perfluoroelastomers.” *Rubber Fibres Plastics Intl* Vol. 10 No. 2 (2015): pp. 122–129.

[150] Dupont, “Perfluoroelastomer (FFKM) and Fluoroelastomer (FKM) Seals for Photovoltaic Cell Manufacturing Processes.”, Technical Information—Rev. 1, Paper Presented at InterSolar SMET 2009, Munich (2010), https://www.dupont.com/content/dam/dupont/amer/us/en/kalrez/public/documents/en/Perfluoroelastomer_and_Fluoroelastomer_Seals_for_Photovoltaic_Cell_Manufacturing_Processes.pdf.

[151] Hofmann, W. *Rubber Technology Handbook* Carl Hanser Verlag, Munich (1989).

[152] Klingender, R. C. *Handbook of Specialty Elastomers* CRC Press, Boca Raton (2008).

[153] Solvay Solexis, “Tecnoflon: A Guide to Fluoroelastomers.” (2005), http://20.210.105.67/research/wp-content/uploads/2008/11/fkm_guide_rev113004.pdf.

[154] Ferry, J. D. *Viscoelastic properties of Polymers* John Wiley and Sons, New York (1980).

[155] Sadd, Martin H., “Chapter 6 - Constitutive relations and formulation of classical linear theories of solids and fluids.”. *Continuum Mechanics Modeling of Material Behavior*. Academic Press (2019): pp. 159–261.

[156] Burnay, S. G. and Hitchon, J. W., “Prediction of service lifetimes of elastomeric seals during radiation ageing.” *Journal of Nuclear Materials* Vol. 131 No. 2 (1985): pp. 197–207. https://doi.org/10.1016/0022-3115(85)90458-1.

[157] Rajagopal, K.R and Wineman, A.S, “A note on viscoelastic materials that can age.” *International Journal of Non-Linear Mechanics* Vol. 39 No. 10 (2004): pp. 1547–1554. https://doi.org/10.1016/j.ijnonlinmec.2003.09.001.

[158] Martin, G., Barrès, C., Cassagnau, P., Sonntag, P., and Garois, N., “Viscoelasticity of randomly crosslinked EPDM networks.” *Polymer* Vol. 49 No. 7 (2008): pp. 1892–1901. https://doi.org/10.1016/j.polymer.2008.02.003.

[159] ISO 7743:2017, “Rubber, vulcanized or thermoplastic — Determination of compression stress-strain properties.” International Organization for Standarization, Geneva, Switzerland, https://www.iso.org/standard/72784.html#lifecycle.

[160] Andrews, R. D., Tobolsky, A. V., and Hanson, E. E., “The Theory of Permanent Set at Elevated Temperatures in Natural and Synthetic Rubber Vulcanizates.” *Journal of Applied Physics* Vol. 17 No. 5 (1946): pp. 352–361. https://doi.org/10.1063/1.1707724.

[161] Kömmling, A., Jaunich, M., and Wolff, D., “Revealing effects of chain scission during ageing of EPDM rubber using relaxation and recovery experiment.” *Polymer Testing* Vol. 56 (2016): pp. 261–268. https://doi.org/10.1016/j.polymertesting.2016.10.026.

[162] Ehrenstein, G. W. and Pongratz, S. *Beständigkeit von kunststoffen* Hanser München (2007).

[163] Maldonado Magnere, S., Toledo, E., Yazdani-Pedram, M., Fuentealba, P., Contreras-Soto, A., Bascuñan-Heredia, A., Alvarez-Cortes, G., Zagal, A., Molina, F., Hernández-Santana, M., and Aguilar-Bolados, H., “High performance fluoroelastomer composites filled with graphite and/or bismuth oxide for applications in gamma-ray shielding.” *Polymer Composites* Vol. 45 No. 8 (2024): pp. 6901–6913. https://doi.org/10.1002/pc.28237.

[164] Mitra, S., Ghanbari-Siahkali, A., Kingshott, P., Almdal, K., Kem Rehmeier, H., and Christensen, A. G., “Chemical degradation of fluoroelastomer in an alkaline environment.” *Polymer Degradation and Stability* Vol. 83 No. 2 (2004): pp. 195–206. https://doi.org/10.1016/S0141-3910(03)00235-0.

[165] Surve, K., Cai, M., Yun, J., Zolfaghari, A., Krishnamoorti, R., and Bhowmick, A. K., “Effect of extreme environments on aging of fluoroelastomers.” *Polymer Degradation*

and Stability Vol. 227 (2024): p. 110875. https://doi.org/10.1016/j.polymdegradstab.2024.110875.

[166] Sugama, T., Pyatina, T., Redline, E., McElhanon, J., and Blankenship, D., "Degradation of different elastomeric polymers in simulated geothermal environments at 300 °C." *Polymer Degradation and Stability* Vol. 120 (2015): pp. 328–339. https://doi.org/10.1016/j.polymdegradstab.2015.07.010.

[167] Redline, Erica Marie, Celina, Mathias C., Sugama, Toshifumi, and Pyatina, Tatiana, "Evaluation of High Temperature Elastomers for Geothermal Wells." SAND2015-9580. Sandia National Laboratories, Albuquerque, NM (2015). https://doi.org/10.2172/1504859, https://www.osti.gov/biblio/1504859, journal =.

[168] Wang, Qi-Long, Pei, Jing-Ke, Li, Gao, He, Xi, Niu, Yan-Hua, and Li, Guang-Xian, "Accelerated Aging Behaviors and Mechanism of Fluoroelastomer in Lubricating Oil Medium." *Chinese Journal of Polymer Science* Vol. 38 No. 8 (2020): pp. 853–866. https://doi.org/10.1007/s10118-020-2410-1.

[169] Zaghdoudi, M., Kömmling, A., Böhning, M., and Jaunich, M., "Ageing of elastomers in air and in hydrogen environment: A comparative study." *International Journal of Hydrogen Energy* Vol. 63 (2024): pp. 207–216. https://doi.org/10.1016/j.ijhydene.2024.03.053.

[170] Kader, M. A. and Bhowmick, A. K., "Thermal ageing, degradation and swelling of acrylate rubber, fluororubber and their blends containing polyfunctional acrylates." *Polymer Degradation and Stability* Vol. 79 No. 2 (2003): pp. 283–295. https://doi.org/10.1016/S0141-3910(02)00292-6.

[171] Bulut, D., Krups, T., Poll, G., and Giese, U., "Lubricant compatibility of FKM seals in synthetic oils." *Industrial Lubrication and Tribology* Vol. 72 No. 5 (2020): pp. 557–565. https://doi.org/10.1108/ILT-02-2019-0065.

[172] Zolfaghari, A., Yun, J., and Singh, V., "Operational envelope prediction of fluoroelastomer seals for downhole operation in the oil and gas industry." *Journal of Applied Polymer Science* Vol. 139 No. 5 (2022): p. 51575. https://doi.org/10.1002/app.51575.

[173] Rinnbauer, M., Osen, E., Viol, M., and Peterseim, V., "FKM sealings for alternative fuel mixtures." *MTZ worldwide* Vol. 69 No. 4 (2008): pp. 28–31. https://doi.org/10.1007/BF03226901.

[174] Akhlaghi, S., Pourrahimi, A. M., Sjöstedt, C., Bellander, M., Hedenqvist, M. S., and Gedde, U. W., "Degradation of fluoroelastomers in rapeseed biodiesel at different oxygen concentrations." *Polymer Degradation and Stability* Vol. 136 (2017): pp. 10–19. https://doi.org/10.1016/j.polymdegradstab.2016.12.006.

[175] Simon, A., Pepin, J., Berthier, D., and Méo, S., "Degradation mechanism of FKM during thermo-oxidative aging from mechanical and network structure correlations." *Polymer Degradation and Stability* Vol. 208 (2023): p. 110271. https://doi.org/10.1016/j.polymdegradstab.2023.110271.

[176] Zhuo, W. Y., Wang, Q. L., Li, G., Yang, G., Zhang, H., Xu, W., Niu, Y. H., and Li, G. X., "Detection of the Destruction Mechanism of Perfluorinated Elastomer (FFKM) Network under Thermo-oxidative Aging Conditions." *Chinese Journal of Polymer Science* Vol. 40 No. 5 (2022): pp. 504–514. https://doi.org/10.1007/s10118-022-2692-6.

[177] ISO 11346:2023, "Rubber, vulcanized or thermoplastic — Estimation of life-time and maximum temperature of use." International Organization for Standarization, Geneva, Switzerland, https://www.iso.org/standard/80469.html.

[178] Kömmling, A., Jaunich, M., Pourmand, P., Wolff, D., and Hedenqvist, M., "Analysis of O-Ring Seal Failure under Static Conditions and Determination of End-of-Lifetime Criterion." *Polymers* Vol. 11 No. 8 (2019). https://doi.org/10.3390/polym11081251.

[179] Kömmling, A., Jaunich, M., Goral, M., and Wolff, D., "Insights for lifetime predictions of O-ring seals from five-year long-term aging tests." *Polymer Degradation and Stability* Vol. 179 (2020): p. 109278. https://doi.org/10.1016/j.polymdegradstab.2020.109278.

[180] Pazur, R. J., "Activation energy of poly(isobutylene) under thermo-oxidative conditions from 40 to 100 °C." *Polymer Degradation and Stability* Vol. 104 No. 6 (2014): pp. 57–61. https://doi.org/10.1016/j.polymdegradstab.2014.03.028.

[181] Kömmling, A., "Alterung und Lebensdauervorhersage von O-Ring-Dichtungen." Dissertation. TU Berlin, Berlin, Germany, https://doi.org/10.14279/depositonce-5827.

[182] Gillen, K. T., Bernstein, R., and Celina, M., "Challenges of acceletrated ageing techniques for elastomer lifetime predictions." *Rubber Chemistry and Technology* Vol. 88 No. 1 (2015): pp. 1–27. https://doi.org/10.5254/rct.14.85930.

[183] Gillen, K. T., Bernstein, R., and Wilson, M. H., "Predicting and confirming the lifetime of O-rings." *Polymer Degradation and Stability* Vol. 87 No. 2 (2005): pp. 257–270. https://doi.org/10.1016/j.polymdegradstab.2004.07.019.

[184] Brown, R. P. *Practical guide to the assessment of the useful life of rubbers* iSmithers Rapra Publishing (2001).

[185] Le Huy, M. and Evrard, G., "Methodologies for lifetime predictions of rubber using Arrhenius and WLF models." *Die Angewandte Makromolekulare Chemie* 261-262 No. 1 (1998): pp. 135–142. https://doi.org/10.1002/(SICI)1522-9505(19981201)261-262:1<135:AID-APMC135>3.0.CO;2-W.

[186] Gillen, K. T., Wise, J., Celina, M., and Clough, R. L., “Evidence that Arrhenius high-temperature aging behavior for an EPDM o-ring does not extrapolate to lower temperatures.”, United States, 1997.

[187] Gillen, K. T., Celina, M., and Bernstein, R., “Validation of improved methods for predicting long-term elastomeric seal lifetimes from compression stress–relaxation and oxygen consumption techniques.” *Polymer Degradation and Stability* Vol. 82 No. 1 (2003): pp. 25–35. https://doi.org/10.1016/S0141-3910(03)00159-9.

[188] Nikas, G. K., “Research on the tribology of hydraulic reciprocating seals.” *Tribology research trends* (2008): pp. 11–56.

[189] Aderikha, V. N. and Shapovalov, V. A., “Mechanical and tribological behavior of PTFE–polyoxadiazole fiber composites. Effect of filler treatment.” *Wear* Vol. 271 No. 5 (2011): pp. 970–976. https://doi.org/10.1016/j.wear.2011.04.011.

[190] Burris, D. L., Zhao, S., Duncan, R., Lowitz, J., Perry, S. S., Schadler, L. S., and Sawyer, W. G., “A route to wear resistant PTFE via trace loadings of functionalized nanofillers.” *Wear* Vol. 267 No. 1 (2009): pp. 653–660. https://doi.org/10.1016/j.wear.2008.12.116.

[191] Su, F., Zhang, Z. Z., and Liu, W., “Tribological behavior of hybrid glass/PTFE fabric composites with phenolic resin binder and nano-TiO2 filler.” *Wear* Vol. 264 No. 7 (2008): pp. 562–570. https://doi.org/10.1016/j.wear.2007.04.007.

[192] Xie, G. Y., Zhuang, G. S., Sui, G. X., and Yang, R., “Tribological behavior of PEEK/PTFE composites reinforced with potassium titanate whiskers.” *Wear* Vol. 268 No. 3 (2010): pp. 424–430. https://doi.org/10.1016/j.wear.2009.08.032.

[193] Su, H., Zhang, C., and Sun, S., “Research on the wear model of carbon/carbon composite finger seal.” *Wear* Vol. 476 (2021): p. 203682. https://doi.org/10.1016/j.wear.2021.203682.

[194] Wang, L. N., Wang, Y., Sun, H. C., Ren, G. H., Sun, L. C., and Meng, D. H., “Dynamic analysis and experimental verification of the carbon–carbon composite finger seal under complex working states.” *Proceedings of the Institution of Mechanical Engineers, Part G: Journal of Aerospace Engineering* Vol. 233 No. 8 (2018): pp. 2914–2922. https://doi.org/10.1177/0954410018788790.

[195] Shen, C., Khonsari, M. M., Spadafora, M., and Ludlow, C., “Tribological Performance of Polyamide-Imide Seal Ring Under Seawater Lubrication.” *Tribology Letters* Vol. 62 No. 3 (2016): p. 39. https://doi.org/10.1007/s11249-016-0686-7.

[196] Waterman, A. W., Gay, B. F., Robison, E. D., Srinath, S. K., and Nelson, W. G., “Application of polyimide actuator rod seals.” D6-54351. The Boeing Company, Commercial Airplane Group, Seattle, Washington, USA (1972), https://core.ac.uk/download/pdf/80647009.pdf.

[197] Gong, R., Liu, M., Zhang, H., and Xu, Y., "Experimental investigation on frictional behavior and sealing performance of different composites for seal application." *Wear* 342–343 (2015): pp. 334–339. https://doi.org/10.1016/j.wear.2015.10.001.

[198] Wolff, D., Jaunich, M., Probst, U., and Nagelschmidt, S., "Understanding the long-term behavior of sealing systems and neutron shielding material for extended dry cask storage.", *Probabilistic Safety Assessment and Management PSAM 12,* Honolulu, Hawaii, USA, June 22-27, 2014.

[199] Jaunich, M., Kömmling, A., Ehe, K. von der, Völzke, H., and Wolff, D., "Long-term Behavior of Elastomer Seals and Polymers for Neutron Shielding.", *18th International Symposium on the Packaging and Transportation of Radioactive Materials PATRAM,* Kobe, Japan, September 18-23, 2016.

[200] Thongyoug, P., Tungtrongpairoj, J., Sooksaen, P., and Doungkeaw, K., "Effects of reinforcements on the hardness of composite seal rings." *Materials Today: Proceedings* Vol. 52 (2022): pp. 2377–2380. https://doi.org/10.1016/j.matpr.2021.10.233.

[201] Wang, J., Li, Y., and Lian, Z., "Numerical Investigations on the Sealing Performance of a Reciprocating Seal Based on the Inverse Lubrication Method." *Journal of Tribology* Vol. 141 No. 11 (2019). https://doi.org/10.1115/1.4044297.

[202] Crudu, M., Fatu, A., Cananau, S., Hajjam, M., Pascu, A., and Cristescu, C., "A numerical and experimental friction analysis of reciprocating hydraulic 'U' rod seals." *Proceedings of the Institution of Mechanical Engineers, Part J* Vol. 226 No. 9 (2012): pp. 785–794. https://doi.org/10.1177/1350650112445973.

[203] Fatu, A. and Hajjam, M., "Numerical modelling of hydraulic seals by inverse lubrication theory." *Proceedings of the Institution of Mechanical Engineers, Part J* Vol. 225 No. 12 (2011): pp. 1159–1173. https://doi.org/10.1177/1350650111417046.

[204] Gadari, M. El and and Hajjam, M., "Effect of the Grooved Rod on the Friction Force of U-Cup Hydraulic Rod Seal with Rough Lip." *Tribology Transactions* Vol. 61 No. 4 (2018): pp. 661–670. https://doi.org/10.1080/10402004.2017.1388457.

[205] Stupkiewicz, S. and Marciniszyn, A., "Elastohydrodynamic lubrication and finite configuration changes in reciprocating elastomeric seals." *Tribology International* Vol. 42 No. 5 (2009): pp. 615–627. https://doi.org/10.1016/j.triboint.2008.08.008.

[206] Feuchtmüller, O., Hörl, L., and Bauer, F., "Oil film generation of a hydraulic rod seal: an experimental study using ellipsometry." *Tribology International* Vol. 162 (2021): p. 107102. https://doi.org/10.1016/j.triboint.2021.107102.

[207] Azzi, A., Maoui, A., Fatu, A., Fily, S., and Souchet, D., "Experimental study of friction in pneumatic seals." *Tribology International* Vol. 135 (2019): pp. 432–443. https://doi.org/10.1016/j.triboint.2019.03.018.

[208] Ovaert, T. C. and Badger, J. A., "Sliding Friction and Heat Generation in Pressurized U-Cup Seals Under Low-Speed Reciprocating Conditions." *Journal of Tribology* Vol. 120 No. 2 (1998): pp. 325–331. https://doi.org/10.1115/1.2834430.

[209] Weber, D. and Haas, W., "Wear behaviour of PTFE lip seals with different sealing edge designs, experiments and simulation." *Sealing Technology* Vol. 2007 No. 2 (2007): pp. 7–12. https://doi.org/10.1016/S1350-4789(07)70082-X.

[210] Shibo, W., Niu, C.o, and Teng, B., "Tribological Behavior of Polytetrafluoroethylene: Effect of Sliding Motion." *Journal of Tribology* Vol. 139 No. 1 (2016). https://doi.org/10.1115/1.4033130.

[211] Klaiber, M. and Haas, W., "Influence of Additives in Synthetic Oils on Radial Lip Seals.", *International Joint Tribology Conference,* Los Angeles, California, USA, October 24-26, 2011.

[212] Flitney, R. K., "Rotary Shaft Lip Seals.". *Encyclopedia of Tribology*. Springer US, Boston, MA (2013): pp. 2947–2954.

[213] Yuan, X. D. and Yang, X., "A study on friction and wear properties of PTFE coatings under vacuum conditions." *Wear* Vol. 269 No. 3 (2010): pp. 291–297. https://doi.org/10.1016/j.wear.2010.04.014.

[214] Buckley, D. H., "Adhesion, Friction, Wear and Lubrication in Vacuum." *Japanese Journal of Applied Physics* Vol. 13 S1 (1974): p. 297. https://doi.org/10.7567/JJAPS.2S1.297.

[215] Bauer, F. and and Haas, W., "A New Approach to Analyze the Hydrodynamic Flow in Sealing Aids—PTFE-Lip Seals with Spiral Grooves." *Tribology Transactions* Vol. 50 No. 3 (2007): pp. 435–443. https://doi.org/10.1080/10402000701260955.

[216] Paulisch, A., Heilig, M., and Knezic, P., "Dynamic Shaft Seal with High Vacuum Capability." *MTZ worldwide* Vol. 78 No. 6 (2017): pp. 52–57. https://doi.org/10.1007/s38313-017-0037-6.

[217] Feuchtmüller, O., Stoll, Mario, and Hörl, L. Bauer, F., "Can a hydraulic seal ring wipe out structures on the rod surface?: Viscoelastic FE investigations on a PU groove ring on different rod surfaces.", *20th International Sealing Conference,* Stuttgart, Germany, October 10-11, 2018.

[218] Huang, Y. and and Salant, R. F., "Simulation of the Effects of a Plunge Ground Rod on Hydraulic Rod Seal Behavior." *Tribology Transactions* Vol. 56 No. 6 (2013): pp. 986–996. https://doi.org/10.1080/10402004.2013.807531.

[219] Huang, Y. and Salant, R. F., "Simulation of a hydraulic rod seal with a textured rod and starvation." *Tribology International* Vol. 95 (2016): pp. 306–315. https://doi.org/10.1016/j.triboint.2015.11.024.

[220] Ran, H., Di L., and Wang, S., “A Numerical Wear Simulation Method of Reciprocating Seals with a Textured Rod.” *Materials* Vol. 13 No. 19 (2020). https://doi.org/10.3390/ma13194458.

[221] Feuchtmüller, O., Hörl, L., and Bauer, F., “An Empirical Study on the Wear of Reciprocating Hydraulic Rod Seals Using 15 Different Oils.” *Chemical Engineering & Technology* Vol. 46 No. 1 (2023): pp. 86–94. https://doi.org/10.1002/ceat.202200351.

[222] Technische Dichtungen, Maschinen und Anlagen GmbH, “MultiSeal Special Technical Data.”. Tedima, Krefeld (2025), https://tedima.de/en/multiseal-special/multiseal-special-technical-data/.

[223] Parker Hannifin Corporation, “Fluid power seal design guide: Catalog EPS 5370.” (2008), https://www.parker.com/content/dam/Parker-com/Literature/Engineered-Polymer-Systems/5370.pdf.

[224] Ebnesajjad, Sina, Ed. *Introduction to Fluoropolymers* William Andrew Publishing, Oxford (2013).

[225] Iwasaki, M., “On the helical structure of polytetrafluoroethylene.” *Journal of Polymer Science Part A: General Papers* Vol. 1 No. 4 (1963): pp. 1099–1104. https://doi.org/10.1002/pol.1963.100010402.

[226] Domininghaus, H. *Kunststoffe: Eigenschaften und Anwendungen* Springer-Verlag, Heidelberg, Germany (2013).

[227] Tevrüz, T., “Tribological behaviours of carbon filled polytetrafluoroethylene (PTFE) dry journal bearings.” *Wear* Vol. 221 No. 1 (1998): pp. 61–68. https://doi.org/10.1016/S0043-1648(98)00258-0.

[228] Pleskachevsky, Y. M. and Smurugov, V. A., “Thermal fluctuations at PTFE friction and transfer.” *Wear* Vol. 209 No. 1 (1997): pp. 123–127. https://doi.org/10.1016/S0043-1648(97)00034-3.

[229] Blanchet, T. A. and Kennedy, F. E., “Sliding wear mechanism of polytetrafluoroethylene (PTFE) and PTFE composites.” *Wear* Vol. 153 No. 1 (1992): pp. 229–243. https://doi.org/10.1016/0043-1648(92)90271-9.

[230] Briscoe, B. J., Lin Heng Yao, and Stolarski, T. A., “The friction and wear of poly(tetrafluoroethylene)-poly (etheretherketone) composites: An initial appraisal of the optimum composition.” *Wear* Vol. 108 No. 4 (1986): pp. 357–374. https://doi.org/10.1016/0043-1648(86)90013-X.

[231] Babuska, T. F., Pitenis, A. A., Jones, M. R., Nation, B. L., Sawyer, W. G., and Argibay, N., “Temperature-Dependent Friction and Wear Behavior of PTFE and MoS2.” *Tribology Letters* Vol. 63 No. 2 (2016): p. 15. https://doi.org/10.1007/s11249-016-0702-y.

[232] Tanaka, K. and Kawakami, S., “Effect of various fillers on the friction and wear of polytetrafluoroethylene-based composites.” *Wear* Vol. 79 No. 2 (1982): pp. 221–234. https://doi.org/10.1016/0043-1648(82)90170-3.

[233] Bagale, D., Shekhawat, S., and Chaudhari, J., “Wear analysis of polytetrafluoroethylene and it’s composites under dry conditions using Design-Expert.” *International Journal of Scientific and Research Publications* Vol. 3 No. 1 (2013): pp. 1–5.

[234] Burris, D. and Sawyer, W., “A low friction and ultra low wear rate PEEK/PTFE composite.” *Wear* Vol. 261 No. 3 (2006): pp. 410–418. https://doi.org/10.1016/j.wear.2005.12.016.

[235] Khedkar, J., Negulescu, I., and Meletis, E. I., “Sliding wear behavior of PTFE composites.” *Wear* Vol. 252 No. 5 (2002): pp. 361–369. https://doi.org/10.1016/S0043-1648(01)00859-6.

[236] Klaas, N. V., Marcus, K., and Kellock, C., “The tribological behaviour of glass filled polytetrafluoroethylene.” *Tribology International* Vol. 38 No. 9 (2005): pp. 824–833. https://doi.org/10.1016/j.triboint.2005.02.010.

[237] Conte, M. and Igartua, A., “Study of PTFE composites tribological behavior.” *Wear* Vol. 296 No. 1 (2012): pp. 568–574. https://doi.org/10.1016/j.wear.2012.08.015.

[238] Yan, F., Xue, Q., and Yang, S., “Debris formation process of PTFE and its composites.” *Journal of Applied Polymer Science* Vol. 61 No. 7 (1996): pp. 1223–1229. https://doi.org/10.1002/(SICI)1097-4628(19960815)61:7<1223:AID-APP19>3.0.CO;2-Y.

[239] Yang, Xue‐Bin, Jin, Xin‐Qiao, Du, Zhi‐Min, Cui, Tian‐Sheng, and Yang, Shao‐Kan, “Frictional behavior investigation on three types of PTFE composites under oil‐free sliding conditions.” *Industrial Lubrication and Tribology* Vol. 61 No. 5 (2009): pp. 254–260. https://doi.org/10.1108/00368790910976087.

[240] Huang, X. L., Martinez-Vega, J., and Malec, D., “Morphological evolution of polytetrafluoroethylene in extreme temperature conditions for aerospace applications.” *Journal of Applied Polymer Science* Vol. 131 No. 3 (2014). https://doi.org/10.1002/app.39841.

[241] Ahmad, J. and Niasar, M. G., “Aging Behavior of PEEK, PTFE, and PI Insulation Materials Under Thermal Oxidative and Humid Conditions for Aerospace Applications.” *Journal of Applied Polymer Science* Vol. 142 No. 19 (2025): e56858. https://doi.org/10.1002/app.56858.

[242] Huang, T., Lin, C., and Liao, K., “Experimental and numerical investigations of the wear behavior and sealing performance of PTFE rotary lip seals based on the elasto-

hydrodynamic analysis with considerations of the asperity contact." *Tribology International* Vol. 187 (2023): p. 108747. https://doi.org/10.1016/j.triboint.2023.108747.

[243] Huang, T.-C., Lin, C.-Y., and Liao, K.-C., "Numerical sealing performance assessments of PTFE rotary lip seals based on the elasto-hydrodynamic analysis with the consideration of asperity interactions and accelerated wear experimental validations." *Wear* 564-565 (2025): p. 205706. https://doi.org/10.1016/j.wear.2024.205706.

[244] Li, W., Mays, S., and and Lam, D., "Material and finite element analysis of poly(tetrafluoroethylene) rotary seals." *Plastics, Rubber and Composites* Vol. 31 No. 8 (2002): pp. 359–363. https://doi.org/10.1179/146580102225004974.

[245] Sui, H., Pohl, H., Oppermann, A., Schomburg, U., Upper, G., and Hatch, F., "Material and Computational Analysis of PTFE Seals." *SAE Technical Paper* Vol. 951055 (1995): pp. 1–8. https://doi.org/10.4271/951055.

[246] Archard, J. F., Hirst, W., and Allibone, Thomas Edward, "The wear of metals under unlubricated conditions." *Proceedings of the Royal Society of London. Series A. Mathematical and Physical Sciences* Vol. 236 No. 1206 (1997): pp. 397–410. https://doi.org/10.1098/rspa.1956.0144.

[247] Lee, S. H., Yoo, S. S., Kim, D. E., Kang, B. S., and Kim, H. E., "Accelerated wear test of FKM elastomer for life prediction of seals." *Polymer Testing* Vol. 31 No. 8 (2012): pp. 993–1000. https://doi.org/10.1016/j.polymertesting.2012.07.017.

[248] Zhao, X., He, X., Wang, L., and Chen, P., "Research on pressure compensation and friction characteristics of piston rod seals with different degrees of wear." *Tribology International* Vol. 142 (2020): p. 105999. https://doi.org/10.1016/j.triboint.2019.105999.

[249] Zhen, J., Han, Y., Wang, H., Jiang, Z., Wang, L., Huang, Y., Jia, Z., and Zhang, R., "High Temperature Friction and Wear Behavior of PTFE/MoS2 Composites." *Lubricants* Vol. 11 No. 8 (2023). https://doi.org/10.3390/lubricants11080312.

[250] Zhang, Z., Gao, D., Guan, T., Liang, Y., Zhao, J., Wang, L., and Tang, J., "Experimental Study on Friction and Wear Characteristics of Hydraulic Reciprocating Rotary Seals." *Lubricants* Vol. 11 No. 9 (2023). https://doi.org/10.3390/lubricants11090385.

[251] Şahin, Y., "Dry Wear and Metallographic Study of PTFE Polymer Composites." *Mechanics of Composite Materials* Vol. 54 No. 3 (2018): pp. 403–414. https://doi.org/10.1007/s11029-018-9751-7.

[252] Liu, D., Zhao, J., Li, S., Zhao, X., and Huang, L., "Experimental Study on Tribological and Leakage Characteristics of a Rotating Spring-Energized Seal under High and Low Temperature." *Machines* Vol. 11 No. 2 (2023). https://doi.org/10.3390/machines11020221.

[253] Kato, K., “Classification of wear mechanisms/models.”, Proceedings of the Institution of Mechanical Engineers, Part J: *Journal of Engineering Tribology* Vol. 216 No. 6 (2002): pp. 349–355.

[254] Briscoe, B. J. and Sinha, S. K., “Tribology of polymeric solids and their composites.” *Wear–materials, mechanisms and practice* (2005): pp. 223–267.

[255] Biswas, S. K. and Vijayan, Kalyani, “Friction and wear of PTFE — a review.” *Wear* Vol. 158 No. 1 (1992): pp. 193–211. https://doi.org/10.1016/0043-1648(92)90039-B.

[256] Briscoe, B. J., Steward, M. D., and Groszek, A., “The Effect of Carbon Aspect Ratio on the Friction and Wear of PTFE.” *Wear* Vol. 42 (1977): pp. 99–107.

[257] Unal, H., Mimaroglu, A., Kadıoglu, U., and Ekiz, H., “Sliding friction and wear behaviour of polytetrafluoroethylene and its composites under dry conditions.” *Materials & Design* Vol. 25 No. 3 (2004): pp. 239–245. https://doi.org/10.1016/j.matdes.2003.10.009.

[258] Song, F., Yang, Z., Zhao, G., Wang, Q., Zhang, X., and Wang, T., “Tribological performance of filled PTFE-based friction material for ultrasonic motor under different temperature and vacuum degrees.” *Journal of Applied Polymer Science* Vol. 134 No. 39 (2017): p. 45358. https://doi.org/10.1002/app.45358.

[259] Tzanakis, I., Conte, M., Hadfield, M., and Stolarski, T. A., “Experimental and analytical thermal study of PTFE composite sliding against high carbon steel as a function of the surface roughness, sliding velocity and applied load.” *Wear* Vol. 303 No. 1 (2013): pp. 154–168. https://doi.org/10.1016/j.wear.2013.02.011.

[260] Duan, X., Di L., Wang, S., and Shang, Y., “A Hydraulic Reciprocating Rod Seal’s Life Evaluation Method Incorporating Failure Mechanism Analysis and Test Observation Data.” *Lubricants* Vol. 11 No. 8 (2023). https://doi.org/10.3390/lubricants11080319.

[261] Liu, D., Wang, S., and Tomovic, M. M., “Degradation modeling method for rotary lip seal based on failure mechanism analysis and stochastic process.” *Eksploatacja i Niezawodność – Maintenance and Reliability* Vol. 22 No. 3 (2020): pp. 381–390. https://doi.org/10.17531/ein.2020.3.1.

[262] Peng, W., Li, Y., Yang, Y., Huang, H., and Zuo, M., “Inverse Gaussian process models for degradation analysis: A Bayesian perspective.” *Reliability Engineering & System Safety* Vol. 130 (2014): pp. 175–189. https://doi.org/10.1016/j.ress.2014.06.005.

[263] Lin, Z., Gao, H., Zhang, E., Cao, W., and Li, K., “Diamond-Coated Mechanical Seal Remaining Useful Life Prediction Based on Convolution Neural Network.” *International Journal of Pattern Recognition and Artificial Intelligence* Vol. 34 No. 05 (2019): p. 2051007. https://doi.org/10.1142/S0218001420510076.

[264] Zhou, J. F. and Gu, B. Q., "Lifetime prediction of mechanical seal based on artificial neural networks." *Fluid Mach* Vol. 34 No. 3 (2006): pp. 19–22.

[265] J. J. Sun, X. Y. He, L. Wei, and X. Feng, "Failure analysis and seal life prediction for contacting mechanical seals.", *SPIE 7375, ICEM 2008: International Conference on Experimental Mechanics, 73753L,* August 25, 2008. https://doi.org/10.1117/12.839260.

[266] Bekgulyan, S., Feldmeth, S., Feuchtmüller, O., Hörl, L., and Bauer, F., "Regenerative Thermoplastic Polyurethane for Hydraulic Rod Seals – Time-Accelerated Testing.", *21st International Sealing Cofnerence,* Stuttgart, Germany, October 12-13, 2022.

[267] Escobar, L. A. and Meeker, W. Q., "A Review of Accelerated Test Models." *Statistical Science* Vol. 21 No. 4 (2006): pp. 552–577.

[268] Bhushan, B. *Principles and applications of tribology* John Wiley and Sons, New York, USA (1999).

[269] Kurita, M., Mizumoto, M., and Takahashi, Y., "Study On the Characteristics of Lip Seals for Gasoline." *Tribology Transactions* Vol. 43 No. 3 (2000): pp. 554–558. https://doi.org/10.1080/10402000008982377.

[270] Pedersen, J. F., Schlanbusch, R., Meyer, T. J. J., Caspers, L. W., and Shanbhag, V. V., "Acoustic Emission-Based Condition Monitoring and Remaining Useful Life Prediction of Hydraulic Cylinder Rod Seals." *Sensors (Basel, Switzerland)* Vol. 21 No. 18 (2021). https://doi.org/10.3390/s21186012.

[271] Buck, R. C., Franklin, J., Berger, Urs, Conder, J. M., Cousins, I. T., Voogt, P. de, Jensen, Allan Astrup, Kannan, Kurunthachalam, Mabury, Scott A., and van Leeuwen, Stefan P. J., "Perfluoroalkyl and polyfluoroalkyl substances in the environment: Terminology, classification, and origins." *Integrated Environmental Assessment and Management* Vol. 7 No. 4 (2011): pp. 513–541. https://doi.org/10.1002/ieam.258.

[272] Kissa, E. *Fluorinated surfactants and repellents* CRC Press, New York, USA (2001).

[273] Glüge, J., Scheringer, M., Cousins, I., DeWitt, J., Goldenman, G., Herzke, D., Lohmann, R., Ng, C., Trier, X., and Wang, Z., "An overview of the uses of per- and polyfluoroalkyl substances (PFAS)." *Environmental Science: Processes & Impacts* Vol. 22 No. 12 (2020): pp. 2345–2373. https://doi.org/10.1039/D0EM00291G.

[274] Cousins, I. T., Ng, C. A., Wang, Z., and Scheringer, M., "Why is high persistence alone a major cause of concern?" *Environmental Science: Processes & Impacts* Vol. 21 No. 5 (2019): pp. 781–792. https://doi.org/10.1039/C8EM00515J.

[275] European Commision, "Regulation (EC) No 1907/2006 of the European Parliament and of the Council of 18 December 2006 concerning the Registration, Evaluation, Authorisation and Restriction of Chemicals (REACH).", 2006, https://echa.europa.eu/regulations/reach/, [May 20, 2025].

[276] European Chemicals Agency, “Opinion of the Committee for Risk Assessment and Opinion of the Committee for Socio-economic Analysis on an Annex XV dossier proposing restrictions of the manufacture, placing on the market or use of a substance within the EU.”, 2015, https://echa.europa.eu/documents/10162/13641/rest_pfoa_compiled_opi, [May 20, 2025].

[277] United States Environmental Protection Agency, “2010/15 PFOA Stewardship Program - Guidance on Reporting Emissions and Product Content.”, 2006, https://www.epa.gov/assessing-and-managing-chemicals-under-tsca/201015-pfoa-stewardship-program-guidance-reporting, [May 20, 2025].

[278] European Union, “Regulation (EU) 2019/1021 of the European Parliament and of the Council of 20 June 2019 on persistent organic pollutants (recast) (Text with EEA relevance).”, 2019, https://eur-lex.europa.eu/legal-content/en/TXT/?uri=CELEX:02019R1021-20241017&from=EN, [May 20, 2025].

[279] Henry, B. J., Carlin, J. P., Hammerschmidt, J. A., Buck, R. C., Buxton, L. W., Fiedler, H., Seed, J., and Hernandez, O., “A critical review of the application of polymer of low concern and regulatory criteria to fluoropolymers.” *Integrated Environmental Assessment and Management* Vol. 14 No. 3 (2018): pp. 316–334. https://doi.org/10.1002/ieam.4035.

[280] Arp, H. P. H., Gredelj, A., Glüge, J., Scheringer, M., and Cousins, I. T., “The Global Threat from the Irreversible Accumulation of Trifluoroacetic Acid (TFA).” *Environmental Science & Technology* Vol. 58 No. 45 (2024): pp. 19925–19935. https://doi.org/10.1021/acs.est.4c06189.

[281] Cui, J., Guo, J., Zhai, Z., and Zhang, J., “The contribution of fluoropolymer thermolysis to trifluoroacetic acid (TFA) in environmental media.” *Chemosphere* Vol. 222 (2019): pp. 637–644. https://doi.org/10.1016/j.chemosphere.2019.01.174.

[282] Lohmann, R., Cousins, I. T., DeWitt, J. C., Glüge, J., Goldenman, G., Herzke, D., Lindstrom, A. B., Miller, M. F., Ng, C. A., Patton, S., Scheringer, M., Trier, X., and Wang, Z., “Are Fluoropolymers Really of Low Concern for Human and Environmental Health and Separate from Other PFAS?” *Environmental Science & Technology* Vol. 54 No. 20 (2020): pp. 12820–12828. https://doi.org/10.1021/acs.est.0c03244.

[283] European Chemicals Agency, “Annex XV Restriction report: Proposal for a Restriction: Subtance name: Per- and polyfluoroalkyl substances (PFASs).”, Helsinki, Finnland, 2023, https://echa.europa.eu/documents/10162/1c480180-ece9-1bdd-1eb8-0f3f8e7c0c49, [May 20, 2025].

[284] European Chemicals Agency, “Progress update on the per- and polyfluoroalkyl substances (PFAS) restriction process.”, Helsinki, Finnland, 2024,

https://echa.europa.eu/documents/10162/67348133/pfas_status_update_report_en.pdf/fc30b694-cfb1-e9ed-7897-d9f3e4ef9ab7?t=1732088416751, [May 20, 2025].

[285] European Parliament, "Newsletter - Meetings of 23-25 April and 5 May 2025: Committee on Environment, Climate and Food Safety.", 2025, https://www.europarl.europa.eu/cmsdata/295056/Envi%20News%2023-24%20April%20&%205%20May%202025.pdf, [May 20, 2025].

[286] RATH AG, "Altraform KVR 164-502.", Data Sheet, Online (2017): p. 5, https://www.rath-group.com/fileadmin/content/Rath-Group/Downloads/Broschueren_Produkte/RATH_VacuumFormedShapes_201710_DE.pdf.

[287] C. Otto Gehrckens GmbH & Co. KG, "Technisches Datenblatt Vi 665.". COG, Pinnenberg, Germany (2024), https://www.cog.de/uploads/tx_datenblattgenerator/pdf/de/vi-665.pdf.

[288] Ansys® Academic Research Mechanical, Release 22.1, "Computer Software Material Library, ANSYS, Inc.".

[289] Vega Puga, Estefanía, Brendelberger, Stefan, Weber, Anika, and Sattler, Christian, "Modeling Development of a Receiver–Reactor of Type R2Mx for Thermochemical Water Splitting1." *Journal of Solar Energy Engineering* Vol. 146 No. 5 (2024): p. 51011. https://doi.org/10.1115/1.4065975.

[290] Lapp, J., Davidson, J. H., and Lipiński, W., "Heat Transfer Analysis of a Solid-Solid Heat Recuperation System for Solar-Driven Nonstoichiometric Redox Cycles." *J. Sol. Energy Eng* Vol. 135 No. 3 (2013): p. 031004. https://doi.org/10.1115/1.4023357.

[291] Ackermann, S., Takacs, M., Scheffe, J., and Steinfeld, A., "Reticulated porous ceria undergoing thermochemical reduction with high-flux irradiation." *Int. J. Heat Mass Transfer* Vol. 107 No. 4 (2017): pp. 439–449. https://doi.org/10.1016/j.ijheatmasstransfer.2016.11.032.

[292] Grobbel J., "Modeling Solar Particle Receivers with the Discrete Element Method.", Ph.D. Thesis. RWTH Aachen University, DLR, Aachen, NRW, Germany (2019), https://doi.org/10.18154/RWTH-2020-01764.

[293] Blumm, J., Lindemann, A., Meyer, M., and Strasser, C., "Characterization of PTFE Using Advanced Thermal Analysis Techniques." *International Journal of Thermophysics* Vol. 31 No. 10 (2010): pp. 1919–1927. https://doi.org/10.1007/s10765-008-0512-z.

[294] MatWeb, "Chemours Viton® A-601C Fluoroelastomer (FKM).", 2023, https://www.matweb.com/search/datasheet.aspx?MatGUID=13bac792747344e980ad9b58db36d715, [June 2023].

[295] Chemours, “Properties of Viton.”, 2023, https://chemours-util.my.salesforce-sites.com/CRG_VitonProperties, [June 2023].

[296] Touloukian, Y. S. and DeWitt, D. P. *Thermophysical properties of matter - the TPRC data series. Volume 8. Thermal radiative properties - nonmetallic solids. (Reannouncement). Data book*, United States (1972). https://www.osti.gov/biblio/5447756.

[297] Modest, M. *Radiative Heat Transfer* Academic Press, Oxford, UK (2013).

[298] ASME Research and Technology Committee on Water and Steam in Thermal Systems, Subcommittee on Properties of Steam. *ASME international steam tables for industrial use based on the IAPWS Industrial Formulation 1997 for the Thermodynamic Properties of Water and Steam (IAPWS-IF97)* American Society of Mechanical Engineers, New York, N.Y. (2000).

[299] Weber, A., “Simulation of a new receiver reactor concept.”, M. Ed. thesis. University Koblenz-Landau, Koblenz, NRW, Germany (2021).

[300] C. Otto Gehrckens GmbH & Co. KG, “Technisches Datenblatt Perlast G75B.”. COG, Pinnenberg, Germany (2021), https://www.cog.de/uploads/tx_datenblattgenerator/pdf/de/perlast-g75b.pdf.

[301] Vega Puga, E., Wachtendorf, V., Kömmling, A., Brendelberger, S., Jaunich, M., and Sattler, C., “Lifetime prediction and degradation assessment of FKM and FFKM O-rings under high temperature thermo-oxidative ageing.” *Polymer Testing* Vol. 147 (2025): pp. 1–17. https://doi.org/10.1016/j.polymertesting.2025.108820.

[302] Gillen, K. T. and Clough, R. L., “Rigorous experimental confirmation of a theoretical model for diffusion-limited oxidation.” *Polymer* Vol. 33 No. 20 (1992): pp. 4358–4365. https://doi.org/10.1016/0032-3861(92)90280-A.

[303] Wise, J., Gillen, K. T., and Clough, R. L., “Quantitative model for the time development of diffusion-limited oxidation profiles.” *Polymer* Vol. 38 No. 8 (1997): pp. 1929–1944. https://doi.org/10.1016/S0032-3861(96)00716-1.

[304] Hoffman, M. D., “Dynamic mechanical signatures of Viton A and plastic bonded explosives based on this polymer.” *Polymer Engineering & Science* Vol. 43 No. 1 (2003): pp. 139–156. https://doi.org/10.1002/pen.10012.

[305] ISO 188:2023, “Rubber, vulcanized or thermoplastic — Accelerated ageing and heat resistance tests.” International Organization for Standarization, Geneva, Switzerland, https://www.iso.org/standard/80468.html.

[306] ISO 48-4:2018, “Rubber, vulcanized or thermoplastic — Determination of hardness: Part 4: Indentation hardness by durometer method (Shore hardness).” International

Organization for Standarization, Geneva, Switzerland, https://www.iso.org/standard/74969.html.

[307] ISO 815-1:2019, "Rubber, vulcanized or thermoplastic — Determination of compression set: Part 1: At ambient or elevated temperatures." International Organization for Standarization, Geneva, Switzerland, https://www.iso.org/standard/74943.html.

[308] ISO 3384-1:2024, "Rubber, vulcanized or thermoplastic — Determination of stress relaxation in compression." International Organization for Standarization, Geneva, Switzerland, https://www.iso.org/standard/86478.html.

[309] Vega Puga, E., Brendelberger, S., Pierno, F., Wischek, J., and Sattler, C., "Sealability analysis of aged elastomer O-rings for usage in solar thermochemical water-splitting reactors." *Key Engineering Materials* Vol. 1007 (2025): pp. 37–48. https://doi.org/10.4028/p-p5fm2q.

[310] Song, I., Lee, T., Ryu, K., Kim, Y. Jin, K., Myung S., Park, J. W., and Kim, J. H., "Effects of heat and gamma radiation on the degradation behaviour of fluoroelastomer in a simulated severe accident environment." *Nuclear Engineering and Technology* Vol. 54 No. 12 (2022): pp. 4514–4521. https://doi.org/10.1016/j.net.2022.08.006.

[311] Lee, P.-C., Kim, S. Y., Ko, Y. K., Ha, J. U., Jeoung, S. K., Lee, J.-Y., and Kim, M., "Durability and Service Life Prediction of Fluorocarbon Elastomer under Thermal Environments." *Polymers* Vol. 14 No. 10 (2022): pp. 1–11. https://doi.org/10.3390/polym14102047.

[312] Zhang, Z., Liang, T., Jiang, Z., Jiang, X., Hu, J., and Pang, G., "Application of Infrared Spectroscopy in Research on Aging of Silicone Rubber in Harsh Environment." *Polymers* Vol. 14 No. 21 (2022). https://doi.org/10.3390/polym14214728.

[313] Mihaly, J., Sterkel, S., Ortner, H., Kocsis, L., Hajba, L., Furdyga, É., and Mink, J., "FTIR and FT-Raman Spectroscopic Study on Polymer Based High Pressure Digestion Vessels." *Croatica Chemica Acta* Vol. 79 No. 3 (2006).

[314] Trisna, B. A., Park, S., Park, I., Lee, J., and Lim, J. S., "Measurement report: Radiative efficiencies of (CF 3) 2 CFCN, CF 3 OCFCF 2 and CF 3 OCF 2 CF 3." *Atmospheric Chemistry and Physics* Vol. 23 No. 7 (2023): pp. 4489–4500. https://doi.org/10.5194/acp-23-4489-2023.

[315] Hiltz, J. A., "Characterization of fluoroelastomers by various analytical techniques including pyrolysis gas chromatography/mass spectrometry." *Journal of Analytical and Applied Pyrolysis* Vol. 109 (2014): pp. 283–295. https://doi.org/10.1016/j.jaap.2013.06.008.

[316] Rabinowitch, E. and Wood, W. C., “The collison mechanism and the primary photochemical process in solutions.” *Transactions of the Faraday Society* Vol. 32 No. 0 (1936): pp. 1381–1387. https://doi.org/10.1039/TF9363201381.

[317] Schutte, E., Weakley, T. J. R., and Tyler, D. R., “Radical Cage Effects in the Photochemical Degradation of Polymers: Effect of Radical Size and Mass on the Cage Recombination Efficiency of Radical Cage Pairs Generated Photochemically from the (CpCH2CH2N(CH3)C(O)(CH2)nCH3)2Mo2(CO)6 (n = 3, 8, 18) Complexes.” *Journal of the American Chemical Society* Vol. 125 No. 34 (2003): pp. 10319–10326. https://doi.org/10.1021/ja035030r.

[318] Kömmling, A., Jaunich, M., Pourmand, P., Wolff, D., and Gedde, U. W., “Influence of Ageing on Sealability of Elastomeric O‐Rings.” *Macromolecular Symposia* Vol. 373 No. 1 (2017). https://doi.org/10.1002/masy.201600157.

[319] Zaghdoudi, Maha, Kömmling, Anja, Jaunich, Matthias, and Wolff, Dietmar, “Scission, Cross-Linking, and Physical Relaxation during Thermal Degradation of Elastomers.” *Polymers* Vol. 11 No. 8 (2019). https://doi.org/10.3390/polym11081280.

[320] Salazar, E. A., Curro, J. G., and Gillen, K. T., “Physical and chemical stress relaxation of a fluoroelastomer.” *Journal of Applied Polymer Science* Vol. 21 No. 6 (1977): pp. 1597–1605. https://doi.org/10.1002/app.1977.070210615.

[321] Brown, R. and Forrest, M. *Long-term and accelerated ageing tests on rubbers*, Rapra Technology (2000).

[322] Repplinger, C., Sellen, S., Kedziora, S., Zürbes, A., and Maas, S., “Material modeling for numerical simulation of elastomer O-rings with experimental verification at low temperatures.” *International Journal of Hydrogen Energy* Vol. 80 (2024): pp. 1046–1061. https://doi.org/10.1016/j.ijhydene.2024.06.427.

[323] ITER, “ITER Vacuum Handbook.”, ITER-19-004 (2019), https://www.iter.org/sites/default/files/media/2024-04/iter_vacuum_handbook.pdf.

[324] Kalfayan, S. H., Silver, R. H., Mazzeo, A. A., and Liu, S. T., “Long Term Aging of Elastomers: Chemorheology of Viton B Fluorocarbon Elastomer.” *JPL Quart. Tech. Rev.* Vol. 2 No. 3 (1972).

[325] Omnes, B., “Arrhenius seal life prediction project: results and analysis.”. Valve World Publisher (2023), https://valve-world.net/arrhenius-seal-life-prediction-project-results-and-analysis/.

[326] Huang, R., Ma, S., Zhang, M., Yang, J., Wang, D., Zhang, L., and Xu, J., “Wear Evolution of the Glass Fiber-Reinforced PTFE under Dry Sliding and Elevated Temperature.” *Materials* Vol. 12 No. 7 (2019). https://doi.org/10.3390/ma12071082.

[327] Sujuan, Y., Quan, Y., Kunquan, L., Feng, T., Qing, F., Guibin, T., and Xing, H., "The Tribological and Sealing Properties of PFA Composites." *International Journal of Polymer Science* Vol. 2018 No. 1 (2018): p. 2302407. https://doi.org/10.1155/2018/2302407.

[328] Fricker, P., Baumann, M., and Bauer, F., "How different lubricants affect the wear of steel counterfaces in radial lip sealing systems." *Wear* Vol. 477 (2021): p. 203897. https://doi.org/10.1016/j.wear.2021.203897.

[329] DIN EN ISO 683-1, "Heat-treatable steels, alloy steels and free-cutting steels - Part 1: Non-alloy steels for quenching and tempering." DIN Media GmbH, Berlin, Germany, 2018, https://dx.doi.org/10.31030/2862248.

[330] Teyssedre, G., Dinculescu, S., Le Roy, S., Hahner, T., Lagomarsini, C., and Rybski, P., "Thermal Degradation Kinetics of High Temperature Polymers for Aeronautic Cables Insulation.", *2021 IEEE International Conference on the Properties and Applications of Dielectric Materials (ICPADM),* Johor Bahru, Malaysia, July 12-14, 2021. https://doi.org/10.1109/ICPADM49635.2021.9494003.

[331] García Tuero, A., Díez-Valbuena, G., Rivera, N., González, R., and Hernández Battez, A., "Changes in Hardness and Volume of Polymers in Contact with Lubricants Used in Electric Vehicle Transmissions.". *Proceedings of the XV Ibero-American Congress of Mechanical Engineering*: pp. 36–42. Cham, 2023.

[332] Haseeb, A.S.M.A., Jun, T. S., Fazal, M. A., and Masjuki, H. H., "Degradation of physical properties of different elastomers upon exposure to palm biodiesel." *Energy* Vol. 36 No. 3 (2011): pp. 1814–1819. https://doi.org/10.1016/j.energy.2010.12.023.

[333] Ucar, H. and Basdogan, I., "Dynamic characterization and modeling of rubber shock absorbers: A comprehensive case study." *Journal of Low Frequency Noise, Vibration and Active Control* Vol. 37 No. 3 (2017): pp. 509–518. https://doi.org/10.1177/1461348417725954.

[334] Feyzullahoğlu, E., "Abrasive wear, thermal and viscoelastic behaviors of rubber seal materials used in different working conditions." *Proceedings of the Institution of Mechanical Engineers, Part J* Vol. 229 No. 1 (2014): pp. 64–73. https://doi.org/10.1177/1350650114541750.

[335] Nelson, W. B. *Accelerated testing: statistical models, test plans, and data analysis* John Wiley & Sons, New York, USA (2009).

[336] Kennedy, Fr. E. and Tian, X., "The Effect of Interfacial Temperature on Friction and Wear of Thermoplastics in the Thermal Control Regime.". *Tribology Series Dissipative Processes in Tribology*. Elsevier (1994): pp. 235–244.

[337] Li, X., Peng, G., Liu, W., and Li, Z., "Research on dynamic simulation method of leakage prediction for hydraulic system." *Proceedings of the Institution of Mechanical Engineers, Part C* Vol. 229 No. 4 (2014): pp. 771–786. https://doi.org/10.1177/0954406214539469.

[338] Guo, F., Jia, X., Longke, W., Salant, R. F., and Wang, Y., "The Effect of Wear on the Performance of a Rotary Lip Seal." *Journal of Tribology* Vol. 136 No. 4 (2014): pp. 417031–417038. https://doi.org/10.1115/1.4027623.

[339] Avanzini, A. and Donzella, G., "A computational procedure for life assessment of UHP reciprocating seals with reference to fatigue and leakage." *International Journal of Materials & Product Technology* Vol. 30 (2007): pp. 33–51. https://doi.org/10.1504/IJMPT.2007.013107.

[340] Python Software Foundation, "Python 3.11.4 documentation.", 2023, https://docs.python.org/release/3.11.4/.

[341] Linstrom, P., "NIST Chemistry WebBook, NIST Standard Reference Database 69." (1997). https://doi.org/10.18434/T4D303.

[342] Hoes, M., Ackermann, S., Theiler, D., Furler, P., and Steinfeld, A., "Additive-Manufactured Ordered Porous Structures Made of Ceria for Concentrating Solar Applications." *Energy Technology* Vol. 7 No. 9 (2019): p. 1900484. https://doi.org/10.1002/ente.201900484.

[343] Pein, M., Keller, J., Agrafiotis, C., Eltayeb, A., Klaas, L., Neumann, N., Roeb, M., and Sattler, C., "Thermochemical Oxygen Pumping with Perovskite Reticulated Porous Ceramics for Enhanced Reduction of Ceria in Thermochemical Fuel Production." *Advanced Energy Materials* Vol. 14 No. 19 (2024): p. 2304454. https://doi.org/10.1002/aenm.202304454.

[344] Goodwin, D. G., Moffat, H. K., Schoegl, I., Speth, R. L., and Weber, B. W., "Cantera: An Object-oriented Software Toolkit for Chemical Kinetics, Thermodynamics, and Transport Processes." https://www.cantera.org, Version 3.1.0, https://doi.org/10.5281/ZENODO.14455267.

[345] Weber, A., Grobbel, J., Neises-von Puttkamer, M., and Sattler, C., "Swept open moving particle reactor including heat recovery for solar thermochemical fuel production." *Solar Energy* Vol. 266 (2023): p. 112178. https://doi.org/10.1016/j.solener.2023.112178.

Appendix

A. Effect of discretisation level of transport step

During the transport step, where the RMA is moved from the reduction reactor to the oxidation reactor, the seals are expected to experience their highest operating temperatures. To evaluate the effect of the transport trajectory discretisation, different levels of resolution were compared in terms of their influence on the seals' maximum temperature. Three discretisation cases were simulated, incorporating 4, 7, and 14 intermediate positions between the reduction and the oxidation reactors, respectively. Figure 4.4 illustrates an example of the transport step discretisation when 4 positions are examined. In all cases, the total RMA transfer time between the reduction and oxidation reactors is assumed to be 4 s, with a total displacement trajectory of 785 mm. Both of these parameters determine the time step and RMA location at intermediate transport step positions for the evaluated discretisation cases.

Results

Figure A.1 shows the O-ring's maximum temperature development as a function of transport step time and trajectory discretisation level. In general, all discretisation levels (4, 7, and 14 positions) exhibit a similar trend, where the O-ring's maximum temperature increases rapidly to reach a peak before gradually declining towards the end of the transport step. This behaviour arises as the hot RMA moves closer to the O-ring, increasing the radiative heat transfer until reaching a position of closest proximity, after which the RMA moves away, decreasing again radiative heat transfer, until the transport step is completed, when the RMA reaches the oxidation reactor.

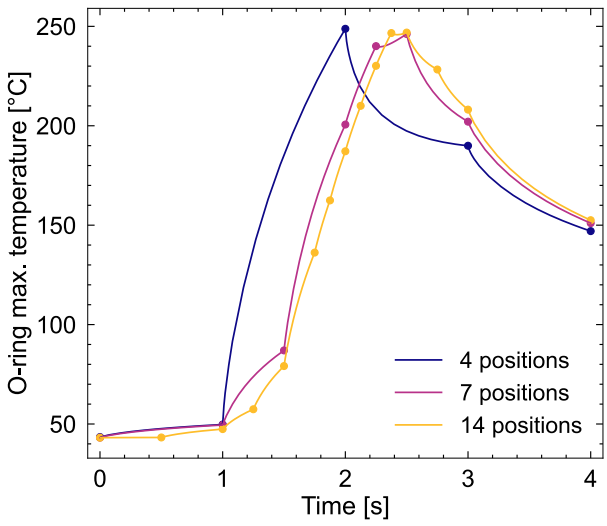

Figure A.1: O-ring maximum temperature as a function of discretisation level and transport step time. Markers are used to indicate the positions at which the different transient heat transfer simulations were conducted.

The peak O-ring temperature occurs at approximately the midpoint of the transport trajectory, where the radiative heat transfer from the hot RPC is most significant due to their close proximity and large view factors. At the lowest discretisation level (4 positions), the peak O-ring temperature reaches 248.8 °C precisely at the midpoint of the transport step. In the cases with higher discretisation levels (7 and 14 positions), the peak temperatures are 246.2 °C and 246.9 °C, respectively, occurring slightly after the midpoint at 2.5 s. The variation between the highest and lowest peak temperature is only 0.7%, indicating that even lower discretisation levels provide a reasonable approximation of the O-ring's maximum temperature. Nevertheless, higher discretisation levels result in a smoother temperature curve, while the lowest discretisation level leads to more abrupt changes. By the end of the transport step, the O-ring's maximum temperature decreases to 147 °C, 151 °C, and 152 °C for 4, 7, and 14 transport step positions, respectively. The slightly higher final temperatures observed at higher discretisation levels may be attributed to the peak temperature occurring later in the transport step, reducing the time available for O-ring cooling.

In the transport step simulation, the maximum rod seal temperature was also investigated. Figure A.2 shows the rod seal's maximum temperature throughout the transport step for different discretisation levels. In all discretisation cases, the rod seal's temperature increases in a stepwise manner as the transport step progresses. At higher discretisation levels, these temperature increments become more gradual and frequent, reflecting a more accurate representation of the continuous movement of the transport rod. Particularly, towards the end of the transport step, peak temperatures are observed due to the direct contact between the rod seal and the hottest section of the transport rod, the region closest to the RMA. For the lowest discretisation level (4 positions) the maximum rod seal temperature reaches 149.1 °C, while for higher discretisation levels peak temperatures are 154.1 °C and 153.9 °C for 7 and 14 positions, respectively. The difference between highest and lowest peak temperatures is only 3.2%, suggesting that even lower discretisation levels provide a reasonable approximation of the rod seal's maximum temperature. Furthermore, despite differences in discretisation, all cases converge to similar final temperatures (~150 °C) at the end of the transport step.

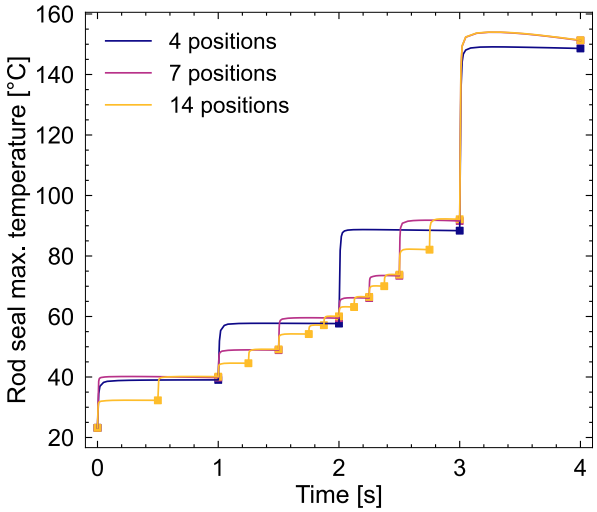

Figure A.2: Rod seal maximum temperature as a function of discretisation level and transport step time. Markers are used to indicate the positions at which the intermediate transient heat transfer simulations were performed.

In summary, though there are small differences between the discretisation levels, 4 positions give a good approximation of the expected maximum temperatures and provides a reasonable temperature profiles for the O-ring and rod seals.

B. Rod seal experiment

Figure B.1: Image of a rough rod used for testing at ambient temperature after 4 days of use. Black PTFE film is observable on the surface.

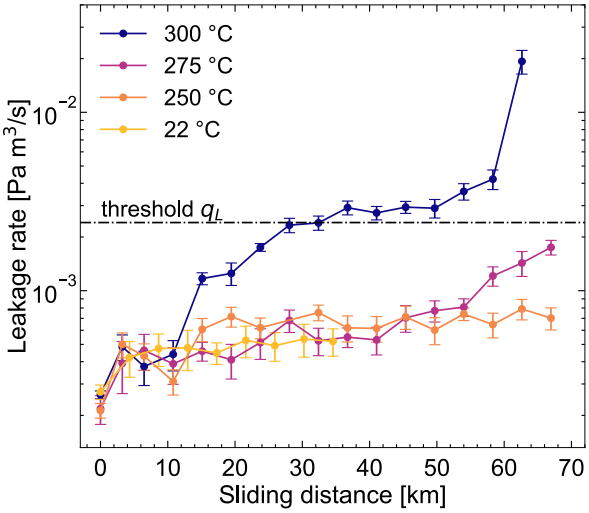

Figure B.2: Leakage rate of PTFE lip seals as a function of testing temperature and sliding distance. Threshold leakage value is represented by a black dash dot line.

Table B.1: Standard deviation of leakage rate measurements of lip seals tested with a rough rod as a function of sliding distance and testing temperature. These error measurements refer to the data plotted in Figure 6.13.

Sliding distance	**Testing temperature [°C]**		
[km]	*250*	*275*	*300*
0.00	2.00E-04	4.00E-04	1.31E-04
3.24	8.00E-04	1.27E-03	8.00E-04
6.48	7.24E-04	1.06E-03	8.20E-04
10.80	5.00E-04	9.04E-04	8.50E-04
15.12	9.04E-04	5.52E-04	9.00E-04
19.44	9.10E-04	9.02E-04	1.80E-03
23.76	8.27E-04	1.00E-03	8.77E-04
28.08		9.80E-04	2.16E-03
32.40	7.60E-04	9.18E-04	2.20E-03
36.72	1.03E-03	6.90E-04	2.60E-03
41.04	1.01E-03	9.37E-04	2.36E-03
45.36	1.06E-03	1.20E-03	2.27E-03
49.68	1.04E-03	1.05E-03	3.45E-03
54.00	5.97E-04	9.13E-04	3.80E-03
58.32	1.02E-03	1.50E-03	5.31E-03
62.64	1.04E-03	2.28E-03	2.93E-02
66.96	9.96E-04	1.65E-03	

C. Peak efficiency set

Table C.1: Data corresponding to the peak efficiency set from Brendelberger [26]

Variable name	Value	Unit
Temperature of cavity	2100	K
Partial pressure of oxygen	105	Pa
Radius of RMA	0.01	m
Concentration factor	4600	-
Maximum surface fraction	15	-
Heat-to-electricity conversion efficiency	0.4	-
Steam conversion rate	0.35	-
Number of apertures	8	-
Radius of aperture	0.18	m
Oxidation temperature	1200	K
Optimal reduction time	100	s
Number of RMAs	1491.12	-
Heat flux solar	7014.57	kW
Heat flux in the receiver	3745.78	kW
Heat flux during ox.	365.62	kW
Energy flow from H_2	737.59	kW
Pump number	0.00131	-
Receiver efficiency	0.752253	-
Receiver-reactor efficiency	0.17411	-
Optical efficiency	0.534	-
Plant efficiency	0.104772	-